Investigating directed differentiation strategies in hiPSCs to model cell type-specific vulnerability in ALS

Jamie Mitchell

Institute of Neurology

and

The Francis Crick Institute

PhD Supervisors: Professor Rickie Patani and Professor Nicholas Luscombe

A thesis submitted for the degree of

Doctor of Philosophy

University College London

May 2021

Declaration

I, Jamie Samuel Mitchell, confirm that the work presented in this thesis is my own. Where information has been derived from other sources, I confirm that this has been indicated in the thesis.

Abstract

The concept of vulnerability is highly relevant to neurodegenerative diseases, whereby specific subsets of neurons display marked and devastating disease-related pathologies, but neighbouring cells may not. Amyotrophic lateral sclerosis (ALS) provides a perfect example, where spinal pathology manifests in lower motor neurons (MNs), with neighbouring cells remaining relatively unaffected, at least until late-stage disease. Interestingly, spinal MNs display selective vulnerability, with larger and more heavily myelinated alpha motor neurons degenerating the earliest. Additionally, the role of cell types surrounding MNs in contributing to ALS pathogenesis have become more evident over recent years. This includes non-cell-autonomous toxicity mediated by astrocytes and the denervation of Renshaw interneurons (INs) from MNs. Subsequent elucidation of mechanisms underlying cell type-specific vulnerability in ALS would drastically improve our understanding of ALS, the spectrum of cell types affected and provide alternative and tractable cellular targets for therapeutic intervention.

The advent of human induced pluripotent stem cells (hiPSCs) has revolutionised disease modelling, providing a virtually inexhaustible source of patient-specific material. As a consequence, a variety of cell types has been generated using ontogeny-driven directed differentiation strategies. However, there is a pressing need for deeper phenotyping and further refinement of differentiation strategies, in order to generate more enriched and disease-relevant populations.

With this in mind, I employed an established hiPSC-derived MN protocol and manipulated extrinsic signalling cues during two distinct developmental phases; patterning and terminal differentiation. In this manner, I was able to induce post-mitotic motor columnar diversity, resulting in the specification of lateral motor column phenotype; highly susceptible to degeneration in ALS. Separately, I was able to generate hiPSC-derived dorsal spinal INs arising from dI4-6, which subserve pain, temperature, itch and touch sensations (dI4&5) or indeed those regulating left-right coordination (dI6). Importantly, these INs retain the same axial identity, but are positioned more dorsally in the absence of sonic hedgehog signalling.

Lastly, hiPSC-derived INs and MNs were investigated in a valosin-containing protein (VCP) mutant model of ALS. This revealed key differences relating to cell type vulnerability between MNs and INs, including RNA binding protein mislocalisation and alternative splicing events. Overall, the results of this PhD present novel ontogeny-driven directed differentiation strategies of hiPSC-derived cell types and a robust platform for modelling mechanisms of selective vulnerability in ALS. The experiments contained herein also demonstrate that iPSC models can capture neuronal subtype-selective vulnerability.

Impact Statement

Amyotrophic lateral sclerosis (ALS) is a devastating neurodegenerative disorder stemming from the degeneration of upper and lower motor neurons (MNs) of the motor cortex and spinal cord respectively. As a result, ALS is considered a 'MN-centric' disorder characterised by progressive loss of muscle control through atrophy, weakness and spasticity and often resulting in death from respiratory failure within 2-5 years of diagnosis.

Recently; however, the role of surrounding cell types such as astrocytes has been interrogated, revealing prominent mechanisms of cell autonomous and non-cell-autonomous toxicity. Despite this, the spinal cord is extraordinarily complex, with a large array of molecularly distinct neuronal cell types involved in an array of spinal circuits. Therefore, elucidating the full spectrum of vulnerability, cell autonomous and non-cell-autonomous mechanisms of toxicity from surrounding cell types will greatly increase our understanding of ALS and mechanisms underlying selective vulnerability of MNs. Further, this will assist in the identification of novel therapeutic targets, which are greatly needed in ALS.

The results of this thesis detail robust and highly characterised directed differentiation strategies for the generation of subpopulations of lateral motor column MNs innervating limb muscles; highly susceptible to degeneration in ALS. Crucially, MN subtype diversity is generated at post-mitotic stages, closely aligning with that seen during endogenous development. Further mechanisms of ontogeny-driven methods for the specification of dorsal populations of dI4-6 interneurons (INs) responsible for pain, temperature, itch and touch sensations and also subserving motor outputs, were also elucidated. Importantly, these dorsally positioned INs possess the same axial identity as hiPSC-derived MNs.

Together, the generation of these hiPSC-derived cell types provide a powerful tool to model cell type-specific vulnerability in ALS. Indeed, ALS mutant MNs and INs were observed to display differential vulnerability to RNA binding protein mislocalisation, a highly studied pathological hallmark of ALS. As such, these data form the basis for an in-depth characterisation of the role of INs in ALS, and provide a crucial model to study cell type-specific vulnerability in ALS.

Acknowledgements

Firstly, I would like to extend my immense gratitude to Professor Rickie Patani for giving me the opportunity, support and guidance throughout my PhD. Your limitless capacity for support and excellent advice, enthusiasm and dedication to ALS as a researcher and clinician is second to none and a huge inspiration to me.

Additionally, I would like to thank every member of the Patani lab both former and current. It is a special feeling to be able to work amongst such a capable and intelligent group of scientists.

To complete a PhD in Neuroscience at UCL and the Francis Crick Institute was never something that I imagined I could achieve. The highs and the lows have all taught me valuable lessons in mental resilience and have cemented my love for this subject.

I would also like to extend my sincerest thank you to everyone at the Wakefield Street site at UCL where I first embarked on this journey. I will always treasure the amazing times we had both in and out of the lab. In particular, our frequent visits to the Harrison's pub where many a good night was had.

I would also like to thank Filipa for helping me through the peaks and troughs of PhD life and always being there to pull me through and lend an ear when needed.

Lastly, I would like to thank my family and in particular my mum, dad and sister for all of their help and support throughout.

Table of Contents

List of Figures

List of Tables

Abbreviations

AD	Alzheimer’s disease
ALS	Amyotrophic lateral sclerosis
AS	Alternative splicing
BCA	Bicinchoninic acid assay
bHLH	Basic helix-loop-helix
BMP	Bone morphogenetic protein
BSA	Bovine serum albumin
cDNA	Complementary DNA
CPG	Central pattern generator
CYP26A1	Cytochrome P450 26A1
DDX39A	DExD-box helices 39A
dI	Dorsal interneuron
DMSO	Dimethyl sulfoxide
DNA	Deoxyribonucleic acid
dP	Dorsal progenitor
E8	Essential 8
EDTA	Ethylenediaminetetraacetic acid
fALS	Familial amyotrophic lateral sclerosis
FF	Fast-twitch fatigable
FFR	Fast-twitch fatigue resistant
FGF	Fibroblast growth factor
FUS	Fused in sarcoma
GRN	Gene regulatory network
H3K27me3	Histone 3 lysine27 trimethylation
HD	Homeodomain
hiPSC	Human induced pluripotent stem cell
HMC	Hypaxial motor column
hnRNPA1	Heterogenous nuclear ribonucleoprotein A1
IBM	Inclusion body myositis
IN	Interneuron
IR	Intron retention

IRT	Intron retained transcript
KCl	Potassium chloride
LMC	Lateral motor column
MAPT	Microtubule associated protein tau
mESC	Mouse embryonic stem cell
MMC	Median motor column
MN	Motor neuron
MND	Motor neuron disease
MOPS	3-(N-morpholino)propanesulfonic acid
MSP	Multisystem proteinopathy
OPC	Oligodendrocyte precursor
PBS	Phosphate buffered saline
PBST 0.1%	Phosphate buffered saline – 0.1% tween
PCR	Polymerase chain reaction
PD	Parkinson's disease
PGC	Preganglionic motor column
qICC	Quantitative immunocytochemistry
qPCR	Quantitative polymerase chain reaction
RA	Retinoic acid
RALDH2	Retinaldehyde dehydrogenase 2
RAN	Non-AUG-dependent
RAR	Retinoic acid receptor
RARE	Retinoic acid response element
RBP	RNA binding protein
RCF	Relative centrifugal force
RNA	Ribonucleic acid
RNAseq	RNA sequencing
RT	Reverse transcriptase
RXR	Retinoid X receptor
sALS	Sporadic amyotrophic lateral sclerosis
SFPQ	Splicing factor proline and glutamine rich
SFR	Slow-twitch fatigue resistant

SHH	Sonic hedgehog
SMA	Spinal muscular atrophy
SOD1	Superoxide dismutase 1
TARDBP	TAR DNA binding protein
TDP-43	TAR DNA-binding protein 43
TGF-β	Transforming growth factor-beta
VCP	Valosin-containing protein
WNT	Wingless-related integration site

Chapter 1. General Introduction

1.1 Spinal cord development

The function of the spinal cord is to integrate sensory information from the periphery and generate an appropriate motor response (Sagner & Briscoe. 2019). Sensory information in the form of pain, touch, temperature, chemoreception and proprioception are relayed from peripheral sites including skin, muscles and internal organs, to the spinal cord (Lai et al. 2016). Cell bodies of these somatosensory neurons reside in the dorsal root ganglia and peripheral information is predominantly integrated in the dorsal horn of the spinal cord. Next, motor responses are either generated directly, as demonstrated with spinal reflexes, or the information is relayed to higher brain centres via ascending spinal tracts (Arber. 2012). Descending spinal tracts then relay motor responses that are mediated by ventrally positioned motor neuron (MN) effectors (Jessell. 2000). As such, the spinal cord is a complex structure comprised of heterogeneous populations of cells (Alaynick et al. 2011; Lu et al. 2015; Lai et al. 2016). Despite this complexity, research predominantly in mice has detailed a developmental logic underlying the organisation of the spinal cord that is based on a modular organisation (Jessell. 2000). Subsequently, cells with similar functional properties occupy stereotypical settling positions, forming these modules. This organisation is accomplished during embryonic development of the neural tube, whereby intricately regulated spatial and temporal cues first establish a matrix of regional identities, with the governing principle underlying the generation of neuronal diversity being that of positional identity. As a result, three main axes are prefigured from which regional identity in the developing neural tube emanates including the rostral-caudal and dorsal-ventral axes (Jessell. 2000; Sagner & Briscoe. 2019). Additionally, progenitors migrate laterally from initial medial locations in the ventricular zone of the neural tube, thus generating the third (medial-lateral) developmental axis. Subsequent characterisation of spinal cord populations has been achieved through the identification of molecular expression profiles, cell body settling positions, axonal trajectories and target cell types, neurotransmitter/s used and neuronal connectivity patterns (Alaynick et al. 2011; Lu et al. 2015; Lai et al. 2016).

1.1.1 Rostral-caudal patterning

Rostral-caudal patterning of the spinal cord is predominantly governed by the complex interplay between retinoic acid (RA), fibroblast growth factors (FGF), Wingless-related integration site (WNTs) and GDF11 that act to enhance/repress the expression of different HOX genes (Ensini et al. 1998; Liu et al. 2001; Bel-Vialar et al. 2002; Dasen et al. 2003). HOX genes are a highly conserved subset of homeobox genes defined by the presence of a unique 60 amino acid region that acts as a DNA binding motif (reviewed by Philippidou & Dasen. 2013). In vertebrates, a total of 39 HOX genes have been identified; although it should be noted that not all are present in each vertebrate species. These HOX genes can be pooled into four distinct clusters: HOXA, HOXB, HOXC and HOXD and each cluster be further separated into sub-classes containing 13 paralog groups (HOX1-13). However, not all paralogs are found in every cluster. Interestingly, HOX genes exhibit a property known as 'spatial colinearity', in which HOX genes are arranged in a contiguous cluster and their expression patterns along the rostral-caudal axis match the gene position along the chromosome (Figure 1.1) (Kmita & Duboule. 2003). In addition, HOX genes also display temporal colinearity, whereby HOX genes positioned at the 3' end of the cluster become transcriptionally active earlier and at more rostral levels than those at the 5' end; delineating more caudal positions (Gellon & McGinnis. 1998). This is thought to be a result of progressive chromosomal modifications (Soshnikova & Duboule. 2009). Overall, HOX genes display a remarkable level of spatial and temporal regulation culminating in their strict, but overlapping, domain expression profiles along the rostral-caudal axis. Broadly, HOX1-5 paralogs denote a hindbrain position, HOX4-7 cervical, HOX9 thoracic and HOX10-11 lumbar segments (Figure 1.1) (Dasen et al. 2003; Philippidou et al. 2012; Philippidou & Dasen. 2013). During gastrulation, the combinatorial effects of FGF and WNT signalling induce the formation of a proliferative 'stem-zone' at the posterior end of the embryo (Akai et akl. 2005). Progenitors are maintained in a proliferative state within this 'stem-zone', and on exit; give rise to both mesodermal and neuronal derivatives. These progenitor populations are therefore termed the neuromesodermal stem cell population (Stern et al. 2006). Subsequently, as the spinal cord axis elongates, progenitors in the 'stem-zone' are exposed to a range of signalling molecules that progressively activate the expression of more caudal HOX genes located at more distal sites within the clusters (Philippidou & Dasen. 2013). HOX expression is therefore essential during axis elongation, in which the proliferative 'stem-zone' is

associated with the growth of the caudal tail bud, resulting from the removal of repressive chromatin marks from HOX loci and subsequent HOX gene activation (Soshnikova & Duboule. 2009). This leads to the establishment of distinct and overlapping domains of HOX expression profiles along the rostral-caudal axis.

The process of spinal cord axis elongation and the establishment of the HOX code stems from a complex interplay between FGF and RA signalling (Figure 1.1). Indeed, FGFs are directly responsible for maintaining the caudal 'stem-zone', actively establishing the caudal limit of RA signalling by inducing CYP26A1 and repressing RALDH2 expression (Diez del Corral & Storey. 2004). In turn, RA represses FGF signalling, thereby delineating the rostral limit of FGF and subsequent 'stem-zone' activity (Liu et al. 2001; Bel-Vialar et al. 2002; Sirbu & Duester. 2006; Kumar & Duester. 2014). Progenitors exiting the proliferative 'stem-zone' are exposed to high concentrations of RA secreted from the adjacent somites. It should be noted that FGF signalling plays a crucial role in the timing of somitogenesis from the presomitic mesoderm (Naiche et al. 2011). Indeed, somitogenesis occurs in the aftermath of high concentrations of caudal FGF4 and FGF8, when FGF signalling and respective motility have reduced to low levels. Furthermore; RA generated by RALDH2 in the presomitic mesoderm during the late primitive streak stage acts directly to confine the expression of FGF8 to the primitive streak tissue posterior to the node (Sirbu & Duester. 2006). Indeed, RALDH2 null mouse embryos exhibit ectopic expression of FGF8 in the neuroectoderm and node ectoderm lying just anterior to the epiblast ectoderm. This resulted in excessive FGF8 signalling in the presomitic mesoderm in RALDH2 null mice, leading to smaller somites and the induction of left-right asymmetry in the presomitic mesoderm, that does not normally occur (Meyers & Martin. 1999). RA signalling from adjacent pairs of somites acts by binding to heterodimers of retinoic acid receptors (RARs) and retinoid X receptors (RXRs), which then bind to specific DNA motifs called retinoic acid response elements (RAREs); often present in promotor regions of genes (Mahony et al. 2011). Indeed, a conserved RARE has been identified in the promotor region of FGF8 in human and rodents further supporting the direct repression of FGF8 by RA (Brondani et al. 2002; Balmer & Blomhoff. 2005; Kumar & Duester. 2014). Alternatively, liganded RAR-RXR also recruits histone acetylase complexes and trithorax proteins that promote chromatin relaxation and gene activation (Gillespie & Gudas. 2007; Mazzoni et al. 2013). This

rapidly induces the removal of polycomb repressive complex 1 (PRC1) and PRC2 and the repressive chromatin mark; histone 3 lysine27 trimethylation (H3K27me3) from HOX genes predominantly at the 3' end (Mahony et al. 2011; Mazzoni et al. 2013). The actions of RA have been studied extensively in hindbrain development where RA signalling leads to a more caudal rhombomere identity (Marshall et al. 1992). Conversely, removing RA promotes a more rostral rhombomere identity (Niederreither et al. 2000). FGF signalling is mediated by the induction of the expression of Cdx proteins that are sufficient to induce caudal HOX gene expression (Bel-Vialar et al. 2002). Similar to RA, the combination of FGF and Cdx transcription factors function to remove H3K27me3 from posterior HOX paralogs (Mazzoni et al. 2013). Lastly, FGF acts in tandem with WNT and GDF11 signalling to induce HOX10 gene expression at lumbar levels (Liu et al. 2001; Gouti et al. 2014; Metzis et al. 2018).

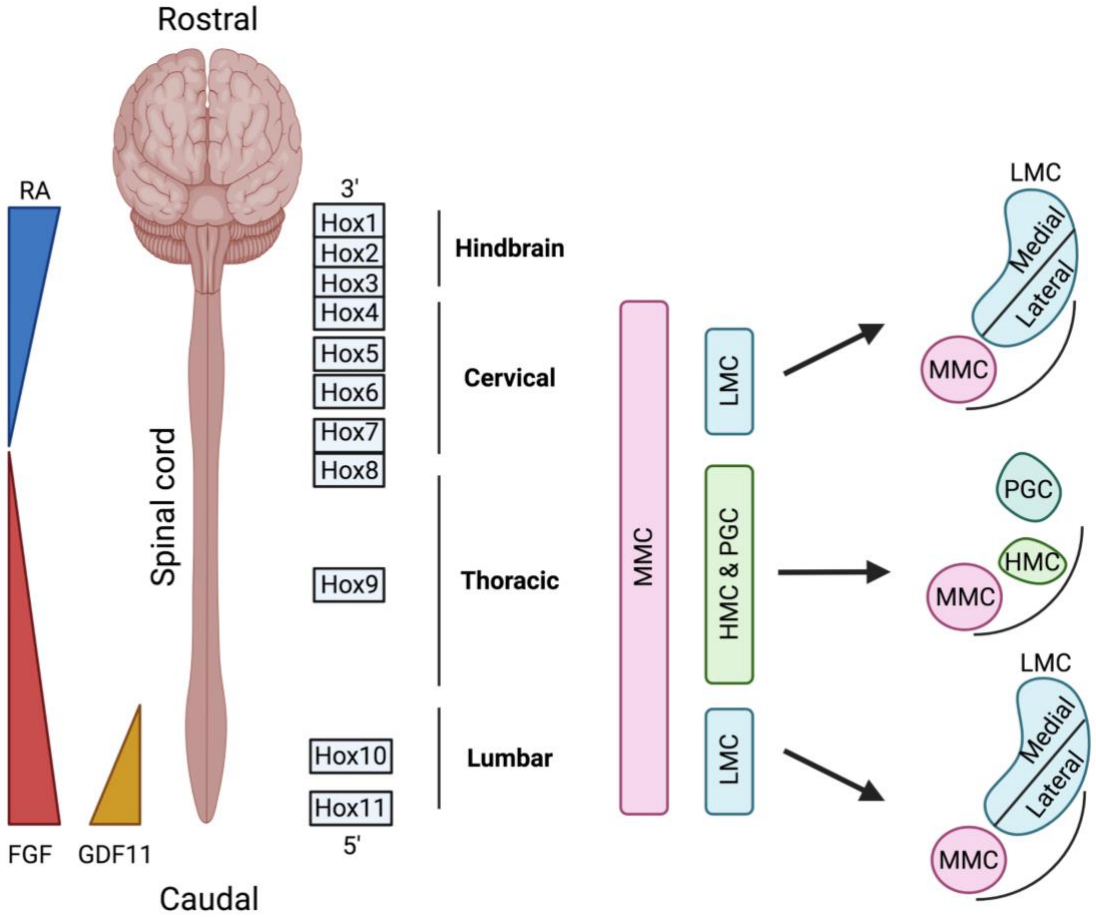

Figure 1.1 Rostral-caudal patterning of the neural tube

Rostral-caudal patterning of the neural tube is established by the complex interplay of retinoid, FGF and GDF11 signalling and their effects on chromatin remodelling of HOX genes. These signals are predominantly secreted from surrounding mesodermal tissue such as presomitic mesoderm, somites and paraxial mesoderm. The subsequent HOX code delineates rostral-caudal regionality of the spinal cord and also contributes to the establishment of distinct motor columns at different rostral-caudal levels. This includes the presence of the lateral motor column (LMC) at brachial and lumbar levels, that is induced by retinoid signalling from adjacent somites. Figure created using BioRender. Retinoic acid (RA), fibroblast growth factor (FGF), growth differentiation factor 7 (GDF7), median motor column (MMC), lateral motor column (LMC), hypaxial motor column (HMC), preganglionic motor column (PGC).

1.1.2 Dorsal-ventral neural tube patterning

Dorsal-ventral patterning is mediated by the secretion of specific signalling molecules termed morphogens (Jessell. 2000; Briscoe & Small. 2015). These morphogens are distinct from other signalling molecules in their ability to induce distinct cellular responses in a concentration-dependent manner and are also able to exert their effects at a distance; acting in an autocrine and/or paracrine manner (Christian. 2011). Opposing gradients of diffusible morphogens, secreted from distinct ‘organising centres’, give rise to a matrix of regional identities which form discrete precursor domains, from which molecularly distinct subclasses of neurons emerge (Jessell 2000; Butler & Bronner. 2015). Sonic hedgehog (SHH) is secreted initially from the notochord and later by the floor plate and acts to induce a ventral subtype specification (Figure 1.2) (Marti et al. 1995; Roelink et al. 1995; Jessell. 2000; Ingham & McMahon. 2001). Conversely, bone morphogenetic proteins (BMPs), WNTs and transforming growth factor-beta (TGF-β) are secreted from the roof plate, establishing dorsal fate specification (Liem et al. 1997; Wodarz & Nusse. 1998; Lee et al. 2000; Massague & Chen. 2000; Wine-Lee et al. 2004). Spatial organisation of the neural tube stems from tight temporal regulation in the timing and concentration of these secreted morphogens, with autocrine and paracrine regulation providing further nuanced control. Anti-parallel morphogen gradients act to induce the expression of two classes of transcription factors: the homeodomain (HD) and basic helix-loop-helic (bHLH) classes (Briscoe et al. 2000; Alaynick et al. 2011). This multidimensional and stereotyped program of neural tube patterning yields eleven

progenitor domains in the spinal cord including six dorsal (dP1-6) and five ventral progenitor domains (P0, P1, P2, pMN and P3) from which neurons arise (Figure 1.2) (Alaynick et al. 2011; Lu et al. 2015; Lai et al. 2016). Progenitors then migrate laterally from the ventricular / progenitor zone of the neural tube, forming dorsal interneuron (dI) domains 1-6 (dI1-6) and ventral V0, V1, V2, pMN and V3 domains with discrete populations of post-mitotic neurons. Studies from mouse models show that spinal cord interneurons (INs) originate and migrate from the ventricular zone at e10.5-e11.5 (Lai et al. 2016). Following the first developmental 'wave' of interneuronogenesis, a subsequent wave (e11-13) yields two additional IN pools from the dI4 and dI5 progenitor domains, termed dIL^{A} and dIL^{B}. It is noteworthy that no IN populations derive from the pMN domain, from which MNs arise. Neurogenesis takes place for only a brief period of time before progenitors switch to give rise to glial populations (Rowitch & Kriegstein. 2010).

Spinal cord domains can be molecularly discriminated at the progenitor and post-mitotic stage through their differential expression of HD and bHLH transcription factors (Lu et al. 2015; Lai et al. 2016; Alaynick et al. 2011). Importantly, these transcription factors exhibit extensive cross-regulation, leading to the establishment of gene regulatory networks (GRNs) that modify gene expression and specify cell identity (Kutejova et al. 2016). During early development, neural tube progenitors possess multiple GRN components that are necessary to specify all progenitor fates (reviewed by Sagner & Briscoe. 2019). However, exposure to morphogens in a concentration and time-dependent manner results in the repression of specific GRN elements and the enhancement of others (Kutejova et al. 2016). This acts as a lineage restriction mechanism for a defined neural tube cell fate, with the active repression of alternate lineages. The ventral neural tube presents a typical example of this, where graded responses to SHH secreted from the notochord and floor plate establish class II (activated by high levels of SHH) and class I (repressed by high levels of SHH) transcription factors (Briscoe et al. 2000; Peterson et al. 2012; Nishi et al. 2015). As a result, the proximity of progenitors relative to the floor plate determines the level of exposure to SHH signalling and subsequently their identity (Dessaud et al. 2007; Balaskas et al. 2012; Cohen et al. 2014). Extensive cross-repression of GRN transcription factors in this region of the neural tube is essential for correct specification of the ventral-most P3, pMN and P2 domains. This is mediated through the actions of four main transcription factors (NKX2.2, OLIG2, PAX6 and IRX3) whose

expression profiles can discriminate P3, pMN and P2 domain identities (Figure 1.2) (Alaynick et al. 2011; Lu et al. 2015; Lai et al. 2016). High levels of SHH signalling drive the expression of OLIG2 in the pMN domain and NKX2.2 in the P3 domain and these transcription factors in turn, actively repress the expression of IRX3 and PAX6 (Jeong & McMahon. 2005; Balaskas et al. 2012; Kutejova et al. 2016). This results in lower expression levels of PAX6 in the pMN and no expression in the P3 domain. In contrast, the P2 domain expresses high levels of PAX6 and IRX3, both of which act to repress OLIG2 and NKX2.2 expression in this domain. This highlights the key spatial and temporal dynamics of the ventral GRN; governed by SHH signalling, and the importance of cross-repressive transcription factors in the establishment of sharp boundaries between domains (Briscoe & Small. 2015; Cohen et al. 2013).

The dorsal neural tube is patterned by a structure called the roof plate, consisting of a group of glial cells positioned at the dorsal midline of the neural tube (Liem et al. 1997; Lee et al. 2000; Massague & Chen. 2000; Wine-Lee et al. 2004; Andrews et al. 2017). Importantly, these glial populations exit the cell cycle earlier than any other dorsal progenitor population, where they then secrete BMPs and WNTs that are crucial for the accurate patterning of the dorsal spinal cord (Parr et al. 1993; Liem et al. 1995). Indeed, genetic mouse models that lack roof plate-derived BMP and WNT signalling exhibit marked differences in dorsal domain specification, with the ablation of dI1 and dI2 domains and a dorsal shift in dI3, dI4, dI5 and dI6 (Lee et al. 2000; Muroyama et al. 2002; Wine-Lee et al. 2004). This has led to the classification of class A progenitors (dP1-3) that are defined by the expression of the bHLH transcription factor OLIG3 and are BMP/WNT-signalling dependent (Muller et al. 2005). In contrast, class B progenitors are BMP/WNT-signalling independent and constitute the ventrally adjacent dP4-6 domains that predominantly express LBX1 at post-mitotic stages (Gross et al. 2002; Muller et al. 2002). Indeed, WNT over-expression models expand the OLIG3 progenitor pool at the expense of class B populations (Zechner et al. 2007; Alvarez-Medina et al. 2008). Despite this, there is some debate as to whether BMPs act as diffusible morphogens. Indeed, multiple BMP members are present and influence patterning in the developing neural tube including BMP4, 5, 6, 7 and GDF7 (Andrews et al. 2017). This suggests that morphogen patterning, similar to diffusible SHH signalling in the ventral neural tube, would be more difficult to achieve. Furthermore, knockout studies of specific BMPs such

as BMP4, BMP7 and GDF7 were found to result in the targeted ablation of specific dorsal IN subtypes, depending on the BMP ligand (Lee et al. 1998; Butler & Dodd. 2003; Le Dreau et al. 2012). This implies that BMPs may have signal-specific effects, promoting the generation of specific dorsal subtypes, as suggested in a separate study (Andrews et al. 2017). However, evidence supporting the role of BMPs as morphogens include observations of the pattern of downstream BMP signalling effects in the developing neural tube. This, as assessed by levels of phosphorylated SMAD, indicated a dorsal-ventral gradient of BMP activity (Tozer et al. 2013; Zagorski et al. 2017). Furthermore, a temporal component to BMP signalling has been identified in BMP4, where longer exposure to this particular BMP ligand resulted in more dorsal progenitor identities in chicken neural plate explants (Tozer et al. 2013). A potential explanation for these contradictory findings stems from observations that the timing of exposure to BMP4, and therefore the competence of cells to respond to BMP4 signalling, underlies the response and subsequent neural tube subtypes specified (Duval et al. 2019).

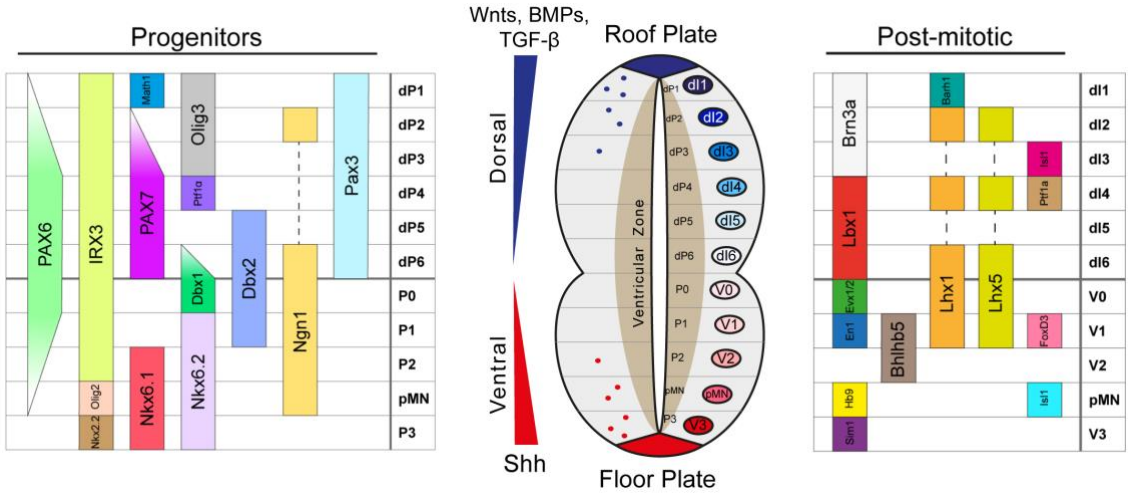

Figure 1.2 Dorsal-ventral patterning of the neural tube

Dorsal-ventral patterning of the neural tube by WNTs, BMPs and TGF-β secreted from the roof plate and SHH from the floor plate. This establishes a gene regulatory network within the neural tube and the subsequent generation of 11 progenitor domains, whereby progenitors emerge from the ventricular zone. These progenitors then migrate laterally, giving rise to 11 domains from which neurons arise, with glia and oligodendrocytes generated at later timepoints. Progenitors and neurons can be molecularly distinguished by a transcription factor 'postcode'. Figure created

using BioRender. Sonic hedgehog (shh), wingless-related integration site (Wnt), bone morphogenic protein (BMP), transforming growth factor-β (TGF-β).

1.1.3 Intra-domain diversity & temporal dynamics

Further complexity is introduced when one considers *intra*-domain in addition to *inter*-domain molecular and functional heterogeneity. Indeed, recent studies have employed more sensitive sequencing techniques in an attempt to resolve intra-domain heterogeneity with much greater sensitivity and resolution (Delile et al. 2019). This has revealed a large number of molecularly distinct neuronal subtypes present in the spinal cord that migrate laterally from common progenitor pools (Helms & Johnson. 2003; Le Dreau & Marti. 2013). For example, the pMN domain gives rise to over 50 pools of MNs with distinct molecular and target muscle innervation profiles at brachial levels (Dasen et al. 2005; Landmesser. 2001; Philippidou & Dasen. 2013). Furthermore, substantial heterogeneity has also been observed in the IN-producing V1 domain where over 50 transcriptionally distinct subtypes were found at limb-innervating levels and based on the combinatorial expression of 19 transcription factors (Bikoff et al. 2016; Gabitto et al. 2016). Whilst these studies provide evidence of the remarkable heterogeneity present in distinct neural tube domains, the mechanisms underlying this are yet to be elucidated. Indeed, in a subsequent study, Delile et al (2019) employed single cell RNA sequencing to capture intra-domain heterogeneity resulting from temporal dynamics, providing further resolution beyond bulk sample/tissue methods. In this manner, a highly coordinated programme of intra-domain neuronal subtype diversity was observed, dictated by the time of generation. This manifested through the sequential and modular expression of distinct transcription factors during neural tube development. Expression of Onecut transcription factors was able to delineate early-born neurons derived before E10. Furthermore, E10-E11 neurons were defined by Pou2f2 and Zfhx2-4 expression and late-born (E11.5 onwards) neurons expressed Nfia, Nfib, Neurod2 and Neurod6. Importantly, these expression patterns were maintained throughout the dorsal-ventral axis in multiple populations, demonstrating a shared intrinsic and temporally regulated mechanism. Furthermore, these findings share key similarities with studies of early- and late-born neurons in the retina, which also display temporally regulated expression of Onecut and Nfia and Nfib transcription factors, respectively (Clark et al. 2019; Sapkota et al. 2014).

This suggests a shared mechanism for temporally regulated neuronal diversity in the CNS. One possible mechanism for this temporal code is through the influence of extrinsic signalling factors. Indeed, downregulation of Onecut transcription factor expression at E10 coincides with the loss of RA signalling from adjacent somites that stems from the loss of key RA synthesising enzymes (Niederreither et al. 1997). Alternatively, a temporally regulated change in gene expression profile in progenitors could underline this subtype diversity. This is supported by the upregulation of Nfia and Nfib in progenitors at E10-11.5 that are known to be involved in the specification of glial cells at later timepoints (Deneen et al. 2006). Overall, the mechanisms underlying temporal regulation of intra-domain neuronal diversity are yet to be elucidated. However, the use of techniques including RNA sequencing will undoubtedly provide clear experimental utility in the elucidation of these complex mechanisms.

1.2 Spinal cord populations

1.2.1 Motor neurons

MNs consist of two populations found in layer V of the cerebral motor cortex (upper MNs) and the brainstem and spinal cord (lower MNs) (reviewed by Stifani. 2014). Despite both forming the basic neuronal circuit that is essential for driving motor output, there are key differences between upper and lower MNs. Indeed, some have suggested that the role of glutamatergic upper MNs does not reflect their actual biological role. This is because upper MNs provide the initial instructions to cholinergic lower MNs, which are the final neuronal component, projecting to peripheral muscles and directly stimulating muscle responses. This section will focus on lower MNs, since they form a major subject of this thesis. As mentioned previously, all lower MNs are derived from a common progenitor domain; the pMN domain (Jessell. 2000). In addition, MN diversity stems from the temporally controlled ventral-to-dorsal and rostral-caudal expansion within the pMN domain and throughout the body axis respectively (Sagner & Briscoe. 2019). This forms a temporal gradient of MN specification with those situated more ventral and rostral born earliest, and also contributes to the establishment of motor columns throughout the hindbrain and spinal cord and extending across the rostral-caudal axis (Nornes & Carry. 1978). Indeed, a critical component of motor column formation

stems from the establishment of the rostral-caudal HOX code, involving extensive cross-regulation of HOX paralogs (Ensini et al. 1998; Lance-Jones et al. 2001; Philippidou & Dasen. 2013). This leads to the formation of four main motor columns that can be classified by anatomical position, gene expression profiles, uniform axonal projection patterns and target muscle types (Figure 1.3) (Shah et al. 2004; Dasen et al. 2005; Jung et al. 2010).

The median motor column (MMC) comprises medially positioned MNs that project to, and innervate epaxial muscles that predominantly control body posture (Tsuchida et al. 1994; Jessell. 2000; Francius & Clotman. 2014; Patani. 2016; Stifani. 2014). The MMC extends throughout the full rostral-caudal axis. As such, the MMC is speculated to be the evolutionary origin from which other motor columns were founded. MMC MNs are defined by their unique expression of the LIM domain protein LHX3 and its interaction with ISL1 is thought to underlie the independence of the MMC to rostral-caudal HOX patterning (Thaler et al. 2002; Song et al. 2009). Importantly, the LHX3-ISL1 complex, present in the pMN domain but not in the adjacent LHX3 positive IN producing V2 domain, is thought to underlie the transition of MN fate through the induction of cholinergic gene expression profiles (Cho et al. 2014; Kania. 2014). The lateral motor columns (LMC) constitute MNs responsible for the innervation of limb musculature and, as such, are present in brachial (C5-T1 innervating the arms) and lumbar (L1-L5 innervating the legs) spinal segments (Hollyday & Hamburger. 1977; Hollyday & Jacobson. 1990). As such, the LMC motor columns are highly dependent on local HOX gene expression, with HOX6 and HOX10 driving brachial and lumbar LMC specification respectively (Liu et al. 2001; Dasen et al. 2003). Further subdivision of the LMC motor columns include populations of medial (LMCm) and lateral (LMCl) MNs that can be defined molecularly and through their limb targets in ventral or dorsal regions respectively (Tosney et al. 1995). Interestingly, the mechanisms underlying LMCm and LMCl diversification are well understood and stem from RA secretion from the paraxial mesoderm (Niederreither et al. 1997). This stimulates the expression of RA synthesising enzymes and subsequent local production of RA from these early-born LMC neurons that eventually become LMCm MNs (Ensini et al. 1998; Sockanathan et al. 2003; Vermot et al. 2005). RA secreted from these cells acts in a paracrine manner to induce the expression of LHX1 and the downregulation of ISL1 in later-born LMC neurons that eventually give

rise to the LMCl subdivision. The hypaxial motor column (HMC) is present at thoracic levels, with MNs extensively innervating ventral hypaxial muscles controlling body wall musculature (Tsuchida et al. 1994; Sharma et al. 2000). Subsequently, HMC MNs have important roles in respiration. Lastly, preganglionic motor column (PGC) MNs are located in spinal segments T1-L2 and comprise the majority of visceral MNs providing CNS muscle control of the autonomic nervous system (Prasad & Hollyday. 1991; Thaler et al. 2004). Indeed, PGC MNs are the only MNs that do not innervate muscle targets, instead synapsing onto sympathetic ganglia. Beyond the columnar organisation, MNs are subdivided into pools that innervate individual muscles, with the LMC and HMC containing approximately 60 and 10 motor pools, respectively (Stifani. 2014).

Somatic MNs can be divided into three categories: alpha, beta or gamma, based on the fiber type of the muscle target they innervate (Stifani. 2014). The muscle fiber types that they innervate are termed extrafusal; providing the force generation of the muscle spindle through contraction, or intrafusal muscle fibers; mainly acting as specialised sensory organs and proprioceptors. Extrafusal muscle fibers can be further subdivided into fast-twitch fatigable (FF), fast-twitch fatigue resistant (FFR) and slow-twitch fatigue resistant (SFR) types (Burke et al. 1973). This is based on a number of physiological properties such as anatomical, physical and metabolic properties. Alpha MNs exclusively innervate extrafusal muscle fibers and therefore have large diameters to mediate high activity and muscle contraction. Similar to extrafusal muscle fibers, alpha MNs can also be categorised based on the type of extrafusal muscle fiber it innervates: FF, FFR or SFR alpha MNs (Burke et al. 1973). Beta MNs are more poorly characterised but are thought to innervate both intrafusal and extrafusal muscle fibers and therefore control aspects of contraction and sensory feedback (Bessou et al. 1965). Gamma MNs solely innervate intrafusal muscle fibers and therefore do not possess any input on motor function through contraction (Eccles et al. 1960).

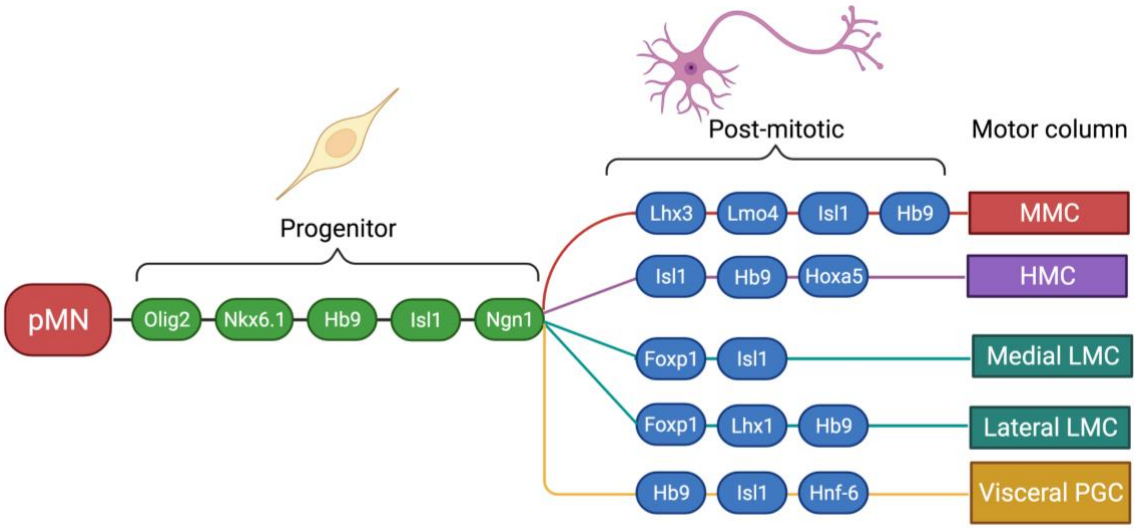

Figure 1.3 Lateral motor column diversity

All MNs arise from a common progenitor pool called the pMN domain of the neural tube. MNs then form motor columns, dependent on the spinal region they are located. These motor columns innervate distinct muscle types, for example the LMC; present at brachial and lumbar levels, innervates limb muscles of the arms and legs respectively. MNs from different motor columns can be molecularly distinguished by differential transcription factor expression profiles. Figure based on schematic from Alaynick et al. 2011 and created using BioRender. Median motor column (MMC), hypaxial motor column (HMC), lateral motor column (LMC), preganglionic motor column (PGC).

1.2.2 Interneurons

The term ‘spinal inter-neuron’ stems from the relative position of a highly specialised, but diverse set of neurons within the spinal cord circuitry. As such, the majority of INs are positioned as second order neurons, targeted by incoming sensory information from somatosensory neurons and synapsing onto third order neurons such as ventrally positioned spinal MNs or higher brain centres; that are able to elicit motor responses in peripheral muscle effectors (Arber. 2012; Lai et al. 2016). Consequently, INs are widely considered as the key integrators of somatosensory information within the spinal cord, further defining and shaping this activity into an appropriate motor response. However,

spinal INs also have additional roles in the modulation of the activity of MNs directly, playing key roles in complex motor outputs such as walking and breathing.

It is important to note that INs are the most abundant cell type within the spinal cord and as such, display a remarkable heterogeneity with differences in molecular, axonal projection, target innervation and functional profiles (Alaynick et al. 2011; Lu et al. 2015; Lai et al. 2016). As mentioned previously, this is achieved throughout neural tube development and across the dorsal-ventral axis, with heterogeneity achieved as a result of temporally and spatially regulated morphogenetic cues and extrinsic signalling factors (Jessell. 2000; Sagner & Briscoe. 2019). The dorsal INs (dIs) are represented by 6 IN domains (dI1-6) that are derived from common progenitor pools (dP1-6). dIs have distinct roles as somatosensory relay INs and as such, are the target of first order somatosensory neurons relaying sensory information from the periphery (Alaynick et al. 2011; Lu et al. 2015; Lai et al. 2016). Recently, many of these dorsal INs have been characterised, with dI1s largely mediating proprioception (Bermingham et al. 2001; Yuengert et al. 2015) and dI3s involved in mechanosensation and behaviours such as grasping (Bui et al. 2013; Goetz et al. 2015). dI4 and dI5 INs mediate multiple sensory modalities including itch, touch and pain (Abraira et al. 2017; Duan et al. 2014; Bourane et al. 2015) and dI6 INs are more involved in the regulation of motor output (Lai et al. 2016). The ventrally positioned V0, V1, V2 and V3 INs have more direct influence on complex motor behaviours (Gosgnach et al. 2017). V0 and V2 domains consist of a mix of excitatory and inhibitory INs with roles in left/right alternation of motor activities (Crone et al. 2008; Griener et al. 2015). However, the V2 domain has additional roles in the coordination of flexor/extensor activities, similar to the V1 domain (Zhang et al. 2014). The V1 domain consists of predominantly inhibitory INs including Renshaw cells that mediate reciprocal inhibition of ventral MNs and also have roles in modulating motor speed (Gosgnach et al. 2006). V3 INs have extensive roles in ensuring accurate motor activity and performance (Zhang et al. 2008).

INs also form a critical component of central pattern generators (CPGs) networks, being involved in their generation, maintenance and modification (Buchanan & Grillner. 1987; Friesen. 1994; Li & Moult. 2012). CPGs are neural circuits that can produce rhythmic network activity independent of sensory feedback and input from higher centres via

descending modulation. CPGs are essential for behavioural outputs such as locomotion, respiration and the generation of cardiac rhythmicity (Marder & Bucher. 2001). There are two proposed models whereby CPGs generate auto-rhythmicity: through the use of a pacemaker cell type that can generate membrane oscillations under endogenous conditions, or through a network of reciprocal inhibition (Kiehn. 2016). Pacemaker cells, due to their unique intrinsic membrane properties and subsequent resting membrane potential fluctuations; are able to fire in bursts, influencing second order neurons that they synapse onto (Feldman. 2013). CPG networks that do not rely on a cell-autonomous subset of pacemaker cells instead function through reciprocal inhibition, whereby inhibitory INs are the driving force, generating patterns of alternating rhythmic activity (Friesen. 1994; Kiehn. 2016). The complexity of even simple locomotor movements delineates a similar level of complexity in the patterning and configuration of CPG networks within the spinal cord. Indeed, sensory feedback plays a critical role in shaping motor output, especially where cycle-by-cycle corrections are required; such as with proprioceptive sensory feedback or walking (Pearson. 2004). Indeed, the process of walking requires exquisite control of flexor/extensor muscles and their antagonists along with the precise coordination between ipsi- and contralateral legs (Hinckley et al. 2015). This complex motor output is coordinated by multiple layers of spinal cord CPGs and is subject to constant cycle-by-cycle alterations (Kiehn. 2016). Sensory feedback in the form of proprioceptive and mechanical feedback from peripheral sensory afferents can influence and recruit adjacent CPGs and oscillators resulting in alterations to motor output (Pearson. 2004). These sensory afferents often synapse onto INs in the dorsal spinal cord that are subsequently able to induce these changes and recruit other CPGs. The fundamental role of INs in locomotion and sensorimotor integration commands a striking complexity both in their molecular diversity and functional circuitry. This also places INs at a precarious position whereby any slight interneuronal defect could lead to the potentiation of a host of motor abnormalities.

1.2.3 Non-neuronal cell types

Non-neuronal cell types constitute a significant proportion of cells within the spinal cord and have a range of diverse functions (Franklin et al. 2020; Clarke et al. 2021). Astrocytes are generated following the initial wave of neurogenesis within the neural tube. As

mentioned previously, this coincides with the upregulation of Sox9 and NFIA/B in ventricular zone progenitors (e11.5), but these markers do not become astrocyte-specific until later timepoints (e13.5-16.5) (Molofsky et al. 2012). Gain and loss of function experiments have indicated that Nfia/b and Sox9 are necessary and sufficient for astrocyte specification (Stolt et al. 2003; Deneen et al. 2006; Rakic. 2007; Kang et al. 2012). Astrocytes have crucial homeostatic functions within the spinal cord, along with roles in synapse formation and maintenance and providing metabolic support (Chung et al. 2013; Clarke & Barres. 2013; Vasile et al. 2017). Astrocytes also respond to stimuli such as injury, undergoing context-dependent alterations in gene expression profile and leading to the induction of a 'reactive' phenotype (Anderson et al. 2016; Liddelow et al. 2017). The precise effects of this change in state are yet to be elucidated, particularly with regards to whether the resultant phenotype is detrimental or protective.

Oligodendrocyte production is also regulated by Nfia/b and Sox9 expression in neural precursors; however, this only takes place in the OLIG2-expressing pMN domain (Stolt et al. 2003; Deneen et al. 2006; Kang et al. 2012). As with astrocytes, a comparative 'gliogenic switch' occurs in the pMN domain causing a shift from the production of MN precursors, to oligodendrocyte precursors (OPCs) (Lu et al. 2002; Takebayashi et al. 2002; Zhou & Anderson. 2002). These oligodendrocytes are involved in ensheathing CNS axons, and in particular those with diameters above 0.2μm, with myelin; drastically enhancing action potential conduction velocities (Yu et al. 1994).

In contrast to astrocytes and oligodendrocytes that have ectodermal lineages, microglia are derived from the mesodermal yolk sac and from primitive macrophages (Ginhoux et al. 2010; Clarke & Patani. 2020). Subsequently, microglia are highly motile cells that constitute part of an immune defence system for the CNS. This includes their ability to function in infection protection, but also in other diverse roles such as synapse regulation (Davalos et al. 2005; Nimmerjahn et al. 2005; Schafer et al. 2013).

1.3 Amyotrophic lateral sclerosis

1.3.1 ALS aetiology

Amyotrophic lateral sclerosis (ALS), also known as motor neuron disease (MND), Charcot's disease or Lou Gehrig's disease, is the most common form of motor neuron disease, first identified in studies conducted by Jean-Martin Charcot between 1865-69 (Goetz. 2000; Kumar et al. 2011). These ultimately led to the identification of a specific neurological disorder with distinct pathology, manifesting through progressive muscle weakness and paralysis (Kumar et al. 2011). It was subsequently determined that lesions within the lateral column and anterior horn of the spinal cord were the underlying causes. Indeed, these distinct features led to the naming of this neurological disease as ALS by Charcot in 1874, where 'a-myo-trophic' has Greek origins meaning a lack of ('a') muscle ('myo') nutrients ('trophic'), 'lateral' signifying the presentation of pathology in the lateral spinal columns, and 'sclerosis'; also with Greek origins meaning a hardening of tissue that is often seen in the focal regions. The pioneering studies of Jean-Martin Charcot have formed the basis of ALS research to date, including notable observations of the separation of the motor system into two components.

ALS is subsequently characterised by initial dysfunction, followed by degeneration and ultimately death of MNs (Cleveland and Rothstein 2001) within the cerebral cortex (upper MNs), brainstem and spinal cord (lower MNs) (Hughes. 1982; Hammer et al. 1979; Maekawa et al. 2004). Symptoms manifest as progressive muscle weakness, spasticity and paralysis from somatic muscle denervation, leading to death, which normally occurs within 3-5 years of diagnosis (Brown & Al-Chalabi. 2017). The leading cause of death stems from breathing difficulties resulting from the degeneration of MNs innervating breathing apparatus (Logroscino et al. 2010). There is remarkable phenotypic heterogeneity between ALS cases represented by typical and atypical ALS-associated symptoms (Brown & Al-Chalabi. 2017; Connolly et al. 2020). This variability has been hypothesised to stem from the multiple mechanisms that have been implicated in ALS and also through the range of mutations that cause ALS. Indeed, heterogeneity has even been observed within members of the same family harbouring the same mutation. This has led to hypotheses suggesting that ALS is actually a multi-system disorder caused by many underlying pathological mechanisms (Grossman. 2019). Phenotypic heterogeneity has been well documented to manifest through differences in focal initiating sites, the progression pattern and relative speed of progression and which body regions are affected (Brown & Al-Chalabi. 2017). Clinically, this is observed through a striking dissimilarity

in the degree of upper and lower MN involvement (Ravits & La Spada. 2009). Typical ALS cases present with simultaneous upper and lower MN involvement at disease onset with a focal anatomical starting point normally within the arms, legs or face; manifesting as muscle weakness (Brown & Al-Chalabi. 2017). Indeed, initial onset presenting in the limbs occurs in 2/3rds of ALS cases making this the most common form, and is subsequently termed limb-onset ALS. It should be noted that focal onset is rarely exhibited in muscles of the trunk or respiratory system, where only 3-5% of ALS patients exhibit this phenomenon (Kiernan et al. 2011; Baumer et al. 2014). Furthermore, some patients present with ALS phenotypes that are not represented by components of motor pathways. This includes a decline in cognitive ability that is associated with fronto-temporal dementia (FTD) (Lillo & Hodges. 2009). Indeed, the two conditions are now considered to have a well-established genetic overlap with 15% of FTD patients presenting with symptoms of motor decline; synonymous with ALS. Conversely, 20.5% of ALS patients exhibit FTD-like symptoms with around 31% overall exhibiting cognitive dysfunction and behavioural impairment (Chio et al. 2019).

1.3.2 ALS epidemiology

ALS is the most common neurodegenerative disease of mid-life and has a prevalence of between 4.1 and 8.4 per 100,000 (Longinetti & Fang. 2019), but a life-time prevalence of around 1 in 400 (Johnston et al. 2006; Ingre et al. 2015). The incidence rates of ALS are between 0.6-3.8 per 100,000 per year, but this is highly variable per country. Indeed, in European countries, ALS incidence is much higher, averaging between 2.1-3.8 per 100,000 (Longinetti & Fang. 2019). Furthermore, time-course studies of ALS incidence rates have revealed significant upward trends, including a 36% increase in ALS incidence over a 25-year window in Scotland (Leighton et al. 2019). As a consequence, disease projection modelling has indicated a dramatic increase in the number of ALS cases; with one study predicting an increase of 69% by 2040 (Arthur et al. 2016). A significant gender bias is also found in ALS, with males displaying a significantly higher prevalence (Logroscino et al. 2010). Indeed, some studies have indicated a risk factor ratio of 1 and 2 between males and females (Leighton et al. 2019; Longinetti & Fang. 2019). The median age of onset is between 51 and 66 years (Longinetti & Fang. 2019), but this varies greatly between familial (genetically linked) and sporadic (no known genetic link) ALS

cases, with familial patients exhibiting a much lower age of onset (Camu et al. 1999; Kiernan et al. 2011).

1.3.3 ALS genetics

ALS has a strong genetic component to its aetiology, with around 10% of cases being familial (fALS) and therefore harbouring a known genetic link (Table 1.1) (Mejzini et al. 2019). These fALS mutations are primarily autosomal dominant mutations passing through Mendelian-inherited patterns of transmission. The remaining 90% of cases have no known genetic history of ALS and are termed sporadic (sALS). It should be noted that fALS and sALS are clinically indistinguishable. The first gene identified to harbour ALS-causing mutations linked to the onset of fALS was in the superoxide dismutase 1 gene (SOD1) (Rosen et al. 1993). Since this study, mutations in over 30 genes have been linked to ALS and as shown in Table 1 (Zou et al. 2017; Vijayakumar et al. 2019; Mejzini et al. 2019; Connolly et al. 2020). Interestingly, these mutations only account for around 70% of fALS and 10% of sALS cases, leaving a large percentage of patients with unknown ALS causes.

Gene	Protein	Year Discovered	% of fALS cases	Endogenous Role	Original Publication
SOD1	Superoxide dismutase	1993	14.8%	Cytosolic antioxidant	Rosen et al. 1993
ALS2	Alsin	2001	<1%	Endosomal dynamics	Yang et al. 2001
PRPH	Peripherin	2004	<1%	Cytoskeletal roles	Gros-Louis et al. 2004
SETX	Senataxin	2004	<1%	RNA/DNA metabolism	Chen et al. 2004
ANG	Angiogenin	2004	<1%	RNA processing/stress granules	Greenway et al. 2004
VAPB	Vesicle-associated membrane protein-associated protein B/C	2004	<1%	endoplasmic reticulum/unfolded protein response	Nishimura et al. 2004
DCTN1	Dynactin subunit 1	2005	<1%	Axonogenesis, Endoplasmic reticulum and Golgi functions	Munch et al. 2005
CHMP2B	Charged multivesicular body protein 2b	2006	<1%	Lysosome/protein trafficking	Parkinson et al. 2006
TARDBP	TAR DNA-binding protein 43	2008	4.2%	RNA/DNA binding protein	Van Deerlin et al. 2008
FUS	Fusined in sarcoma	2009	2.8%	RNA/DNA binding protein	Kwiatkowski et al. 2009
FIG4	Polyphosphoinositide phosphatase	2009	<1%	Vesicle trafficking/autophagy	Chow et al. 2009
OPTN	Optineurin	2010	4.0%	Membrane trafficking/autophagy	Maruyama et al. 2010
SPG11	Spatacsin	2010	<1%	Lysosomal/cytoskeletal functions	Orlacchio et al. 2010
VCP	Valosin-containing protein	2010	2.0%	Ubiquitination and protein degradation	Johnson et al. 2010
ATXN2	Ataxin 2	2010	<1%	RNA stability/translation	Elden et al. 2010
SIGMAR1	Sigma non-opioid intracellular receptor 1	2010	<1%	Endoplastmic reticulum/mitochondrial axonal transport	Luty et al. 2010

DAO	D-amino-acid oxidase	2010	<1%	D-serine metabolism	Mitchell et al. 2010
UBQLN2	Ubiquilin 2	2011	<1%	Proteasomal functions	Deng et al. 2011
SQSTM1	Sequestosome 1	2011	<1%	Unfolded protein response/autophagy	Fecto et al. 2011
C9orf72	Guanine nucleotide exchange C9orf72	2011	33.7%	Transcription and RNA splicing	DeJesus-Hernandez et al. 2011
TAF15	TATA-binding protein associated factor 2N	2011	<1%	Transcription initiation	Couthouis et al. 2011
EWSR1	EWS RNA binding protein 1	2012	<1%	RNA splicing	Couthouis et al. 2012
PFN1	Profilin 1	2012	<1%	Cytoskeletal roles/actin polymerisation	Wu et al. 2012
hnRNPA1	Heterogeneous nuclear ribonucleoprotein A1	2013	<1%	RNA splicing	Kim et al. 2013
TUBA4A	Tubulin alpha-4A chain	2014	<1%	Cytoskeletal/microtubule roles	Smith et al. 2014
MATR3	Matrin 3	2014	<1%	RNA metabolism/splicing	Johnson et al. 2014
CHCHD10	Coiled-coil-helix-coiled-coil-helix domain containing 10	2014	<1%	Mitochondrial protein	Bannwarth et al. 2014
TBK1	Coiled-coil-helix-coiled-coil-helix domain containing 10	2015	1-3%	Autophagy	Borghero et al. 2015
NEK1	Never in mitosis gene A-related kinase 1	2015	<1%	Endosomal trafficking	Cirulli et al. 2015
KIF5A	Kinesin family member 5A	2018	<1%	Neuronal microtubule dynamics	Nicolas et al. 2018

Table 1.1 Genes associated with ALS, their functions and prevalence.

1.3.4 ALS pathology

In addition to the wide range of genes that have been linked to ALS, these genes encode proteins that are involved in a variety of different cellular processes. As detailed in Table 1, this includes functions ranging from RNA metabolism and splicing to protein homeostasis, mitochondrial functions and autophagy. This genetic and phenotypic variation further emphasises how multifactorial ALS is as a disorder and justifies the difficulties in i) elucidating unifying mechanisms underlying pathogenesis and ii) designing effective therapeutics for the treatment of ALS. Subsequent research has focused predominantly on fALS and has revealed key cellular processes that are aberrant in ALS such as impaired protein homeostasis, RNA metabolism and splicing dysfunction, DNA damage and impaired repair mechanisms, axonal transport deficits and mitochondrial dysfunction, amongst many others (Mejzini et al. 2019).

RNA metabolism and splicing dysfunction have long been considered a pathological hallmark of ALS, providing a unifying pathomechanism of ALS in the majority of ALS-causing gene mutations (Butti & Patten. 2018). Indeed, many of the proteins encoded by genes harbouring ALS-causing mutations are directly involved in key aspects of RNA homeostasis and / or splicing. This includes TARDBP, FUS, hnRNPA1, MATR3, SETX, ATXN2, TAF15, EWSR1 and TIA1, all of which serve as a family of proteins called RNA binding proteins (RBPs) (Zhao et al. 2018). As their name suggests, they share a common property in that they all contain one or more RNA binding domain. However; in addition, RBPs also possess a low-complexity domain, which is essential for their ability to associate with stress granules following cellular stress (Jain et al. 2016; Monahan et al. 2016). Furthermore, low-complexity domains are a requisite for these RBPs to undergo a phenomenon called liquid-liquid phase separation (LLPS), allowing the transition between a liquid and gel-like state and the formation of stress granules or to aggregate (Purice & Taylor. 2018). Stress granules are cytoplasmic membrane-less organelles that contain a mixture of RBPs, polyadenylated mRNAs, translation initiation factors and small ribosomal subunits (Protter & Parker. 2016). Whilst the mechanisms of stress granule assembly and their function are yet to be fully elucidated, they are generally thought to be a neuroprotective mechanism in response to stress (Buchan & Paker. 2009; Monahan et al. 2016). Interestingly, mutations in the low-complexity domains of ALS-related RBPs have been extensively documented. This results in altered stress granule

dynamics, stemming from an increased aggregative and fibrillar propensity of RBPs, leading to dysregulated RBP homeostasis and linked to ALS pathogenesis (Zhao et al. 2018). However, it should be noted that ALS pathogenesis can proceed in the absence of stress granule pathology (Mann et al. 2019; Gasset-Rosa et al. 2019). Perhaps more poignant is the shift in RBP LLPS dynamics from that of a reversible to irreversible state in disease conditions, with subsequent fibrillisation and aggregation of RBPs occurring independent of stress granule formation (Patani. 2020). Overall, RNA and protein homeostatic dysregulation are key unifying concepts underlying ALS pathogenesis and are highly correlated. This is evidenced in C9orf72 ALS patients where a hexanucleotide C_4G_2 repeat expansion undergoes bidirectional transcription, resulting in the generation of RNA foci. Essential RBPs are then sequestered into these intra-nuclear RNA foci (Gendron et al. 2013). In addition, these hexanucleotide repeats can undergo unconventional non-AUG-dependent (RAN) translation. This highlights the link between RNA and protein homeostatic dysfunction in ALS.

TDP-43 is a highly conserved RNA and DNA binding protein, involved in a number of cellular processes that are predominantly related to RNA metabolism and alternative splicing (AS) (Buratti & Barelle. 2001; Polymenidou et al. 2011). TDP-43 exhibits a nuclear localisation under endogenous conditions but in 97% of all ALS cases, including ALS-causing TARDBP mutation, exhibits a nuclear-to-cytoplasmic mislocalisation where it then forms hyperphosphorylated and ubiquitinated cytoplasmic aggregates (Neumann et al. 2006; Buratti & Barelle. 2008). The formation of cytoplasmic inclusions of TDP-43 is closely linked to changes in its preference for a liquid or gel-like state, favouring the latter in ALS (Conicella et al. 2016). These cytoplasmic aggregates are highly targeted to MNs in ALS patients and correspond to a nuclear loss-of-function or cytoplasmic gain-of-toxic function (Suk & Rousseaux. 2020). Indeed, TDP-43 is known to be involved in a number of alternative splicing mechanisms, including its role in hnRNPA1 pre-mRNA splicing (Deshaies et al. 2018). Here, it was shown that depletion of nuclear TDP-43 resulted in alternative splicing of hnRNPA1, resulting in the inclusion of exon 7B and the generation of an alternate isoform. This altered isoform was found to be more prone to aggregation and subsequently induced toxicity (Deshaies et al. 2018). This offers an intriguing ALS-related pathomechanism, whereby TDP-43 nuclear loss-of-function leads to alternative splicing defects in another associated RBP, subsequently

causing toxicity. It should be noted that TDP-43 mislocalisation and aggregation is not a unique feature of ALS. Indeed, TDP-43 pathology has been observed in around 57% of Alzheimer's disease (AD) patients (Matej et al. 2019), 45% of FTD cases (Neumann et al. 2006) and other motor neuropathies such as inclusion body myositis (IBM) (Weihl et al. 2008; Huntley et al. 2019) and Paget's disease (Nalbandin et al. 2011). Furthermore, TDP-43 pathology is also observed within the lifespan of healthy individuals and as a product of aging, providing alternative theories that ALS represents a state of early induced ageing (Pandya & Patani. 2020).

Whilst TDP-43 exhibits cytoplasmic mislocalisation and aggregation in 97% of ALS patients, FUS mislocalisation was thought to be a targeted pathology of only FUS-mutant ALS patients (Neumann et al. 2006). Recently; however, FUS mislocalisation was observed as a widespread pathology across a range of ALS-causing mutations including a human induced pluripotent stem cell (hiPSC) model of VCP-mutant ALS, VCP mouse transgenic mice and in sporadic ALS post-mortem tissue, but not in a SOD1 mouse model (Tyzack et al. 2019). Interestingly, whilst FUS mislocalisation was a prominent feature of these ALS models (not including the SOD1 mouse model), inclusions positive for FUS were not observed. Since inclusions positive for FUS are often found in FUS-mutant ALS patients, this could be a product of FUS-mutant ALS where FUS aggregation leads to severe phenotypes, often presenting with earlier-onset ALS (Huang et al. 2010; Liu et al. 2017). Similar to TDP-43, FUS is an RNA and DNA binding protein with many functions including neuronal maintenance and survival, splicing regulation and stress granule assembly (Lagier-Tourenne et al. 2012; Sama et al. 2013). Furthermore, FUS has also been observed to associate with stress granules following cellular stress (Sama et al. 2013). In addition, FUS has thousands of RNA targets and plays an essential role in their splicing regulation (Hoell et al. 2011; Colombrita et al. 2012). This includes the direct involvement of FUS in the removal of minor introns (Lagier-Tourenne et al. 2012; Zou et al. 2013; Reber et al. 2016). Interestingly, FUS has also been found to associate with hnRNPA1 (Kamelgarn et al. 2016), with further roles in cytoskeletal and axonal growth cone functions in neurons; key processes disrupted in ALS (Boillee et al. 2006; Nijssen et al. 2017). This is mediated through the regulation of alternative splicing (AS) of microtubule-associated protein tau (MAPT) by FUS (Ishigaki et al. 2012). FUS plays an active role in exon 10 exclusion from MAPT and this is significantly affected following

knockdown, leading to detrimental MAPT loss of function with cytoskeletal dysfunctions and axonal growth impairment (Orozco et al. 2012).

1.4 VCP

Valosin-containing protein (VCP) is a highly conserved and ubiquitously expressed hexameric AAA+ ATPase with myriad cellular functions (Sun & Qiu. 2020). As such, VCP contains 2 ATPase domains (D1 and D2) that can hydrolyse ATP, thereby generating energy (predominantly through the D2 ATPase) for its multicellular functions. These functions are mainly associated with protein homeostasis and degradation processes, such as endoplasmic reticulum-associated protein degradation and mitochondrial protein degradation pathways, autophagy, ubiquitination and apoptosis (Braun & Zischka. 2008; Ju et al. 2009; Meyer et al. 2012; Xia et al. 2016). The N-terminal domain acts as a co-factor binding domain whereby VCP can interact with a range of co-factor substrates in order to carry out these myriad functions (Meyer et al. 2012).

A prominent role for VCP has also been found in disease, whereby autosomal dominant mutations lead to a host of disorders under the collective label of VCP disease or VCP-related multisystem proteinopathy (MSP) (Ikenaga et al. 2020). VCP-related MSP is the most common form of MSP and patients present with symptoms pertaining to IBM, Paget's disease of bone, FTD, ALS and Parkinson's disease (PD). VCP-related MSP prevalence is 0.66 per 100,000 people and the phenotypic diversity was recently documented, with the vast majority reporting with IBM (90%), 29% with Paget's disease of bone, 14% with dementia and 3% with ALS (Ikenaga et al. 2020). Separately, ALS-causing VCP mutations were first discovered in whole exome sequencing studies and are thought to account for around 2% of all fALS cases (Johnson et al. 2010). Subsequent mutations have also been identified in sporadic patients, although to a lesser extent (Abramzon et al. 2012). However, the mechanisms underlying VCP-mutant ALS pathogenesis are yet to be elucidated. VCP has been demonstrated to play a role in stress granule assembly, maintenance and clearance, particularly in response to specific stressors (Buchan et al. 2013; Turakhiya et al. 2018). Subsequently, knockdown of VCP was found to impair stress granule assembly (Seguin et al. 2014; Turakhiya et al. 2018). Interestingly, the VCP protein has also been observed to directly interact with both TDP-

43 and FUS (Gitcho et al. 2009; Liu et al. 2020). Furthermore, VCP-mutant ALS patients exhibit TDP-43 mislocalisation and aggregation, demonstrating RBP mislocalisation and RNA dysfunction as critical mediators of VCP-mutant ALS pathogenesis (Neumann et al. 2007; Inoue et al. 2018). Mouse models of VCP-mutant ALS have also been generated in order to elucidate the role of VCP in ALS. Indeed, Nalbandian et al (2013) generated an R155H knock-in transgenic mouse model that recapitulated key features of VCP-mutant ALS pathology including muscle weakness, polyubiquitination and TDP-43 pathology. Moreover, R155H and R191Q ALS-causing mutations were also assessed in hiPSC-derived MNs (Hall et al. 2017). This revealed a host of ALS-related pathologies in VCP-mutant MNs, manifesting in a temporally regulated sequence of pathological events starting with primary cytoplasmic TDP-43 mislocalisation and ER stress, followed by mitochondrial dysfunction and oxidative stress and culminating in cell death in VCP-mutant MNs. Furthermore, a novel pathological hallmark of ALS was identified in the same hiPSC-derived VCP-mutant MNs involving aberrant AS events (Luisier et al. 2018). Consequently, a program of AS was identified during early neural differentiation for hiPSC-derived MN specification in VCP, FUS and SOD1 lines. These early AS events were predominated by intron retention (IR) events, which were found to be aberrantly increased in VCP-mutant lines, when compared to control. Further assessment revealed that the most significantly differential IR transcript (IRT) was in intron 9 of the splicing factor proline and glutamine rich (SFPQ) transcript, which was subsequently found to be bound by the SFPQ protein itself. Furthermore, SFPQ protein was found to be mislocalised from the nucleus to the cytoplasm in hiPSC-derived VCP-mutant MNs, MNs from VCP and SOD1 mouse models and also in post-mortem tissue from sporadic ALS patients. Indeed, the SFPQ IRT, along with others identified in VCP-mutant ALS MNs, were found to exhibit an increased binding affinity for RBPs that are commonly mislocalised in ALS, including TDP-43 and FUS (Tyzack et al. 2021). These findings were further validated in VCP-mutant fibroblasts and post-mortem tissue from patients with ALS, AD or ageing patients (Adusumalli et al. 2019; Hogan et al. 2020). Taken together, these studies support an intriguing hypothesis that stems from an increased abundance of IRTs, such as with SFPQ intron 9 and DDX39A intron 6. These retained introns are bound by RBPs, forming complexes that are subsequently translocated from

the nucleus, which might lead to a nuclear loss of function and/or altered cytoplasmic function.

1.5 Cell type-specific vulnerability

Selective vulnerability is a critical aspect of neurodegenerative diseases where pathologies manifest in stereotypical and predictable fashions (reviewed by Fu et al. 2018). The clinical presentation of neurodegenerative diseases reflects the underpinning deterioration of the specific subsets of cells and, as pathology worsens over time, this degeneration then spreads to other regions. A good example of this is in ALS where MNs from the specific MN-producing pMN domain within the ventral spinal cord are predominantly affected, whereas cell-types produced in adjacent or more dorsally situated domains remain largely unaffected. In addition, MNs themselves also display a level of selective vulnerability, with FF MNs being particularly vulnerable when compared to SFR MNs (Kanning et al. 2010; Nijssen et al. 2017). How apparently similar neighbouring populations of cells do not show stereotypical hallmarks of that neurodegenerative disease remains a critical question. This could help us explain the molecular features of neurodegenerative diseases and could also shed light on the basic biology and complexity of neuronal subtypes.

1.6 Human induced pluripotent stem cells

The revolutionary technology that accompanies the ability to generate hiPSCs has transformed the landscape of scientific research and the methods by which we model development and disease and the generation of therapeutic interventions. hiPSCs were first generated by Takahashi & Yamanaka et al in 2007 and are defined by their ability to self-renew and differentiate into any of the three primary germ layers of the early embryo: the endoderm, mesoderm or ectoderm. Cells of these layers give rise to all of the cells in the adult body including some extra-embryonic mesoderm derived tissues, but not the placenta. It should be noted; however, that the concept of pluripotent stem cells predates the advent of iPSCs. Indeed, the pioneering work of Gurdon et al (1962) paved the way for the notion of what is achievable via ‘reprogramming’. Gurdon et al (1962) was able to generate tadpoles from enucleated unfertilised frog egg cells by transplanting the

nucleus of intestinal epithelial somatic cells from tadpoles. This revolutionary work was able to demonstrate not only that somatic cells contain all of the necessary genetic information required to facilitate the generation of a whole living organism, but the egg cell itself also contains the necessary factors required for this 'reprogramming'. Additional work centred on testicular teratocarcinomas in male mice, revealed similar stem-cell-like properties including their immortalisation (Stevens & Little. 1954; Kleinsmith and Pierce. 1964; Solter et al. 1970). Subsequent experiments performed by Gail and Martin (1975) revealed the ability of testicular teratocarcinoma cells to form each of the three germ layers following transplantation. This led to the isolation of the first pluripotent stem cells from mouse embryos (Gail & Martin. 1975). Research into generating embryonic stem cells (ESCs) from humans (hESCs) has been marred by ethical and legal issues. Despite this, methods for the first successful generation of hESC cell lines from humans was achieved by harvesting cells from the inner cell mass of the blastocyst and growing them on a feeder cell layer (Thomson et al 1998). Nearly 2 decades later, Yamanaka et al (2006 & 2007) identified 4 transcription factors: Oct3/4, Sox2, c-Myc and Klf4, also known as the Yamanaka Factors that, when introduced into mouse and human fibroblasts, were sufficient to reprogram their genetic material and induce them to revert to a pluripotent-like state, and thus these cells are known as induced PSCs. Together, these studies all led to paradigm-shifting advancements for stem cell research.

hiPSCs offer a virtually inexhaustible source of patient-specific cells, providing a powerful model system to study developmental mechanisms of cell differentiation, function and dysfunction (reviewed by Haston & Finkbeiner. 2016). Furthermore, hiPSCs provide a more physiologically relevant experimental system, recapitulating patient-specific genomic differences and therefore providing a powerful disease modelling and drug discovery tool. Whilst the potential of hiPSCs appears limitless, there are a number of limitations to consider. This includes the loss of donor age status and respective epigenetic markers of aging following reprogramming. This means that the respective age of hiPSCs and hiPSC-derived cell types represent that of a fetal age. As a result, using hiPSCs to model diseases of aging such as ALS could have respective drawbacks. However, as demonstrated recently, hiPSC-derived VCP-mutant MNs were found to exhibit extensive ALS-related pathology (Hall et al. 2017) and a novel developmental

ALS phenotype was identified using this culture system (Luisier et al. 2018). A key requisite for maximising the potential of hiPSCs is the ability to reliably differentiate enriched cultures of hiPSC-derived cell types (Thiry et al. 2020). Studies of these specialised cell-types hold the greatest potential for disease modelling and drug discovery research. Therefore, deep phenotyping of hiPSC-derived cultures is a necessity for maximising the potential of hiPSCs.

1.7 Aims

It is clear that ALS is a multi-factorial disease, with multiple pathways involved; culminating in the primary pathology – the death of motor neurons. Recently; however, research has shifted away from the 'motor neuron-centric' views of ALS, with the elucidation of cell autonomous and non-cell autonomous effects in alternate neighbouring cell types. Indeed, the concept of cell type-specific vulnerability is hugely important to neurodegenerative diseases, where distinct populations of cells exhibit vastly different disease severity. The full spectrum and roles of neighbouring cell types in the pathophysiology of ALS remains unresolved.

Therefore, the specific aims of this Thesis are to:

1) Investigate hiPSC-derived directed differentiation strategies to generate disease relevant motor neuron subtypes.
2) Establish novel hiPSC-derived differentiation strategies for generating spinal cord interneuron populations.
3) Investigate cell type-specific vulnerability in ALS with regards to hiPSC-derived spinal interneurons and motor neurons.

Chapter 2. Materials & Methods

2.1 hiPSC culture

2.1.1 Ethics statement

Informed consent was obtained from all patients for human iPSC work performed in this study. Experimental protocols were all undertaken in compliance with approved regulations and guidelines set by UCLH's National Hospital for Neurology and Neurosurgery and UCL's Institute of Neurology joint research ethics committee (09/0272).

2.1.2 Fibroblast reprogramming & hiPSC lines

Experimental work on hiPSC lines consisted of the use of 6 control lines, 4 of which were commercially available and purchased from Coriell (ND41866*C), ThermoFisher Scientific (A18945), Cedars Sinai (CS02iCTR-NTn4) and NIH CRM (CRMi003-A). The other 2 control lines were reprogrammed by the lab of Professor Selina Wray, and by Luke Hill from the Patani lab using episomal reprogramming methods with the following plasmids: pCXLE hOct4 shp53, pCXLE hSK and pCXLE hUL (Addgene) on patient fibroblasts obtained by skin biopsy (Okita et al. 2011). hiPSCs were subsequently assessed for episomal plasmid integration using RT-PCR and upregulation of pluripotency markers such as OCT4, SSEA4 and NANOG by immunocytochemistry, as shown in Figure 2.1. Karyotyping was also carried out in order to assess for chromosomal abnormalities. Experiments on VCP-mutant ALS lines involved the use of 4 lines derived from 2 patients (2 clones per patient) harbouring an R155C or R191Q mutation in the VCP gene. These lines were also reprogrammed by the lab of Professor Selina Wray using methods described above.

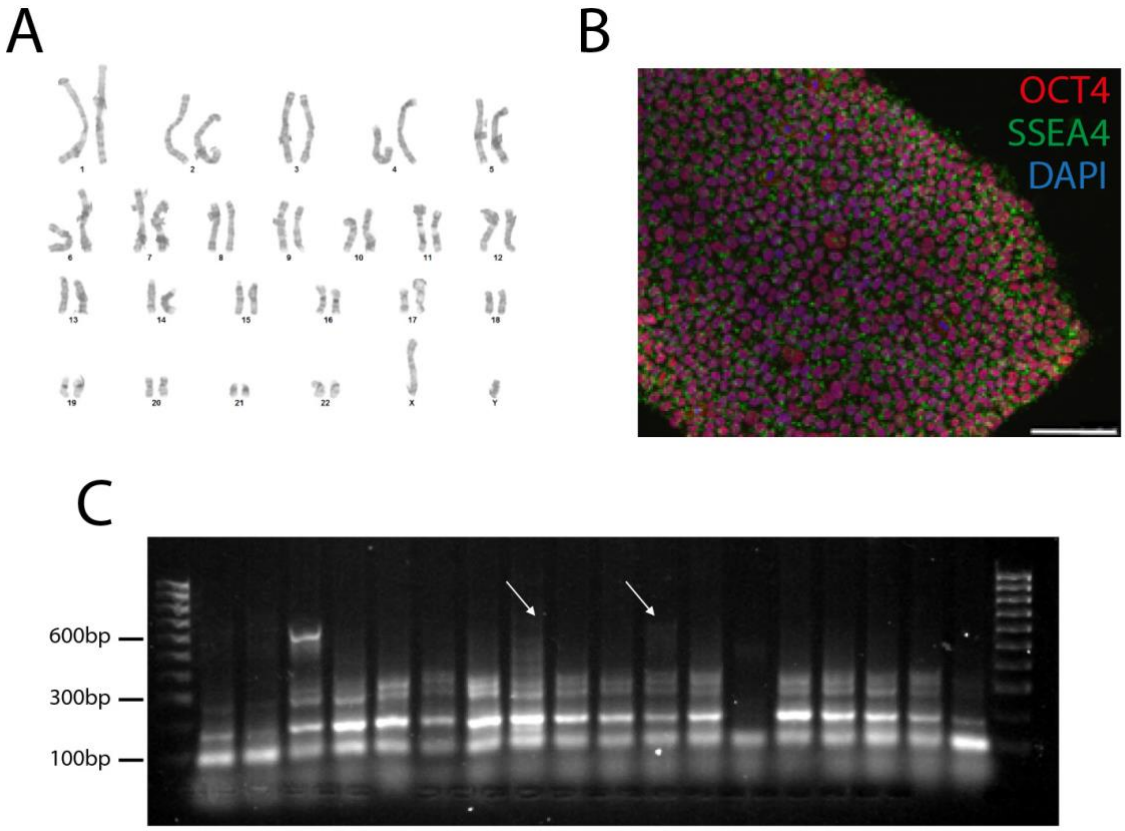

Figure 2.1 Authentication of hiPSC lines generated by episomal plasmid reprogramming. All hiPSC lines that were reprogrammed from fibroblasts (see section 2.12) in this study were extensively validated by the lab of Professor Selina Wray. (A) Representative images of G-banding karyotype analysis conducted on episomally reprogrammed hiPSC lines. (B) All hiPSC lines were observed to express a combination of pluripotency markers such as OCT4, SSEA4 or NANOG. (C) Although episomal reprogramming is reported as an integration-free method, episome integration has been reported on occasion. Therefore, specific primers, designed against a section of the episomal plasmids, were tested by PCR on extracted hiPSC DNA and visualised using DNA gel electrophoresis. Plasmid integration was assessed in all clones by the absence of a band at 666bp representing the target weight of the episome fragment. Arrows represent picked clones that were expanded for use. This Figure displays example images that were provided by Dr Christopher Lovejoy.

2.1.3 hiPSC maintenance and cryo-preservation

All cultures were maintained at 37°C in 5% carbon dioxide humidified incubators. hiPSCs were cultured on feeder-free Nunc treated plates coated with 150 μg/ml Geltrex

(ThermoFisher Scientific, A1413302) in Essential 8 (E8) media (ThermoFisher Scientific, A1517001). E8 media was changed daily and hiPSCs were passaged using 0.5 mM ethylenediaminetetraacetic acid (EDTA) (Life Technologies, 15575038) every 2-3 days when cultures reached a confluency of 60-90%. hiPSCs were cryopreserved in freezing medium containing 90% E8 and 10% dimethyl sulfoxide (DMSO) (Sigma-Aldrich, D2650). Briefly, hiPSCs were washed in phosphate buffered saline (PBS) (Life Technologies 14190144), before incubation for 5 minutes in EDTA. hiPSCs were then carefully lifted from the plates using a P1000 pipette and centrifuged at 270 relative centrifugal force (rcf) for 5 minutes in 10 ml PBS in 15ml falcon tubes. The supernatant was then aspirated and the pellet resuspended in freezing medium and placed into cryovials within Mr Frosty cryo-containers and placed in a -80°C freezer overnight. Cryovials were subsequently removed and transferred to liquid nitrogen storage for long term storage. Thawing of hiPSCs from cryopreserved stock involved maintaining the vial of cells at room temperature until mostly thawed. hiPSCs were then resuspended in 10 ml PBS and centrifuged at 270 rcf for 5 minutes to dilute the toxic DMSO. The supernatant was then removed and hiPSC pellets were gently resuspended in E8 containing 10 μM ROCK inhibitor (Y-27632) (Tocris, 129830-38-2) for one day before media was changed to E8 only.

2.1.4 hiPSC-directed motor neuron differentiation protocol

hiPSC-directed differentiation strategies were initiated once hiPSCs had reached a confluency of 95-100%. From this point onwards, media was changed from E8 to 1:1 N2-B27 containing DMEM-F12 GlutaMAX (ThermoFisher Scientific, 10565018), Neurobasal Media (ThermoFisher Scientific, 12348017), B27 supplement (ThermoFisher Scientific, 17504044), N2 supplement (ThermoFisher Scientific, 17502048), 100 μM 2-mercaptoethanol (ThermoFisher Scientific, 21985023), 100 μM MEM-non essential amino acids (ThermoFisher Scientific, 11140050), 2 mM L-glutamine (ThermoFisher Scientific, 25030024) and 5 μg/ml Human Insulin Solution (Sigma-Aldrich, I9278), which constituted the base media throughout the differentiation process. First, confluent hiPSCs underwent a process of neural induction through the addition of 1:1 N2-B27 media supplemented with 3.3 μM CHIR9902 (Miltenyi Biotech, 130-104-172), 2 μM SB431542 (Tocris, 1614) and 1 μM Dorsomorphin (Tocris, 3093) for 7 days, with daily

media changes. Additionally, cells were passaged between day 4-5 using 10 mg/ml of the enzyme dispase (ThermoFisher Scientific, 17105041) and split at a 1:2 or 1:3 ratio onto freshly coated Geltrex plates (see section 2.1.3) in neural induction media supplemented with 10 μM ROCK inhibitor for one day to aid in cell survival, before being replaced with neural induction media the following day. On day 7, cells were patterned in 1:1 N2-B27 media supplemented with 0.5 μM Retinoic acid (Sigma-Aldrich, R2625) and 1 μM Purmorphamine (Merck, 540220) for a further 7 days, with daily media changes. Cells were passaged between day 12-13 using 10 mg/ml dispase enzyme and split at a 1:2 or 1:3 ratio onto freshly coated Geltrex plates (see section 2.1.3) in patterning media supplemented with 10 μM ROCK inhibitor for one day to aid in cell survival, before being replaced with neural induction media the following day. On day 14, cells were patterned in 1:1 N2-B27 media supplemented with 0.1 μM Purmorphamine for a further 4 days until day 18, with daily media changes. Next, cells were either expanded in 1:1 N2-B27 supplemented with 10 ng/ml FGF (PeproTech 100-18B) or plated out for terminal differentiation. For terminal differentiation, cells were passaged using the enzyme Accutase (ThermoFisher Scientific A1110501) and plated onto plates coated overnight with Poly(ethyleneimine) (Sigma-Aldrich, 408727) dissolved in 0.1 M Sodium Borate pH 8.4 (Sigma-Aldrich, 221732) and then Geltrex. Cells were plated in 1:1 N2-B27 media supplemented with 10 μM ROCK inhibitor, which was replaced with terminal differentiation media containing 1:1 N2-B27 and 0.1 μM Compound E (Enzo Life Sciences, ALX-270-415-M001).

2.1.5 Alternative hiPSC-directed differentiation protocols

In order to generate different spinal cord populations, two separate phases within the hiPSC-derived differentiation protocol for generating spinal cord motor neurons, detailed in 2.1.4, were modified and assessed. Motor column diversity was evaluated following addition of 0.5 μM Retinoic acid to 1:1 N2-B27 + 0.1 μM Compound E during terminal differentiation between days 18 and 25 and following the final passaging and plating.

Dorsal interneuron specification was assessed following changes to the patterning phase of the protocol between days 7 and 18. This involved patterning in 1:1 N2-B27 supplemented with 0.5 μM Retinoic acid and 10 ng/ml BMP4 (R&D, 314-BP) between days 7 and 18. Separately, an additional paradigm involving the patterning of cells in 1:1

N2-B27 supplemented with 0.5 μM Retinoic acid between days 7 and 18 was also assessed. Lastly, attempts to derive dorsal spinal populations of cells involved their patterning in 0.5 μM Retinoic acid and 5 μM Cyclopamine between days 7 and 18 (Sigma-Aldrich, C4116).

2.2 Transcriptomics

2.2.1 RNA extraction and RT-qPCR analysis

RNA extraction from snap frozen cell pellets was carried out using either the Qiagen RNeasy Mini Kit (Qiagen, 74104) or the Maxwell RSC 48 instrument, employing the Promega Maxwell RSC simplyRNA cells kit (Promega, AS1390) and including DNase treatment, as per manufacturer instructions. Reverse transcription cDNA synthesis was performed using the Revert Aid First Strand cDNA Synthesis Kit (ThermoFisher Scientific, K1621) using 0.5-1 μg of total RNA and 5 μM random hexamers. RT-minus samples were used as negative controls lacking reverse transcriptase enzyme. qPCR was performed using the PowerUP SYBR Green Master Mix (Applied Biosystems, A25778), 0.5 μM primer pairs and cDNA diluted 1:30. Samples were run in duplicate or triplicate alongside an RT-negative and H_2O control, using an Agilent Mx3000P qPCR System or the QuantStudio 6 Flex Real-Time PCR System (Applied Biosystems). Target-specific amplification was determined by melt curve analysis and agarose gel electrophoresis of the PCR products. Primer pairs with 90-110% efficiency were used and are listed in Table 2.1. Expression levels of each individual gene were measured using the *dd*Ct method and normalised to GAPDH as a housekeeping gene.

Target	**Forward 5'-3'**	**Reverse 5'-3'**
HOXA1	CCCTACGCGTTAAATCAGGA	AAAAGTCTGCGCTGGAGAAG
HOXA2	GCTTGCCTCAGCCACAAA	TTGGTGTAAGCAGTTCTCAGG
HOXA3	ACCAGCAGCTCCAGCTCA	CTCTTTCTCCAGCTCCACCA
HOXA4	CCCTGGATGAAGAAGATCCA	GGTGTAGGCGGTTCGAGAG
HOXA5	GCGCAAGCTGCACATAAGTC	CTTCTCCAGCTCCAGGGTCT
HOXA6	ATGCAGCGGATGAACTCCT	CCTTCTCCAGCTCCAGTGTC
HOXA7	ATGCAGCGGATGAACTCCT	AGTGTCTGGTAGCGCGTGTA

HOXA9	GCGCCTTCTCTGAAAACAAT	GAAGCCAGTTGGCTGCTG
HOXB1	CCTTCGACTGGATGAAGGTT	AGCTGCCTTGTGGTGAAGTT
HOXB2	AATCCGCCACGTCTCCTT	CAGCTGCGTGTTGGTGTAAG
HOXB4	CTGGATGCGCAAAGTTCAC	CTGGATGCGCAAAGTTCAC
HOXB6	ACAAGGGCTTTGCCACTTC	CGACTCTTTCTCGCGGTAG
HOXC4	CGACTCTTTCTCGCGGTAG	ACTTGCTGCCGGGTATAGG
HOXC6	CCAGGACCAGAAAGCCAGTA	GGTACCGCGAGTAGATCTGG
HOXC8	GTCTCCCAGCCTCATGTTTC	CAAGGTCTGATACCGGCTGT
HOXC9	CAGCAAGCACAAAGAGGAGA	CAAGGTCTGATACCGGCTGT
HOXC10	GACACCTCGGATAACGAAGC	CCTCTTCTTCCTTCCGCTCT
HOXD1	H_HOXD1_1	Sigma-Aldrich
HOXD3	H_HOXD3_1	Sigma-Aldrich
HOXD4	H_HOXD4_1	Sigma-Aldrich
HOXD8	TCAAATGTTTCCGTGGATGA	TCAAATGTTTCCGTGGATGA
HOXD9	H_HOXD9_1	Sigma-Aldrich
HOXD10	H_HOXD10_1	Sigma-Aldrich
DBX1	GTACATCAGCAAGCCCGACC	AGTTCCGCCATTTCATGCGT
DBX2	CCCAACAGCACTCAAGTCCA	AGCCCCAGTAAGTACACCCT
GAPDH	ATGACATCAAGAAGGTGGTG	CATACCAGGAAATGAGCTTG
NKX2.2	AAACCATGTCACGCGCTCA	GGCGTTGTACTGCATGTGCT
NKX6.1	GTTTGGCCTATTCGTTGGGGA	GTGCTTCTTCCTCCACTTGGT
OLIG2	GGGCCACAAGTTAGTTGGAA	GAGGAACGGCCACAGTTCTA
OLIG3	AGCCTAACCAGAGAGAGGGG	AGCCTAACCAGAGAGAGGGG
PAX6	GTTGGTATCCGGGGACTTCG	CTCAAACTCTTTCTCCAGGGC
PAX7	GTGAGTTCGATTAGCCGCGT	GTCCAGCCGGTTCCCTTTG
SOX10	GCCCACTACAAGAGCGCC	GGCTGATCTCACCAATGTC
FOXP1	GTGGCATCTCATAAACCATC	TTATTCAAAATGGGGAAGGG
ISLET1	CTAATATCCAGGGGATGACAG	CTGGTAACTTTGTACTTCCAC
HB9	H_MNX1_1	Sigma-Aldrich
LHX1	H_LHX1_1	Sigma-Aldrich
LHX3	H_LHX3_1	Sigma-Aldrich

PEA3	H_ETV4_1	Sigma-Aldrich
LBX1	H_LBX1_1	Sigma-Aldrich
CHAT	TGGAAATGTCCACACCTCTGC	CCCAAACTGCTGCACAATG
LHX5	CCGGGAAGCAACTACGACTT	ATCATGTCGGTGAACCTGGG
SOX1	H_SOX1_1	Sigma-Aldrich
OCT4	H_POU5F1_1	Sigma-Aldrich
β3-tubulin	H_TUBB3_1	Sigma-Aldrich
GFAP	GAAGCAGATGAAGCCACCCT	CATTGCCTCATACTGCGTGC

Table 2.1 List of primers used for RT-qPCR

2.2.2 Intron retention

Primers employed to measure intron retention are listed in Table 2.2 and were validated previously (Luisier et al. 2018; Tyzack et al. 2021). Specific amplification was determined by melt curve analysis. Three primer pairs were used to validate intron retention within a specific target and are depicted in Figure 2.2 and Table 2.2. The F1 R1 primer pairs were used to measure gene expression levels and, as such, were designed as intron spanning primers, across the exon-exon junction of a constitutive exon. Primer pair F2 R2 was used to measure intron retention and was designed against the exon flanking the intron to be analysed, the other primer was targeted on the intron. Primer pair F2 R3 was used to measure levels of the spliced transcript for the same exon, designed with both primers annealing to the exons flanking the intron of interest and, if possible, designed across the exon-exon junction. RT-minus samples and H_2O were used as negative controls. Levels of IR (F2 R2) were normalised over the expression level of each individual gene (F1 R1) and then normalised over the average of the control lines. Levels of spliced transcript (F2 R3) were normalised over the expression level of each individual gene (F1 R1) and then normalised over the average of the control lines. Total gene expression levels were measured using the *dd*Ct method with F1 R1 primers normalised to GAPDH as a housekeeping gene and then normalised over the average of the control lines. IR/spliced ratio was calculated by normalising the levels of IR (F2 R2) over the levels of spliced transcript (F2 R3), and then further normalised over the average of the control lines.

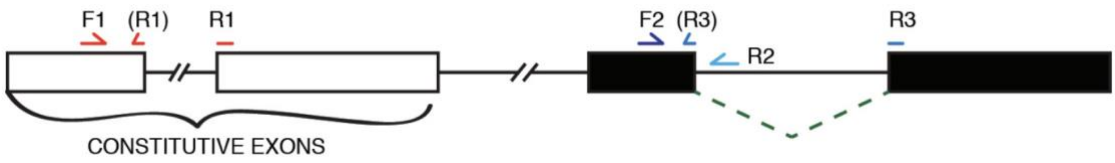

Figure 2.2 Primer design for assessing intron retention by RT-qPCR

Schematic depicting primer design for assessing levels of intron retention (IR) by qPCR using three primer pairs. The F1 R1 primer pair was designed against a constitutive exon flanking the intron of interest and was intron spanning, across the exon-exon junction. F2 R2 primers were designed to measure levels of IR, with one primer targeting the exon flanking the intron and the other primer targeting the intron. F2 R3 primers were designed to measure levels of spliced transcript and were subsequently designed with both primers targeting the exons flanking the intron of interest, and preferably exon-spanning. Image taken from Luisier et al. 2018.

Target	Forward 5'-3'	Reverse 5'-3'
SFPQ constitutive	GCCGAATGGGCTACATGGAT	TCAGTACGCATGTCACTTCCC
SFPQ intron 9 retained	GTGGATCGACTCATTGGTGA	TTCCTCTAGGACCCTGTCCA
SFPQ intron 9 spliced	GATGGGAAGTGACATGCGTA	TTCCTCTAGGACCCTGTCCA
FUS constitutive	GGAAGTGTCCTAATCCCACCT	TAGGGGCCTTACACTGGTTG
FUS intron 6/7 retained	AGCAGTGGTGGCTATGAACC	GCACTAGGGACTGGCTTCAG
FUS intron 6/7 spliced	AGCAGTGGTGGCTATGAACC	GGGCCACCAAATTTATTGAA
DDX39A constitutive	GCAGATTGAGCCTGTCAACG	ACACAGACACCTTGACGCTG
DDX39A intron 6 retained	ACAAAGGAGTCGCCCACTG	CTTGACGAAGATTATCACCTGGT
DDX39A intron 6 spliced	CAGGATCCCATGGAGGTG	CTTGACGAAGATTATCACCTGGT

Table 2.2 List of primers used for intron retention analysis.

2.2.3 RNA sequencing

RNA was extracted from frozen cell pellets as detailed before using the Qiagen RNeasy Mini Kit (Qiagen, 74104) or the Maxwell RSC 48 instrument, employing the Promega Maxwell RSC simplyRNA cells kit (Promega, AS1390). Poly(A)+ selected reverse stranded RNA sequencing libraries were prepared from samples at day 18 neural precursor and day 25 terminally differentiated cultures from three control cell lines using the KAPA mRNA HyperPrep Library kit for Illumina®, with 50 ng of total RNA as input. Libraries were sequenced on a HiSeq 4000 platform at the Francis Crick Institute. All samples passed quality control thresholds. A total of 25 million 100 bp paired-end strand-specific reads were sequenced per sample split over 2 lanes. All libraries generated in this study had <1% mtDNA, >90% strandedness and >70% exonic reads.

Raw mRNA sequencing reads were aligned to hg38 human reference genome using splice-aware aligner, STAR v2.6.1. Aligned reads were quantified with HTseq v0.12.4 at gene-level based on Ensembl GRCh 38.99 annotation. Detailed quality control of the raw RNAseq was assessed utilising the nf-core/rna-seq pipeline (Table 2.3). Differential gene expression was measured using DESeq2 in R v4.0.3. results were generated by comparing patterning conditions and a gene was considered significantly differentially expressed if false discovery rate (FDR) < 0.05.

Note: For the RNAseq described in this thesis, the cells were generated, RNA extracted and cDNA libraries synthesised by myself, sequencing was undertaken by the Advanced Sequencing STP at the Francis Crick Institute and RNAseq analysis by Dr Oliver Ziff, a PhD student in the labs of Professor Rickie Patani and Professor Nicholas Luscombe. RNAseq data analysed by this colleague is indicated in the relevant figure legends.

Sample Name	% rRNA	dupInt	5'-3' bias	M Aligned	% Assigned	M Assigned	% Aligned	M Aligned2	% Trimmed	% GC	M Seqs
RAonly_d18_ctrl1_lane7	0.00%	0.03%	1.16	10.9	63.10%	7.6	92.10%	10.5	4.10%	46%	11.4
RAonly_d18_ctrl1_lane8	0.00%	0.06%	1.17	9.5	63.10%	6.6	92.00%	9.1	2.90%	46%	9.9
RAonly_d18_ctrl2_lane7	0.00%	0.04%	1.14	9.8	63.30%	6.8	92.50%	9.4	4.40%	45%	10.3
RAonly_d18_ctrl2_lane8	0.00%	0.06%	1.15	8.6	63.40%	5.9	92.40%	8.2	4.10%	45%	8.9
RAonly_d18_ctrl3_lane7	0.00%	0.04%	1.1	9.6	64.80%	6.8	93.20%	9.3	3.30%	48%	10
RAonly_d18_ctrl3_lane8	0.00%	0.06%	1.16	8.5	65.00%	6	93.30%	8.1	3.20%	48%	8.8
RAonly_d25_ctrl1_lane8	0.00%	0.07%	1.19	11.3	59.80%	7.4	92.20%	10.8	3.10%	44%	11.8
RAonly_d25_ctrl2_lane7	0.00%	0.05%	1.14	13.4	63.40%	9.2	92.70%	12.9	4.00%	45%	13.9
RAonly_d25_ctrl2_lane8	0.00%	0.08%	1.07	11.5	63.70%	7.9	92.80%	11.1	3.90%	44%	12
RAonly_d25_3_lane7	0.00%	0.04%	1.03	12.4	61.40%	8.2	92.50%	11.9	4.60%	46%	12.9
RAonly_d25_3_lane8	0.00%	0.07%	1.09	10.8	61.40%	7.2	92.30%	10.4	4.30%	46%	11.3
RA+Shh_d18_ctrl1_lane7	0.00%	0.04%	1.2	10	58.50%	6.5	92.40%	9.6	3.80%	46%	10.4
RA+Shh_d18_ctrl1_lane8	0.00%	0.06%	1.11	8.6	58.50%	5.6	92.40%	8.3	3.60%	46%	9
RA+Shh_d18_ctrl2_lane7	0.00%	0.06%	1.1	20.2	62.20%	13.7	91.70%	19.4	5.30%	42%	21.3
RA+Shh_d18_ctrl2_lane8	0.00%	0.09%	1.13	17.4	62.80%	11.8	91.80%	16.7	5.10%	43%	18.3
RA+Shh_d18_ctrl3_lane7	0.00%	0.04%	1.16	10.5	60.30%	7	92.60%	10.1	3.40%	47%	10.9
RA+Shh_d18_crtrl3_lane8	0.00%	0.06%	1.13	9.1	61.20%	6.1	93.10%	8.8	4.10%	46%	9.4
RA+Shh_d25_ctrl1_lane7	0.00%	0.04%	1.12	10.4	65.90%	7.5	92.40%	10	4.50%	47%	10.8
RA+Shh_d25_ctrl1_lane8	0.00%	0.07%	1.14	9.1	66.10%	6.5	92.40%	8.7	3.40%	47%	9.5
RA+Shh_d25_ctrl2_lane7	0.00%	0.04%	1.06	11.4	69.50%	8.5	93.30%	11	3.90%	47%	11.8
RA+Shh_d25_ctrl2_lane8	0.00%	0.07%	1.12	9.9	69.70%	7.4	93.30%	9.5	3.60%	47%	10.2
RA+Shh_d25_ctrl3_lane7	0.00%	0.23%	1.01	25.4	60.80%	17.1	85.10%	24.2	12.50%	41%	29.8
RA+Shh_d25_ctrl3_lane8	0.00%	0.22%	0.98	21.7	60.30%	14.6	85.00%	20.6	12.80%	42%	25.4

Table 2.3 Detailed quality control of raw RNAseq data.

2.3 Protein analysis

2.3.1 Western blot

Immunoblotting was carried out on snap frozen cell pellets, which were resuspended in cOmplete Lysis-M buffer, EDTA-free (Sigma-Aldrich, 15423520) containing a protease inhibitor cocktail (Merck, 4693159001); 1 tablet dissolved in 10 ml lysis buffer. Samples were then placed on a rotator at 4°C for 30 minutes to lyse, before being centrifuged at 20,000 g for 20 minutes at 4°C. The supernatant was next extracted for processing. The protein content of the soluble extract was then quantified using a Pierce™ BCA Protein Assay Kit (ThermoFisher, 23225). 10X SDS Reducing Agent (ThermoFisher Scientific, NP0007) and 4X XT Sample Buffer (Bio-Rad, 1610791) was added to each sample and placed at 100°C for 10 minutes to denature the protein. 10ug protein was then loaded per lane on a 4-12% Bis-Tris protein gel (Bio-Rad, 3450125) and run at 180V for 1-2 hours using MOPS running buffer (Bio-Rad, 161-0788). Protein was then transferred to a PVDF membrane (1704157) using a Trans-blot Turbo™ transfer system. The transfer membrane was then blocked in 5% milk diluted in 0.1% PBS-tween (PBST) for 1 hour, before incubation in primary antibody; also diluted in 5% milk PBST for 2 hours at room temperature or overnight at 4°C on a shaker. Membranes were then washed 3 times for 5 minutes each in PBST, before incubation in secondary antibodies IRdye 680RD and 800CW diluted in 5% milk PBST for 1 hour at room temperature on a shaker. Membranes were then washed 3 times for 10 minutes each in PBST before imaging using a LICOR FC Odyssey and bands were quantified using ImageJ. Relative differences in protein expression were determined following normalisation to a house keeping protein. Antibodies and their concentrations are displayed in Table 2.4.

Antibody	Species	Supplier	Dilution
NKX6.1	goat	R&D (AF5857)	1:500
β-actin	mouse	Sigma-Aldrich (A2228)	1:1000

Table 2.4 List of antibodies and concentrations used for western blot.

2.3.2 Immunocytochemistry

Cells plated on IBIDI 8 well chamber slides (IBIDI, 80826), round glass coverslips (13mm diameter) (ThermoFisher Scientific, 11588492) or clear bottom 96 well plates (Falcon, 353219) and were fixed in 4% paraformaldehyde (PFA) (Insight Biotechnology, AR1068) for 10 minutes at room temperature and stored in PBS at 4°C (wrapped in parafilm and covered in aluminium foil) for subsequent immunolabelling. For immunolabelling, cells were permeabilised and blocked in 5% Bovine Serum Album (BSA) (Sigma-Aldrich, A7030) diluted in 0.3% PBS-Triton (Sigma-Aldrich, Triton X-100) at room temperature for 30 minutes. Cells were then incubated in primary antibody diluted in 5% BSA and 0.3% PBS-Triton for 2 hours at room temperature or overnight at 4°C. Antibodies used for immunostaining and their concentrations are displayed in Table 2.5. Cells were then washed in PBS up to 3 times, depending on the fragility of the cultures, before being incubated for 1 hour with secondary antibodies diluted in 5% BSA and 0.3% PBS-Triton in the dark. Cells were then washed up to 3 times, depending on the fragility of the cultures, before being incubated with DAPI diluted in 5% BSA and 0.3% PBS-Triton for 10 minutes in the dark. Cells were then mounted using DAKO mounting medium (DAKO, S3023) or PBS was added to each well if plated on 96 well plates or IBIDIs.

2.4 Image acquisition and analysis

2.4.1 Microscopy

Coverslips and IBIDIs were imaged using a Zeiss 880 with Airyscan 2019 confocal microscope with a 63x, 1.4 N.A. oil objective. For each well a minimum of 5 images were acquired. Z series of images were acquired using a pinhole diameter of Airy units with a minimum of 5 slices per stack and images displayed as maximum projections. Settings for acquisition and thresholding were kept standard for each experimental set. Image analysis was performed in Fiji (ImageJ). 96 well plates were imaged using the Opera Phenix^{TM} High Content Screening System (Perkin Elmer) with a 20x or 40x water objective. For each well a minimum of 5 fields were acquired. Z stacks of images were acquired with a minimum of 5 slices per stack with images displayed as maximum projections. Settings for acquisition and thresholding were kept standard for each

experimental set. Cells were analysed with the Columbus™ Image Data Storage and Analysis System version 2.8.0.

2.4.2 Nuclear/cytoplasmic ratio

In order to analyse the nuclear/cytoplasmic (N/C) ratio of RBPs, neural precursors were plated onto 96 well plates and terminally differentiated for 6 days in Compound E. Fixed neurons were stained for RBPs such as TDP-43 and FUS, β3-tubulin and DAPI (see Table 2.5) using an Opera Phenix High-Content Screening System (Perkin Elmer). Neurons were then analysed on a cell-by-cell basis using Columbus ™ Image Data Storage and Analysis System (Perkin Elmer) software version 2.8.0 and an analysis pipeline was employed as previously demonstrated (Harley & Patani. 2020). This involved the application of a DAPI mask in order to define the nucleus of cells. Next, a supervised machine learning feature was implemented to identify neuronal populations and exclude dead and non-neuronal cells. This required a linear classification training phase, employing multiple parameters such as texture, morphology, nuclear roundness and intensity to classify sub-populations within the cultures. Background intensity was then removed from each channel and average nuclear intensities were then calculated for each channel. Average cytoplasmic intensities were calculated using a 1.5μm cytoplasmic mask, defined by a cytoplasmic protein and excluding the nuclear area; defined by the nuclear mask. This yielded an average nuclear and cytoplasmic intensity measurement for each individual cell that was used to generate a N/C ratio. These individual N/C ratio values per cell were then averaged for each well and a minimum of 3 wells were measured per line. N/C values were then compared between control and VCP-mutant ALS lines.

2.4.3 Live cell imaging

For live imaging, cells were plated onto clear bottom 96 well plates and Fluo-4 AM (ThermoFisher Scientific, F14201) was added at a working concentration of 1 μM in Hank's Basic Salt Solution (HBSS) (ThermoFisher Scientific, 24020141) along with silicon rhodamine (SiR) tubulin (Tebu-bio, SC002) at a working concentration of 0.1 μM. Neurons were incubated in Fluo-4 AM and SiR tubulin for 30 minutes. Following this, neurons were washed 3 times in HBSS and then left in HBSS throughout the imaging process. Neurons were imaged using a Nikon Ti Eclipse using a KiraLux 5 MP camera from Thorlabs with a pE4000 lightsource from CoolLED and a 20X brightfield air

immersion objective from Nikon. Neurons were imaged using Micro-manager 2.0-Gamma software at 200ms intervals over a period of 50 seconds. For KCl stimulations, KCl was diluted in HBSS and added during imaging to a final concentration of 50mM. Analysis of Fluo-4 AM live imaging was carried out using ImageJ with the TimeSeries Analyzer V3 plugin and ROIs were selected within the soma of neurons. Neurons were determined to have responded to KCl if their average fluorescence signal intensity for 1 second following KCl applicated increased to 150% of the average fluorescence signal intensity analysed during the 'quiescent' period (average intensity preceding KCl stimulation). Time series calcium traces following KCl administration and when measuring spontaneous activity were calculated by the $\Delta F/F_0$ method where $\Delta F = (F-F_0)/F_0$. F_0 is the median of the fluorescence distribution during quiescent timepoints.

Antibody	Species	Supplier	Dilution
SMI-32	mouse	BioLegend (801701)	1:1000
MAP2	chicken	Abcam (ab5392)	1:1000
ChAT	goat	Millipore (AB144P)	1:100
β3-tubulin	chicken	Abcam (ab41489)	1:1000
β3-tubulin	rabbit	BioLegend (802001)	1:1000
β3-tubulin	mouse	BioLegend (801201)	1:1000
TDP-43	rabbit	ProteinTech (12892-1-AP)	1:400
FUS	mouse	Santa Cruz (sc-47711)	1:200
OLIG2	rabbit	Abcam (ab9610)	1:500
OLIG3	mouse	R&D (MAB2456)	1:500
NKX6.1	goat	R&D (AF5857)	1:1000
PAX7	mouse	Santa Cruz (sc-81648)	1:250
PAX3	mouse	R&D (MAB2457)	1:250
LHX5	mouse	DSHB (PCRP-LHX5-1B7)	1:50
LHX3	rabbit	Abcam (ab14555)	1:500
LHX1	rabbit	Abcam (ab14554)	1:500
FOXP1	goat	R&D (AF4534)	1:500
FOXP1	rabbit	Abcam (ab16645)	1:250

PEA3	mouse	Santa Cruz (sc-113)	1:500
GFAP	chicken	Abcam (ab4674)	1:1000
Donkey anti goat IgG 488	donkey	Invitrogen (A11055)	1:1000
Donkey anti mouse IgG 568	donkey	Invitrogen (A10037)	1:1000
Donkey anti rabbit IgG 647	donkey	Invitrogen (A31573)	1:1000
Donkey anti mouse IgG 647	donkey	Invitrogen (A31571)	1:1000
Goat anti chicken IgG 488	goat	Invitrogen (A11039)	1:1000
Goat anti chicken IgG 647	goat	Invitrogen (A21449)	1:1000

Table 2.5 List of antibodies used for immunofluorescence experiments.

2.5 Statistical analysis

The data presented in this thesis are from a range of biological, technical and experimental repeats, which are stated in each figure legend. Data is presented as the mean ± SEM. Statistical analysis was conducted using GraphPad Prism 7.0. Differences between two datasets were assessed using unpaired two-tailed student's t-test with Welch's correction, assuming unequal variance and a Gaussian distribution. A one-way ANOVA with Tukey post-hoc comparison test was used when comparing differences between the means of more than two groups, assuming normal distribution. The statistical test is stated within each figure legend. A p-value of 0.05 or below was considered to be statistically significant (*≤0.05, **≤0.01, ***≤0.001 or ****≤0.0001).

Chapter 3. Generating motor neuron diversity using human induced pluripotent stem cells

3.1 Introduction

The ability to generate defined cellular subtypes from hiPSCs through application of neuro-developmental principles offers a unique experimental opportunity to interrogate the molecular mechanisms underlying human neuronal diversity (Davis-Dusenbery et al. 2014; Patani. 2016). Spinal motor neurons (MNs) are a collection of myriad neuronal subtypes located within the ventral region of the neural tube (Jessell et al. 2011). MNs have distinct connectivity patterns, extensively innervating distal muscle fibers, whereby they can carry out their primary function of muscle fiber contraction. This conveys their primary role in the spinal cord as essential mediators of complex motor behaviours such as breathing and walking (Stifani. 2014).

The molecular mechanisms that choreograph the effects of morphogenetic extrinsic signals with transcription factor expression / repression and subsequent neuronal subtype determination in the spinal cord have been studied extensively both *in vivo* using animal models and *in-vitro* using mouse embryonic stem cells (mESCs) and hiPSC (Li et al. 2005; Davis-Dusenbery et al. 2014). Indeed, application of developmental inductive signals, such as RA and SHH, has enabled directed differentiation of MNs from hiPSCs with a number of methods published (Amoroso et al. 2013; Maury et al. 2015; Du et al. 2015). These protocols attempt to mirror subtype specific generation of neurons during embryological development and necessitate sequential steps including neural induction from embryonic ectoderm, patterning along rostral-caudal and dorsal-ventral axes, and subsequently the terminal differentiation of regionally specified neural progenitors into diverse post-mitotic neuronal subtypes (Jessell et al. 2000; Davis-Dusenbery et al. 2014). *In vivo*, it has been demonstrated that signalling pathways that operate along the rostral-caudal and dorsal-ventral neuraxes first establish a matrix of positional cues, which influence progenitor cell fate specification by orchestrating the identities and concentrations of morphogenetic signals to which they are subjected (Jessell et al. 2000). However, in addition to the neural diversity during precursor ‘patterning’, *in vivo* studies

have also demonstrated that extrinsic signalling post-mitotically is also a key determinant of neuronal subtype diversification (Sockanathan et al. 2003; Thaler et al. 2004).

Retinoid signalling is important in the diversification of MN subtypes from the common MN precursor pool and establishes spinal cord columnar organization (Novitch et al. 2003; Vermot et al. 2005). At limb-innervating levels (i.e. brachio-lumbar regions), spinal motor column precursor cells are allocated to lateral (LMC) and median (MMC) pools (Jessell et al. 2011). Precursors from these distinct pools acquire different fates with respect to axonal trajection and target innervation, and can be discriminated based upon their gene expression profiles. The generation of LMC MNs is initially dependent on extrinsic RA signalling from adjacent somites, inducing local RA synthesis by subpopulations of MNs (expressing RALDH2), and this regulates the differentiation of migrating neurons into subsets of LMC neurons (Sockanathan & Jessell. 1998). The role of RA in MN subtype specification has been shown using heterotopic transplantation of RA synthesis 'hotspots' (brachial and lumbar neural tube/somites) with subsequent phenotyping of regional MN subtypes (Ensini et al. 1998). Additionally, ectopic RALDH2 expression in spinal neurons generates LMC MNs and RALDH2 knock down and knock outs cause a reduction, but not complete elimination, of both lateral and medial LMC neurons (Ensini et al. 1998; Vermot et al. 2005). Together these studies highlight distinct requirements for RA signalling in MN generation and organization.

Whilst much emphasis has been placed on developing shorter protocols with greater enrichment of spinal MN populations, these studies often use generic markers of MNs at both precursor (OLIG2) and post-mitotic (ChAT, HB9 and ISLET1) levels (Amoroso et al. 2013; Maury et al. 2015; Du et al. 2015; Thiry et al. 2020). Despite this, MNs display a remarkable level of heterogeneity beyond these pan-MN markers and this reflects the large amount of diversity in the functional properties of spinal MNs. Indeed, a recent study attempted to characterize the constituent populations of hiPSC-derived MN cultures using single-cell RNA sequencing and revealed a high level of heterogeneity in these MN populations (Thiry et al. 2020).

Spinal MNs have also been shown to exhibit selective vulnerability between different MN subtypes in ALS (Kanning et al. 2010; Nijssen et al. 2017; Tung et al. 2019). Indeed, 75% of ALS patients exhibit a limb-onset progression, thought to be a result of the early

and selective degeneration of FF alpha MNs within the LMC. Therefore, the establishment of hiPSC-derived MN protocols generating enriched populations of distinct motor column subtypes presents a tractable strategy for the elucidation of principles underlying selective vulnerability. Indeed, a mechanism underlying selective LMC MN vulnerability was recently linked to the loss of a specific microRNA (miRNA); mir-17~92 in a SOD1 G93A transgenic mouse model. Subsequent overexpression of mir-17~92 using an adenovirus was able to rescue motor deficits and SOD1 G93A mouse survival. As such, there is a pressing need for both deep phenotyping of current hiPSC-derived MN protocols, and further subtype specific MN differentiation protocols. This will then permit more accurate, and clinically relevant in-vitro model systems of motor neuronopathies.

3.2 Aims

Since there is a pressing need for deep characterisation of MNs derived from hiPSCs in order to allow generation of more clinically-relevant subtypes, the MN protocol commonly employed in the laboratory was dissected and assessed. Currently, no study has systematically studied the influence of a morphogenetic signal during both MN precursor 'patterning' and 'terminal differentiation' to establish the relative contribution of extrinsic signalling during these developmental stages in subtype diversification. Indeed, most protocols for motor neurogenesis from hiPSCs tend to focus primarily on manipulating extrinsic signals during precursor specification only.

Therefore, the specific aims of this chapter are to:

1. Assess the role of extrinsic signalling cues during precursor specification using the hiPSC-derived MN protocol commonly employed in the laboratory.
2. Examine the influence of extrinsic signalling cues during terminal differentiation and subsequent MN heterogeneity.

3.3 Results

3.3.1 Neural induction in hiPSCs

In order to generate hiPSC-derived spinal motor neurons, a previously published accelerated protocol for the efficient and robust conversion of hiPSC into enriched spinal cord motor neurons was employed and further characterised (Figure 3.1) (Hall et al. 2017; Luisier et al. 2018; Tyzack et al. 2019; Smethurst et al. 2020; Tyzack et al. 2021). Cultures were assessed at specific timepoints depicting key developmental stages of the protocol, as mentioned previously and shown in Figure 3.1. Following 7 days of neural induction using dorsomorphin (DM), SB431542 (SB) and CHIR99021 (CHIR), cells were assessed for pluripotency and neural lineage markers. qPCR analysis revealed the pluripotency marker OCT4 was significantly downregulated by day 7 when compared to hiPSC. Furthermore, OCT4 mRNA expression remained significantly low at additional timepoints including day 18 NPC and day 25 MN. This indicates a sustained loss of pluripotency and stem cell-like state during the timecourse of the protocol (Figure 3.2A). Conversely, expression of SOX1, a key marker of neural lineage; including neuroectodermal cells, was significantly upregulated following neural induction (Figure 3.2B). This included time points of day 7 neuroectodermal cells (~22 fold), day 18 NPCs (~16 fold) and day 25 MNs (~52 fold), when compared to hiPSCs. Lastly, SOX2 expression was assessed, showing a significant decrease in expression between hiPSC and D7 neuroectodermal cells, but only a trend towards a decrease was found when comparing hiPSC with D18 NPC and D25 MN timepoints respectively (Figure 3.2C). These expression patterns reflect the dual functions of SOX2 as both a marker of pluripotency and neural lineage. Taken together, these data strongly indicate a decrease in pluripotency markers following neural induction, coinciding with an upregulation of neurogenic markers.

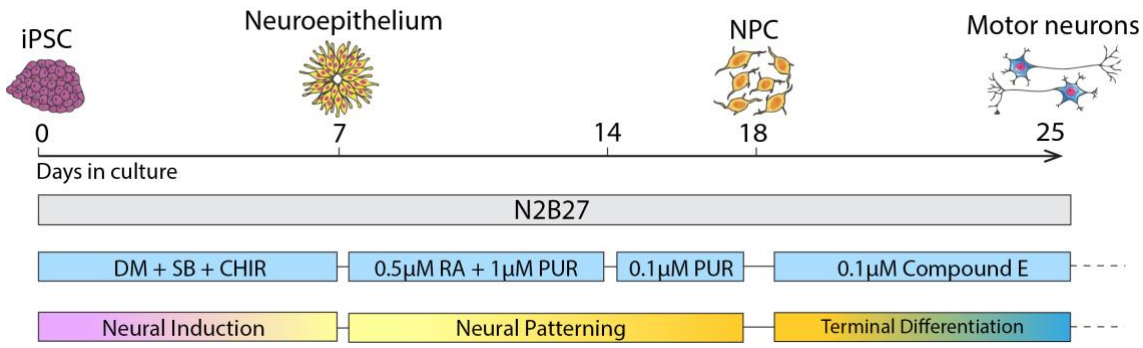

Figure 3.1 hiPSC-directed differentiation strategy for generating spinal cord motor neurons

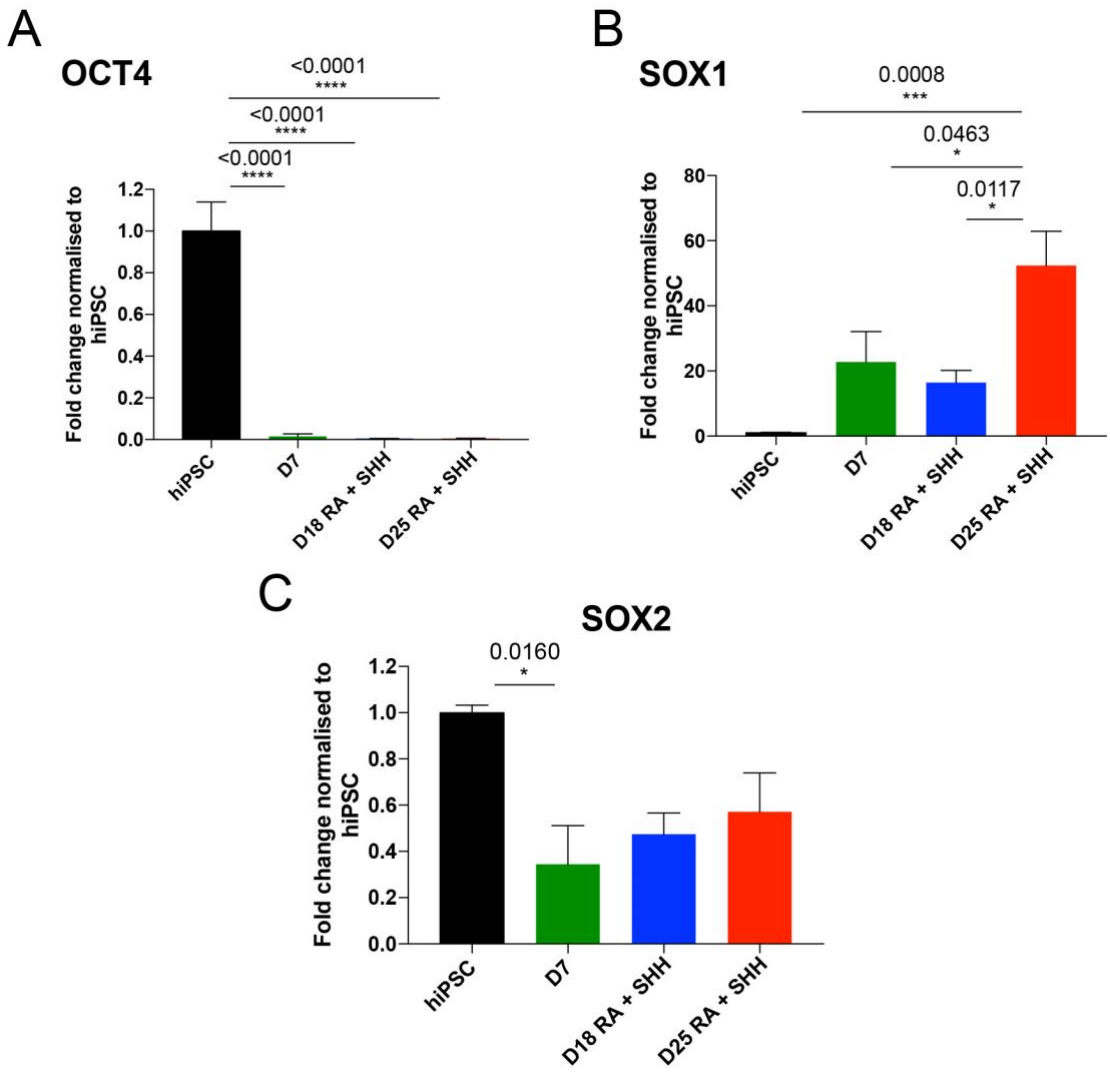

Figure 3.2 Expression of neural lineage markers and pluripotency markers following neural induction

Bar plots depicting mRNA expression levels of (A) the pluripotency marker OCT4, (B) neuroectodermal and neural lineage marker SOX1 and (C) pluripotency and neural lineage marker SOX2 in hiPSC, day 7 neuroepithelial cells (D7) following neural induction, day 18 MN neural precursors (NPCs) (D18 RA + SHH) and day 25 MNs (D25 RA + SHH) following terminal differentiation, as assessed by qPCR. Each sample was normalised over its GAPDH expression level and each timepoint was normalised against hiPSC. n=2 per cell line with 3 independent control lines used (CTRL1-3). Error bars are displayed as mean ± SEM. p value calculated using one-way ANOVA with Tukey correction for multiple comparison, * represents $p < 0.05$, *** represents $p < 0.001$, **** represents $p < 0.0001$.

3.3.2 Precursor patterning from neuroectodermal lineage

As mentioned previously, spinal cord populations can be classified into distinct domains at both progenitor and post-mitotic stages of development (Lai et al. 2016). As such, a common method employed to distinguish neural tube domain populations is through the unique transcription factor 'postcode' that is expressed by cells within each domain (Figure 1.2). These transcription factors include specific basic helix loop helix (bHLH) and homeodomain (HD) factors. In order to characterise the accurate patterning of MNs to the ventral pMN domain of the spinal cord, day 18 NPCs were assessed for ventral neural tube markers spanning, or selective to, the pMN domain. It is important to note that the SHH agonist purmorphamine is crucial for ventralisation (Jessell et al. 2000) and as such, NPCs patterned in the absence of purmorphamine (RA only) were used as a negative control. qPCR analysis revealed significantly higher expression levels of NKX6.1 and OLIG2 in RA + SHH patterned NPCs, when compared to RA only conditions, indicating correct patterning to the ventral pMN domain of the neural tube (Figure 3.3). Interestingly, only an insignificant trend towards a decrease in the P3 ventral domain marker NKX2.2 was found. This suggests that RA + SHH treated NPCs were not 'over-ventralised' significantly to the ventral-most P3 domain that does not yield populations of MNs.

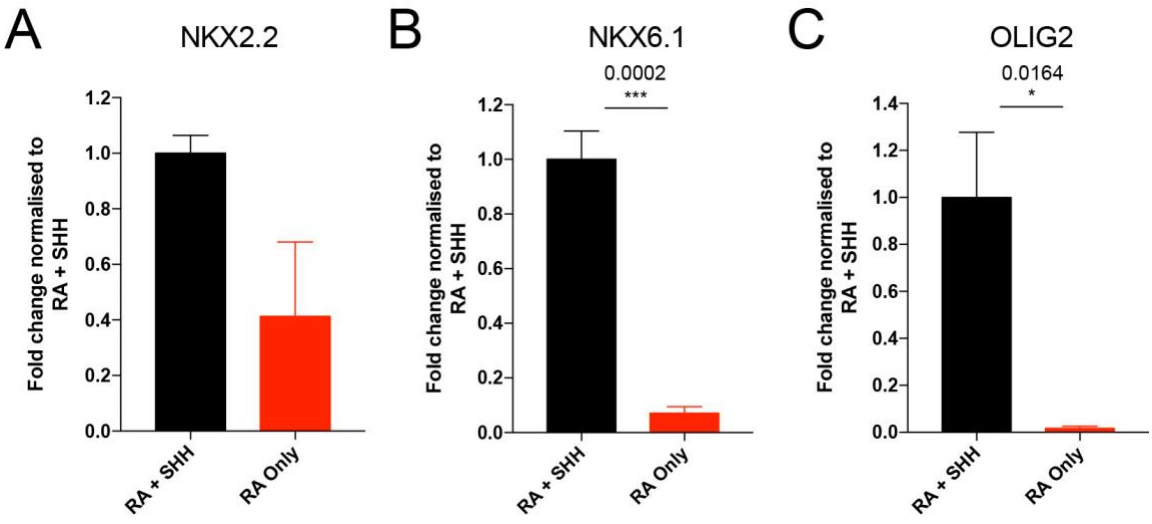

Figure 3.3 Expression profiles of ventral and pMN neural tube domain markers in day 18 motor neuron precursors

Bar plots depicting mRNA expression levels of (A) P3 domain marker NKX2.2, (B) ventral P3, pMN and P2 domain marker NKX6.1 and (C) pMN domain marker OLIG2 in day 18 MN NPCs (RA + SHH) and day 18 cultures patterned with RA but in the absence of SHH (RA only), as

assessed by qPCR. Each sample was normalised over its GAPDH expression level and each timepoint was normalised against RA + SHH. n=3 per cell line with 3 independent control lines used (CTRL1-3). Error bars are displayed as mean ± SEM. p value calculated using unpaired two-tailed t-test with Welch's correction, * represents $p < 0.05$ and *** $p < 0.001$.

3.3.3 A Deeper evaluation of precursor patterning

As mentioned previously, the protocol for deriving spinal MNs involves 2 separate patterning steps, the latter of which occurs between day 14 and day 18 with a reduction in purmorphamine concentration and the removal of RA. The rationale behind this is to mimic developmental signals encountered *in vivo* where progenitors emanating from the ventral end of the ventricular zone are exposed to 2 sources of SHH; from the floor plate and underlying notochord (Jessell et al. 2000). Furthermore, as the neural tube expands, the distance between the pMN domain and SHH producing floor plate increases, reducing the concentration of SHH that the pMN domain is exposed to (Sagner & Briscoe. 2019). In order to investigate the effects of this 4 day period, day 14 and day 18 NPC timepoints were assessed for neural tube progenitor markers. Interestingly, qPCR analysis of day 14 and day 18 samples revealed an insignificant difference between OLIG2, NKX6.1 and NKX2.2 expression between these timepoints (Figure 3.4). Further immunolabeling also showed an insignificant difference in OLIG2 expression between day 14 (~51%) and day 18 (~42%) NPCs (Figure 3.5). However, a significant increase in the number of NKX6.1 positive NPCs was found at day 18 (~93%), when compared to day 14 (~63%) (Figure 3.5). Taken together, these data suggest that the 4 day purmorphamine only period is not necessary for further enrichment of MNs, but does significantly increase the proportion of NKX6.1 and ventral class II SHH activated (i.e. P3, pMN and P2 domain) populations. These data also suggest that there is a ventral shift in the progenitor populations between day 14 and day 18 NPCs from more dorsal but still ventral (i.e. P0, P1) to further ventral domains (P2, pMN and P3). Interestingly, immunolabeling for NKX2.2 revealed low / negligible levels of NKX2.2 expression at both timepoints and in agreement with the qPCR data shown in Figure 3.3A, suggesting that MN NPCs did not appear to acquire characteristics of the ventral-most P3 domain (~0% at day 14, ~1% at day 18) (Figure 3.6).

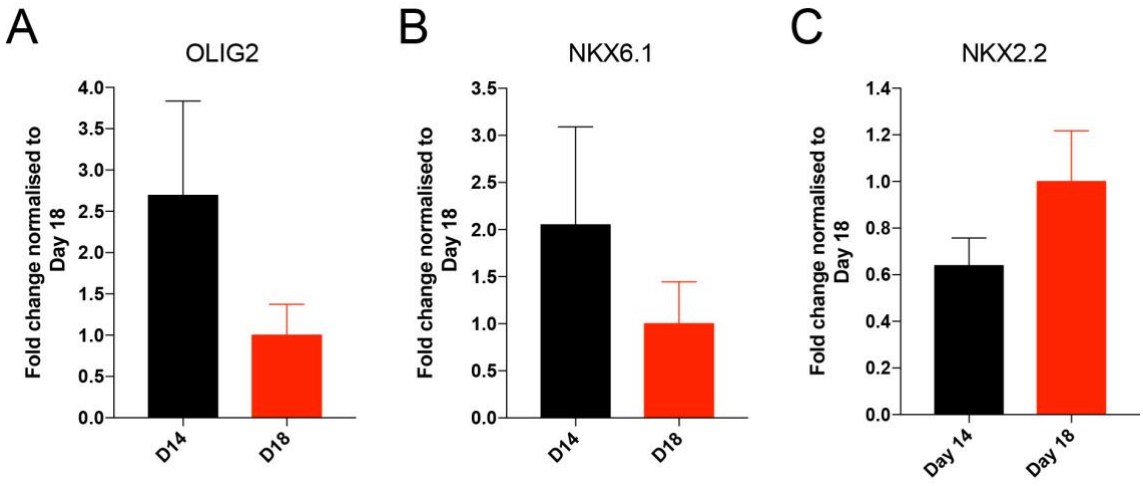

Figure 3.4 Expression profiles of ventral and pMN domain neural tube markers in day 14 and day 18 motor neuron precursors

Bar plots showing mRNA expression levels of (A) pMN domain marker OLIG2, (B) ventral P3, pMN and P2 domain marker NKX6.1 and (C) P3 domain marker NKX2.2 in day 14 MN NPCs (D14) and day 18 MN NPCs (D18), as assessed by qPCR. Each sample was normalised over its GAPDH expression level and normalised to D18 timepoints. n=3 per cell line with 3 independent control lines used (CTRL1-3). Error bars are displayed as mean ± SEM. p value calculated using unpaired two-tailed t-test with Welch's correction.

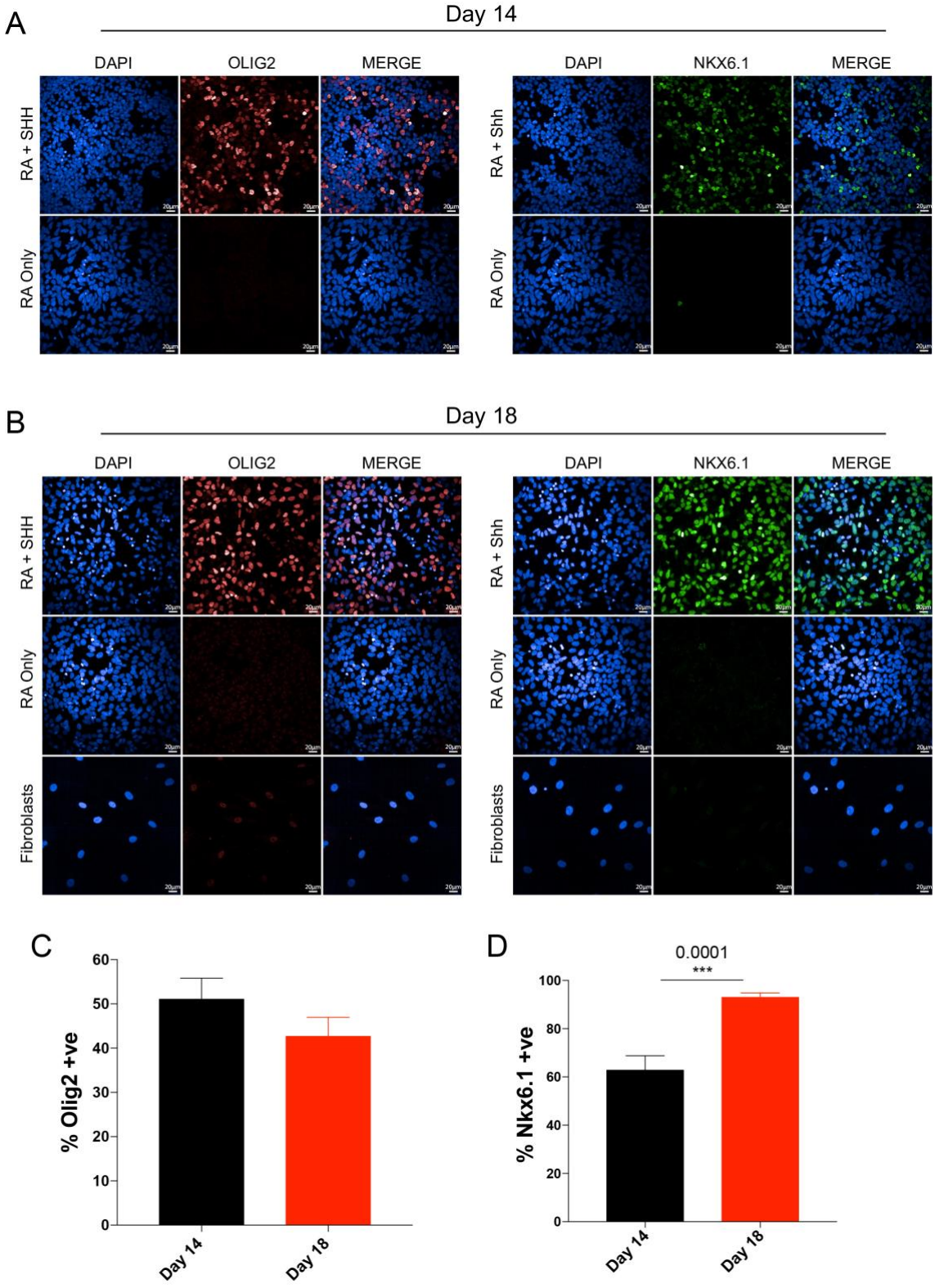

Figure 3.5 Differential expression of ventral and pMN neural tube domain markers in day 14 and day 18 motor neuron precursors

Representative immunocytochemistry images of the CTRL1 line using the cellular marker of ventral spinal progenitors - NKX6.1 and pMN domain progenitors – OLIG2 in (A) day 14 MN NPCs and day 14 cultures patterned with RA but in the absence of SHH (RA only). Scale bar set at 20 μm. (B) Representative immunocytochemistry images using the cellular marker of ventral spinal progenitors - NKX6.1 and pMN domain progenitors – OLIG2 in day 18 MN NPCs and day 18 cultures patterned with RA but in the absence of SHH (RA only) and fibroblasts as a negative control. Scale bar set at 20 μm. Bar plots representing quantitative immunocytochemistry data for (C) percentage of cells expressing OLIG2 and (D) percentage of cells expressing Nkx6.1 in day 14 and day 18 MN NPCs. n=3 per cell line with 3 independent control lines used (CTRL1-3). Error bars are displayed as mean ± SEM. p value calculated using unpaired two-tailed t-test with Welch's correction, *** represents $p < 0.001$.

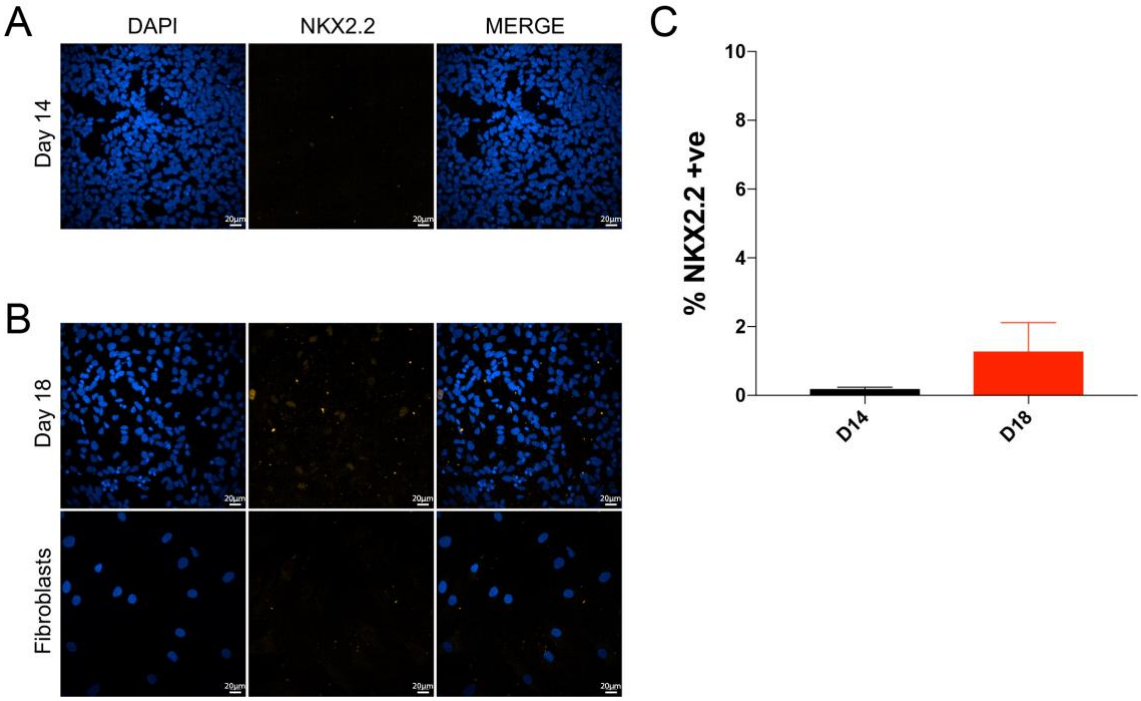

Figure 3.6 Expression of P3 neural tube domain marker NKX2.2 in day 14 and day 18 motor neuron precursors

Representative immunocytochemistry images of the CTRL1 line using the cellular marker of ventral-most P3 domain progenitors – NKX2.2 in (A) day 14 MN NPCs. Scale bar set at 20 μm. (B) Representative immunocytochemistry images using P3 domain progenitor marker – NKX2.2 in day 18 MN NPCs and fibroblasts as a negative control. Scale bar set at 20 μm. (C) Bar plots representing quantitative immunocytochemistry data for percentage of cells expressing OLIG2 in day 14 and day 18 MN NPCs. n=3 per cell line with 3 independent control lines used (CTRL1-

3). Error bars are displayed as mean ± SEM. p value calculated using unpaired two-tailed t-test with Welch's correction.

3.3.4 Terminal differentiation of motor neuron precursors

In order to assess whether day 18 MN NPCs differentiate into highly enriched populations of MNs, 0.1μM CE was administered for 7 day and immunocytochemistry for the pan-motor neuronal markers ChAT and SMI32 was carried out. This revealed a robust enrichment of MN NPCs into MNs, with ~95% of neurons staining positive for ChAT and ~82% for SMI-32 (Figure 3.7). Spinal MNs display a remarkable heterogeneity that must account for their hugely complex and diverse roles in controlling and shaping motor output. This heterogeneity is partially achieved through a complex interplay between retinoids and HOX genes. As a result, distinct motor columns are patterned throughout the spinal cord and along the rostro-caudal axis (Dasen et al. 2008). In order to characterise the rostral-caudal position of MNs throughout the directed differentiation protocol, qPCR analysis of the HOX code was carried out (Figure 3.8). As mentioned previously (Chapter 1.1.1), the HOX code delineates the settling position of populations of cells between the rhombomeres of the hindbrain and the full length of the spinal cord. In this manner, it was shown that day 25 MNs appear to form a lower cervical/brachial rostral-caudal identity with the highest upregulation identified in HOXA4 and HOXA5 by qPCR (Figure 3.8). Supporting this, HOXA3, HOXB4, HOXC4, HOXD4 and HOXA5 were the most abundantly expressed HOX paralogs in day 25 MN cultures (data not displayed). It should be noted that, whilst also highly upregulated in day 18 NPCs and day 25 MNs; HOX6, 7 and 8 also delineate a lower cervical/brachial spinal position, whereas HOX9 paralogs are a prominent marker of thoracic spinal cord. Accordingly, low levels of HOXA9 were identified in cultures, suggesting that thoracic spinal cord identity was not specified. In addition, HOXD10 was not found to be highly upregulated, suggesting neglible lumbar spinal cord specification. Later HOX genes were not examined in this study because they were not expected to be upregulated in RA treated cultures. Rhombomere specification was also identified to be low, due to low levels of HOXB1 and HOXD1. Day 18 NPCs demonstrated similar trends to day 25 MNs, but at reduced expression levels. This suggests that the HOX code may become refined or potentially consolidated throughout terminal differentiation.

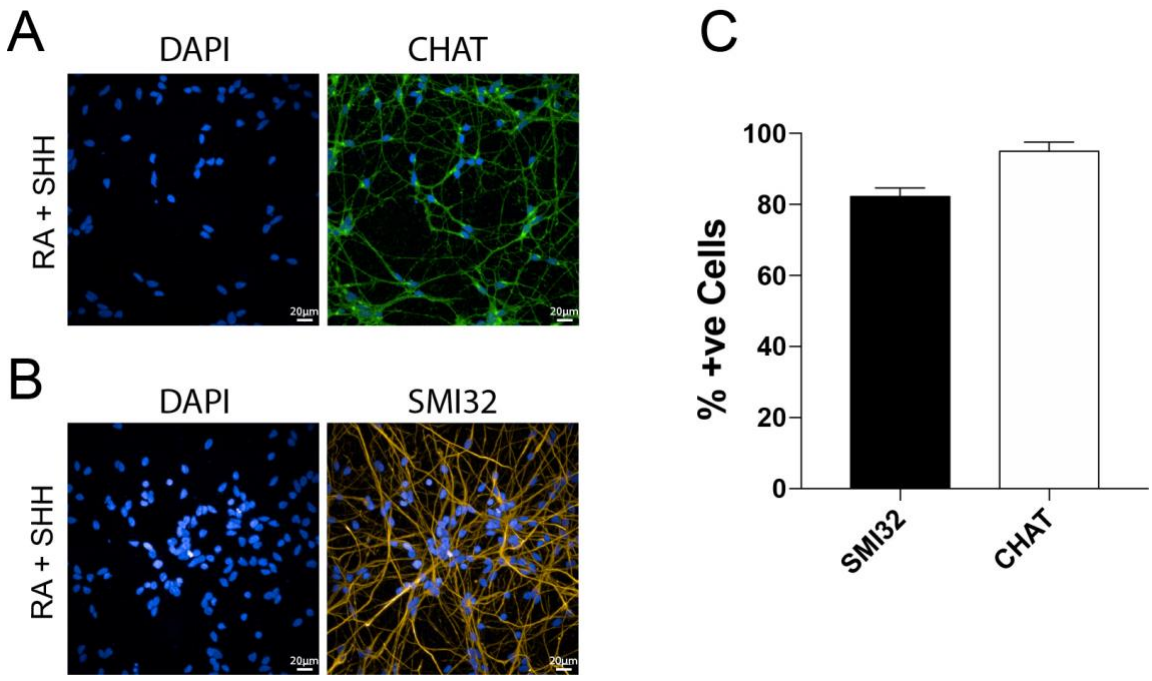

Figure 3.7 Enrichment of pan-motor neuronal markers in day 25 hiPSC-derived motor neurons

(A) Representative immunocytochemistry images of the CTRL3 cell line using the cellular marker of MNs – ChAT and (B) the MN neurofilament marker SMI-32, in day 25 MNs following terminal differentiation for 7 days. Scale bar set at 20 µm. (C) Bar plot representing quantitative immunocytochemistry data for the percentage of cells expressing ChAT or SMI32 in day 25 motor neurons. n=3 per cell line with 3 independent control lines used (CTRL1-3). Error bars are displayed as mean ± SEM.

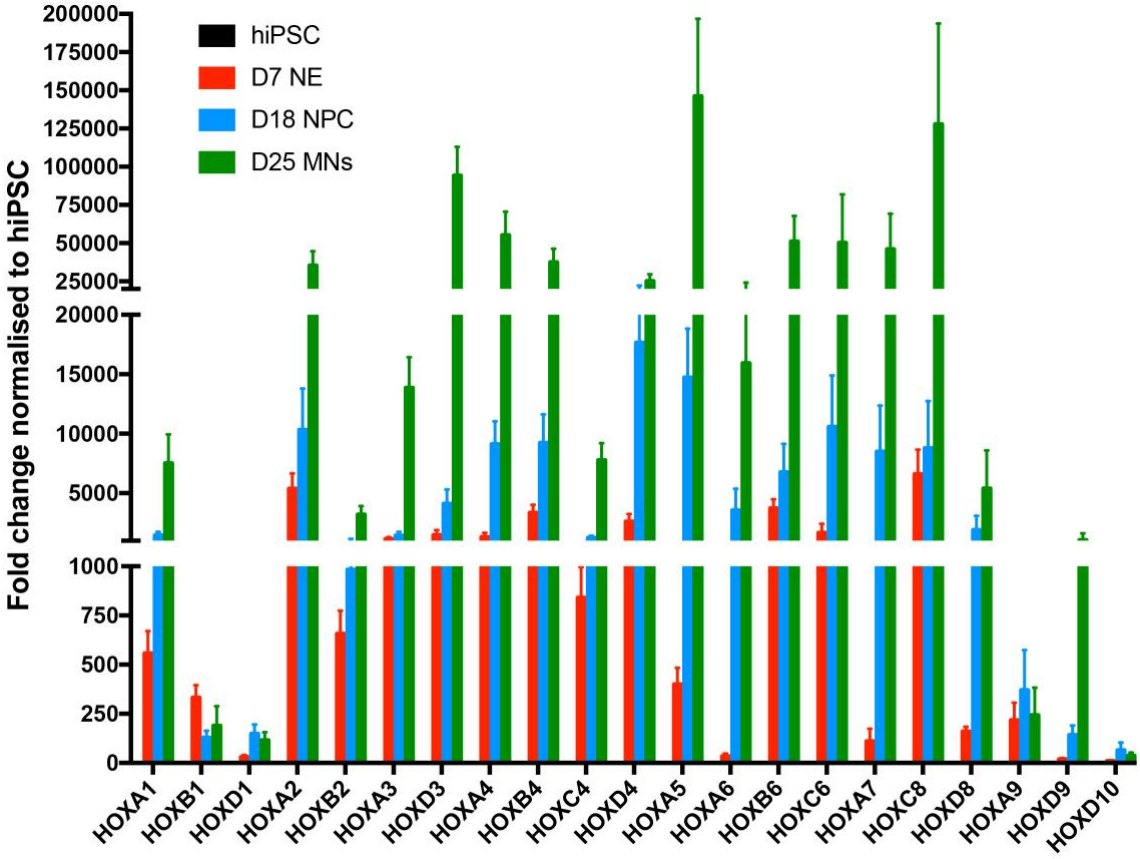

Figure 3.8 Expression profiles of HOX genes during hiPSC-derived motor neuron differentiation

Bar plot depicting mRNA expression levels of an array of HOX genes delineating the full length of the human spinal cord in day 7 neuroepithelial cells (D7 NE), day 18 MN precursors (D18 NPC) and day 25 MNs (D25 MNs), as assessed by qPCR. Each sample was normalised over its GAPDH expression level and each individual timepoint was normalised against hiPSC. n=2 per cell line with 3 independent control lines used (CTRL1-3). Error bars are displayed as mean ± SEM.

3.3.5 Generating motor column diversity during terminal differentiation

An additional layer of complexity in the organisation of MNs stems from their arrangement into motor columns. Indeed, spinal MNs at limb-innervating regions of the spinal cord (brachial and lumbar) give rise to both median motor column (MMC) and lateral motor column (LMC) MNs. Specification of the LMC is imposed by retinoid signals that are derived initially from adjacent somites, and later by earlier-born LMC neurons that start to express the RA synthesising enzyme RALDH2. Subsequent

production of retinoids in these early-born LMC neurons act in a paracrine manner to impose a lateral phenotype on later-born post-mitotic MNs. Importantly, the induction of LMC specification has been demonstrated to occur in MNs that have exited the cell cycle (Hollyday & Hamburger. 1977; Sockanathan & Jessell. 1998; Adams et al. 2015). Given the cervical/brachial position of MN cultures as shown previously, the assessment of motor column identity was next assessed in the presence or absence of RA to determine the importance of post-mitotic RA signalling in forming LMC populations. Thus, from day 18 onwards, 0.5 μM RA was added to the cultures in addition to Compound E during terminal differentiation (RA + CE) (Figure 3.9). qPCR analysis at day 25 timepoints revealed significant differences in MMC and LMC markers between RA + CE treated conditions and CE only treated cultures (Figure 3.10). Indeed, the addition of RA during terminal differentiation resulted in an increase in the LMC co-factor FoxP1 and also the lateral LMC (LMCl) LIM-HD transcription factor LHX1. This correlates with *in vivo* studies demonstrating that the generation of LMCl is dependent on retinoid signalling (Sockanathan & Jessell. 1998). Conversely, there was a significant decrease in expression of LHX3, the LIM-HD marker of the MMC in RA treated post-mitotic cultures. Importantly, no significant difference was found in the expression of MN markers (ChAT, HB9 and ISL1) or the pan-neuronal marker β3-tubulin (Figure 3.10).

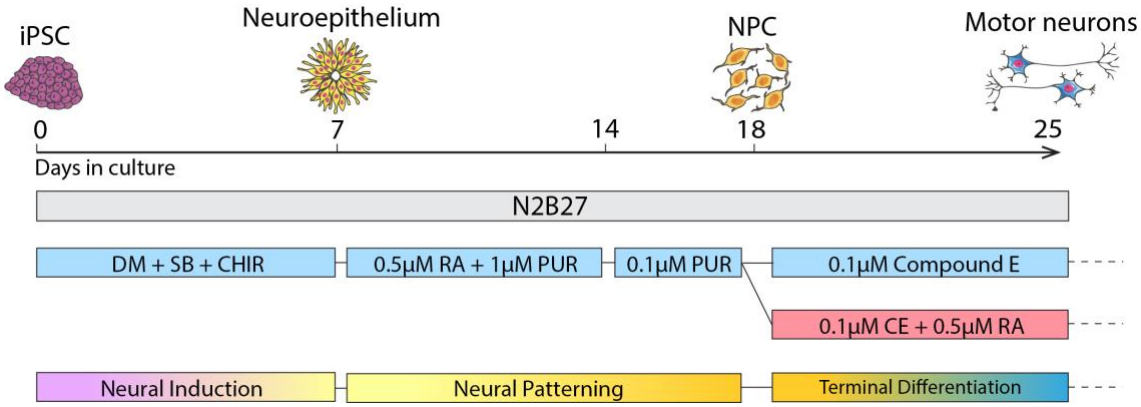

Figure 3.9 hiPSC-directed differentiation strategy for generating post-mitotic motor column diversity

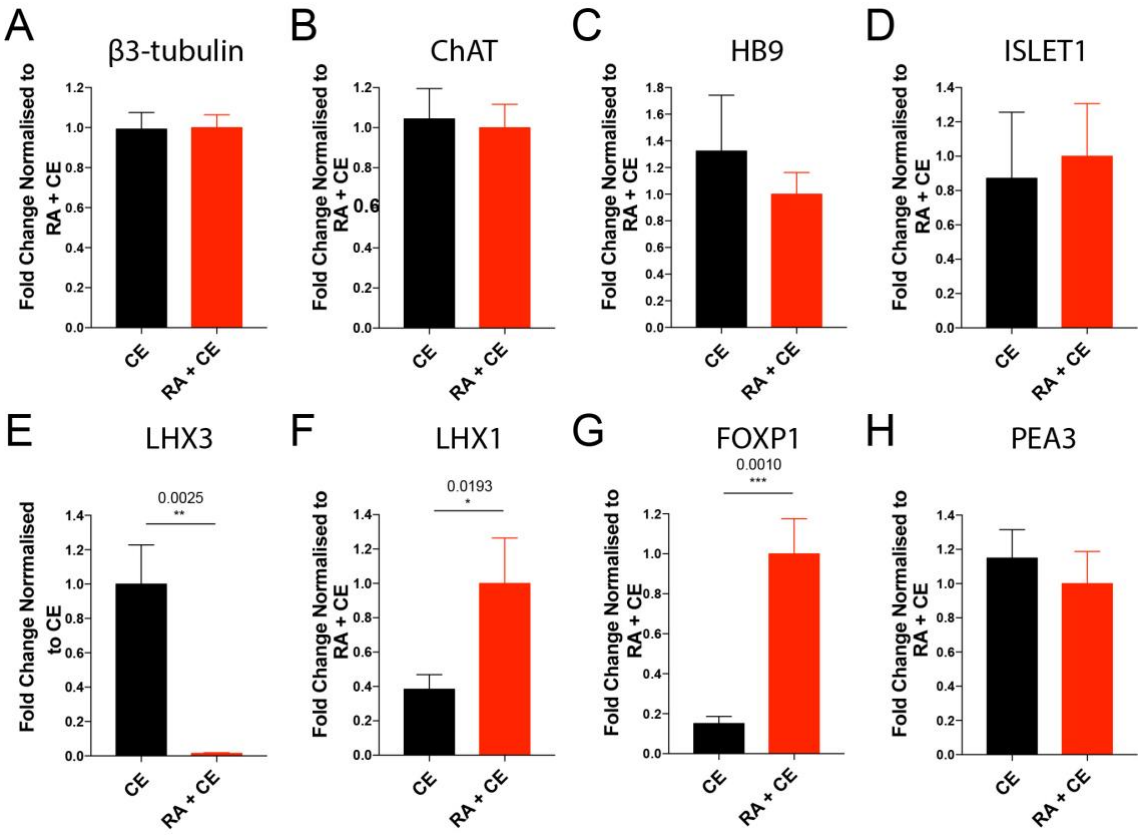

Figure 3.10 mRNA expression levels of motor neuron and motor column markers in motor neurons exposed to retinoids or retinoid-independent during terminal differentiation

Bar plots depicting mRNA expression levels of (A) pan-neuronal marker - β3-tubulin, (B) MN and cholinergic marker - ChAT, (C) MN markers - HB9 and (D) ISLET1, (E) MMC subdivision marker – LHX3, (F) LMCl subdivision marker – LHX1, (G) LMC motor column marker – FOXP1 and (H) the specific LMCl MN subgroup marker – PEA3, in day 25 MNs terminally differentiated in 0.1μM compound E (CE) or 0.5μM retinoic acid and 0.1μM compound E (RA + CE), as assessed by qPCR. Each sample was normalised over its GAPDH expression level and each timepoint was normalised to either CE only or RA + CE conditions (as indicated on each graph). n=2 per cell line with 5 independent control lines used (CTRL1-5). p value calculated using unpaired two-tailed t-test with Welch's correction, * represents $p < 0.05$, ** represents $p < 0.01$, *** represents $p < 0.001$.

Immunolabeling revealed similar findings to the qPCR data, with no significant difference between the percentage of ChAT positive MNs between CE only (~98%) and RA + CE (~96%) conditions, indicating that MN specification was not altered (Figure 3.11). However, there was an increase in the number of FOXP1 positive MNs in RA + CE treated MNs (~45%) compared to CE only (~10%) (Figure 3.12). In contrast, the

number of MNs expressing the MMC marker LHX3 was significantly reduced with the addition of RA during terminal differentiation (RA + CE ~8% vs CE only ~51%) (Figure 3.13). As mentioned previously, the LMC is further subdivided into LMCl and LMCm, targeting ventral and dorsal limb muscles respectively. The lateral subdivision of the LMC (LMCl) and the medial subdivision of the LMC (LMCm) can be distinguished by their differential molecular expression profile, with the exception of FOXP1 as a generic LMC marker. Immunolabeling for LHX1 was therefore carried out in order to investigate the presence of LMCl in RA + CE treated cultures. Indeed, a significant increase in LHX1 positive MNs was identified in RA + CE conditions (~31%), when compared to CE only (~2%), indicating the presence of a small populations of LMCl MNs (Figure 3.14). However, low / negligible levels of PEA3, a specific LMCl pool marker of some brachial MNs such as the cutaneous maximus muscle, was found in RA + CE (~0%) vs CE only (~0%) cultures (Figure 3.15).

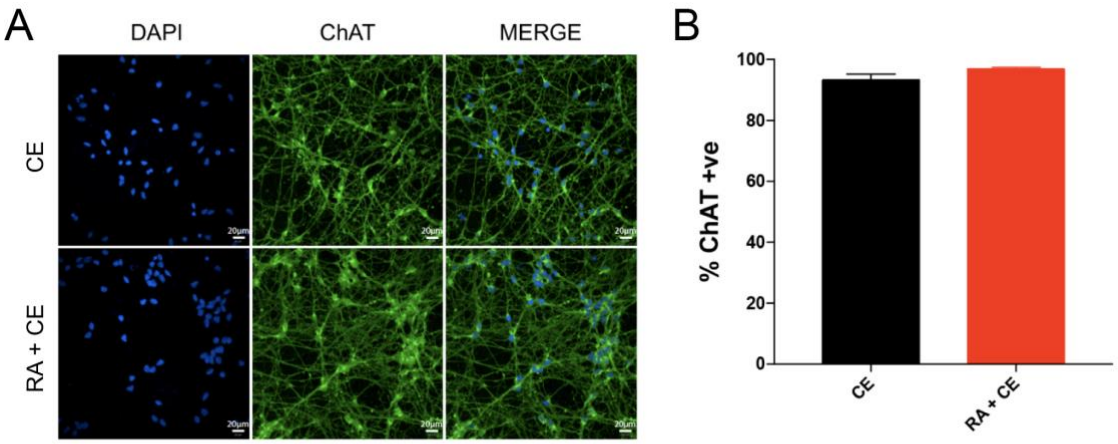

Figure 3.11 Expression of cholinergic and motor neuron marker ChAT in motor neurons exposed to retinoids or retinoid-independent signalling during terminal differentiation

(A) Representative immunocytochemistry images of the CTRL5 cell line using the cellular marker of cholinergic neurons and MNs – ChAT in day 25 MNs terminally differentiated for 7 days in 0.1µM compound E (CE) or 0.5µM retinoic acid and 0.1µM compound E (RA + CE). Scale bar set at 20 µm. (B) Bar plot depicting quantitative immunocytochemistry data for percentage of cells expressing ChAT in day 25 MNs terminally differentiated in CE or RA + CE. n=3 per cell line with 3-5 independent control lines used (CTRL1-5).

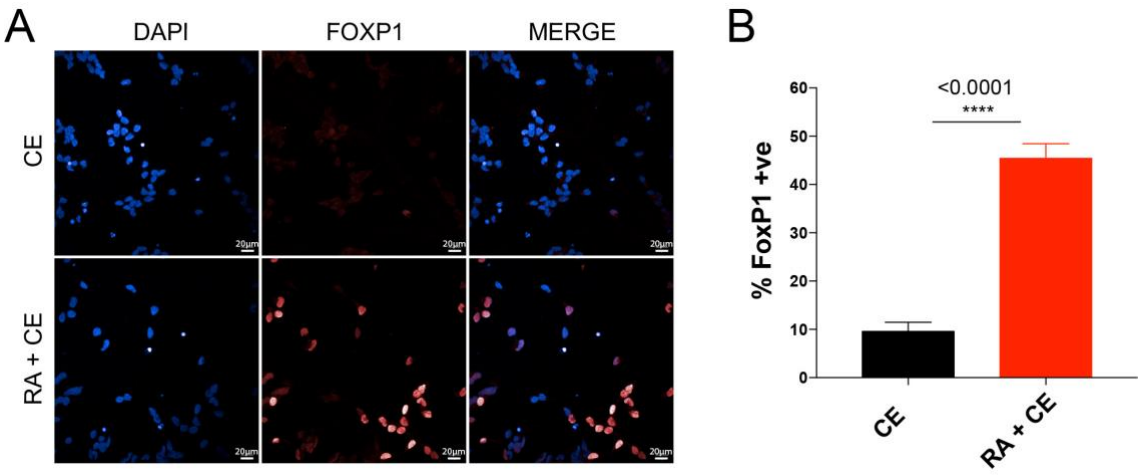

Figure 3.12 Expression of LMC motor column marker FOXP1 in motor neurons exposed to retinoids or retinoid-independent during terminal differentiation

(A) Representative immunocytochemistry images of the CTRL3 cell line using the cellular marker of LMC MNs - FOXP1 in day 25 MNs terminally differentiated for 7 days in 0.1µM compound E (CE) or 0.5µM retinoic acid and 0.1µM compound E (RA + CE). Scale bar set at 20 µm. (B) Bar plot depicting quantitative immunocytochemistry data for percentage of cells expressing FOXP1 in day 25 MNs terminally differentiated in CE or RA + CE. n=3 per cell line with 3-5 independent control lines used (CTRL1-5).. Error bars are displayed as mean ± SEM. p value calculated using unpaired two-tailed t-test with Welch's correction, **** represents $p < 0.0001$.

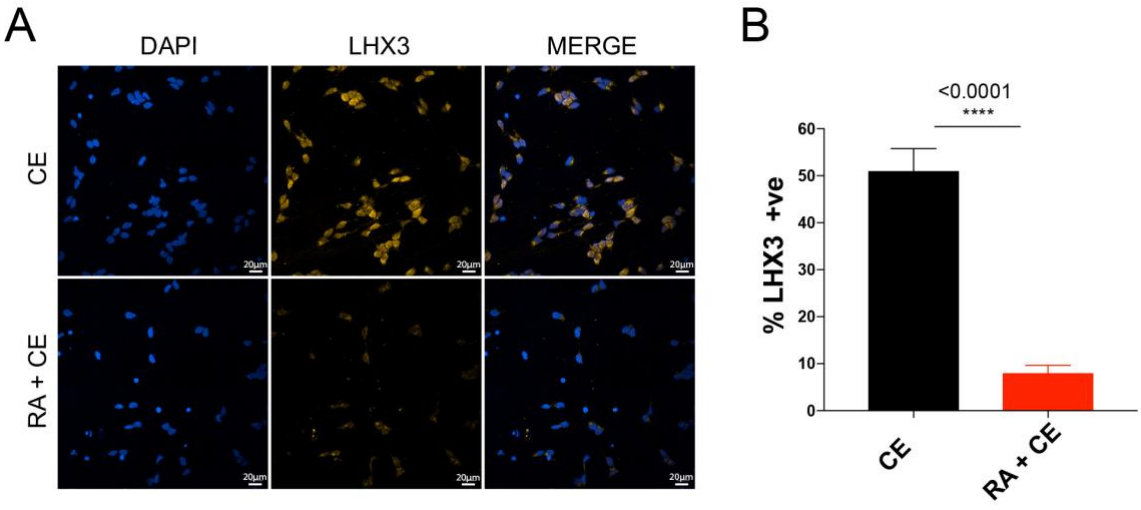

Figure 3.13 Expression of MMC motor column marker LHX3 in motor neurons exposed to retinoids or retinoid-independent during terminal differentiation

(A) Representative immunocytochemistry images of the CTRL1 cell line using the cellular marker of MMC MNs - LHX3 in day 25 MNs terminally differentiated for 7 days in 0.1µM compound E (CE) or 0.5µM retinoic acid and 0.1µM compound E (RA + CE). Scale bar set at 20 µm. (B) Bar plot depicting quantitative immunocytochemistry data for percentage of cells expressing LHX3 in day 25 MNs terminally differentiated in CE or RA + CE. n=3 per cell line with 3-5 independent control lines used (CTRL1-5). Error bars are displayed as mean ± SEM. p value calculated using unpaired two-tailed t-test with Welch's correction, **** represents $p < 0.0001$.

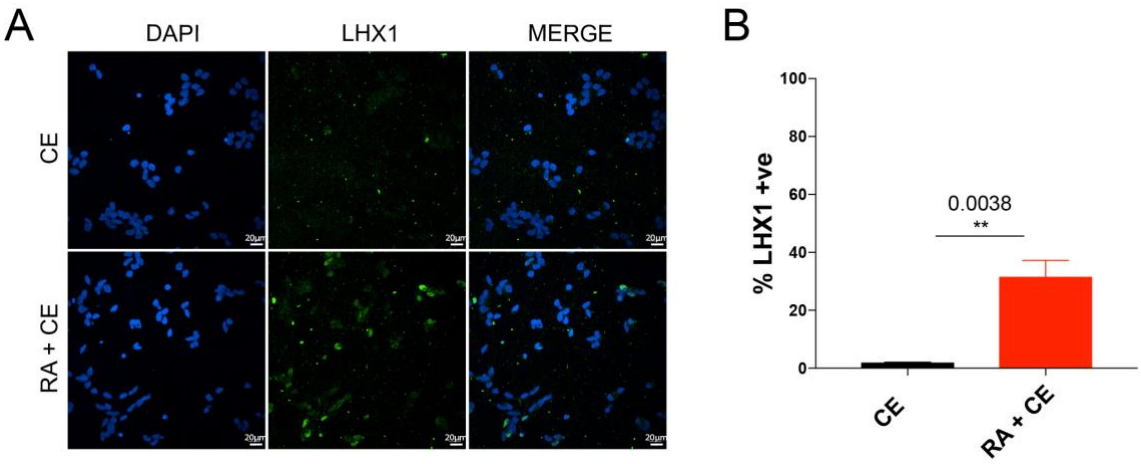

Figure 3.14 Expression of LMCl subdivision marker LHX1 in motor neurons exposed to retinoids or retinoid-independent during terminal differentiation

(A) Representative immunocytochemistry images of the CTRL1 cell line using the cellular marker of LMCl MNs – LHX1 in day 25 MNs terminally differentiated for 7 days in 0.1µM compound E (CE) or 0.5µM retinoic acid and 0.1µM compound E (RA + CE). Scale bar set at 20 µm. (B) Bar plot depicting quantitative immunocytochemistry data for percentage of cells expressing LHX1 in day 25 MNs terminally differentiated in CE or RA + CE. n=3 per cell line with 3-5 independent control lines used (CTRL1-5). Error bars are displayed as mean ± SEM. p value calculated using unpaired two-tailed t-test with Welch's correction, ** represents $p < 0.01$.

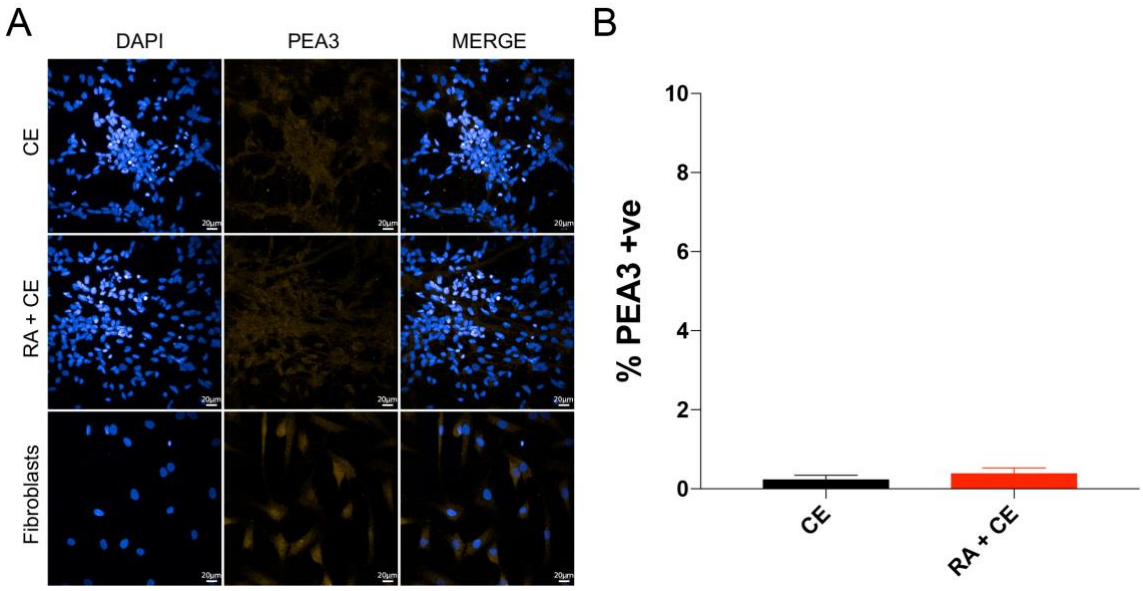

Figure 3.15 Expression of LMCl motor pool marker PEA3 in motor neurons exposed to retinoids or retinoid-independent during terminal differentiation

(A) Representative immunocytochemistry images of the CTRL1 cell line using the cellular marker of a branch of the LMCl division of MNs – PEA3 in day 25 MNs terminally differentiated for 7 days in 0.1µM compound E (CE) or 0.5µM retinoic acid and 0.1µM compound E (RA + CE). Scale bar set at 20 µm. (B) Bar plot depicting quantitative immunocytochemistry data for percentage of cells expressing PEA3 in day 25 MNs terminally differentiated in CE or RA + CE. n=3 per cell line with 3-5 independent control lines used (CTRL1-5). Error bars are displayed as mean ± SEM. p value calculated using unpaired two-tailed t-test with Welch's correction.

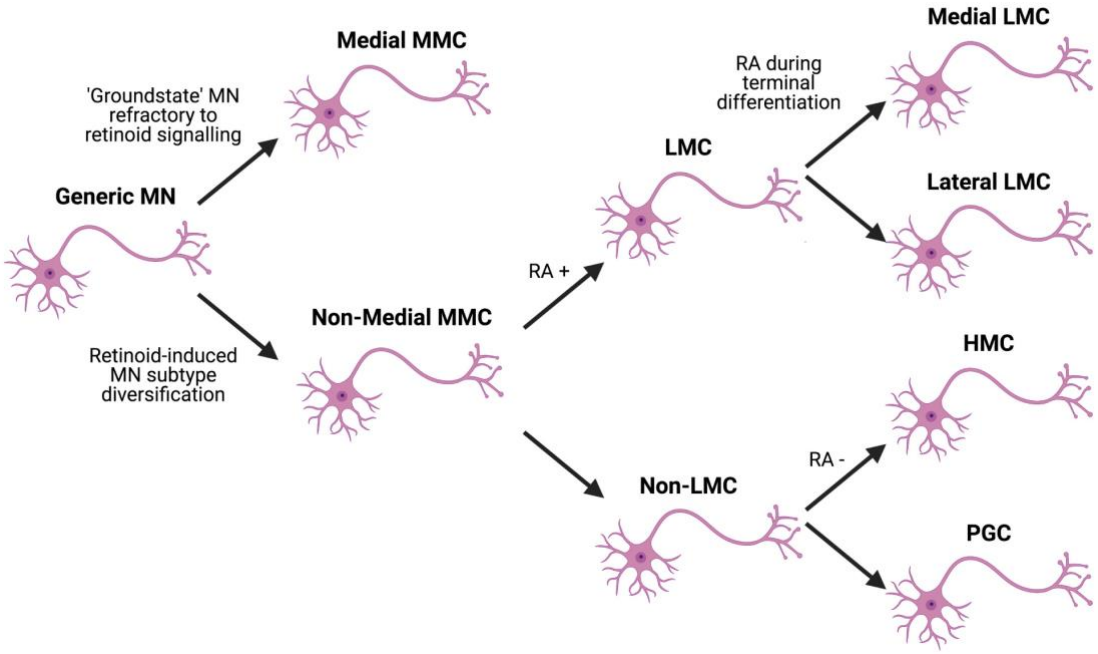

Figure 3.16 Motor column diversity in the spinal cord

Schematic depicting MN subtype diversity as defined by motor column identity. Initially, either a medial or non-medial MMC phenotype is induced by 'patterning' pMN NPCs with or without retinoids, respectively. Following this, retinoid signalling during terminal differentiation in post-mitotic non-medial MMC MNs induces an LMC phenotype, with upregulation of FOXP1. This can cause a medial or lateral LMC fate, with upregulation of LHX1 indicating LMCl specification. In the absence of retinoid signalling during terminal differentiation, this induces an HMC or PGC fate depending on the axial identity and expression of thoracic HOX genes.

3.4 Discussion

The advent of hiPSC technology has revolutionised disease modelling, providing a physiologically relevant human model system with enormous potential. The generation of ontogeny-driven directed differentiation strategies has yielded a vast array of hiPSC-derived cell types, and the drive for deriving novel populations with more refined lineages is ever-expanding. This system; however, is often limited by the ability to reliably generate specific cell types with defined phenotypic traits. As a consequence, deep characterisation and phenotyping of hiPSC-derived populations is a prerequisite for fundamental biological studies, disease modelling and drug discovery efforts (Thiry et al. 2020). Based on this information, a detailed characterisation of the hiPSC-derived MN protocol currently employed in the laboratory was undertaken. Moreover, the influence

of extrinsic morphogen signalling cues on MN subtype specificity was examined during 2 critical timepoints of the protocol: the NPC 'patterning' and terminal differentiation stages.

3.4.1 Neural induction of hiPSCs

BMP signalling during early gastrulation is essential for mesoderm and endoderm formation. Therefore, in order to generate neuroectodermal and spinal cord lineages the combined actions of DM and SB were used to block BMP type I receptor signalling, which inhibit the downstream BMP signalling through the inhibition of SMAD1, 5, 8 and 2, 3, 6, 7 phosphorylation respectively (Anderson et al. 2002; Chambers et al. 2009). As a result, hiPSCs are converted into multipotent neuroepithelial cells, downregulating the pluripotency marker OCT4 (Pan et al. 2002). In addition, the neuroectodermal marker SOX1 was significantly upregulated, indicating correct specification of neuroectodermal lineages (Suter et al. 2009). SOX2 has a more complex role as it is involved in both the maintenance of a pluripotent state and in neuronal fate specification (Zhang & Wei. 2014). Whilst the expression of SOX2 was decreased following neural induction, this matches its more convoluted roles. Morphologically, the switch from hiPSCs to a neuroepithelial sheet is visualised by a shrinking in cell size with more tightly packed cells and the presence of neural rosettes.

Whilst Chambers et al (2009) observed the conversion of hiPSCs into rostral neuroepithelial cells through upregulation of PAX6, nestin, OTX2 and FOXG1B, the WNT agonist CHIR99021 was administered in order to prevent this forebrain consolidation. This mimics the role of WNT signalling in the late blastula stage where WNTs and FGFs act in tandem to promote posteriorisation through the suppression of forebrain fates (Kudoh et al. 2002; Koshida et al. 2002; Diez del Corral et al. 2003). However, despite research showing that FGFs, and in particular FGF2, are able to promote the induction and survival of neural precursors (Streit et al. 2000; Joannides et al. 2007), they have numerous alternate roles such as establishing the extreme caudal boundary through functional antagonism of RA and were thus excluded but not blocked (Diez del Corral et al. 2003). WNT signalling is also thought to promote caudal fates through their actions in suppressing the cytochrome P450 family 26 (CYP26) and upregulating RALDH2 (Diez del Corral et al. 2003). CYP26 metabolises, whereas RALDH2 synthesises, RA. Therefore, the addition of CHIR as a WNT agonist can be

said to 'prime' neuroepithelial cells for caudalisation from the forebrain to the spinal cord by sensitising cells to RA signalling. Interestingly, WNT signalling has also been shown to act independently as a caudalising factor (Bel-Vialar et al. 2002; Nordstrom et al. 2002; Olivera-Martinez & Storey. 2007). This was observed through an upregulation in HOX factors at day 7, when compared to hiPSCs. Although it should be noted that HOX gene expression was further increased beyond day 7 timepoints.

3.4.2 Neural patterning during precursor specification

The initial patterning phase of the MN protocol takes place from day 7 until day 14 and utilises retinoid signalling in the form of RA and SHH signalling through the SHH agonist purmorphamine. The developmental rationale for the 4 day purmorphamine only phase stems from the presence of 2 sources of SHH *in vivo*; the floor plate and the notochord (Jessell et al. 2000). In addition, levels of SHH signalling are high in the pMN domain during the initial phases of neural tube development and pMN progenitor expansion, and lower towards the onset of neurogenesis. This is because SHH acts a mitogen, promoting the symmetric division and proliferation of cells through the expression of the docking protein pericentrin, thus expanding the pMN domain to match the growth of the neural tube (Saade et al. 2017). As the neural tube expands, morphogen signalling becomes increasingly refined to the poles (roof and floor plate) (Balaskas et al. 2012; Zagorski et al. 2017). The reduced purmorphamine phase during day 14 and 18 therefore acts to mimic these endogenous conditions whereby pMN precursors are initially exposed to high levels of SHH, followed by a reduction towards the onset of neurogenesis (Niederreither et al. 1997). The removal of RA from these timepoints also reflects endogenous conditions in which RA secretion from the somites is significantly reduced by E10 in mice. This was evidenced by the reduction in somite expression of the RA synthesising enzyme ALDH1A2. Interestingly, whilst this 4 day period did not influence the overall enrichment of MNs, as measured by OLIG2 immunolabeling, an increase in the proportion of NKX6.1 positive NPCs at day 18 was identified. This suggests that day 14 NPCs occupy a more dorsal settling position than their day 18 counterparts and that SHH signalling alone is sufficient to drive this ventralising effect. In addition, qPCR and immunolabeling also revealed no significant upregulation in P3 NPC domain marker NKX2.2 (<1%) at day 18, indicating that NPCs were not being 'over-ventralised' beyond the pMN domain. Interestingly, whilst the percentage of OLIG2 positive NPCs at day 18

was ~42%, these cultures produced highly enriched populations of MNs (>85%) following terminal differentiation using the notch antagonist CE. Whilst this presents an apparent discrepancy, a number of studies have published observations that neural tube NPCs are relatively plastic with regards to domain specification (reviewed by Sagner & Briscoe. 2019). Indeed, lineage tracing studies have often highlighted this phenomenon where cells in adjacent spinal cord domains are commonly co-labelled (Dessaud et al. 2007; 2010). Furthermore, a form of plasticity has been demonstrated as a key intra-domain characteristic of the pMN domain itself. This manifests as a developmental 'switch' that results in the production of later-generated oligodendrocytes, in place of earlier derived MNs (Wu et al. 2006; Ravanelli & Appel. 2015). Furthermore, a number of domain-restricted neural tube transcription factors, including OLIG3, DBX1, OLIG2 and NKX2.2 have been demonstrated to undergo a characteristic upregulation in expression at the *onset* of neurogenesis (Sagner et al. 2018; Delile et al. 2019). Therefore, a crucial property of the gene regulatory network (GRN), involved in establishing the neural tube domains, is that it must have some level of flexibility to allow for intra-domain cell-state transitions and also in response to the constantly changing extracellular cues as the neural tube grows. However, the GRN and neural tube must remain stable enough to allow for the establishment of sharp inter-domain boundaries, with little intermixing between these domains, and the subsequent differentiation of their respective and independent neuronal populations. Therefore, low-level expression of progenitor transcription factors appears to be crucial for facilitating these properties, where an upregulation immediately prior to the onset of neurogenesis could ensure a robust consolidation of NPCs into their respective and specific neuronal subtypes (reviewed by Sagner & Briscoe. 2019). This makes timing an important feature, particularly with regards to the transition between NPC and post-mitotic neuron and could explain the difference seen between the proportion of OLIG2 positive precursors in comparison to ChAT and SMI-32 positive neurons. A possible experiment that would address the hypothesis in our hiPSC-derived model would involve the assessment of OLIG2 expression immediately/shortly after CE administration.

3.4.3 Motor column diversification during terminal differentiation by retinoid signalling

Whilst retinoid signalling plays a crucial role in spinal cord MN specification, its functions extend far beyond this (Novitch et al. 2003). Indeed, RA signalling has also been implicated in the specification of numerous other neural tube cell types including roof plate, ventral and even some dorsal domain subtypes (Pierani et al. 1999; Niederreither et al. 2000; Wilson et al. 2003; 2004; Appel & Eisen. 2003; Novitch et al. 2003; Okada et al. 2004). This further emphasises its complex and often poorly understood role within the spinal cord. Retinoids also play an integral role in the establishment of the rostral-caudal axis, the basis of which is mediated through its complex interplay with HOX genes (Sockanathan & Jessell. 1998; Liu et al. 2001; Ji et al. 2009). Subsequently, this interaction is thought to be a key contributory factor to the generation of spinal MN heterogeneity. Analysis of the HOX code of spinal MNs generated using the hiPSC-derived MN protocol indicated a lower cervical/brachial positional identity. This was demonstrated by the induction of the highest mRNA expression levels in HOX4 and HOX5 as measured by raw cycle threshold values, with HOX6-8 also displaying high levels of upregulation, synonymous with cervical/brachial positional identity. Brachial spinal MNs can be further characterised based on their molecular expression profiles and settling positions, which delineate their segregation into motor columns. At brachial levels, MNs are segregated into MMC or medial or lateral LMC, each with distinct roles (Dasen et al. 2003; Vermot et al. 2005; Stifani. 2014). As mentioned previously, RA signalling plays a crucial role in LMC specification at brachial and lumbar spinal cord levels. Indeed, RA is secreted by adjacent somites, inducing the expression of the RA synthesising enzyme RALDH2 in a population of earlier-born LMC MNs; destined to become LMCm MNs. As a result, prospective LMCm MNs synthesise and secrete RA that acts in a paracrine manner to induce the specification of an LMCl MN phenotype in adjacent post-mitotic MNs as they migrate past these MNs to occupy a more lateral position (Sockanathan & Jessell. 1998; Sockanathan et al. 2003). In order to replicate this scenario *in vitro* and assess post-mitotic MN motor column plasticity, RA was added during the terminal differentiation period in combination with CE. Intriguingly, this resulted in a significant increase in the essential LMC cofactor FOXP1 at both mRNA and protein level, coinciding with a reduction in the MMC determinant LHX3. Importantly, the apparent shift in motor column subtype specification did not result in an expression change in the generic MN marker ChAT, demonstrating that MN

specification is unchanged by post-mitotic RA signalling. It is interesting to note the apparent MMC bias in MNs that were terminally differentiated in the absence of RA and CE only. Whilst this finding is in contrast to some hiPSC-derived MN studies detailing higher proportions of LMC populations (Thiry et al. 2020; Amoroso et al. 2013), others report either mixed MMC/LMC populations (Maury et al. 2015; Davis-Dusenbery et al. 2014; Du et al. 2014) or a shift towards MMC MN fate specification (Patani et al. 2011). Indeed, Patani et al (2011) demonstrated that MN specification can occur independently of RA signalling and with SHH alone. Further, this study demonstrated that in the absence of RA signalling during 'patterning', precursors revert to a 'default' MMC state. It is possible that, similar to the retinoid independent MN specification study, the removal of RA during day 14-18 timepoints is sufficient to provide similar patterning cues, thereby inducing this default MMC fate. Subsequently, with the addition of RA during terminal differentiation, an LMC phenotype is induced. This also conforms with studies suggesting that LHX3, a hallmark of MMC identity, is initially expressed in all MNs, but by an unknown mechanism is downregulated in future LMC MNs (Sockanathan & Jessell. 1998; Sharma et al. 1998; 2002; Thaler et al. 2002; Agalliu et al. 2009). Subsequently, LHX3 becomes a marker of mature MMC MNs (Thaler et al. 2002; Agalliu et al. 2009). The timing and plasticity of MNs to respond to RA signalling and generate LMC identity is therefore of huge importance. This has also been investigated, revealing that the competence of MNs to respond to RA signalling is lost following the generation of a LMCl phenotype (Sockanathan & Jessell. 1998). The importance of LHX3 for MMC generation is evidenced in a mouse model where misexpression of LHX3 results in MMCm formation (Sharma et al. 1998). FOXP1 is the earliest known determinant of LMC and PGC MN fates and is thought to promote the expression of the RA synthesising enzyme RALDH2 (Dasen et al. 2003; 2008; Amoroso et al. 2013). The importance of FOXP1 in LMC specification is highlighted in FOXP1-deficient mouse models where mice exhibit defects in LMC MN development (Vermot et al. 2005; Rousso et al. 2008). FOXP1 expression in turn, induces the expression of the LMCl determinant LHX1 (Sockanathan and Jessell. 1998). Interestingly, these findings are mirrored in hiPSC-derived MNs subjected to post-mitotic RA signalling. Whilst this was found to promote the expression of FOXP1, LHX1 was also significantly upregulated, suggesting that at least a proportion of these MNs acquire LMCl fate, which is in keeping with the fact that

LMCl formation *in vivo* is influenced by retinoid signalling (Sockanathan & Jessell. 1998). However, little/no expression of the LMCl subdivision marker PEA3 was found in RA + CE treated MNs. PEA3 is a specific LMCl motor pool marker for MNs that innervate brachial muscle targets such as the cutaneous maximus muscle (Ladle & Frank. 2002; Haase et al. 2002; Livet et al. 2002). This poses the question of whether distinct muscle targets are required for further subdivision and refinement of motor column MNs into motor pools. Timing is also an important principle in LMC generation. LMCl MNs are born at a later stage than LMCm and MMC motor neurons, where they migrate in an inside-out arrangement, such that LMC neurons are born in the proliferative ventricular zone of the pMN domain and then migrate through the LMCm to form the LMCl (Sockanathan & Jessell. 1998). Therefore, the generation of LMC MNs may necessitate the presence of MMC MNs in cultures. It would also be interesting to evaluate whether further enrichment of post-mitotic MMC fate specification could be promoted through the inhibition of RA signalling using, for example, RAR antagonists.

Taken together, these findings support the view that the retinoid pathway is differentially relevant at distinct stages of motor neurogenesis. The functional implications of these findings are of considerable interest because motor column organisation in development forms the basis for motor pools and target innervation, and in diseases such as ALS and SMA, MNs have differential vulnerability to degeneration (Kanning et al. 2010; Nijssen et al. 2017). Therefore, it would be of interest to explore the behaviour of RA independent and dependent MNs in experimental models of disease such as ALS and SMA. Additionally, given the growing interest in the potential use of retinoid pathway manipulation as a neuroregenerative therapy, these findings may have implications for either chemical or cell-based therapeutic strategy (Ferreira et al. 2020).

3.5 Summary and conclusions

hiPSC technology has revolutionised our understanding of developmental and disease. Subsequently, a litany of hiPSC-derived protocols have been published detailing the specification of numerous cell-types. Using the hiPSC-derived MN protocol commonly employed in the laboratory, successful characterisation and manipulation of key developmental cues was undertaken and assessed at developmentally relevant timepoints. Crucially, these findings demonstrate:

1. Neural induction using DM, SB and CHIR induces a loss of pluripotency with an upregulation of neuroectodermal markers.
2. MN enrichment is not influenced by alterations in SHH and RA levels during precursor patterning.
3. hiPSC-derived MNs can be characterised into constitutive motor column derivatives.
4. Post-mitotic application of retinoids can bias LMC motor column specification.
5. Retinoid signalling is differentially relevant to distinct stages of the MN protocol.

Chapter 4. Interneuron specification from human induced pluripotent stem cells

4.1 Introduction

The somatosensory system is fundamental for organismal survival by allowing perception and reaction to the environment. Such information is registered peripherally but transmitted (and indeed deciphered) centrally, first by dorsal spinal interneurons (INs), which in turn relay the information to higher levels within the brain. The response to such stimuli is ultimately articulated as motor output through the cortico-spinal tracts. The somatosensory system coordinates the senses of nociception, thermosensation, proprioception and mechanosensation (Lu et al. 2015; Lai et al. 2016). These modalities are routinely examined as part of standard clinical neurology assessments, which further exemplifies their functional significance in human physiology. Studies from mouse models show that spinal cord INs originate and migrate from the ventricular zone at E10.5-E11.5 (Lai et al. 2016). Following the first developmental phase of interneurogenesis, a subsequent phase (mouse E11-13) yields two additional IN pools from the dP4 and dP5 progenitor domains, termed dIL^{A} and dIL^{B} (Müller et al. 2002; Glasgow et al. 2005). It is noteworthy that IN populations derive from all domains of the spinal cord except the pMN domain, from which MNs arise (Rowitch et al. 2002; Briscoe & Novitch. 2008). As such, INs display a high level of diversity, manifesting through their molecular expression profiles, axonal trajectory pathways, cell soma settling positions and overall functions in the spinal cord (Lu et al. 2015).

Whilst there is a host of research detailing methods for attaining efficient conversion of spinal cord MNs from hiPSC, protocols for generating enriched interneuronal populations remain largely understudied (White & Sakiyama-Elbert. 2019). Despite this, generation of INs from various stem cell models has been achieved and the strategy is based on altering developmental cues during dorsal-ventral patterning. As expected, attempts to shift the dorsal-ventral settling position away from the MN-producing pMN domain often involve manipulation/removal of SHH signalling and/or inclusion of dorsalising cues. Indeed, generation of SIM1 positive V3 commissural INs has been demonstrated in mESCs using varying concentrations of the SHH agonist smoothened (SAG), in

combination with RA (Xu & Sakiyama-Elbert. 2015). V3 INs are predominantly glutamatergic (Goulding et al. 2009), with essential roles in central pattern generation (CPG). They have extensive innervation patterns with targets including V1 Renshaw cells, LMC MNs and V2 INs (Zhang et al. 2008). Interestingly, Xu and Sakiyama-Elbert observed an increase in the proportion of SIM1-positive precursors using higher concentrations of SAG and lower levels of RA. This was similarly identified in a separate study by Sternfeld et al (2017) using a SIM1 driven fluorescent reporter line, also in mESCs. It should be noted that there was a low efficiency of conversion for generating SIM1 positive cells (~30%), with V1 and pMN derivatives also present. Furthermore, whilst a small population of V3 INs was observed with the generation of hiPSC-derived MNs (Luisier et al. 2018), no study has demonstrated the generation of highly enriched V3 INs in hiPSCs.

Populations of V2 INs have also been successfully generated through further adaptation of the patterning stages during MN derivation protocols (Brown et al. 2014; Iyer et al. 2016). V2 INs can be divided into excitatory glutamatergic V2a and inhibitory glycinergic or GABAergic V2b subtypes, which extensively innervate adjacent MNs. As such, they have roles in locomotor function, left-right coordination through reciprocal inhibition, CPG and flexor-extensor motor activity (Wang et al. 2008; Crone et al. 2008; 2009, Zhang et al. 2014) V2a and V2b subtypes are specified through delta and notch signalling, respectively (Okigawa et al. 2014). Sinha and Chen (2006) employed a differentiation strategy using purmorphamine instead of SAG, noting that purmorphamine has a weaker potency for SHH agonism than SAG (Sinha and Chen. 2006) and was therefore ideal for providing a ‘weaker’ ventralising cue. Indeed, purmorphamine and RA were observed to drive the specification of more dorsal populations of ventral precursors from mESCs, resulting in the upregulation of CHX10/VSX2 positive cells representing V2a INs (Brown et al. 2014; Lyer et al. 2016). In addition, DAPT was used as a notch antagonist resulting in further enrichment of V2a INs with respective upregulation of CHX10, a V2a marker. Importantly, these findings were subsequently replicated in an hiPSC culture system. Butts et al (2017) were able to generate ~25-50% CHX10-positive precursors using a similar combination of purmorphamine, RA and the Notch antagonist DAPT. This reproducibility in hiPSC-

derived cultures provides key validation of intrinsic stem cell neurodevelopmental principles and their competence to derive spinal cord lineages.

The majority of V0 INs are inhibitory commissural INs with roles in the coordination of left-right alternation (Pierani et al. 2001; Griener et al. 2015). V0 IN specification was demonstrated in a study by Kim et al (2009) using mESCs. In this study, RA signalling was employed alone and was found to result in an upregulation in the V0 domain marker EVX1. Furthermore, there was also a small population of dI4 and dI6 neuronal fates, evidenced through their expression of PAX2 and LIM1/2 in the absence of EVX1/2. A small proportion of neurons were immunopositive for EVX1 but did not co-express LIM1/2; indicating dI1 or dI2 domain specification. Overall, this study highlighted the potential role of RA signalling in mid-neural tube and also dorsal domain specification.

Most recently, Gupta et al. (2018) attempted to induce dorsal IN fate specification by employing a combination of RA and BMP4 as a dorsalising cue in hESCs and hiPSCs. Interestingly, it was found that RA + BMP4 conditions were able to specify dI1 and dI3 but not dI2 domains, as assessed through the expression profiles of LHX2 and ISL1/2 and TLX3 respectively. This was hypothesised to be the result of continued BMP4 signalling, acting to suppress dP2 and subsequent dI2 fate specification. RA signalling alone was found to induce a range of dorsal IN identities including dI1s, dI2s and dI4s. It should be noted, however, that this differentiation protocol was based on embryoid body formation, which often yields more heterogeneous cultures. Building on this, a study by Ogura et al. (2018) employed a 3D induction protocol for the generation of organoid-like spinal cord tissue derived from hiPSCs. A previously established 3D MN protocol was adapted in order to generate several types of ventral and intermediate domain spinal organoids. In this manner, Ogura et al (2018) were able to predictably manipulate the identity of spinal cord populations into dorsal (dI1-3) using BMP4 and intermediate and ventral (V0-V3) structures. dI1-3 INs have broad roles in somatosensory integration and relay circuits. Indeed, dI1 commissural INs are known to receive and relay proprioceptive inputs from the periphery via the spinocerebellar tract (Helms & Johnson. 1998; Bermingham et al. 2001). dI2 INs have been observed to relay signals through the spinothalamic tract to convey sensory information to higher brain centres (Gowan et al. 2001; Gross et al. 2002).

Lastly, dI3 INs have been shown to convey cutaneous input to motor neurons controlling grip movements (Bui et al. 2013).

Interestingly, no study has achieved an *in vitro* protocol for generating enriched 2D populations of dorsal spinal INs and including those of dI4-6 domains. Broadly, INs from dI4&5 are involved in somatosensation with regards to pain, temperature, itch and touch sensations (Gross et al. 2002; Glasgow et al. 2005; Pillai et al. 2007). dI6 INs have been demonstrated to comprise GABAergic inhibitory commissural neurons, with roles in left-right alternation (Goulding et al. 2009).

4.2 Aims

Against this background, these studies provide clear indication that the translation of *in vivo* developmental principles can be applied to *in vitro* stem cell-derived culture models with great success. These *in vitro* studies have established a template for predictable pan-spinal cord fate specification, involving key developmental patterning cues. This template is built on the establishment of extreme ventral identities being specified using potent SHH agonists at reduced concentrations, more dorsal but still ventral domains generated using less potent SHH agonists in combination with RA, intermediate/dorsal identities patterned using RA signalling alone and the most dorsal domains specified with the addition of BMP signalling. Whilst this sets the foundation for predictable manipulation of spinal cord fates *in vitro*, none have assessed these principles in detail in an hiPSC-derived 2D culture system, with the aim of deriving enriched interneuronal populations. Therefore, the specific aims of this chapter are to:

1. Recapitulate *in vivo* spinal cord IN differentiation using a 2D monolayer hiPSC culture system.
2. Evaluate the roles of BMP4, RA and SHH in establishing distinct progenitor domains in this hiPSC model.
3. Establish novel directed differentiation strategies for generating dorsal somatosensory interneuronal populations.

Note: For the RNAseq described in this chapter, the cells were generated by myself, sequencing was undertaken by the Advanced Sequencing STP at the Francis Crick Institute and RNAseq analysis by Dr Oliver Ziff, a PhD student in the Patani and

Luscombe lab. RNAseq data analysed by this colleague is indicated in the relevant figure legends.

4.3 Results

4.3.1 BMP4 induces a dorsal neural tube identity

In order to generate hiPSC-derived spinal INs, a novel differentiation strategy was devised; using developmentally rationalised manipulation of the patterning phase of the MN protocol employed in the lab and described in Chapter 3 (Figure 4.1A). The rationale was based on the observations that INs are derived from all domains of the spinal cord excepting the pMN domain (Lai et al. 2016) and that dorsal dP1-3 neural tube fate specification necessitates BMP signalling from the roof plate (Liem et al. 1997; Wine-Lee et al. 2004) (Figure 4.1B). The patterning phase of the MN protocol was therefore altered through the removal of the SHH agonist purmorphamine and addition of 10ng/ml BMP4 (RA + BMP4). Cultures were assessed at day 18 NPC timepoints and day 18 MN NPCs (RA + SHH) were used as a negative control for dorsal neural tube specification (Figure 4.1A&B).

qPCR analysis of day 18 NPC cultures revealed a significant reduction in expression of ventral (NKX2.2, NKX6.1), pMN domain (OLIG2) and MN/mid-neural tube (PAX6) marker expression at day 18 NPC timepoints in RA + BMP4 conditions, when compared to RA + SHH (Figure 4.2A-D). Coinciding with this, RA + BMP4 day 18 NPCs showed an increase in mRNA expression levels of the dorsal neural tube progenitor markers PAX7 and OLIG3 (Figure 4.2E&F). Importantly, RA + BMP4 treated NPCs showed no difference in mRNA expression of the neural crest marker SOX10 at day 18, when compared to RA + SHH, suggesting that precursors were not ‘over-dorsalised’ towards a neural crest lineage (Figure 4.2G). qICC was next employed to further validate these findings. Affirming this, day 18 RA + BMP4 treated NPCs showed a small but significant increase in the proportion of NPCs expressing OLIG3 at day 18 (~27%), when compared to RA + SHH (~1%) NPCs confirming a modest dorsalisation of precursors to dP1-3 domains in BMP4 treated cultures (Figure 4.3A&B). Day 18 NPCs were then terminally differentiated for 7 days using 0.1μM Compound E, a notch antagonist that initiates

terminal differentiation of progenitors by promoting cell cycle exit. Interestingly, day 25 terminally differentiated RA + BMP4 cultures did not appear to acquire a neuronal morphology, when compared to RA + SHH and following 7 days of terminal differentiation (representative Brightfield images shown in Figure 4.4A). This was further confirmed through ICC staining for β3-tubulin demonstrating low/absent signal at day 25 (Figure 4.5B; images not quantified).

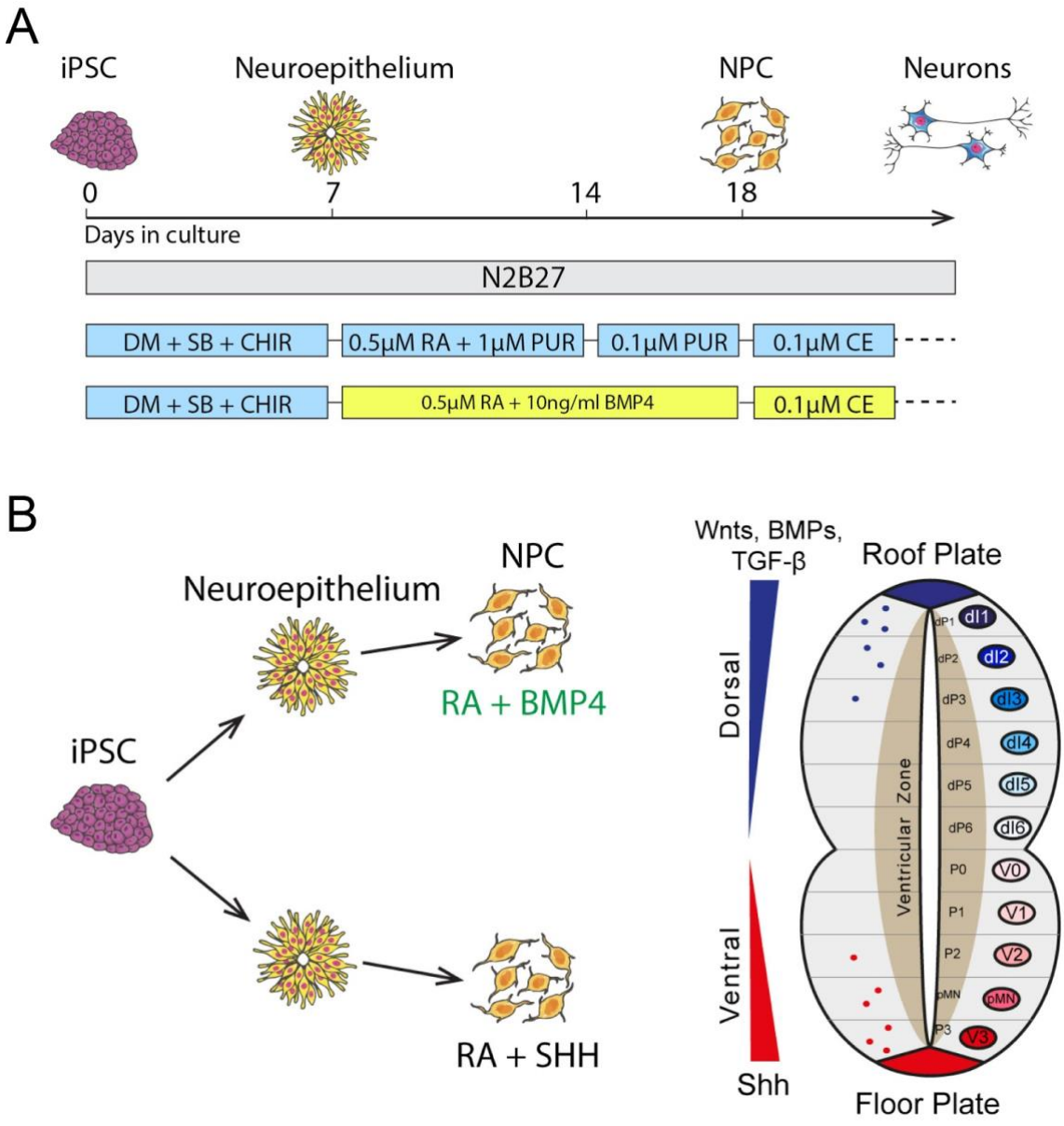

Figure 4.1 Protocol for hiPSC-derived motor neurons and strategy for generating dorsal interneurons

(A) hiPSC-derived differentiation strategy for generating spinal cord MNs and separately, populations of dorsal INs using BMP4 in place of the SHH agonist purmorphamine. (B) Schematic depicting predicted neural tube settling positions using dorsalising (BMP4) and ventralising (SHH) signalling cues.

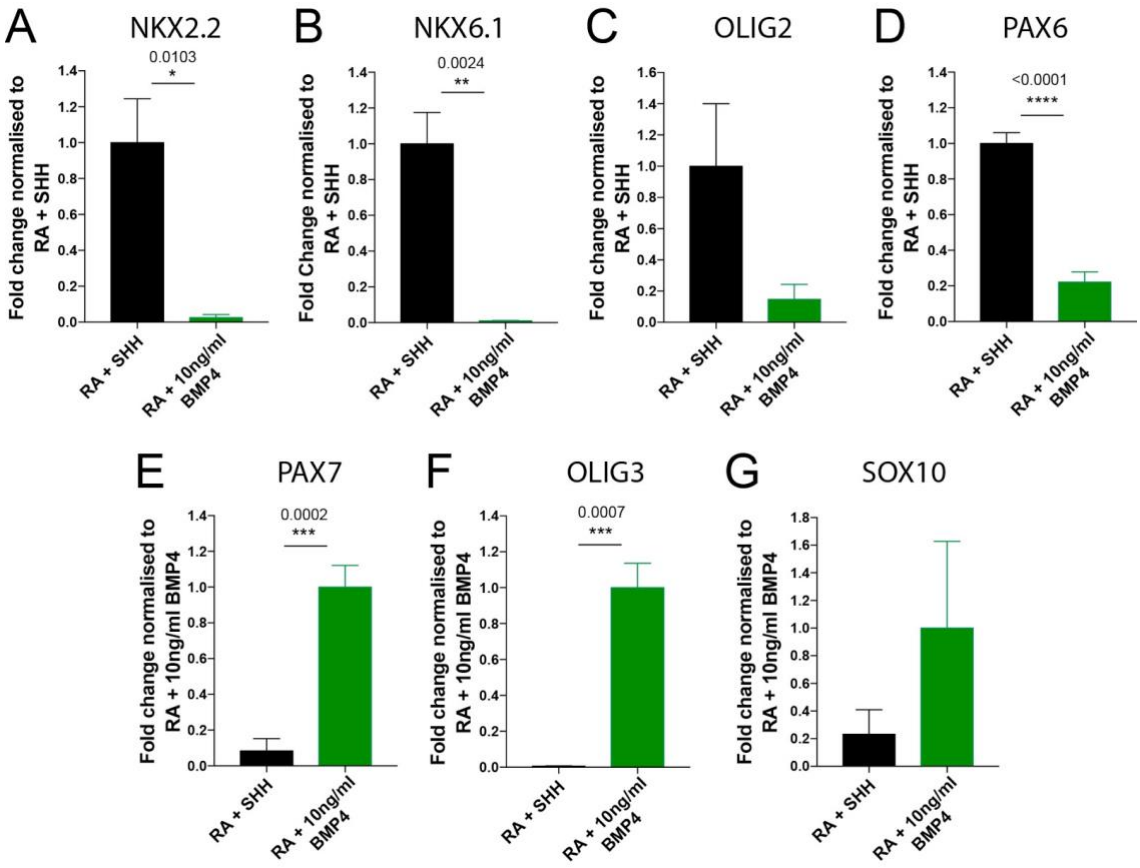

Figure 4.2 NPCs patterned with BMP4 acquire dorsal precursor marker expression

Bar plots depicting mRNA expression levels of the P3 domain marker - NKX2.2 (A), ventral P3, pMN and P2 domain marker - NKX6.1 (B), pMN domain marker - OLIG2 (C), pMN and mid-neural tube marker - PAX6 (D), dorsal neural tube marker - PAX7 (E), dP1-3 dorsal domain marker - OLIG3 (F) and neural crest marker - SOX10 (G) in day 18 NPCs patterned with RA + SHH or RA + 10ng/ml BMP4, as assessed by qPCR. Each sample was normalised over its GAPDH expression level and each condition was normalised against either RA + SHH or RA + 10ng/ml BMP4 (as indicated on each graph). n=2 per cell line with 3 independent control lines used (CTRL1-3). Error bars are displayed as mean ± SEM. p value calculated using unpaired two-tailed t-test with Welch's correction, * represents $p < 0.05$, ** represents $p < 0.01$, *** represents $p < 0.001$, **** represents $p < 0.0001$.

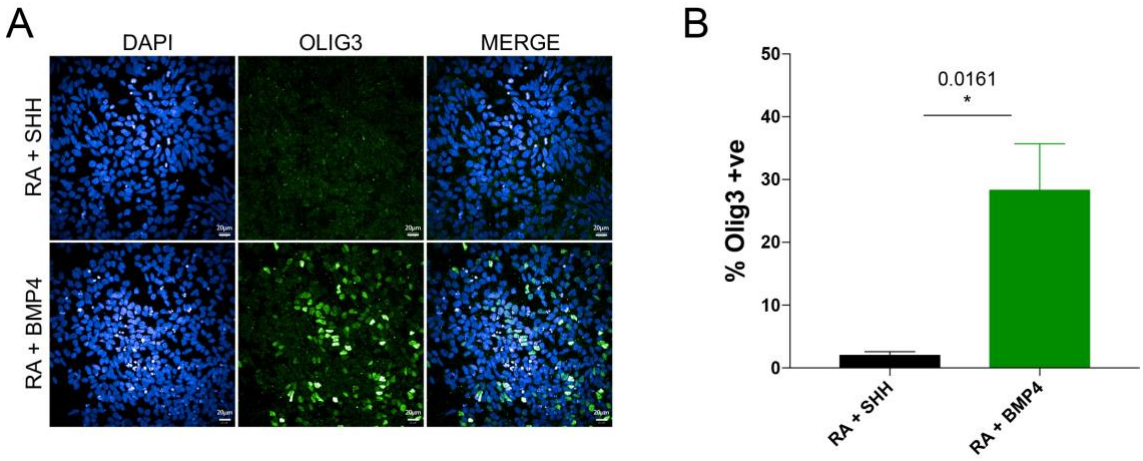

Figure 4.3 Expression of dP1-3 neural tube marker OLIG3 in dorsal NPCs

Representative immunocytochemistry images of the CTRL1 cell line at day 18 NPC stage following patterning with RA + SHH or RA + 10ng/ml BMP4, using the cellular marker of dP1-3 neural tube progenitors - OLIG3 (A). Scale bar set at 20 μm. (B) Bar plot representing quantitative immunocytochemistry data for percentage of cells expressing OLIG3 in day 18 NPCs. n=2 per cell line with 3 independent control lines used (CTRL1-3). Error bars are displayed as mean ± SEM. Data is plotted per well. p value calculated using unpaired two-tailed t-test with Welch's correction, * represents $p < 0.05$.

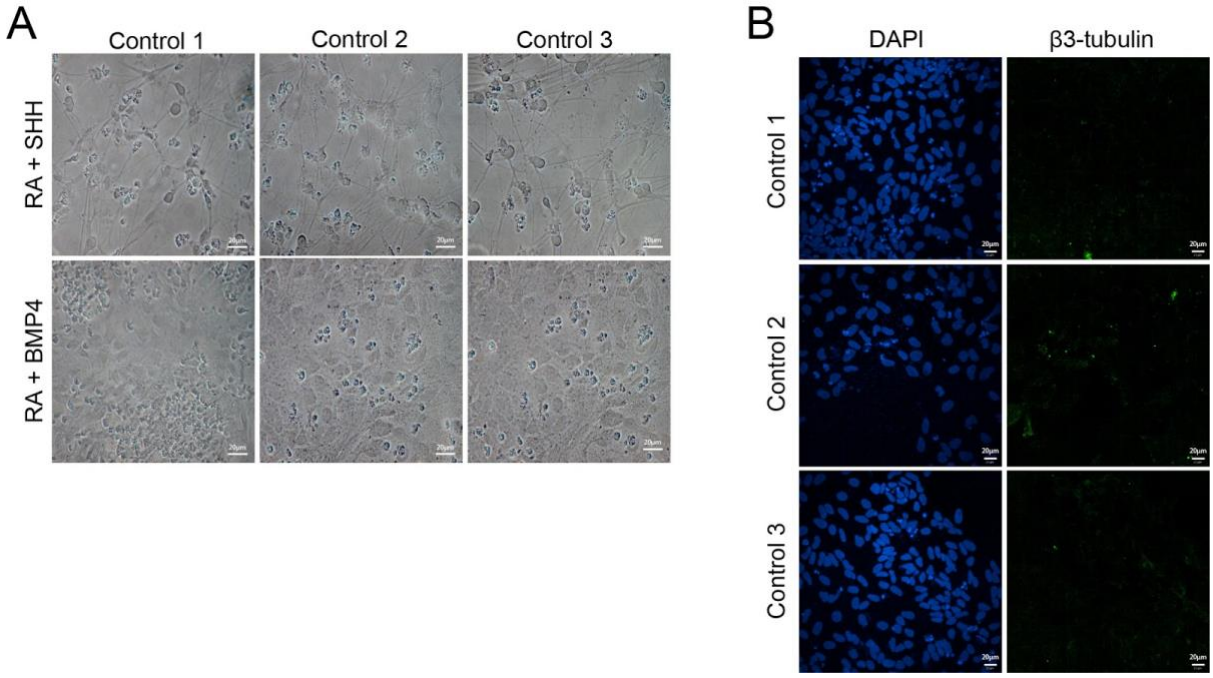

Figure 4.4 Dorsal NPCs are unable to terminally differentiate into neurons

(A) Representative brightfield images of day 25 cells patterned with RA + SHH or RA + 10ngl/ml BMP4 and terminally differentiated for 7 days in compound E. n=2 per cell line with 3 independent control lines used (CTRL1-3). (B) Representative immunocytochemistry images using the cellular pan-neuronal marker - β3-tubulin. Scale bar set at 20 μm. n=1 across 3 different control lines.

4.3.2 Retinoic acid in the absence of SHH agonism generates a dorsal neural tube identity

Noting that BMP4 was only able to induce a modest upregulation in the percentage of dP1-3 NPCs, and was also unable to support their conversion into terminally differentiated neuronal populations. NPCs were next assessed following patterning in RA alone (RA only) and therefore in the absence of dorsalising (BMP4) and ventralising (SHH) cues (Figure 4.5A&B). Whole-cell RNAseq was employed, comparing RA only to RA + SHH cultures at day 18. Principal component analysis and unsupervised hierarchical clustering revealed that samples segregated primarily (PC1) based on differentiation strategy (RA + SHH versus RA only) but also by cell line (PC2) (Figure 4.6A&B). Gene clustering by the most highly variable genes in the dataset further confirmed segregation according to the differentiation strategy, with known key patterning markers found amongst the most variable (e.g. ZIC1, ZIC4, PAX3) (Figure 4.6C&D). Differential gene expression (DGE) analysis revealed 205 DEGs (FDR < 0.05) with 101 and 104 genes upregulated in RA only and RA + SHH conditions respectively (Figure 4.7A). Gene ontology analysis revealed upregulated (RA only) genes to be enriched for neuro-developmental, spinal cord and cellular metabolic processes, whilst downregulated (RA + SHH) genes were overrepresented in cytoskeletal, synaptic and neuronal pathways (Figure 4.7B). Amongst these were genes responsible for the patterning of various neural tube domains, with upregulation of dorsal patterning markers in RA only treated cells (MSX1, OLIG3, PAX7 and PAX3) coinciding with downregulation in motor and ventral domain markers (OLIG2, NKX6.1 and MNX1) (Figure 4.8A&B). Specific gene expression analysis across established neural tube progenitor markers confirmed clustering of samples according to dorsal and ventral regions, with significant differences between RA + SHH and RA only conditions (Figure 4.8A&B).

qPCR was next used to further validate RNAseq findings, using primers designed against typical markers of dorsal and ventral neural tube domains. Comparison of NPCs at day 18 NPC timepoints revealed an increase in expression of more dorsal genes (including PAX6, IRX3, DBX1, DBX2, PAX7) in RA only NPCs relative to cultures treated with RA + SHH, which induced ventral genes (including OLIG2, NKX2.2 and NKX6.1) (Figure 4.9A-I). Importantly, no difference in expression of neural crest marker SOX10 was found, consistent with dorsal neural tube specification (Figure 4.9J).

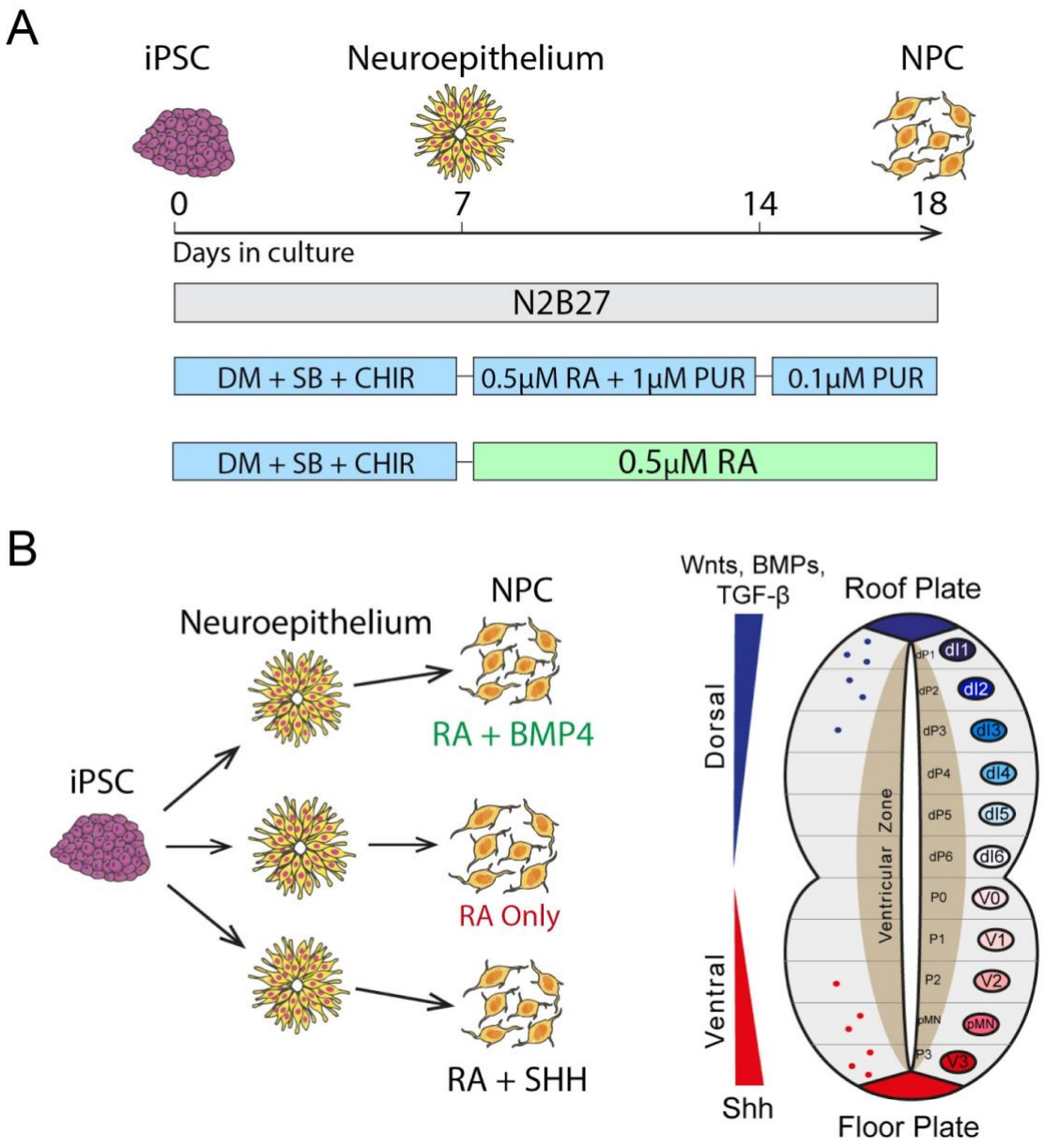

Figure 4.5 hiPSC-directed differentiation strategy for generating dorsal spinal cord interneurons using retinoid signalling alone

(A) hiPSC-derived differentiation protocol for generating spinal cord MNs and separately, populations of dorsal INs using retinoid signalling alone during patterning. (B) Schematic depicting predicted neural tube settling positions using dorsalising (RA + BMP4) cues, retinoid signalling alone (RA only) or MNs using retinoid and ventralising SHH signalling cues (RA + SHH).

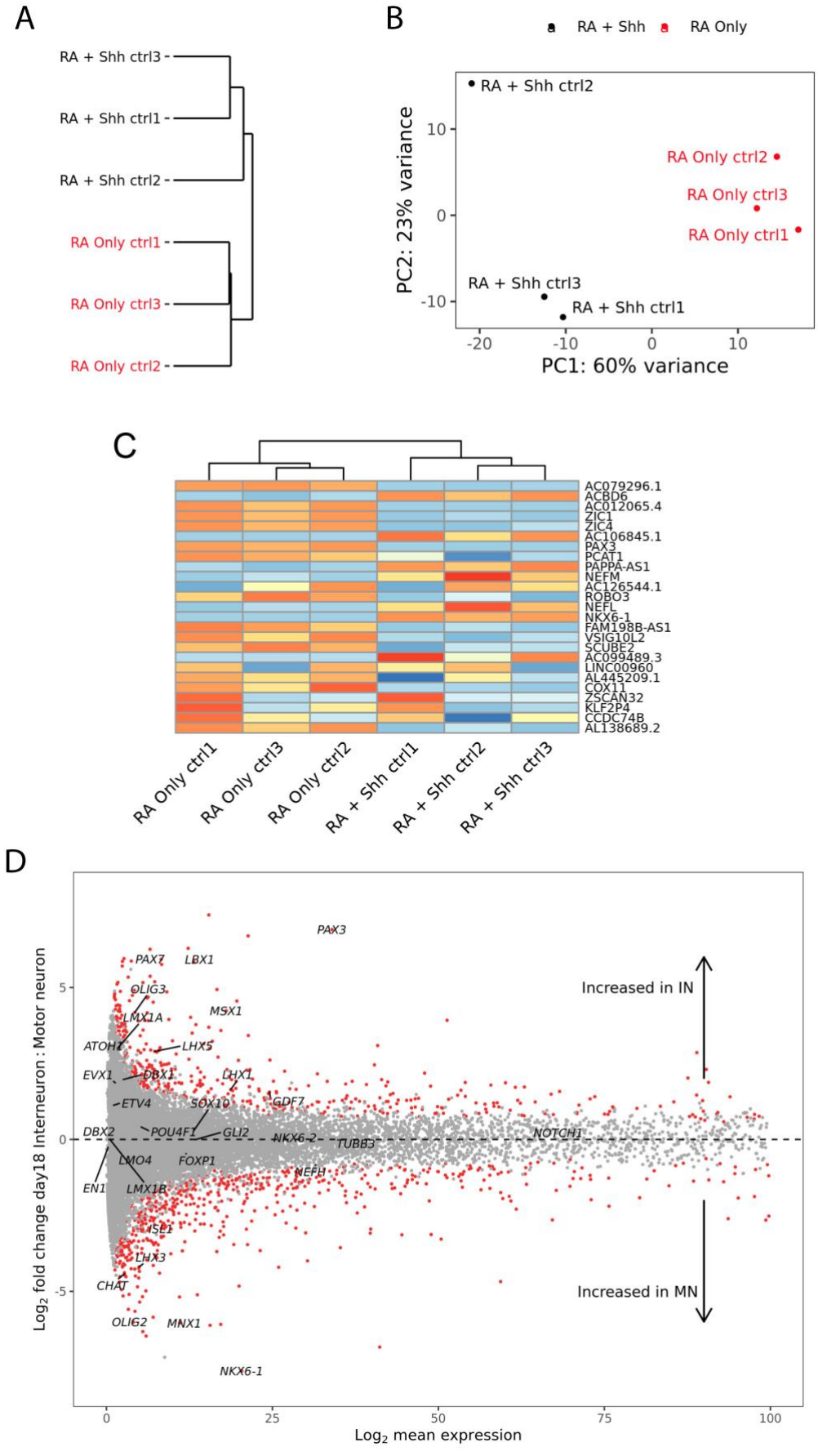
A
RA + Shh ctrl3
RA + Shh ctrl1
RA + Shh ctrl2
RA Only ctrl1
RA Only ctrl3
RA Only ctrl2
B
RA + Shh
RA Only
RA + Shh ctrl2
RA Only ctrl2
RA Only ctrl3
RA Only ctrl1
RA + Shh ctrl3
RA + Shh ctrl1
PC2: 23% variance
PC1: 60% variance
C
AC079296.1
ACBD6
AC012065.4
ZIC1
ZIC4
AC106845.1
PAX3
PCAT1
PAPPA-AS1
NEFM
AC126544.1
ROBO3
NEFL
NKX6-1
FAM198B-AS1
VSIG10L2
SCUBE2
AC099489.3
LINC00960
AL445209.1
COX11
ZSCAN32
KLF2P4
CCDC74B
AL138689.2
RA Only ctrl1
RA Only ctrl3
RA Only ctrl2
RA + Shh ctrl1
RA + Shh ctrl2
RA + Shh ctrl3
D
PAX3
PAX7
LBX1
OLIG3
LMX1A
MSX1
ATOH1
LHX5
EVX1
DBX1
LHX1
ETV4
SOX10
GDF7
DBX2
POU4F1
GLI2
NKX6-2
TUBB3
NOTCH1
LMO4
FOXP1
NEFH
EN1
LMX1B
ISL1
LHX3
CHAT
OLIG2
MNX1
NKX6-1
Increased in IN
Increased in MN
Log2 fold change day18 Interneuron : Motor neuron
Log2 mean expression

Figure 4.6 Differential expression of neural tube domain markers in RA only patterned NPCs

(A) Dendrogram showing unsupervised hierarchical clustering of variance stabilised gene counts across all day 18 samples. RA + SHH labelled in black and RA only labelled red. (B) Principal component analysis (PCA) on variance stabilised gene counts across day 18 NPC samples plotted by their coordinates along the first two principal components. Samples are coloured by their patterning conditions (RA + SHH shown in black and RA only in red) and labelled by their cell line. (C) Heatmap showing hierarchical clustering based on the highest 25 variably expressed genes across all samples at day 18 NPC stage. (D) Volcano plot depicting differential gene expression between RA only and RA + SHH cells at day 18 NPC. Significantly up- or down-regulated genes are highlighted in red (FDR < 0.05) with traditional dorsal-ventral progenitor patterning genes annotated.

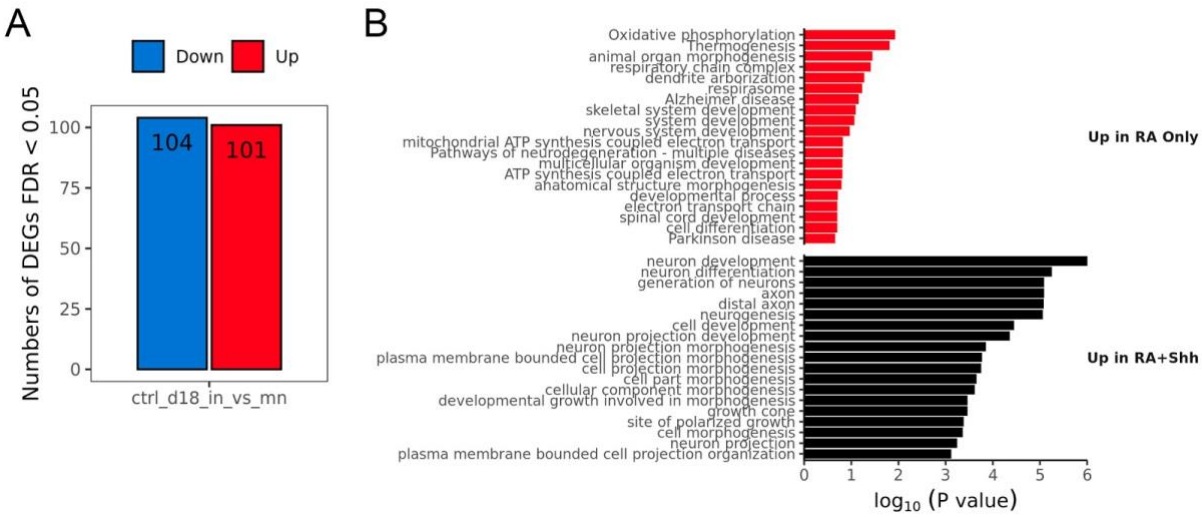

Figure 4.7 Differentially expressed gene and gene ontology analysis of RA only and RA + SHH treated NPCs

(A) Bar plot showing the number of differentially expressed genes (FDR < 0.05) that are up- and down-regulated in RA only vs RA + SHH conditions at day 18 NPC timepoints. (B) Gene Ontology terms enriched in up- and down-regulated differentially expressed genes in RA only vs RA + SHH conditions.

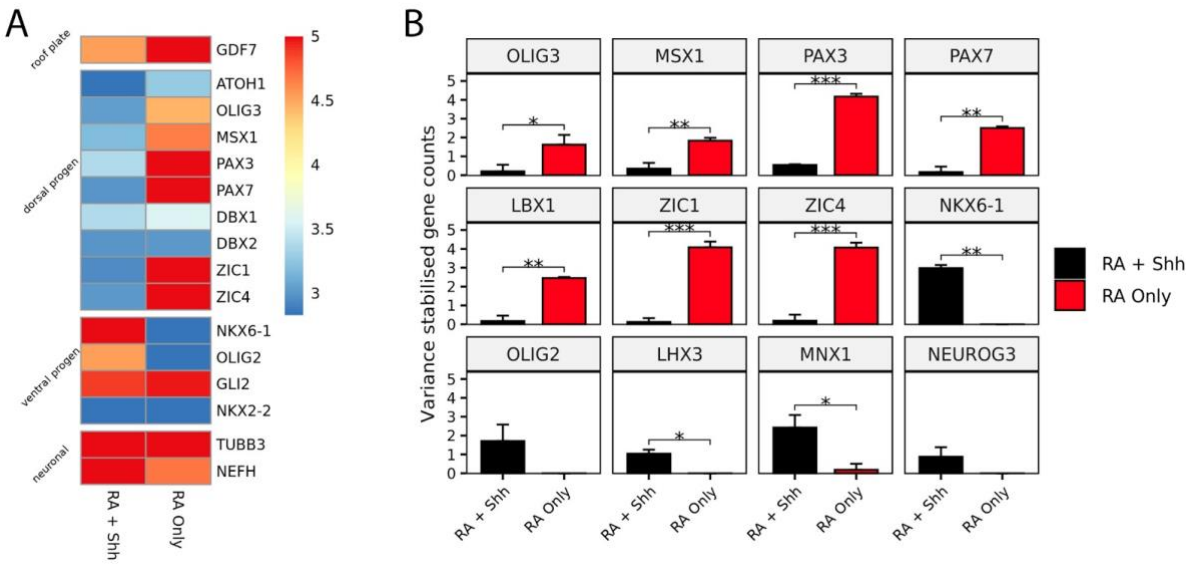

Figure 4.8 RA only signalling in the absence of SHH induces a dorsal precursor identity by day 18 NPC timepoint

(A) Heatmap showing the mean variance stabilised gene counts for established dorsal-ventral markers between RA + SHH and RA only conditions at day 18 NPC timepoints. (B) Bar plots showing the mean variance stabilised gene counts (y-axis) of specific dorsal-ventral progenitor markers between RA + SHH and RA only conditions (x-axis). Bulk RNA sequencing was performed on 3 independent control lines (CTRL1, 5 and 6). Error bars are displayed as mean ± SEM. p value calculated using unpaired two-tailed t-test with Welch's correction, * represents $p < 0.05$, ** represents $p < 0.01$, *** represents $p < 0.001$.

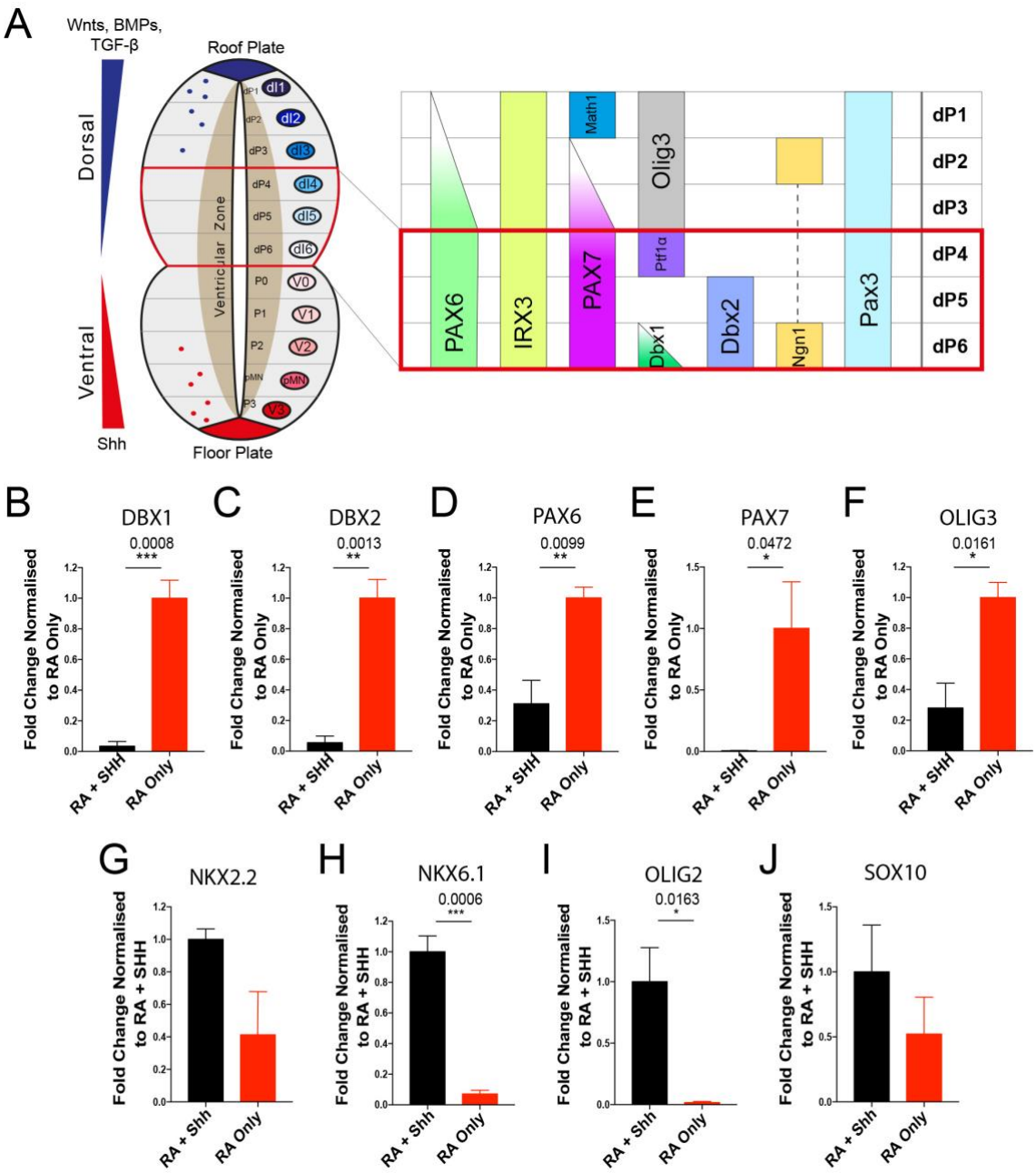

Figure 4.9 Upregulation of dorsal dP4-6 markers in RA only patterned NPCs

(A) Schematic depicting transcription factor expression profile of the dorsal neural tube at the progenitor stage, with dP4-6 highlighted. Bar plots depicting mRNA expression levels of the mid-neural tube markers - DBX1 (B) and DBX2 (C), mid-neural tube and pMN domain marker - PAX6 (D), dorsal neural tube marker - PAX7 (E), dP1-3 domain marker - OLIG3 (F), P3 domain marker - NKX2.2 (G), ventral P3, pMN and P2 domain marker - NKX6.1 (H), pMN domain marker - OLIG2 (I) and neural crest marker - SOX10 (J) in day 18 NPCs patterned with RA + SHH or RA only, as assessed by qPCR. Each sample was normalised over its GAPDH expression level and each condition was normalised against either RA + SHH or RA only (as indicated on

each graph). n=3 per cell line with 3 independent control lines used (CTRL1-3). Data is plotted per line. Error bars are displayed as mean ± SEM. p value calculated using unpaired two-tailed t-test with Welch's correction, * represents $p < 0.05$, ** represents $p < 0.01$, *** represents $p < 0.001$.

4.3.3 hiPSC-derived dorsal neural precursor characterization reveals a dP4-dP6 identity

qICC was then performed in order to validate precursor identity at the protein level, which confirmed significant upregulation of both PAX7 (~93%) (Figure 4.10A&B) and PAX3 (~84%) (Figure 4.11A&B), suggesting precursor patterning to the dorsal neural tube. In order to gain further insight into dorsal positional identity, qICC for OLIG3, a marker of dP1-dP3, was examined. Only a small but significant increase in expression was found in RA only compared to RA + SHH NPCs (~5%) (Figure 4.12A&B). Cumulatively, these data suggest that RA, in the absence of other extrinsic patterning cues, permits a dorsal-ventral identity of dP4-dP6 domains within the dorsal neural tube.

In order to assess the role of endogenous SHH signalling on cultures, and the effect of eliminating these endogenous ventralising cues that could potentially result in further dorsal specification of NPCs, cyclopamine was added as an antagonist of SHH signalling (RA + Cyclo) (Figure 4.13A). This was hypothesised to further enhance dorsal precursor specification in cultures by inhibiting the formation of ventral neural tube fates. Interestingly, a significant decrease in NKX2.2 and OLIG2 expression was observed in RA + cyclo conditions at day 18 NPC timepoints, when compared to RA only (Figure 4.13). However, no significant difference in expression of dorsal markers was observed between RA only and RA + Cyclo conditions (Figure 4.13). qICC at day 18 NPC timepoints revealed a significant downregulation in the expression of the ventral neural tube marker NKX6.1 between RA + SHH (~94%) and both RA only (~1%) and RA + Cyclo (~1%) conditions (4.14A&B). However, no difference in the expression of NKX6.1 was detected in either condition excluding SHH (i.e. RA only and RA + Cyclo) suggesting that there are low / negligible levels of endogenous SHH signalling in these conditions (Figure 4.14A&B). Western blotting also mirrored these findings, with an antibody targeting NKX6.1 showing strong protein bands in day 18 RA + SHH NPC conditions, but with negligible levels in RA only and RA + Cyclo (Figure 4.14C).

Collectively, these data suggest that removing the ventralising SHH cue leads to a loss of pMN domain specification and a subsequent increase in mRNA expression of dorsal neural tube markers.

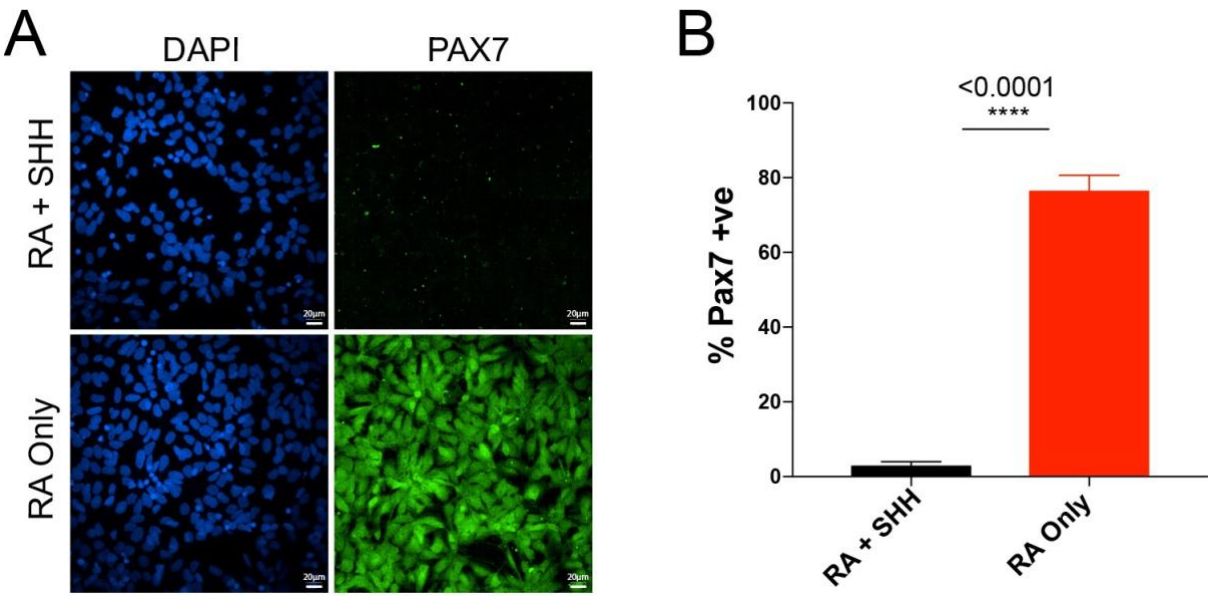

Figure 4.10 Upregulation of dorsal marker PAX7 in RA only patterned NPCs

(A) Representative immunocytochemistry images of the CTRL1 cell line using the dorsal progenitor marker - PAX7 in day 18 NPCs patterned with RA + SHH or RA only. Scale bar set at 20 µm. (B) Quantitative immunocytochemistry for PAX7. n=2 per cell line with 3-5 independent control lines used (CTRL1-5). Error bars are displayed as mean ± SEM. p value calculated using unpaired two-tailed t-test with Welch's correction, **** represents $p < 0.0001$.

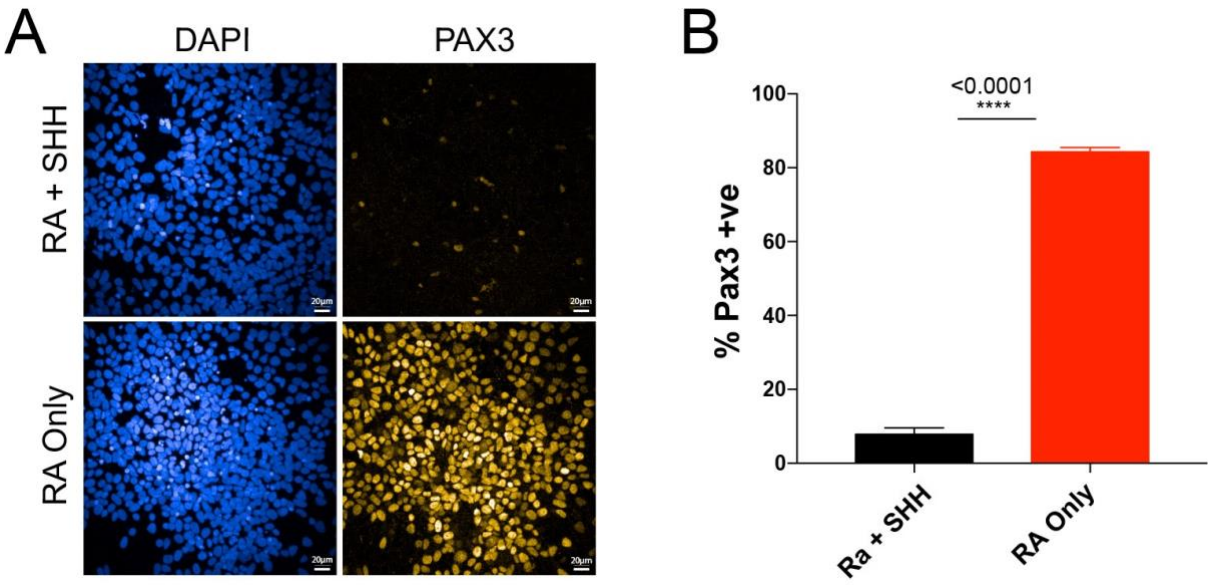

Figure 4.11 Upregulation of dorsal domain marker PAX3 in RA only patterned NPCs

(A) Representative immunocytochemistry images of the CTRL3 cell line using the dorsal progenitor marker - PAX3 in day 18 NPCs patterned with RA + SHH or RA only. Scale bar set at 20 μm. (B) Quantitative immunocytochemistry for PAX3. n=2 per cell line with 5 independent control lines used (CTRL1-5). Error bars are displayed as mean ± SEM. p value calculated using unpaired two-tailed t-test with Welch's correction, **** represents $p < 0.0001$.

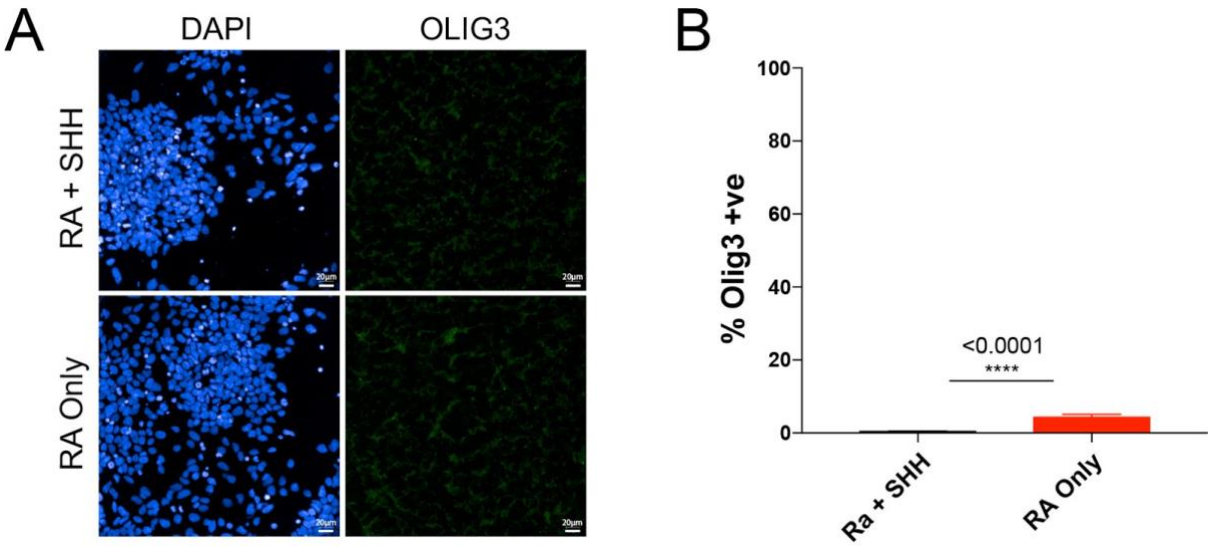

Figure 4.12 Modest upregulation in dP1-3 dorsal domain marker OLIG3 in RA only patterned NPCs

(A) Representative immunocytochemistry images of the CTRL1 cell line using the dorsal dP1-3 progenitor marker - OLIG3 in day 18 NPCs patterned with RA + SHH or RA only. Scale bar set

at 20 µm. (B) Quantitative immunocytochemistry for OLIG3. n=3 per cell line with 3-5 independent control lines used (CTRL1-5). Error bars are displayed as mean ± SEM. p value calculated using unpaired two-tailed t-test with Welch's correction, **** represents $p < 0.0001$.

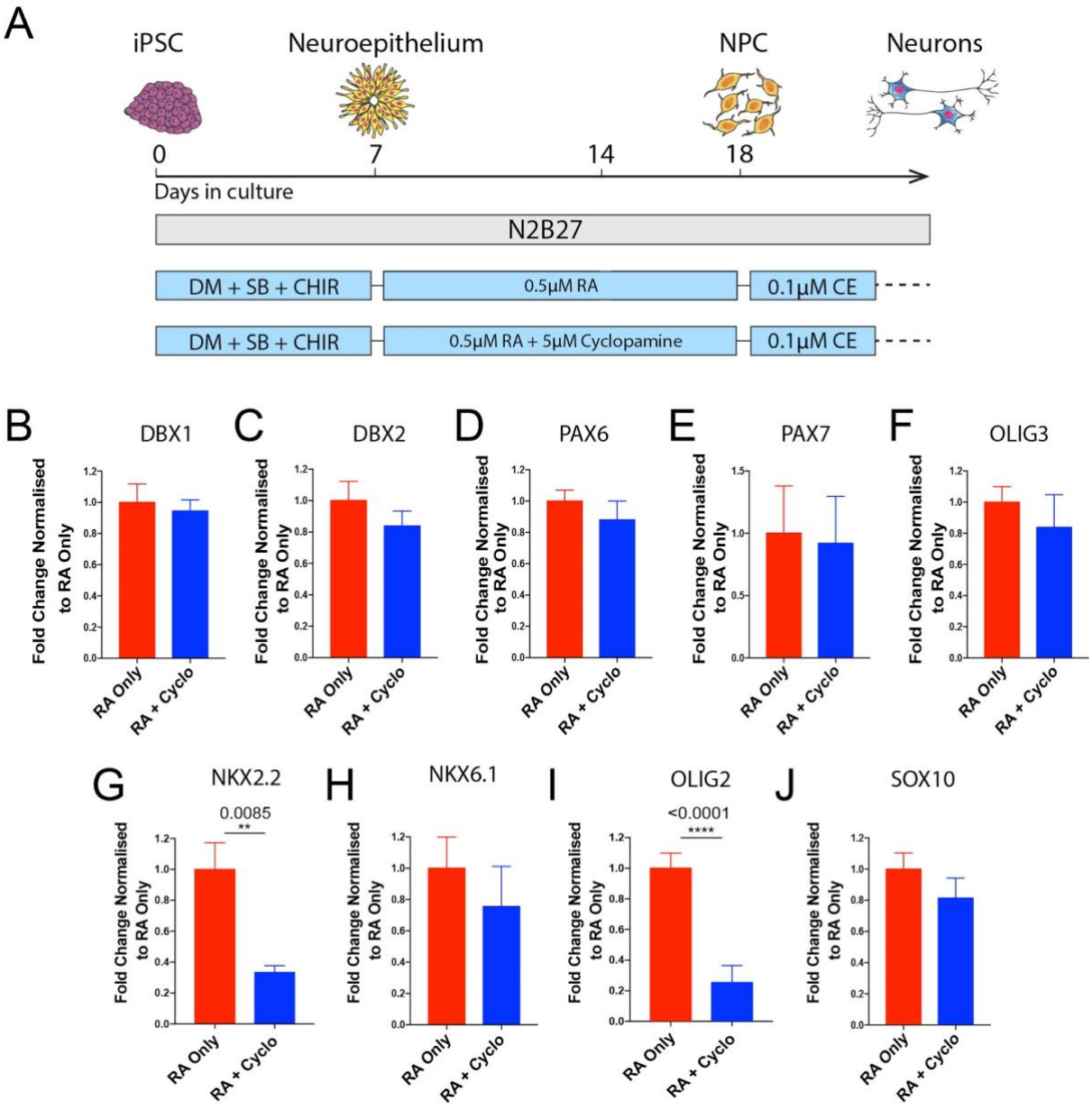

Figure 4.13 SHH signalling does not impact dorsal domain identity in RA only patterned NPCs

(A) Schematic depicting hiPSC-derived directed differentiation strategy for generating dorsal IN NPCs (RA only) and also in the presence of the SHH antagonist cyclopamine (RA + Cyclo) in order to eliminate endogenous SHH signalling. Bar plots depicting mRNA expression levels of

the mid-neural tube markers - DBX1 (B) and DBX2 (C), mid-neural tube and pMN domain marker - PAX6 (D), dorsal neural tube marker - PAX7 (E), dP1-3 domain marker - OLIG3 (F), P3 domain marker - NKX2.2 (G), ventral P3, pMN and P2 domain marker - NKX6.1 (H), pMN domain marker - OLIG2 (I) and neural crest marker - SOX10 (J) in day 18 NPCs patterned with RA only or RA + Cyclo, as assessed by qPCR. Each sample was normalised over its GAPDH expression level and each condition was normalised against the RA only condition. n=3 across 3 different cell lines. Data is plotted per line. Error bars are displayed as mean ± SEM. p value calculated using unpaired two-tailed t-test with Welch's correction, ** represents $p < 0.01$, **** represents $p < 0.0001$.

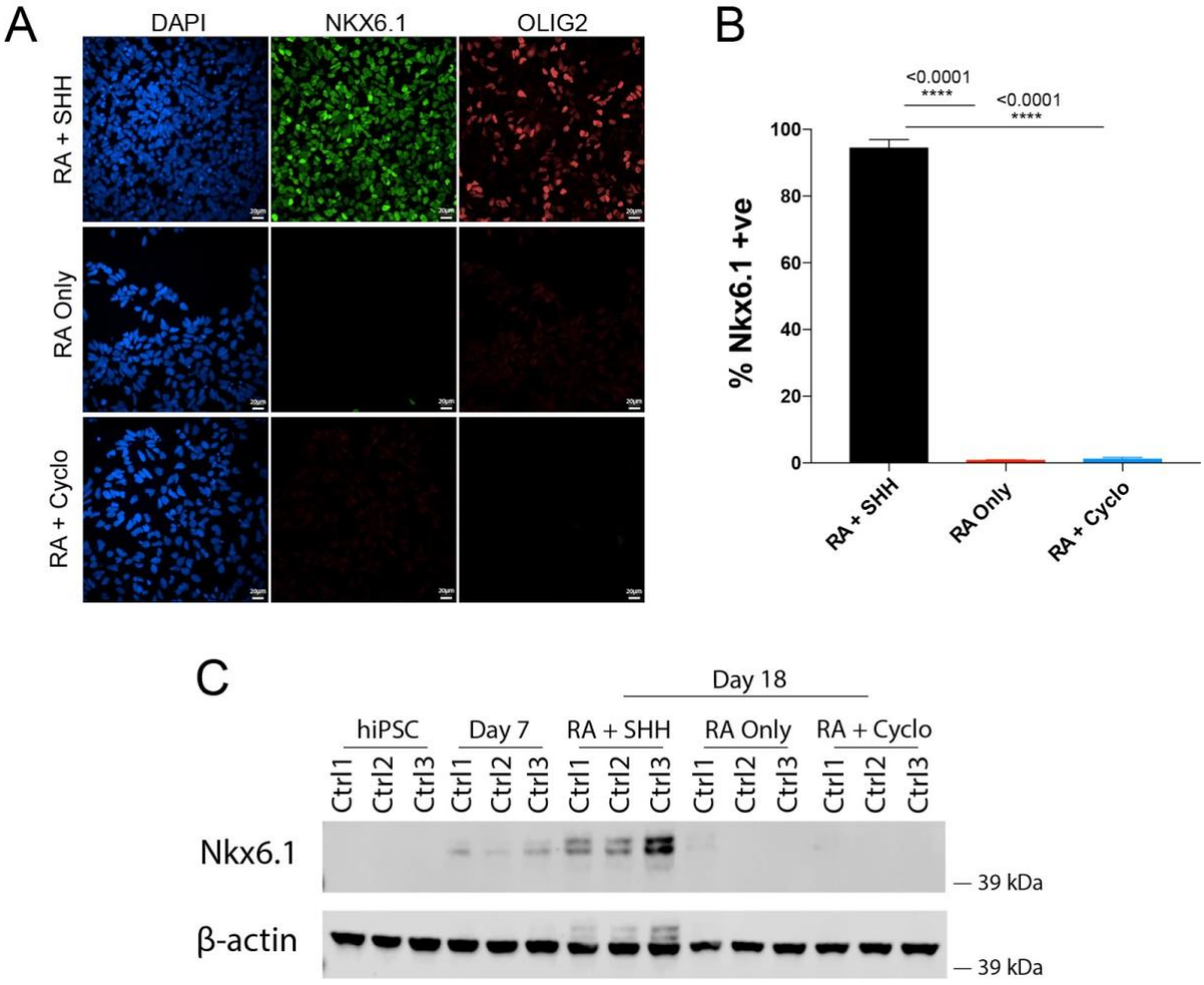

Figure 4.14 SHH antagonism using cyclopamine does not alter ventral marker NKX6.1 in RA only patterned NPCs at the protein level

Representative immunocytochemistry images of the CTRL1 cell line using (A) the cellular marker for p3, pMN and P2 domains - NKX6.1 and pMN domain marker - OLIG2 in day 18 NPCs patterned with RA + SHH, RA only or RA + Cyclo. Scale bar set at 20 μm. (B) Quantitative

immunocytochemistry for NKX6.1. n=3 per cell line with 3-5 independent control lines used (CTRL1-5). Error bars displayed as mean ± SEM. p value calculated using one-way ANOVA with Tukey correction for multiple comparison, **** represents $p < 0.0001$. (C) Western blot probing for NKX6.1 and β-actin in 3 control lines with hiPSC, day 7, day 18 RA + SHH, day 18 RA only and day 18 RA + Cyclo conditions. n=1 per cell line with 3 independent control lines used (CTRL1-3).

4.3.4 hiPSC-derived dorsal neural tube precursors differentiate into enriched spinal interneurons

Next, dP4-6 neural precursors were terminally differentiated and evaluated for enrichment of neuronal and post-mitotic domain markers. This was achieved using the notch antagonist CE to promote cell cycle exit and cultures were assessed at day 25 using RNA sequencing (Figure 4.15A&B). As with day 18 NPC samples, principal component analysis and unsupervised hierarchical clustering revealed segregation based on differentiation strategy (RA + SHH versus RA only) and cell line (Figure 4.15C&D). Gene clustering by the most highly variable genes in the dataset further confirmed segregation according to the differentiation strategy, with established markers ONECUT1, ONECUT3, ZIC1 and CRABP2 amongst the most variable genes (Figure 4.15E&F). Comparing RA only versus RA + SHH gene expression patterns, 402 DEGs were identified (FDR < 0.05) with 239 and 163 genes upregulated in RA only and RA + SHH conditions respectively (Figure 4.16A). Gene ontology analysis revealed upregulated (RA only) genes to be enriched for cell-matrix adhesion, neuronal development and DNA binding processes, whilst downregulated (RA + SHH) genes were overrepresented in synaptic, axonal and ALS pathways (Figure 4.16B). Amongst these were genes responsible for the patterning of various neural tube domains, with upregulation of post-mitotic dorsal markers in RA only cultures (ZIC1, ZIC4, POU4F1) coinciding with downregulation in motor and ventral domain markers (CHAT, ISL1, MNX1) (Figure 4.17A). Gene expression across established progenitor markers confirmed clustering of samples according to post-mitotic dorsal and ventral markers, with significant differences between RA + SHH and RA only conditions (Figure 4.17B).

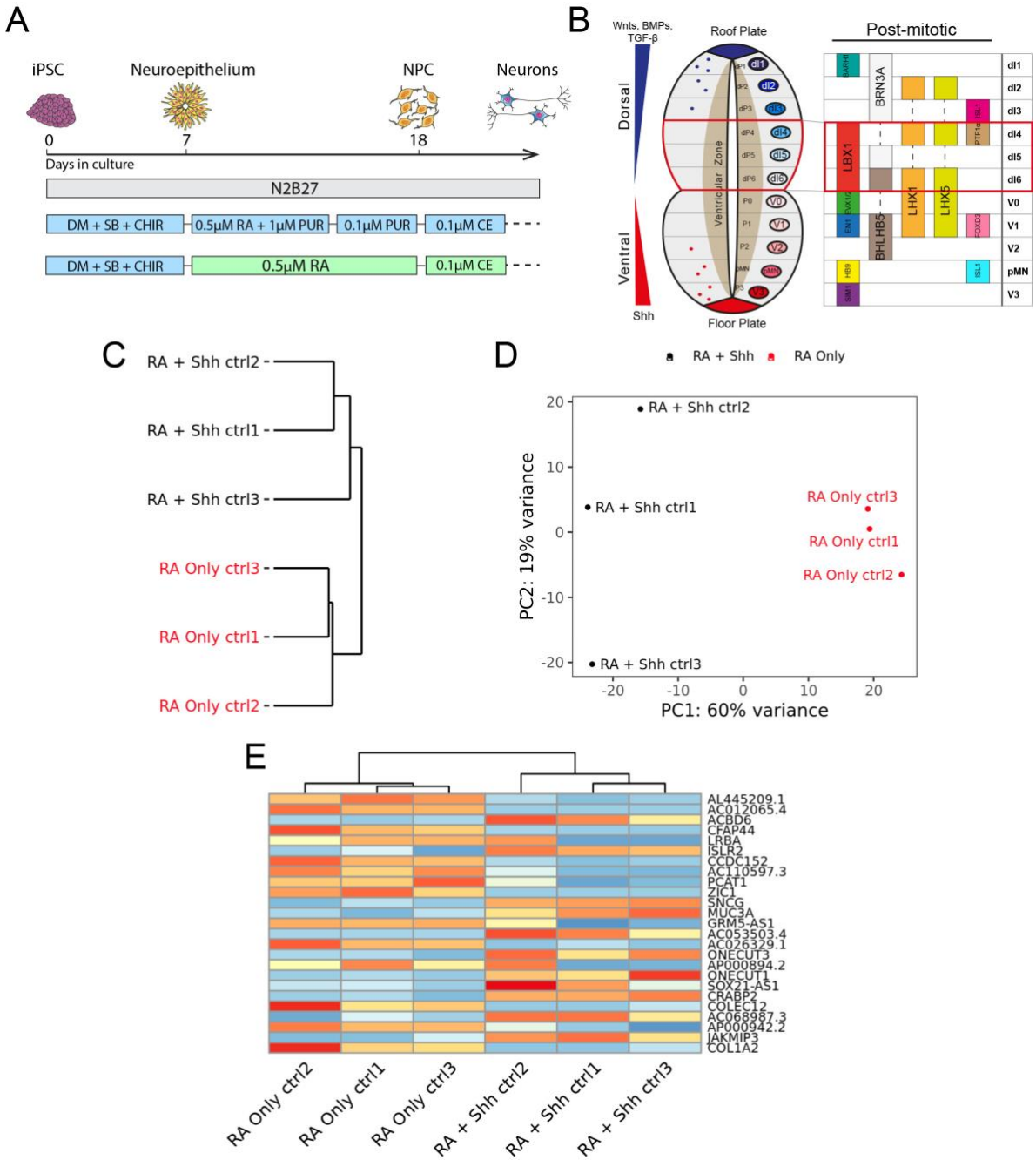
A
iPSC
Neuroepithelium
NPC
Neurons
0
7
18
Days in culture
N2B27
DM + SB + CHIR
0.5μM RA + 1μM PUR
0.1μM PUR
0.1μM CE
DM + SB + CHIR
0.5μM RA
0.1μM CE
B
Wnts, BMPs, TGF-β
Roof Plate
Dorsal
Ventricular Zone
Ventral
Shh
Floor Plate
Post-mitotic
dI1
dI2
dI3
dI4
dI5
dI6
V0
V1
V2
pMN
V3
BRN3A
LBX1
LHX1
LHX5
BHLHB5
C
RA + Shh ctrl2
RA + Shh ctrl1
RA + Shh ctrl3
RA Only ctrl3
RA Only ctrl1
RA Only ctrl2
D
RA + Shh
RA Only
PC2: 19% variance
PC1: 60% variance
E
AL445209.1
AC012065.4
ACBD6
CFAP44
LRBA
ISLR2
CCDC152
AC110597.3
PCAT1
ZIC1
SNCG
MUC3A
GRM5-AS1
AC053503.4
AC026329.1
ONECUT3
AP000894.2
ONECUT1
SOX21-AS1
CRABP2
COLEC12
AC068987.3
AP000942.2
IAKMIP3
COL1A2
RA Only ctrl2
RA Only ctrl1
RA Only ctrl3
RA + Shh ctrl2
RA + Shh ctrl1
RA + Shh ctrl3

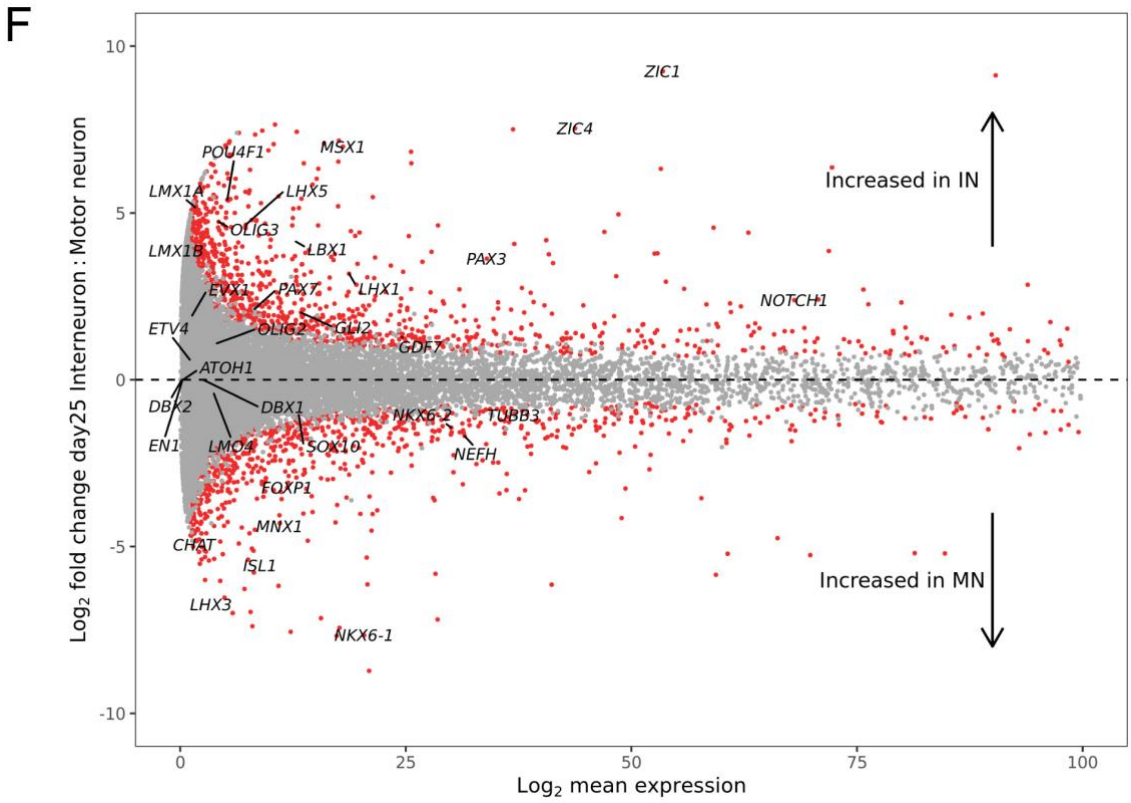

Figure 4.15 Upregulation of dorsal post-mitotic expression markers in RA only patterned and terminally differentiated cultures

(A) Schematic depicting hiPSC-derived directed differentiation strategy for generating dorsal IN NPCs (RA only) and also incorporating terminal differentiation using the notch antagonist compound E. (B) Schematic illustrating the embryonic neural tube with its respective classification into domains, along with post-mitotic transcription factor expression profiles. Highlighted in red are the post-mitotic domains dI4-6 that are derived from dP4-6. (C) Dendrogram showing unsupervised hierarchical clustering of variance stabilised gene counts across all samples at day 25 post-mitotic stage. (D) Principal component analysis (PCA) on variance stabilised gene counts across day 25 samples plotted by their coordinates along the first two principal components. Samples are coloured by their patterning conditions (RA + SHH shown in black and RA only in red) and labelled by their cell line. (E) Heatmap showing the mean variance stabilised gene counts for established dorsal-ventral markers between RA + SHH and RA only conditions. (F) Volcano plot depicting differential gene expression between RA only and RA + SHH cells at day 25 post-mitotic stage. Significantly up- or down-regulated genes are highlighted in red (FDR < 0.05) with traditional dorsal-ventral progenitor patterning genes labelled.

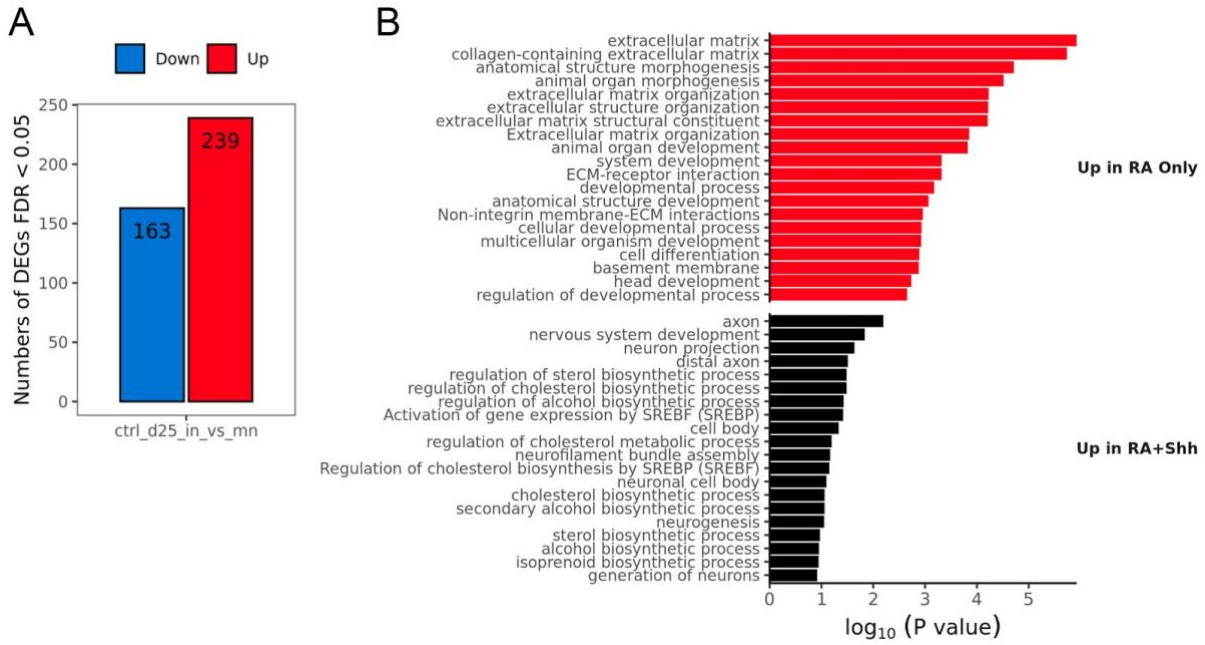

Figure 4.16 Differentially expressed genes and gene ontology analysis of post-mitotic RA only patterned cultures

(A) Bar plot showing the number of differentially expressed genes (FDR < 0.05) that are up- and down-regulated in RA only vs RA + SHH conditions at day 25. (B) Gene Ontology terms enriched in up- and down-regulated differentially expressed genes in RA only vs RA + SHH conditions.

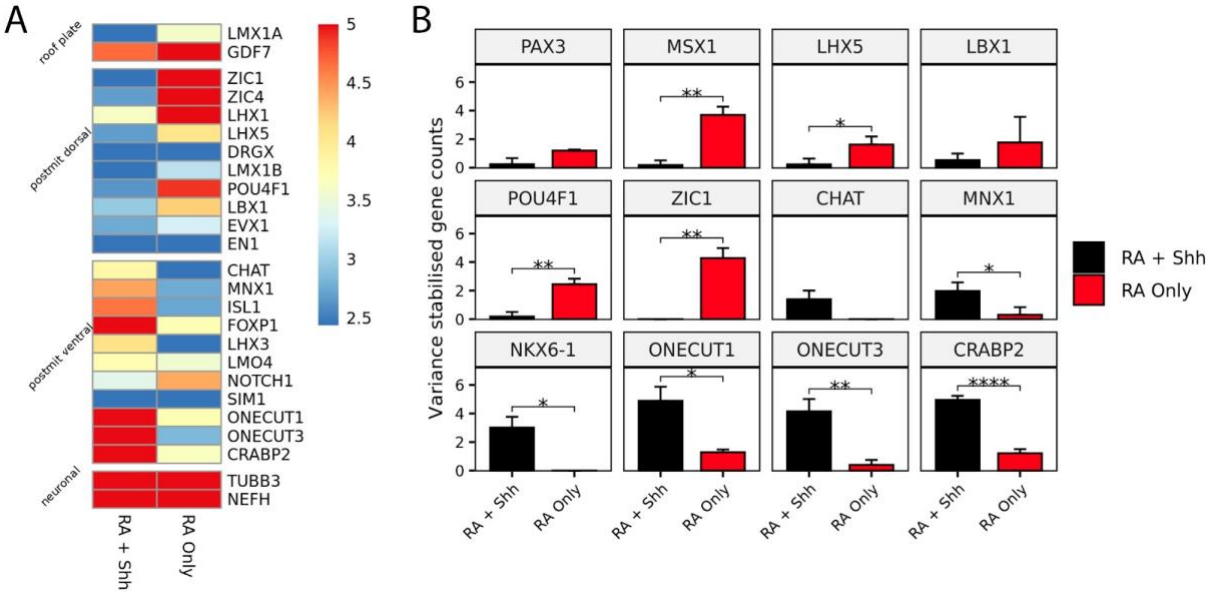

Figure 4.17 Upregulation of post-mitotic dorsal spinal cord markers in terminally differentiated RA only patterned cultures by RNA sequencing

(A) Heatmap showing the mean variance stabilised gene counts for established dorsal-ventral markers between RA + SHH and RA only conditions. (B) Bar plots showing the mean variance stabilised gene counts (y-axis of specific dorsal-ventral post-mitotic markers between RA + SHH and RA only conditions (x-axis). Bulk RNA sequencing was performed on 3 independent control lines (CTRL1, 5 and 6). p value calculated using unpaired two-tailed t-test with Welch's correction, * represents $p < 0.05$, ** represents $p < 0.01$, **** represents $p < 0.0001$.

qPCR was next employed to examine the expression profiles of the dorsal neural tube markers LHX5 and LBX1 along with the pan-motor neuronal marker ChAT (Figure 4.18). Similar to RNAseq findings, a significant increase in mRNA expression levels of LHX5 and LBX1 was identified in RA only conditions, when compared to RA + SHH (Figure 4.18A&B). Furthermore, this increase in dorsal neural tube marker expression coincided with a significant decrease in ChAT expression (Figure 4.18C).

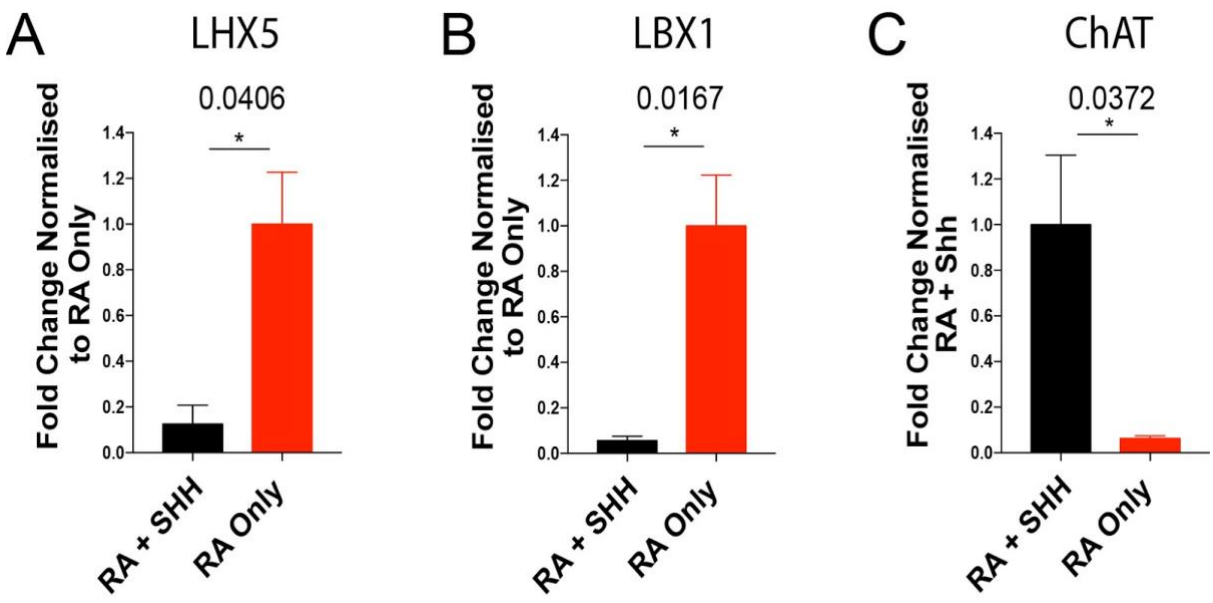

Figure 4.18 Upregulation of post-mitotic dorsal spinal cord markers in terminally differentiated RA only patterned cultures by qPCR

Bar plots depicting mRNA expression levels of post-mitotic neural tube transcription factors - LHX5 (A) and LBX1 (B) and pan-motor neuronal marker - ChAT (C) in day 25 terminally differentiated RA + SHH and RA only treated cultures, as assessed by qPCR. Each sample was normalised over its GAPDH expression level and each condition was normalised against either RA + SHH or RA only (as indicated on each graph). n=3 per cell line with 3-6 independent control

lines used (CTRL1-6). Error bars are displayed as mean ± SEM. Data is plotted per line. p value calculated using unpaired two-tailed t-test with Welch's correction, * represents $p < 0.05$.

The rostral-caudal settling position and neuronal purity of dI4-6 terminally differentiated cultures were then assessed. It has previously been demonstrated that hiPSC-derived MNs (RA + SHH) occupy a lower cervical/brachial settling position (Chapter 3). Therefore, RNAseq was used in combination with qPCR for a spinal cord-spanning array of HOX genes. This revealed that the rostral-caudal identity of RA only and RA + SHH treated neurons was not altered post-mitotically, supporting a similar lower cervical/brachial rostral-caudal axial position (Figure 4.19A&B). Evaluation for neuronal enrichment and the efficiency of neuronal conversion in RA only treated cells was next assessed. qPCR analysis revealed a significant decrease in expression levels of the astrocyte marker GFAP, when compared to enriched astrocyte cultures obtained through protocols detailed elsewhere (Figure 4.20A) (Hall et al. 2017). Additionally, qICC using an antibody against GFAP confirmed this low / negligible expression levels (~2%) in RA only day 25 terminally differentiated cultures (Figure 4.20A&B). Overall, these data demonstrate that dorsal dP4-6 NPCs differentiate into highly enriched neuronal populations with low levels of glial specification.

In order to validate these data at the protein level, qICC was carried out using an antibody for LHX5, a dorsal IN marker. This revealed a significant increase in the specification of this molecular subtype of dorsal INs in RA only (~42%) compared to RA + SHH (~3%) (Figure 4.21A&B). In aggregate, these data are consistent with the specification of human dorsal spinal INs from hiPSCs, which originate from dP4-dP6 domains and ultimately specify ~41% LHX5 expressing INs consistent with derivatives from dI4 and dI6 domains.

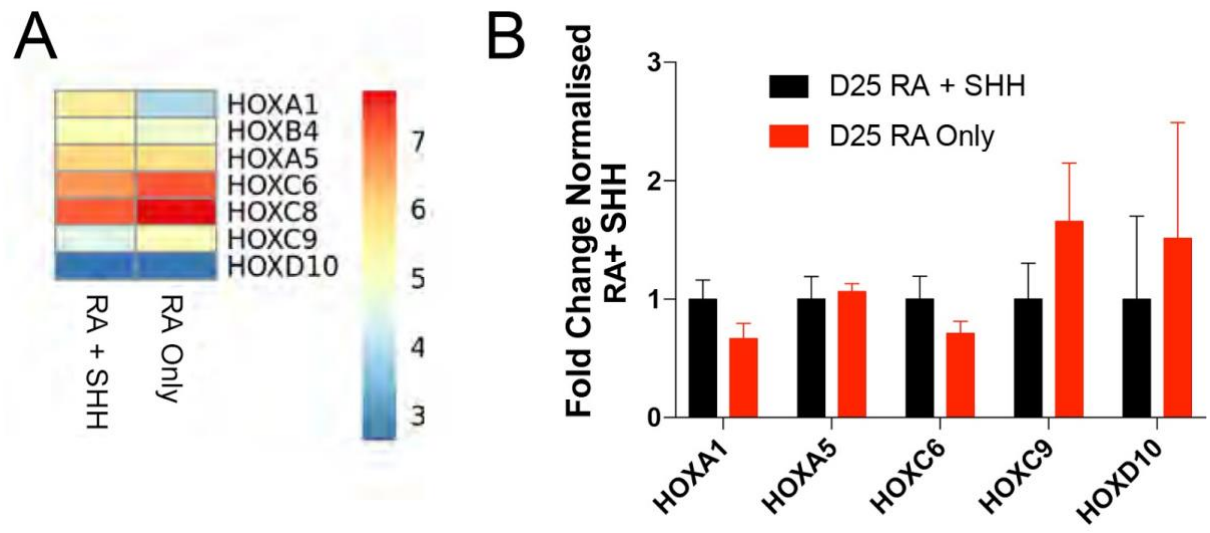

Figure 4.19 Axial identity of RA only patterned and terminally differentiated neurons does not differ from RA + SHH MNs

(A) Heatmap depicting the mean variance stabilised gene counts for a range of HOX genes expressed throughout the spinal cord in RA + SHH and RA only samples at day 25. (B) Bar plot showing mRNA expression levels of a range of spinal cord-spanning HOX genes, each sample normalised over its own GAPDH level and further normalised against RA + SHH conditions, as assessed using qPCR. n=2 per cell line with 3-6 independent control lines used (CTRL1-6). Error bars displayed as mean ± SEM. Significance determined using unpaired two-tailed t-test with Welch's correction.

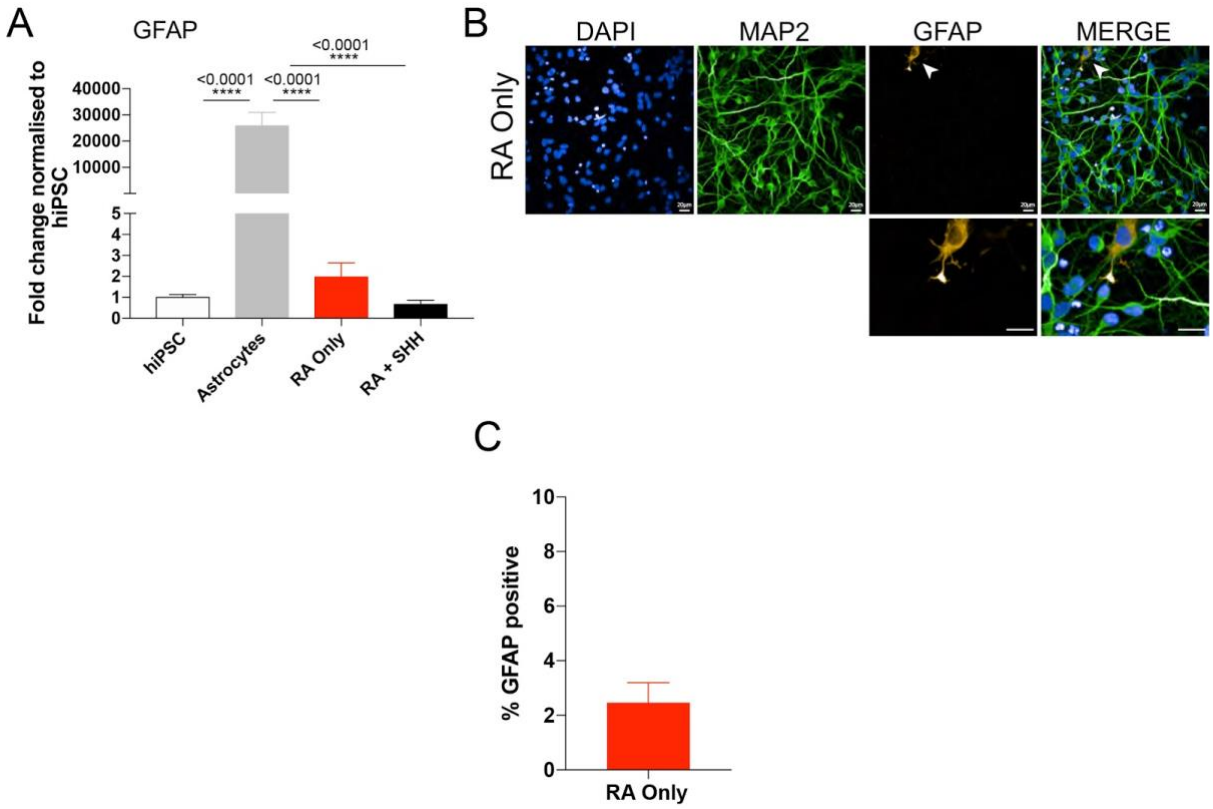

Figure 4.20 Terminally differentiated cultures derived from RA only patterned NPCs generate enriched neuronal populations

(A) Bar plots showing the qPCR data for mRNA expression levels of the astrocyte marker GFAP in day 25 terminally differentiated RA + SHH and RA only populations, each normalised over GAPDH and additionally to hiPSCs as a control. n=3 per cell line with 3-6 independent control lines used (CTRL1-6). Error bars displayed as mean ± SEM. Significance determined using one-way ANOVA with Tukey correction for multiple comparison, **** represents $p < 0.0001$. (B) Representative immunocytochemistry images of the CTRL1 cell line using the astrocyte marker GFAP and neuronal marker MAP2. quantitative. Scale bar set at 20 µm. (C) Quantitative immunocytochemistry for GFAP. Error bars displayed as mean ± SEM. n=3 per cell line with 3-6 independent control lines used (CTRL1-6).

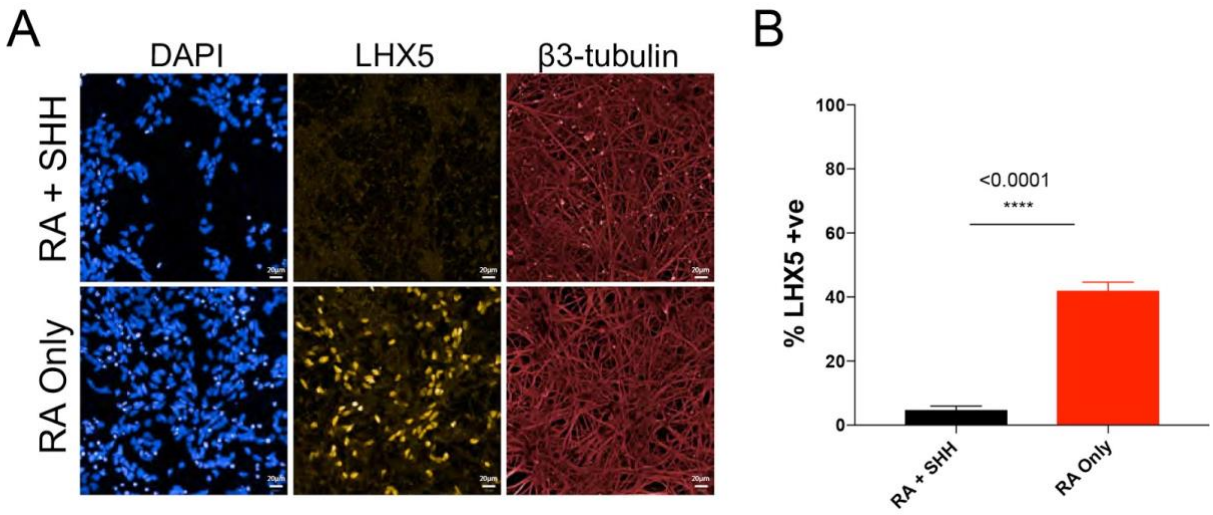

Figure 4.21 Upregulation of mid-dorsal neural tube marker LHX5 in terminally differentiated RA only patterned cultures

Representative immunocytochemistry images of the CTRL6 cell line using the post-mitotic dorsal neural tube domain marker - LHX5 in day 25 post-mitotic neurons patterned with RA + SHH or RA only. Scale bar set at 20 µm. (B) Quantitative immunocytochemistry for LHX5. n=3 for INs, n=2 for MNs, per cell line with 3-6 independent control lines used (CTRL1-6). Error bars displayed as mean ± SEM. p value calculated using unpaired two-tailed t-test with Welch's correction, **** represents $p < 0.0001$.

4.3.5 Terminally differentiated dorsal interneurons demonstrate functional calcium signalling

Since this differentiation protocol specified highly enriched neuronal populations, as determined by qICC and qPCR, evaluation of neuronal functionality was next employed to validate the functionality of neurons. Fluo-4AM was used as a calcium indicator in combination with a silicon-rhodamine dye to label the cytoskeleton. Calcium signalling was monitored following application of 50mM KCl. This live imaging paradigm is predicated on the presence of voltage gated calcium channels in active neuronal populations. The addition of KCl acts to reverse the concentration gradient of potassium between the intra- and extracellular space leading to depolarization. This in turn results in a large influx of calcium ions into the neuron that can be visualised using the Fluo-4AM dye. The proportion of cells that responded to KCl stimulation was 82% at day 39 (Figure 4.22), thus demonstrating that the vast majority of neurons within cultures exhibit cytosolic calcium responses to physiological calcium stimuli. The decline in calcium

transient amplitude potentially reflects the de-esterification of the Fluo-4AM dye throughout the imaging process. Spontaneous activity is also a crucial characteristic of neuronal activity, particularly within the spinal cord where it has been demonstrated as a key feature of CPG activity and maintenance. Indeed, spontaneous activity was also observed within interneuronal populations at day 39 (Figure 4.23A&B) providing further functional validation of these IN populations. Importantly, the $\Delta F/F_0$ values reached similar amplitudes following KCl stimulation and during spontaneous spiking activity - both ~2.

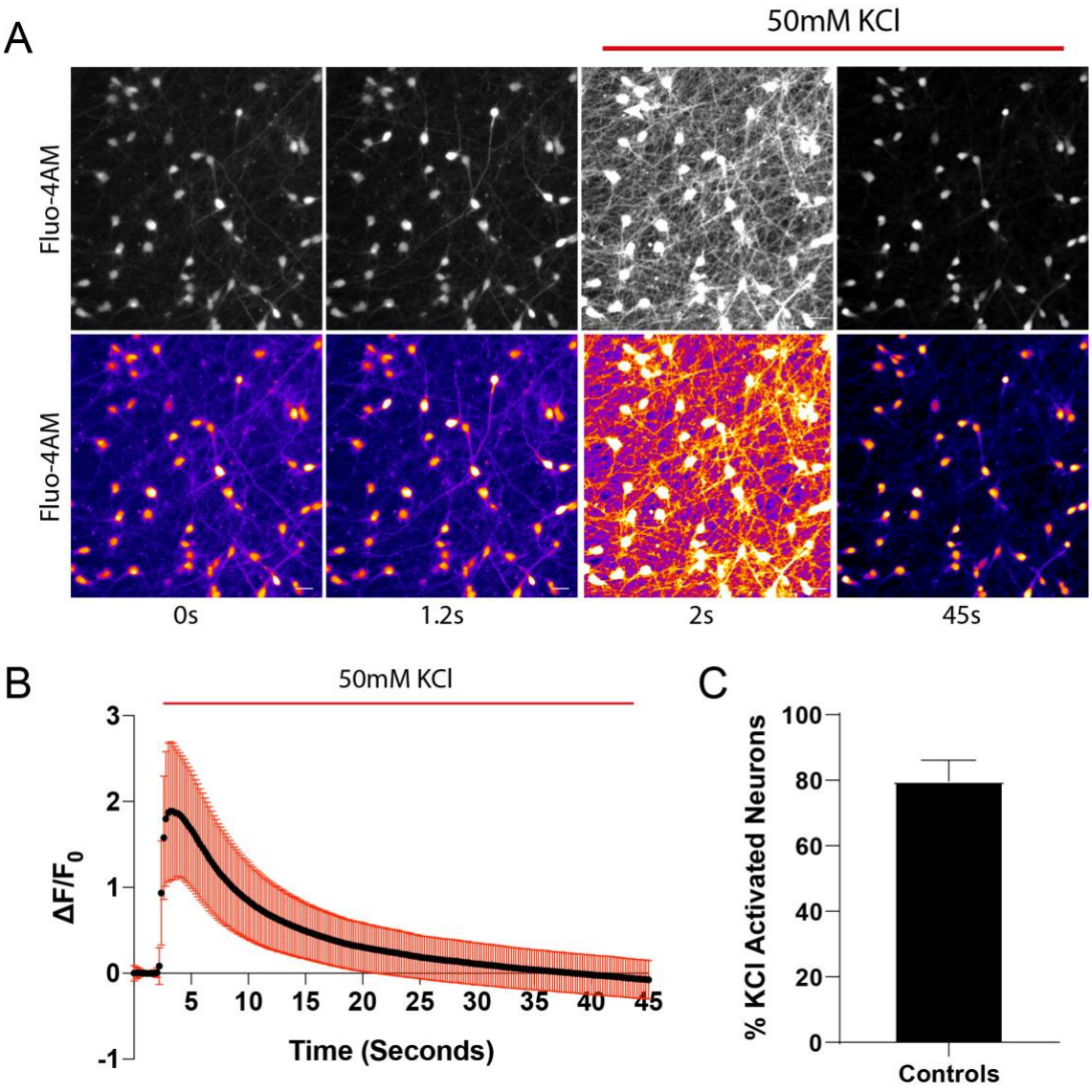

Figure 4.22 RA only patterned neurons exhibit cytosolic calcium responses to KCl stimulation

Representative time series of the CTRL4 control cell line using Fluo-4AM calcium signalling in day 39 RA only treated cultures before and after KCl administration to a final concentration of 50mM. (B) Representative fluorescence intensity traces of INs at day 39 and following KCl administration. n=20 cells per line, from 3 independent control lines across 1 neuronal induction. Error bars are displayed as mean ± SD. (C) Quantification of the proportion of neurons that exhibited calcium spiking following 50mM KCl administration at day 39. n=~200 cells per line, from 3 independent control lines across 1 neuronal induction. Error bars are displayed as mean ± SEM. Data presented as $\Delta F/F_0$, with F_0 calculated as the median of the initial 2.4s quiescent.

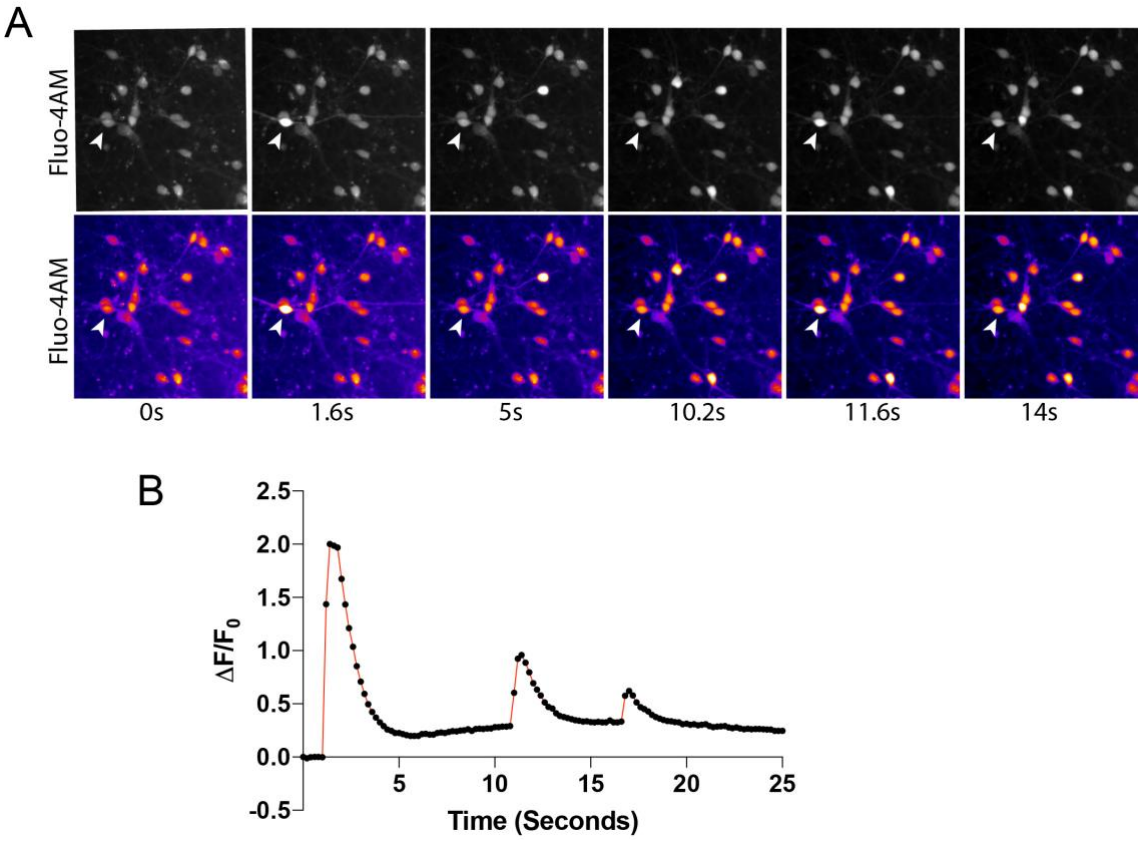

Figure 4.23 Terminally differentiated RA only patterned NPCs exhibit spontaneous calcium signalling

(A) Representative time series images of spontaneous Fluo-4AM calcium activity in IN populations from the CTRL4 cell line at day 39. (B) Example of spontaneous activity from a single interneuron highlighted in A and traced over the timecouse of the experiment. Data presented as $\Delta F/F_0$, with F_0 calculated as the median of the initial 1.2s quiescent period where no activity was observed.

4.4 Discussion

Since the founding of hiPSC technology, myriad differentiation strategies have emerged to specify clinically relevant and region-specific neurons and glia (Zirra et al. 2016), including the generation of peripheral sensory neurons (Chambers et al. 2009) and a subset of spinal interneurons (dl1-dl3) (Gupta et al. 2018; Ogura et al. 2018). Additionally, a subset of last-order V2a interneurons has been successfully derived from hiPSCs (Butts et al. 2017). Although previous studies have demonstrated the generation of dorsal INs, no study has yet successfully generated dI4-6 domain human INs in adherent monolayer format. INs from these domains have crucial functions in pain, temperature, itch and touch sensations, the perturbations of which bear clinical significance (Lu et al. 2015; Lai et al. 2016). It follows that a cellular model of these IN subtypes has clear utility in developmental studies, disease modelling and drug screening. Beyond these uses, such cellular populations form powerful comparative standpoints for ventral spinal MNs to begin to address the basis of neuronal subtype selective vulnerability in disorders such as ALS. The results of this Chapter suggest that a more dorsal neural tube identity can be achieved through the exclusion of SHH signalling and by RA signalling alone, in comparison to ventrally derived pMN domain MNs that require SHH. The more dorsalised populations acquire a dP4-6 IN precursor fate. Further dorsalisation likely requires the addition of additional TGF-β paralogs, as evidenced by the small upregulation of dP1-3 markers in BMP4 treated conditions that were unable to be terminally differentiated into neurons. Subsequently, dP4-6 IN precursors derived using RA only can be terminally differentiated into functionally active, but immature, interneuronal populations of corresponding dI4-6 domains.

4.4.1 BMP4 as a dorsalising cue

In order to generate neurons from dorsal domains of the neural tube, BMP4 was added to cultures in place of purmorphamine (RA + BMP4). BMP4 is secreted from the roof plate and is critical to dP1-3 domain specification, deficient mice exhibiting an almost complete ablation of these domains (Liem et al. 1997; Lee et al. 2000; Butler & Dodd. 2003). Whilst qPCR analysis of RA + BMP4 cultures demonstrated a significant

upregulation in both PAX7 and OLIG3, qICC showed only a modest increase in the percentage of OLIG3 positive precursors at day 18 timepoints. 2 separate studies by Gupta et al (2018) and Ogura et al (2018) have reported similar findings of increased dorsal fate specification using BMP4 in 3D embryoid body and organoid-like culture systems, respectively. Interestingly, a small upregulation in dI1-3 specification was also observed in these studies, although it should be noted that dorsal fate specification was assessed at the post-mitotic stage (i.e. not through OLIG3 expression). Furthermore, 3D culture models are known to have a significant increase in heterogeneity when compared to 2D, with cultures often unable to produce enriched populations of specific cell types (Gupta et al. 2018; Ogura et al. 2018). An additional finding of these studies was that exclusion of RA from BMP4 treated cultures led to an enrichment in dI1 and dI3 neuronal populations with an apparent and specific ablation of dI2 populations. These findings suggested an important role of RA signalling in dI2 domain specification. Therefore, one could speculate that the OLIG3 positive cultures generated from RA + BMP4 treatment in this 2D system could represent dP2 dorsal domain precursors, requiring both RA and BMP4 signalling. This could also explain the relatively small increase in dP1-3 fate specification, since RA and BMP have been demonstrated to have opposing roles in the activation/repression of PAX6 expression (Novitch et al. 2003; Timmer et al. 2002). Subsequently, dP1-dP3 enrichment may require the reduction or removal of RA signalling, as explored in a separate study (Ogura et al. 2018). Another factor to consider is the competence state of cells to respond to developmental cues. Indeed, BMP4 competence was shown to be lost after a specific period of time and importantly, this was further reduced in the presence of RA (Gupta et al. 2018). Whilst the effects of RA may have influenced the efficacy of BMP4 during neural patterning, RA has a significant role in rostral-caudal patterning and its use in these cultures is a requisite in order to specify cultures with the same axial identity as the hiPSC-derived MNs.

There are 15 known BMP members, many of which have important roles in early embryonic development during gastrulation and mesoderm formation (Wang et al. 2014). Whilst BMP4, 5, 6, 7 and GDF7 have been shown to play essential roles in patterning the dorsal-most dI1-3 domains of the neural tube (Liem et al. 1997; 2000), the efficacy by which they can each induce these fates has been suggested to vary greatly (Andrews et al. 2017). *In vivo*, dorsal precursors are subject to a range of signalling cues raising the

possibility that a combination of BMPs or other TGF-β family members may be required, or that the BMP4 concentration was insufficient for accurate *in vitro* specification and subsequent differentiation into interneuronal populations. Subsequently, it would be interesting to assess the endogenous levels of BMP and/or TGF-β signalling in these cultures.

Further analysis of the differentiation capacity of RA + BMP4 treated precursors highlighted the apparent inability of these cultures to terminally differentiate into neurons. This was evidenced through their flat morphology with little polarisation found following terminal differentiation in the notch antagonist CE. This could be due to the role of BMP4 in the promotion of the gliogenic switch (Bond et al. 2012). Indeed, a combination of BMP4 and leukemia inhibitory factor (LIF) is used to produce astrocytes from MN NPCs using the hiPSC-derived MN protocol detailed in Chapter 3 (Hall et al. 2017). The resultant population could therefore represent dorsal glial populations. However, this requires further experimentation. Interestingly, BMP4 signalling has been suggested to be unable to direct the differentiation of cells to a unique fate, instead driving an organised collection of distinct cell types. This stereotyped cell fate organisation within the dorsal neural tube is heavily influenced by concentration, timing and duration of BMP4 signalling. Therefore, additional temporal control could provide further nuance to the generation of dorsal interneuronal and glial populations, especially when considering that spinal cord dorsal sensory INs develop over a different timeline to MNs and also to glial derivatives (Andrews et al. 2017; Le Dreau & Marti. 2012).

4.4.2 Retinoic acid is sufficient for dorsal precursor specification

Noting that patterning in the presence of BMP4 did not induce the specification of an enriched population of dP1-dP3 precursors, nor were these cells able to terminally differentiate into neuronal populations, an alternate strategy was employed. This involved the removal of all exogenously administered dorsalising and ventralising cues and relying solely on RA signalling alone (RA only). It should be noted that this does not preclude from the possibility that endogenous TGF-β/BMP signalling could at sufficient levels to influence cultures. As such, additional experiments could have been employed in order to antagonise any potential endogenous dorsalising signalling cues, thereby revealing the precise role of RA signalling alone in neural tube dorsal-ventral patterning. Indeed, RA

is an important signalling cue during NPC patterning, with diverse roles in cell-fate specification across the neural tube (Pierani et al. 1999; Niederreither et al. 2000; Wilson et al. 2003; 2004; Appel & Eisen. 2003; Novitch et al. 2003; Okada et al. 2004). Whilst neural tube signalling molecules such as SHH and BMP are classified as morphogens and are thus limited by their diffusion-mediated concentration gradients, an essential property of RA signalling stems from the fact that it does not act as a typical diffusible morphogen. Instead, the competence of a cell to respond to RA depends on whether that cell has been 'primed' to respond to RA. This is mediated through the differential expression of retinol and retinaldehyde dehydrogenases (synthesising enzymes such as RALDH2) and levels of the cytochrome P450 family 26 (CYP26 - degrading enzymes) and subsequently not by its diffusion properties (Diez del Corral et al. 2003). Therefore, whilst RA signalling has been demonstrated to play an important role in MN specification, it can also mediate the specification of numerous other spinal cord cell-types throughout the structure. Indeed, RALDH2 is expressed in populations of dorsal INs and even in the roof plate of the avian spinal cord (Wilson et al. 2004). Targeted deletion of RA signalling was found to promote a dorsal expansion of ventral domains, at the expense of roof plate and dorsal patterning transcription factors. Lastly, ablation of RA signalling was also found to promote selective loss of EN-1 positive V1 INs (Wilson et al. 2004). Overall, it appears that whilst the specification of numerous spinal cord subtypes may necessitate RA signalling, RA itself is not thought to directly contribute to the establishment of the neural tube domains. Instead, this is achieved by the secretion of diffusible morphogens from the roof/floor plate. However, it should be noted that the intermediate neural tube domains are exposed to relatively low levels of these morphogens. Therefore, the many roles of RA that have been demonstrated in multiple neural tube fates could be as a result of its combined effects with other morphogens across the neural tube. Spinal cord MN specification presents a good example of this, where RA is known to play an important role in spinal cord motor neurogenesis (Novitch et al. 2003). However, the predominant molecular cue required for MN specification is SHH. Motor neurogenesis cannot occur without SHH signalling, but retinoid independent motor neurogenesis has been shown (Patani et al. 2011). Despite this, RA is critical for enrichment of MNs in combination with SHH, and is also necessary for MN columnar subtype diversification.

In support of these findings and using hiPSC-derived MNs as a negative control in order to assess dorsal fate specification, removal of the SHH agonist purmorphamine and subsequent patterning in RA only resulted in significant differences based on differentiation strategy. This was assessed using principal component analysis and unsupervised hierarchical clustering from RNAseq datasets. Further analysis revealed that RA only treated conditions displayed a significant downregulation of pMN and MN markers at NPC stage, including NKX6.1 and OLIG2. Furthermore, although the addition of the SHH antagonist cyclopamine resulted in a significant decrease in mRNA expression of OLIG2 and NKX2.2, this was not accompanied by a detectable difference at the protein level. In addition, no difference in the mRNA expression profile of dorsal domain markers was found with the inclusion of cyclopamine. This suggests that endogenous SHH levels are low within cultures and at a level insufficient to direct fates to a ventral positional identity. Taken together, these findings demonstrate the prerequisite for SHH in motor neurogenesis in this 2D culture system.

RA only and RA + SHH samples also displayed a clear difference in dorsal transcription factor expression profiles. Indeed, RA signalling alone and in the absence of SHH signalling was found to be sufficient to positionally specify NPCs to a dorsal spinal identity, as evidenced by an upregulation in MSX1, PAX3 and PAX7, using bulk RNAseq. Importantly, these findings were further validated using qPCR and qICC for PAX3 and PAX7 indicating dorsal domain specification. A significant increase in the transcription factor PAX6 was also found in RA only conditions using qPCR. PAX6 is a transcription factor that is found most abundantly expressed between dP4-6 and P0 domains (Novitch et al. 2003), highlighting this region as a potential positional identity. Interestingly, a small but significant population of dP1-3 NPCs was identified in RA only treated cultures through their expression of OLIG3. These findings relate back to previous comments suggesting that dP2 cell fate specification is promoted by RA signalling in the absence/reduction of BMP4 (Ogura et al. 2018; Gupta et al. 2018). Subsequently, OLIG3 positive precursors could represent dP2 cells, although further characterisation is required. OLIG3 expression at the progenitor level has also been shown to repress the expression of the post-mitotic dI4-6 transcription factor LBX1. This, in part, leads to the establishment of a definitive boundary between dP1-3 and dP4-6 domains with subsequent cell-type differences (Gross et al. 2002; Müller et al. 2002; Müller et al. 2005).

Indeed, the addition of BMP4 to 3D neural tube cultures was found to significantly decrease the amount of LBX1 positive neurons (Ogura et al. 2018). Additionally, BMP signalling from the roof plate was found to repress the expression of PAX6, further contributing to the definitive boundaries between dP1-dP3 and dP4-dP6 domains (Timmer et al. 2002; Timer et al. 2005; Zechner et al. 2007). One possible explanation for the presence of OLIG3 positive NPCs in RA only conditions could stem from a low but significant level of endogenous BMP signalling within cultures. Indeed, this could have been evaluated by examining endogenous BMP/TGF-β levels through RNAseq and controlled for by administering BMP/ TGF-β antagonists during the patterning phase. Alternatively, CHIR-mediated WNT signalling from the neural induction phase of the directed differentiation protocol might also contribute to this small upregulation in dP1-dP3 fate (Zechner et al. 2003). Indeed, dorsal roof plate and dP1-dP3 (and subsequent dI1-dI3) specification has been demonstrated in the absence of BMP agonists but in the presence of WNT agonism in a 3D culture system (Ogura et al. 2018). Overall, these findings align with previous studies that have demonstrated a role for RA in dorsal spinal cord patterning. Indeed, RA signalling has been employed to specify dorsal spinal cord progenitor populations using human embryonic stem (hES) cells and hiPSC-derived 3D differentiation cultures (Appel & Eisen. 2003; Okada et al. 2004; Gupta et al. 2018; Ogura et al. 2018).

4.4.3 Dorsal precursors terminally differentiate into dI4-6 interneurons

Clear differences in the neurogenic capacity of hiPSC-derived NPC populations were observed when comparing RA only and RA + BMP4 patterned cultures. Indeed, bulk RNA sequencing analysis, qPCR and qICC were employed and yielded no significant difference in the pan-neuronal marker β3-tubulin between RA only and the highly enriched neuronal RA + SHH MN cultures. Additional evaluation of the astrocyte marker GFAP also revealed no significant difference in mRNA expression, nor significant upregulation by immunostaining. It is interesting to note that the combined signalling of RA + BMP4 appeared to reduce the propensity for post-mitotic neural conversion, whilst RA signalling alone was found to promote neurogenesis. RA has long been recognised as a potent neuralising signal. During axis elongation, cells that migrate out of an FGF-dependent proliferative stem zone are exposed to high levels of RA that induce the neuralisation of progenitors and terminal differentiation (Diez del Corral et al. 2003).

Taken together, these findings suggest that BMP4 could act to override the neuralising RA cue, thus preventing the terminal differentiation of cultures into post-mitotic neuronal cultures and driving alternative fates such as glial derivatives. This could have been assessed by using generic markers for glial/astrocytic populations such as GFAP or ALDH1A1.

Separately, and as mentioned in Chapter 3, 2 independent patterning phases are employed for the generation of hiPSC-derived spinal MNs. This includes a 4 day window between day 14 and 18 where RA is excluded and the purmorphamine concentration is reduced (RA present between days 8-14). Interestingly, the rostral-caudal position of RA only treated neurons (patterned with RA between days 8-18) was not significantly altered from RA + SHH MNs despite an additional 4 days exposed to RA signalling. This suggests that HOX dynamics and spinal position along the rostral-caudal axis could be established within the first several days of patterning (i.e. between days 8-14) and become further enhanced, but without significant axial identity changes during terminal differentiation.

Evaluation of the post-mitotic identity of terminally differentiated NPCs, previously shown to be derived from dP4-6 domains, once again revealed differences in clustering between differentiation strategies, and as assessed using principle component and unsupervised hierarchical clustering analysis. Amongst the differentially expressed genes, there was a significant reduction in MN markers such as ChAT, MNX1 and ISL1 in RA only treated cultures, when compared to RA + SHH. This coincided with a significant increase in dorsal dI4-6 markers in MSX1, LHX5, LBX1 and POU4F1. Importantly, these findings were further verified using qPCR, demonstrating a significant increase in LHX5 and LBX1 in RA only samples, along with an increase in LHX5 immunostaining by qICC.

It is interesting to note that ZIC1 and ZIC4 were identified as 2 of the most differentially expressed genes, being largely upregulated in IN cultures at both NPC day 18 and post-mitotic day 25 timepoints. ZIC1 has been shown to be important for the early specification of dorsal spinal cord neurons, but also acts as a negative regulator of the differentiation of dorsal horn neurons in mice (Aruga et al. 2000; 2002). Indeed, ZIC1 overexpression in a transgenic mouse model was found to inhibit neuronal differentiation, with the extension of a progenitor state in the dorsal spinal cord (Aruga et al. 2002). This

pathway was hypothesised to act through a cross-repressive interaction of ZIC1 with the transcription factor MATH1, expressed in the dorsal-most dP1 and corresponding dI1 domain. Indeed, whilst both ZIC1 and MATH1 were found to be induced by BMP signalling, they exhibited cross-repressive actions on each other in a transgenic mouse model (Ebert et al. 2003). MATH1 was also shown to promote neuronal differentiation, as opposed to ZIC1. This was further evidenced in a zebrafish model where a role for both ZIC1 and ZIC4 was observed in promoting progenitor cell proliferation and also in dorsal roof plate specification (Elsen et al. 2008).

Taken together, these data indicate that hiPSC-derived dP4-6 precursors can be terminally differentiated into enriched post-mitotic dI4-6 IN cultures. Crucially, these INs maintained the same axial identity (lower cervical/brachial spinal cord level) as their ventral spinal MN counterparts, derived from the original differentiation paradigm. Live cell calcium imaging was used to functionally validate dorsal IN cultures and as such, it was demonstrated that the majority of cells exhibit cytosolic calcium responses to KCl stimulation. Importantly, these cultures also exhibited spontaneous activity.

4.5 Summary and conclusions

The generation of a novel hiPSC-derived protocol for the specification of an enriched population of neurons presents a unique opportunity to further our understanding of fundamental developmental principles and also provides clear utility as a disease modelling tool. The findings in this Chapter detail developmentally rationalised alterations to the hiPSC-derived MN protocol currently employed in the laboratory, in order to generate dorsally positioned and molecularly distinct IN cultures from dI4-6 domains. Importantly, these hiPSC-derived INs possess the same axial identity as hiPSC-derived MNs. Subsequently, this model has clear utility for the elucidation of developmental principles underlying dorsal spinal cord fate specification. Furthermore, patient-specific disease modelling and drug screening for the central (spinal) component of sensory neurological disorders, including neuropathic pain, can be addressed using this differentiation paradigm. Lastly, the combination of MNs and INs that can be generated from this hiPSC-derived model present a unique opportunity to interrogate mechanisms of cell type-specific vulnerability in disease such as amyotrophic lateral sclerosis (ALS) and spinal muscular atrophy (SMA). Overall, these findings demonstrate that:

1. BMP4 can be employed to promote dorsal NPC specification in 2D hiPSC-derived cultures.
2. BMP4 patterned NPCs, however, do not appear to terminally differentiate into neuronal cultures in our 2D differentiation protocol.
3. Retinoid signalling, in the absence of any dorsalising and ventralising cues, leads to the specification of dP4-6 dorsal identities.
4. These dP4-6 NPCs can be terminally differentiated into corresponding dI4-6 domain neuronal cultures.
5. dI4-6 interneuronal cultures exhibit spontaneous and evoked calcium responses demonstrating their functional neuronal properties.

Chapter 5. Cell type-specific vulnerability in VCP-mutant ALS

5.1 Introduction

Amyotrophic lateral sclerosis (ALS) is a rapidly progressive adult-onset neurodegenerative disease that affects upper motor neurons (MNs) in layer V of the primary motor cortex and lower MNs in the brainstem and ventral pMN domain of the spinal cord (Hughes. 1982; Hammer et al. 1979; Maekawa et al. 2004). The disease is characterised by muscle weakness rapidly leading to paralysis and death within 2-5 years from diagnosis (Brown & Al-Chalabi. 2017). Typically, the cause of death in ALS patients is a direct result of the degeneration of MNs innervating the respiratory muscles (Niedermeyer et al. 2019). In recent years, animal models have provided a valuable resource underpinning research attempts aimed at elucidating pathomechanisms and testing novel therapeutics for treating ALS (Lutz. 2018). However, the limitations of animal models are demonstrated by the lack of clinically effective therapies. Riluzole and Edaravone remain the only viable therapeutic option but has modest efficacy, extending life by approximately 3 months only (Miller et al. 2012; Hinchcliffe & Smith. 2017; Jaiswal. 2019). Against this background, the emergence of patient-specific hiPSCs has transformed disease modelling, providing a virtually inexhaustible source of patient-, and therefore mutation-, specific human stem cells to model disease using ontogeny-driven directed differentiation strategies. For this reason, hiPSCs provide an attractive strategy as a complementary model in order to more precisely capture clinical pathophysiology, whilst avoiding interspecies differences and the need for artificial overexpression, knockdown or knockout models (Devine & Patani. 2017).

The concept of cell type-specific vulnerability is hugely relevant to neurodegenerative diseases, whereby pathologies manifest in stereotypical patterns (Fu et al. 2018; Pandya & Patani. 2021). Often, an initial focal cell type is affected and, as the disease progresses, pathology spreads to alternate cell types and regions (Pandya & Patani. 2020). As a result, the clinical presentation of these neurodegenerative diseases often correlates with the dysfunction / degeneration of the specific cell type that is predominantly affected. This property of pathological spread between cell types and anatomical regions raises a fundamental question as to how juxtaposed cells can exhibit such a substantial contrast

in pathology and disease state. Indeed, ALS presents a perfect example of this, where clinico-pathological observations have identified the key cell type-specific hallmarks of ALS, manifesting through compensated dysfunction, followed by decompensated dysfunction and ultimately cell death of MNs of the corticospinal tract (Hardiman et al. 2017). As such, spinal cord ALS pathology is restricted to the MN-producing pMN domain, with neurons situated in adjacent domains remaining relatively unaffected until later stages in the disease. As a result, ALS is often considered a MN-centric disorder with a multitude of research directed towards the study of intrinsic MN dysfunction. Interestingly; however, wider research has started to unravel the roles of alternate cell types in the pathogenesis of ALS. Indeed, studies from this laboratory investigated the role of spinal cord astrocytes in an hiPSC-derived model of ALS, revealing striking cell autonomous and non-cell autonomous mechanisms of degeneration (Hall et al. 2017; Ziff et al. 2021).

INs are the most abundant cell type in the spinal cord, present in all domains excepting the pMN domain (Lu et al. 2015; Lai et al. 2016). As such, INs comprise the majority of CNS and peripheral nervous system (PNS) inhibition, thereby forming an essential component of the excitatory/inhibitory balance. This is highly relevant in ALS, where hyperexcitability is considered an important clinical symptom (reviewed by Gunes et al. 2020). Indeed, Cleveland and Rothstein (2001) postulated that excess glutamate signalling is a major cause of hyperexcitability in ALS, disrupting the excitatory/inhibitory balance that then leads to MN loss directly. In addition to their role in the excitatory/inhibitory balance, INs form critical components of all spinal networks, being involved in their generation, maintenance and modification whilst some also receive supra- and intra-spinal input, carefully orchestrating locomotor output (Guertin. 2013). Their fundamental role in locomotion and sensorimotor integration commands a striking complexity both in their molecular diversity and functional circuitry. However, this also places INs at a precarious position whereby any slight IN defect could lead to the potentiation of a host of motor abnormalities. As such, INs present an intriguing platform for the evaluation of cell type-specific vulnerability in ALS (Do-Ha et al. 2018; Crabé et al. 2020).

Against this background, interest in INs and their potential role in the pathogenesis of ALS has progressed from speculation. Whilst numerous studies have reported conditions of hyperexcitability in models of ALS, the mechanism and cell types involved in this phenomenon are yet to be fully elucidated (reviewed by Gunes et al. 2020). Evidence of IN dysfunction has been demonstrated in several studies employing transcranial magnetic stimulation (TMS) in order to measure short-intracortical inhibition (SICI) in the motor cortex (Ziemann et al. 1997). SICI is a measure of basal inhibition that is driven by IN circuitry within the motor cortex. Interestingly, a significant reduction and/or ablation of SICI was observed in 14 patients with clinically defined sporadic ALS, compared to 13 healthy and age-matched controls; suggesting either dysfunction or degeneration of inhibitory INs within the cortex (Ziemann et al. 1997). Similar findings were also demonstrated in studies by Vucic & Kiernan (2006), Kanai et al (2006) and Menon et al (2015) in 23, 24 and 24 ALS patients respectively. Furthermore, cortical hyperexcitability was also found to precede lower MN dysfunction, as assessed by compound muscle action potential (CMAP) amplitude recordings (Menon et al. 2015). A number of studies have also identified ALS-dependent alterations to reflex arcs, for which INs have a key role (Raynor & Shefner. 1994). Interestingly, a significant reduction in the density of parvalbumin staining was observed in the motor cortices of 13 patients with pathologically defined ALS, when compared to healthy patients (Nihei et al. 1993). INs are the most abundant parvalbumin expressing cell type within the motor cortex and were therefore proposed to be the predominant cell type affected. Moreover, IN loss was found to be independent of the degeneration of SMI-32 positive pyramidal Betz cells, which were also significantly reduced in ALS patients. A loss of the GABA receptor α1 subunit mRNA was also identified in the primary motor cortex of 5 ALS patients, when compared to age-matched control patient post-mortem tissue (Petri et al. 2003). However, levels of the GABA synthesizing enzyme glutamic acid decarboxylase (GAD) were unchanged. Reconfiguration of GABA subunit composition in ALS patients was suggested to be the cause of this.

One line of convincing evidence in favour of spinal cord interneuronopathy in ALS was reported in a study using a SOD1 zebrafish model (McGown et al. 2013). This model employed a heat shock protein 70 gene conjugated to a DsRed reporter that was inserted adjacent to the wild-type or mutant SOD1 gene. Interestingly, the earliest heat shock

response was found in discrete populations of predominantly glycinergic spinal cord INs. Importantly, these stress events occurred even before MN stress was visualised and within a few days after birth. A loss of spontaneous glycinergic current input onto MNs was also identified, which preceded MN stress and neuromuscular junction degeneration. Whilst this study provides important evidence for interneuronopathy in ALS, the primary readout was heat shock response, which is unlikely to be the earliest pathological event observed in ALS.

Another important consideration is that selective vulnerability has also been observed within subsets of MNs themselves (Hedlund et al. 2010; Kanning et al. 2010; Brockington et al. 2013; Nijssen et al. 2017). In numerous models of ALS, it has been shown that FF MNs are the earliest and most affected MN subtype; displaying synaptic decoupling and loss at the NMJ even at pre-symptomatic stages and before onset in FFR or SFR MNs (Frey et al. 2000; Hegedus et al. 2007). Importantly, these FF MNs have a greater number of inhibitory pre-synaptic contacts than any other MN subtype (Allodi et al. 2020). Subsequent studies using SOD1 G93A transgenic mice revealed a pre-symptomatic decoupling of INs from these highly vulnerable MNs in the spinal cord (Casas et al. 2013). This was evaluated through a reduction in cholinergic C-boutons from INs onto MNs. Interestingly, synaptic decoupling was also temporally linked to the accumulation of TAR-DNA binding protein-43 (TDP-43) within the nucleus of MNs and the acquisition of an oxidative stress phenotype through iNOS upregulation in G93A mice (Casas et al. 2013). However, it should be noted that TDP-43 accumulation in the nucleus is not recognised as a pathological hallmark of ALS. Subsequent evaluation of this decoupling phenomenon was undertaken in a separate study, revealing that V1 domain glycinergic Renshaw cells were the predominant IN subtype affected in this G93A mouse model (Allodi et al. 2020). It was also determined that G93A mice exhibited specific locomotor defects manifesting as a loss of speed and reduction in stride length. Perhaps more intriguing was that these locomotor deficits were phenocopied with selective loss of V1 domain interneurons through the use of inhibitory DREADDs targeting the transcription factor EN-1. It is also important to note that V1 Renshaw cells did not display a death phenotype in the same G93A mouse model, even by late-stage disease. This is an important finding in itself as it provides evidence for a non-cell-autonomous effect of ALS mutant INs on MNs and also provides an example of neuronal subtype-

specific vulnerability in ALS. Furthermore, these studies give cause to re-evaluate the use of general excitability dampening drugs such as Riluzole, since their modest efficacy could be a result of non-specific dampening of spinal cord IN activity. It should be noted; however, that Riluzole and the antioxidant Edaravone are the only disease modifying therapeutics currently in use (Jaiswal. 2019).

VCP mutations account for ~2% of all fALS cases and have also been identified in sALS patients (Johnson et al. 2010; Abramzon et al. 2012). Importantly, patients harbouring ALS-causing VCP mutations display the key pathological hallmark of ALS, with TDP-43 mislocalisation from the nucleus to the cytoplasm where it then accumulates to form cytoplasmic aggregates (Neumann et al. 2007; Inoue et al. 2018). Indeed, TDP-43 pathology occurs in 97% of all ALS cases. A subsequent R155H N-terminal domain mutant knock-in transgenic mouse model displayed significant ALS-related TDP-43 pathology, with additional ALS-related behavioural phenotypes manifesting through significant and progressive muscle weakness (Nalbandian et al. 2013). Furthermore, using the hiPSC-directed MN differentiation strategy detailed in Chapter 3, ALS-causing R155C and R191Q VCP mutations were found to cause a significant nuclear-to-cytoplasmic mislocalisation of TDP-43 at day 21 (Hall et al. 2017) and day 24 MNs (Harley & Patani. 2020). FUS is another RBP that is mislocalised and forms cytoplasmic aggregates in FUS-mutant ALS patients (Vance et al. 2009; Kwiatkowski et al. 2009). Interestingly; cytoplasmic mislocalisation of FUS, but not aggregation was observed in day 7 and day 14 MNs using the same hiPSC-derived protocol detailed in Chapter 3 (Tyzack et al. 2019). FUS mislocalisation was also detected in a mouse model of VCP-mutant ALS and sporadic post-mortem tissue, indicating that this may be a more prevalent ALS-related pathology. Indeed, FUS mislocalisation was also identified at later timepoints in VCP-mutant MNs using this protocol and at day 24 (Harley & Patani. 2020; Harley et al. 2020).

An aberrant program of alternative splicing (AS) was also observed during early neural differentiation of hiPSC-derived MNs in VCP, FUS and SOD1 lines (Luisier et al. 2018. Indeed, these AS events predominantly manifested through intron retention (IR) events, that were aberrantly increased in ALS mutant, when compared to control lines. The most significantly differentially upregulated intron retained transcripts (IRT)s were found in

intron 9 of SFPQ, intron 6 of FUS and intron 6 of DDX39A. Interestingly, the SFPQ protein was subsequently found to directly bind to the SFPQ IRT (Tyzack et al. 2020), with the SFPQ protein exhibiting cytoplasmic mislocalisation from the nucleus (Tyzack et al. 2018). Furthermore, cytoplasmic IRTs were found to exhibit an increased binding affinity for RBPs that are commonly mislocalised in ALS, including TDP-43 and FUS (Tyzack et al. 2021). Separate studies have further validated this phenotype in ALS and Alzheimer's disease post-mortem tissue, and as a product of normal aging (Tyzack et al. 2018; Adusumalli et al. 2019; Hogan et al. 2020) Taken together, these studies support an intriguing hypothesis, whereby an increased abundance of IRTs bind to and sequester RBPs, resulting in their translocation from the nucleus to the cytoplasm. Indeed, this could lead to a nuclear loss of function and/or altered cytoplasmic function. In a separate study, transcriptomic and proteomic analysis of nuclear and cytoplasmic fractions of control and VCP-mutant astrocytes revealed a striking decrease in IRTs in SOD1, C9orf72 and VCP-mutant ALS lines (Ziff et al. 2021). Furthermore, transcripts that exhibited a decrease in IRTs displayed a significant upregulation in translation and subsequent expression. This was especially prominent with nuclear IRTs that were significantly downregulated with ALS mutation, resulting in enhanced nonsense mediated decay and a subsequent increase in cytoplasmic transcripts expressing glial reactivity markers. Taken together, these findings highlight cell type-specific mechanisms of vulnerability in ALS mediated through AS and resulting in an altered cellular phenotype and/or vulnerability.

5.2 Aims

Against this background, hiPSC-derived cell types provide clear utility as a powerful disease modelling platform. More specifically within ALS research, this hiPSC-derived VCP-mutant model has been shown to recapitulate key pathological hallmarks of ALS that could be crucial for guiding the development of novel therapeutics (Hall et al. 2017; Tyzack et al. 2019). Furthermore, this model has also been used to identify a novel developmental pathological hallmark of ALS, that was subsequently validated in animal models and post-mortem tissue (Tyzack et al. 2018; Tyzack et al. 2020). In addition, non-cell autonomous mechanisms of degeneration were also revealed, implicating the role of astrocytes in ALS pathogenesis (Hall et al. 2017; Ziff et al. 2021). As such, the generation

of hiPSC-derived INs, robustly characterised in Chapter 4, presents a unique opportunity to interrogate mechanisms of cell type-specific vulnerability in ALS, and in comparison to the previously studied hiPSC-derived MNs that display ALS-related pathology. Importantly, these hiPSC-derived INs have the same axial identity as their ventral MN counterparts, but are molecularly distinct, being derived from more dorsal neural tube domains.

Therefore, the specific aims of this chapter are to:

1. Examine whether VCP mutation disrupts the specification of dorsal INs, when compared to control counterparts.
2. Assess TDP-43 and FUS RBP mislocalisation in VCP-mutant and control INs and MNs.
3. Investigate SFPQ intron 9, FUS intron 6 and DDX39A intron 6 IRTs in VCP-mutant and control INs and MNs in a temporal manner.

5.3 Results

5.3.1 Altered specification of interneurons in VCP-mutant ALS lines

In order to assess cell type-specific vulnerability in ALS with regards to dorsal INs and ventral MNs, 4 VCP lines were employed from 2 separate patients (2 lines per patient), harbouring an R191Q or R155C mutation. Whilst the generation of hiPSC-derived INs was robustly demonstrated in control hiPSC lines in Chapter 4, detailed characterisation of dorsal IN specification was next carried out in these 4 VCP-mutant hiPSC lines, in comparison to controls and in order to assess any mutation-driven changes in subtype specification. qPCR analysis for dorsal neural tube precursor markers including DBX2, PAX3 and PAX7 at NPC day 18 NPC timepoints revealed no significant difference between control and VCP lines (Figure 5.1). However, a trend towards an increase in PAX6 mRNA expression was detected in VCP-mutant ALS lines, when compared to control. Conversely, no significant difference was observed in mRNA expression levels of the dorsal-most dP1-3 marker OLIG3.

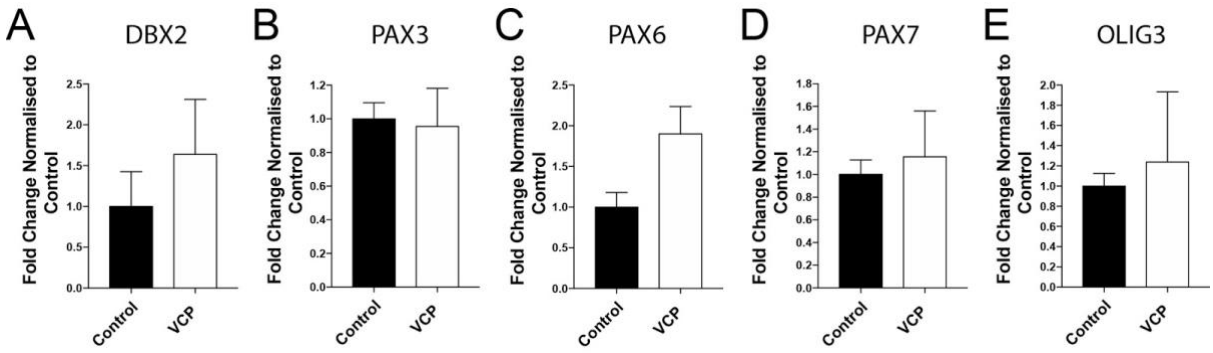

Figure 5.1 Control and VCP-mutant ALS lines acquire dorsal progenitor marker expression

Bar plots depicting mRNA expression levels of the mid-neural tube domain marker - DBX2 (A), dorsal domain markers - PAX3, PAX6 and PAX7 (B, C, D), and dorsal dP1-3 domain marker - OLIG3 (E) in control and VCP-mutant ALS lines in day 18 NPCs patterned with RA only, as assessed by qPCR. Each sample was normalised over its GAPDH expression level and control and VCP-mutant lines were normalised against the mean of the control lines (as indicated on each graph). n=2 per cell line with 5 independent control lines (CTRL1-6) and 4 VCP-mutant cell lines (GLiA, GLiB, CB1D, CB1E) used. Data is plotted per line, with error bars displayed as mean ± SEM. p value calculated using unpaired two-tailed t-test with Welch's correction.

Quantitative immunocytochemistry (qICC) was next employed to further validate these findings. Interestingly, whilst qICC results for the dorsal domain marker PAX3 revealed similar levels of upregulation in the percentage of PAX3 positive NPCs in VCP lines at day 18, there was a small but significant increase when compared to control (~85% in control, ~87% in VCP lines) (Figure 5.2). Moreover, no significant difference was observed in the proportion of cells expressing NKX6.1 (~4% in control, ~3% in VCP lines) indicating little / no ventralisation of RA only treated NPCs (Figure 5.2). In order to further assess differences in dorsal domain specification, immunostaining for the dP1-3 dorsal domain marker OLIG3 was carried out. This revealed low expression levels of OLIG3 in day 18 NPCs in both control (~4%) and VCP (~3%) lines that were not statistically different (Figure 5.3). Taken together, these data suggest that RA only treated control and VCP day 18 NPCs achieve a similar dorsal neural tube progenitor domain identity.

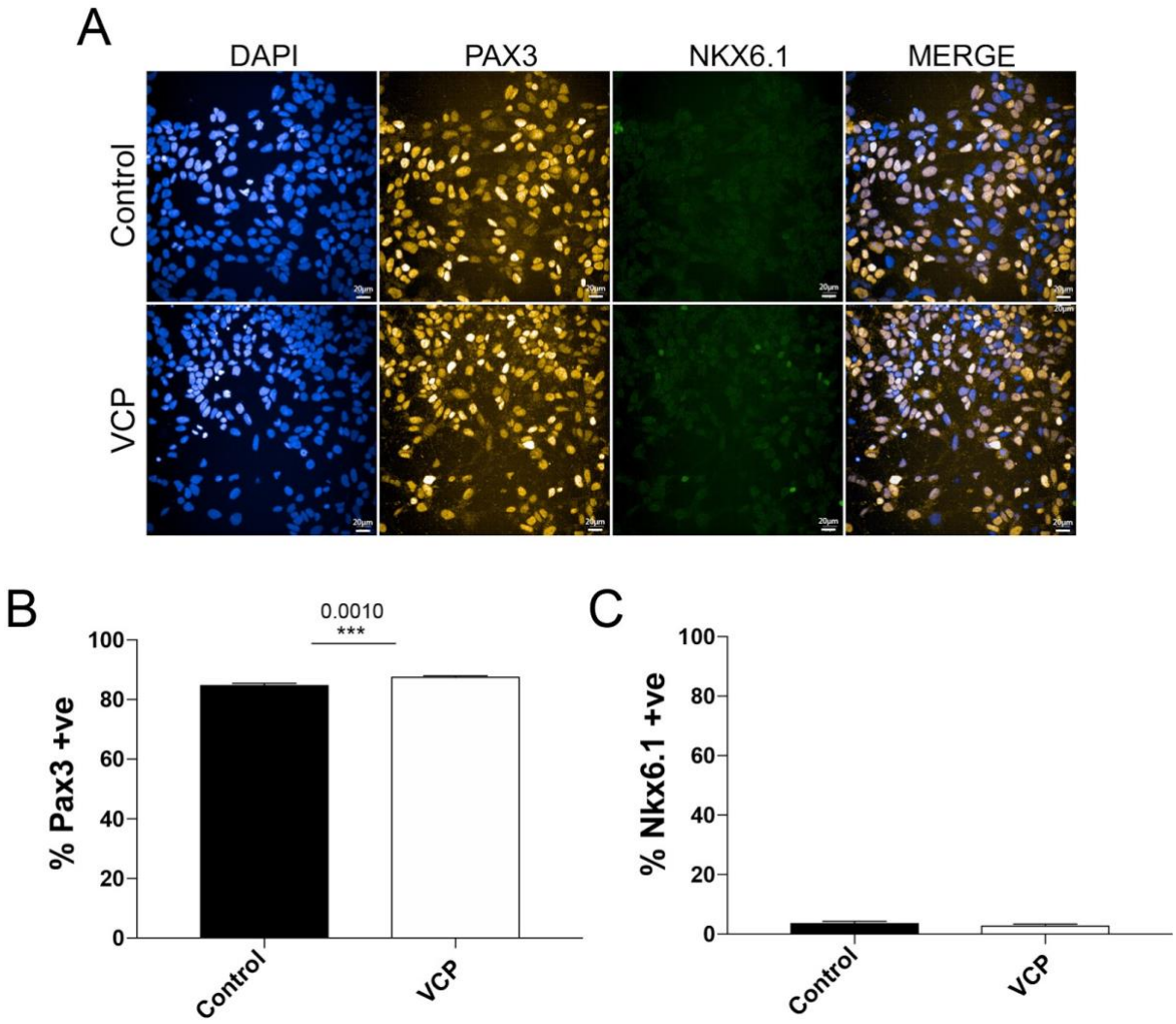

Figure 5.2 Expression of PAX3 and NKX6.1 in control and VCP-mutant NPCs

(A) Representative immunocytochemistry images of the CTRL3 control line and VCP-mutant ALS line GLiA in day 18 NPCs patterned with RA only, using the cellular marker of dorsal neural tube progenitors - PAX3 and the ventral P3, pMN and P2 domain marker - NKX6.1. Scale bar set at 20 μm. (B) Bar plot representing quantitative immunocytochemistry data for the percentage of cells expressing PAX3 in control and VCP day 18 NPCs. n=2 across 5 different control and 4 VCP lines. (C) Bar plot representing quantitative immunocytochemistry analysis for the percentage of cells expressing PAX3 in control and VCP day 18 NPCs. n=2 per cell line with 5 independent control lines (CTRL1, 3-6) and 4 VCP-mutant cell lines (GLiA, GLiB, CB1D, CB1E) used. Data is plotted per well, with error bars displayed as mean ± SEM. p values calculated using unpaired two-tailed t-test with Welch's correction, *** represents $p < 0.001$.

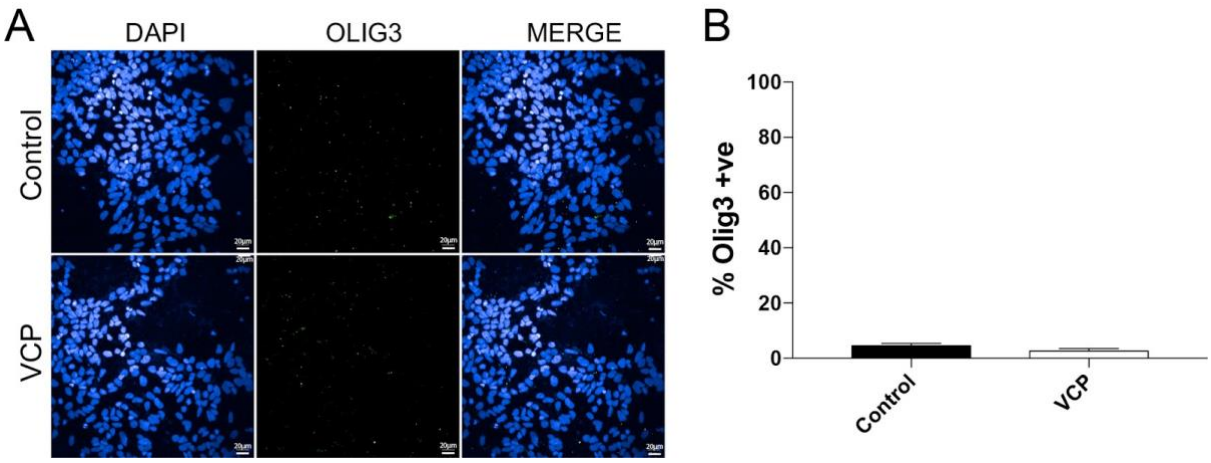

Figure 5.3 Expression of dP1-3 neural tube marker OLIG3 in control and VCP NPCs

(A) Representative immunocytochemistry images of the CTRL5 control line and VCP-mutant ALS line CB1D in day 18 NPCs patterned with RA only, using the cellular marker of dorsal dP1-3 domain progenitors - OLIG3. Scale bar set at 20 μm. (B) Bar plot representing quantitative immunocytochemistry data for the percentage of cells expressing OLIG3 in control and VCP day 18 NPCs. n=2 per cell line with 5 independent control lines (CTRL1, 3-6) and 4 VCP-mutant cell lines (GLiA, GLiB, CB1D, CB1E) used. Data is plotted per well, with error bars displayed as mean ± SEM. p value calculated using unpaired two-tailed t-test with Welch's correction.

Next, control and VCP lines were assessed for upregulation of rostral-caudal and post-mitotic IN markers at day 25 following terminal differentiation for 7 days in CE. qPCR analysis for HOX markers delineating different spinal regions revealed no significant differences between control and VCP lines, indicating similar rostral-caudal axial identities (Figure 5.4). Furthermore, no significant difference was found in mRNA expression levels of β3-tubulin, suggesting that control and VCP lines achieve similar levels of neuronal fate specification (Figure 5.5A). Interestingly; however, a significant increase in mRNA expression of the dorsal post-mitotic markers LHX5 and LBX1 was observed in day 25 post-mitotic VCP-mutant populations, when compared to control (Figure 5.5B&C). This was further validated using qICC, where a significant increase in the proportion of neurons expressing LHX5 was observed in day 25 post-mitotic VCP-mutant lines (~59%), when compared to control (~39%) (Figure 5.6). Collectively, these data suggest that, whilst dorsal NPC fate specification is not altered with VCP mutation,

there is a significant enrichment of LHX5 subpopulations of dorsal INs in VCP-mutant ALS lines following terminal differentiation, when compared to control.

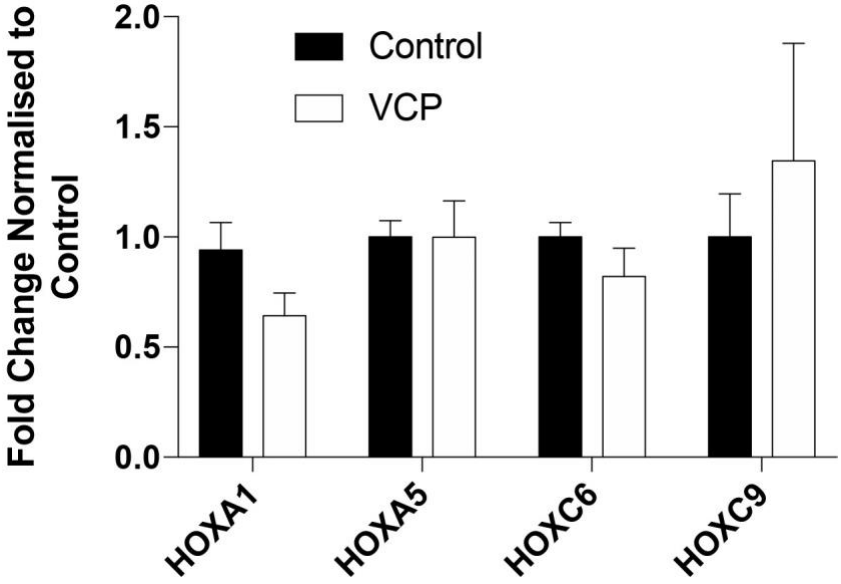

Figure 5.4 Axial identity of terminally differentiated dorsal interneurons in control and VCP lines

(A) Bar plot showing mRNA expression levels of a range of spinal cord-spanning HOX genes in control and VCP-mutant lines in day 25 RA only patterned post-mitotic neurons, as assessed using qPCR. Each sample was normalised over its own GAPDH level and further normalised against the average of controls. n=2 per cell line with 5 independent control lines (CTRL1-6) and 4 VCP-mutant cell lines (GLiA, GLiB, CB1D, CB1E) used. Error bars displayed as mean ± SEM. p value assessed using unpaired two-tailed t-test with Welch's correction.

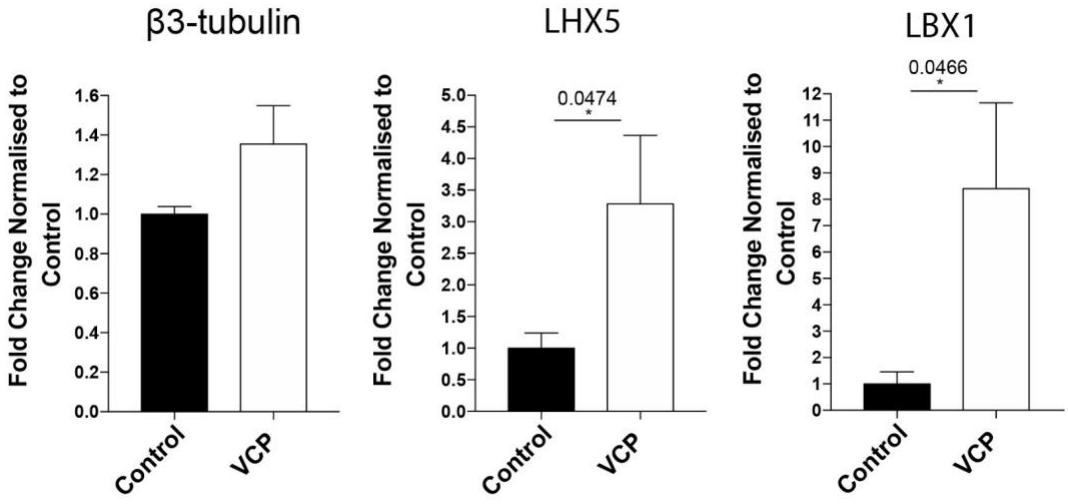

Figure 5.5 Upregulation of post-mitotic dorsal spinal cord markers in control and VCP dorsal populations

(A) Bar plots depicting mRNA expression levels of the pan-neuronal marker - β3-tubulin (A) and post-mitotic dorsal domain markers - LHX5 (B) and LBX1 (C) in control and VCP-mutant ALS lines at day 25 following patterning with RA only and 7 days of terminal differentiation in CE, as assessed by qPCR. Each sample was normalised over its GAPDH expression level and control and mutant lines were normalised against the mean of the control lines (as indicated on each graph). n=2 per cell line with 6 independent control lines (CTRL1-6) and 4 VCP-mutant cell lines (GLiA, GLiB, CB1D, CB1E) used. Data is plotted per line, with error bars displayed as mean ± SEM. p value calculated using unpaired two-tailed t-test with Welch's correction * represents P < 0.05.

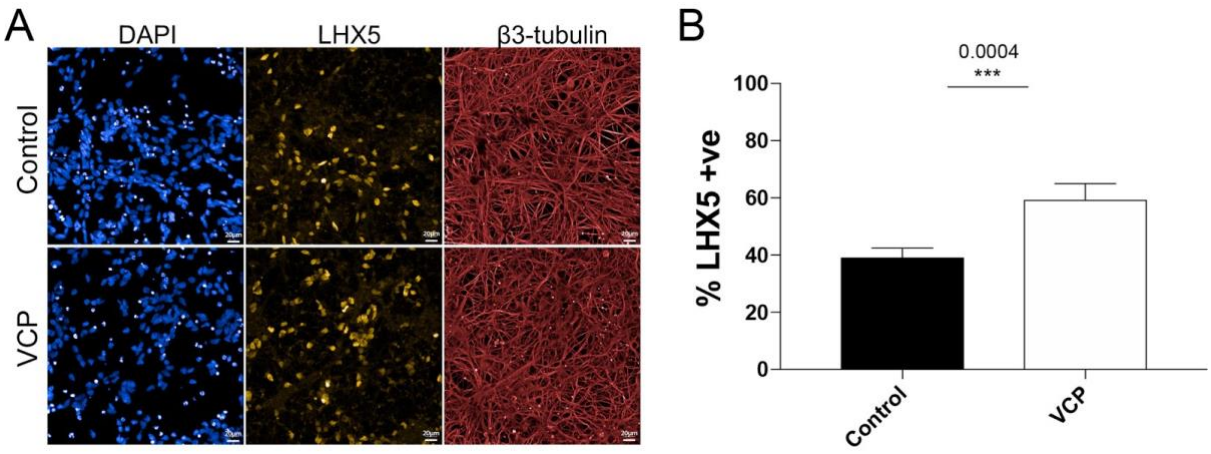

Figure 5.6 Protocol for hiPSC-derived motor neurons and strategy for generating dorsal interneurons

(A) Representative immunocytochemistry images of the CTRL5 control line and VCP-mutant ALS line GLiA using the mid-dorsal neural tube domain marker - LHX5 in control and VCP-mutant ALS lines at day 25 following patterning with RA only and terminal differentiation for 7 days in CE. Scale bar set at 20 μm. (B) Quantitative immunocytochemistry for LHX5. n=2 per cell line with 5 independent control lines (CTRL1, 3-6) and 4 VCP-mutant cell lines (GLiA, GLiB, CB1D, CB1E) used. Data is plotted per well, with error bars displayed as mean ± SEM. p value calculated using unpaired two-tailed t-test with Welch's correction, *** represents p < 0.001.

5.3.2 RNA binding protein mislocalisation in VCP-mutant motor neurons and interneurons

RBP mislocalisation from the nucleus to the cytoplasm is a key pathological feature of ALS and has been observed in numerous ALS models and post-mortem tissue. The main RBPs implicated in ALS include TDP-43 and FUS, with TDP-43 exhibiting additional cytoplasmic aggregation in 97% of all ALS cases (Neumann et al. 2006). Most recently it was shown that FUS (Tyzack et al. 2019; Harley & Patani. 2020) and TDP-43 (Hall et al. 2017; Harley & Patani. 2020) were mislocalised from the nucleus to the cytoplasm in a VCP model of ALS using the hiPSC-derived MN protocol described in Chapter 3. Separately, a comprehensive characterisation of RBP mislocalisation, including their unique responses to heat, osmotic and oxidative stress was further detailed by Harley et al (2020). In this study, a novel analysis pipeline was employed by defining a nuclear and perinuclear region, restricted by a cell mask (detailed in Methods section 2.4.2). The mean average intensity within this perinuclear region was employed as a representative measure of the neuronal soma and enabled the calculation of a nuclear-to-cytoplasmic ratio (N/C). It was subsequently observed that TDP-43 and FUS exhibit a predominantly nuclear localisation under basal conditions in hiPSC-derived MNs using the differentiation protocol described in Chapter 3 (Harley & Patani. 2020). Furthermore, this analysis pipeline also revealed that VCP-mutant hiPSC-derived MNs exhibit a decrease in TDP-43 and FUS N/C ratio (Harley & Patani. 2020).

Therefore, in order to assess cell type-specific vulnerability in ALS with regards to RBP mislocalisation in INs, the same experimental design and analysis pipeline was applied to populations of control and VCP-mutant hiPSC-derived INs, with MNs used as a positive control (Harley & Patani. 2020). N/C ratios were assessed in >10,000 INs and MNs. Consistent with previous findings, a significant decrease in N/C ratio for TDP-43 was observed in VCP-mutant MNs at day 24 timepoints, when compared to control (Figure 5.7A&B). In contrast, no significant difference in N/C ratio was observed for TDP-43 in IN cultures between VCP-mutant lines and controls (Figure 5.7C&D). Furthermore, FUS also displayed a similar pattern of N/C mislocalisation in MN cultures, with a significant decrease in N/C ratio in VCP-mutant MNs at day 24 timepoints, when compared to controls (Figure 5.8A&B). However, as with TDP-43 in day 24 INs, no

significant difference in FUS N/C mislocalisation was also observed in these populations. Taken together, these data further validate and confirm that RBP mislocalisation can be identified in this VCP-mutant hiPSC-derived MN model. Moreover, these findings demonstrate that RBP mislocalisation at this timepoint is a selective pathology intrinsic to MNs and were subsequently not observed as a pathological feature of hiPSC-derived INs. This highlights the potential for hiPSC-derived culture models to recapitulate features of cell type-specific vulnerability *in vitro* and could provide an important platform to study this hallmark in further mechanistic detail.

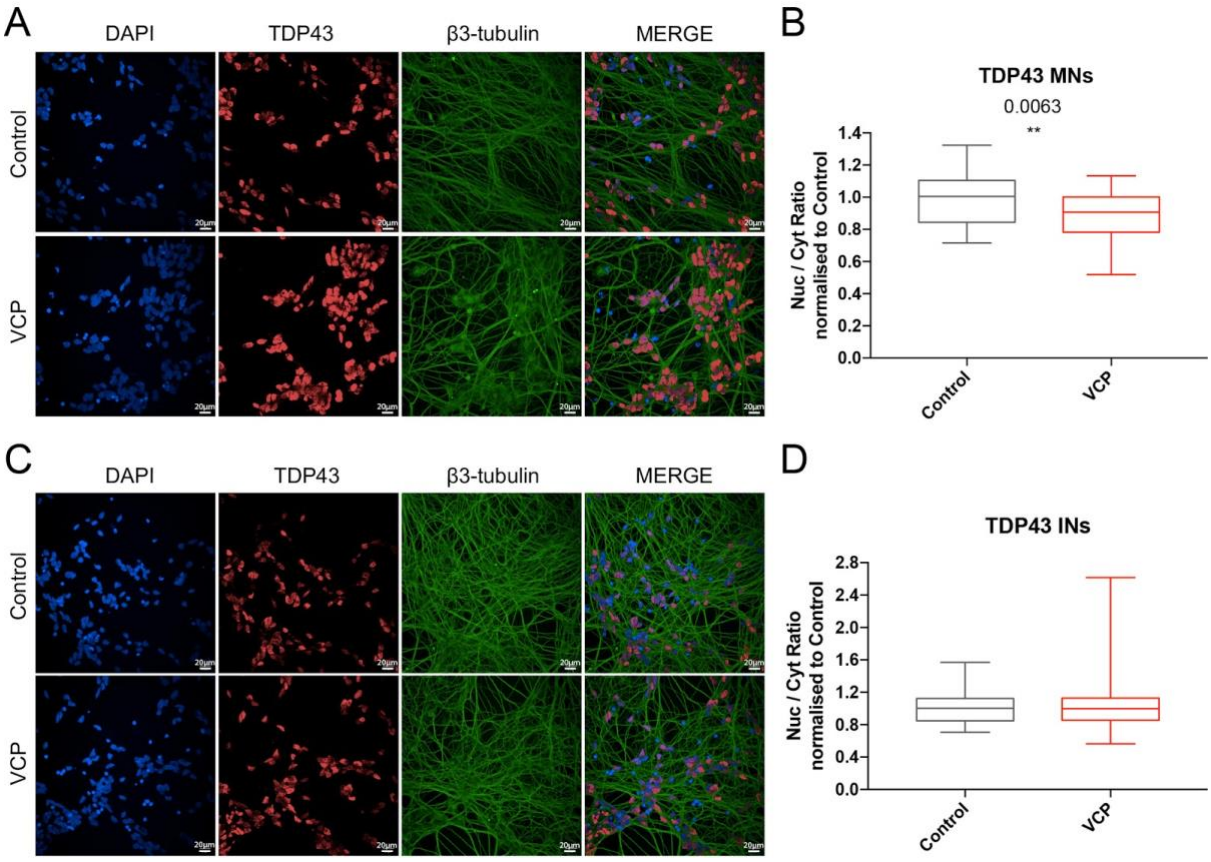

Figure 5.7 TDP-43 nuclear/cytoplasmic localisation in control and VCP motor neurons and interneurons

(A) Representative immunocytochemistry images of the CTRL3 control line and VCP-mutant ALS line GLiA using the cellular marker of TDP-43 in control and VCP MNs at day 24, following patterning in RA + SHH and terminal differentiation for 6 days in CE. Scale bar set at 20 μm. (B) Box and whisker plot representing quantitative immunocytochemistry cell-by-cell analysis of the nuclear/cytoplasmic ratio of TDP-43 in >10,000 neurons. (C) Representative immunocytochemistry images using the cellular marker of TDP-43 in control and VCP INs at day 24, following patterning in RA only and terminal differentiation for 6 days in CE. Scale bar set

at 20 μm. (D) Box and whisker plot representing quantitative immunocytochemistry cell-by-cell analysis of the nuclear/cytoplasmic ratio of TDP-43 in >10,000 neurons. Data is plotted per well, with error bars displayed as mean ± minimum and maximum values. n=3 for MNs and INs, per cell line with 5 independent control lines (CTRL1, 3-6) and 4 VCP-mutant cell lines (GLiA, GLiB, CB1D, CB1E) used. p value calculated using unpaired two-tailed t-test with Welch's correction, ** represents $p < 0.01$.

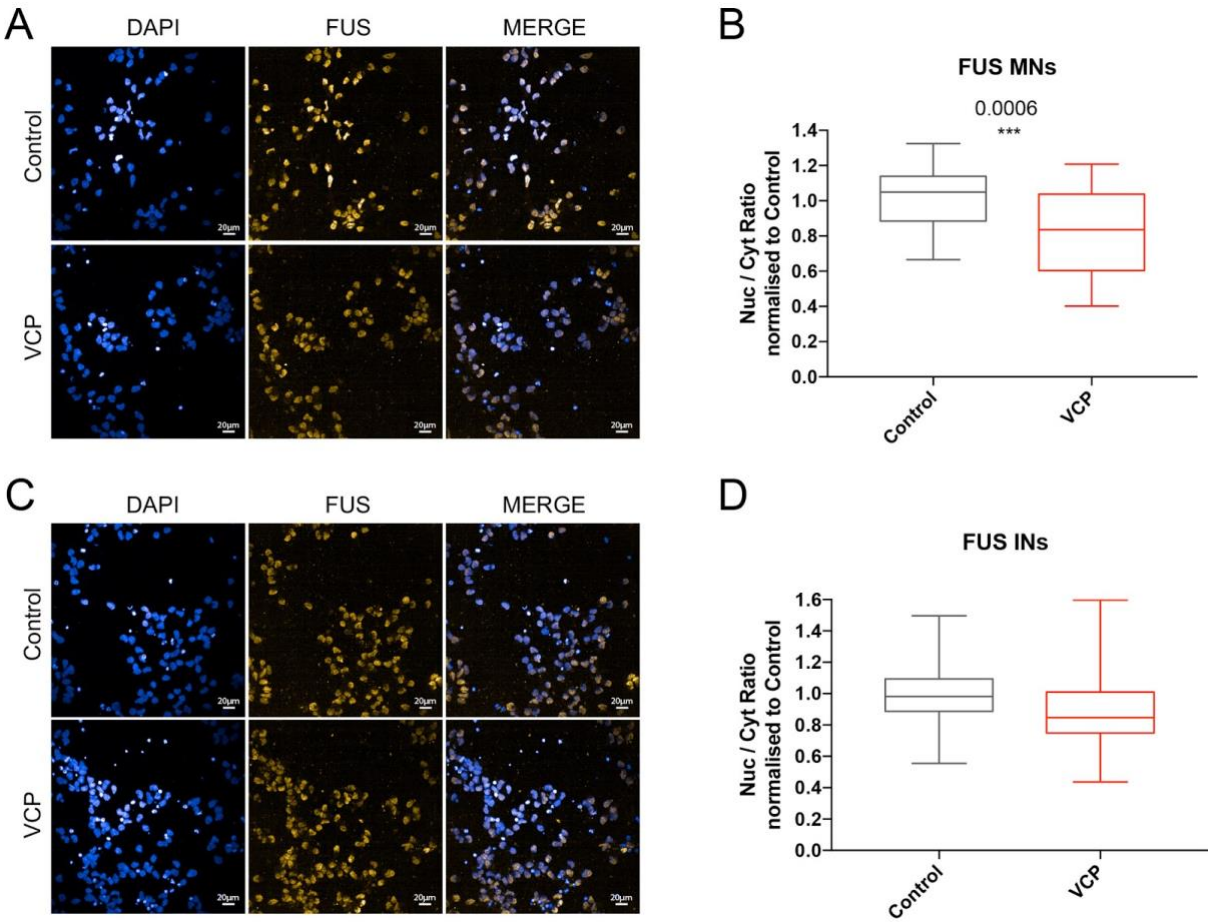

Figure 5.8 FUS nuclear/cytoplasmic localisation in control and VCP motor neurons and interneurons

Representative immunocytochemistry images of the CTRL1 control line and VCP-mutant ALS line GLiA using the cellular marker of FUS in control and VCP MNs at day 24, following patterning in RA + SHH and terminal differentiation for 6 days in CE. Scale bar set at 20 μm. (B) Box and whisker plot representing quantitative immunocytochemistry cell-by-cell analysis of the nuclear/cytoplasmic ratio of FUS in >10,000 neurons. (C) Representative immunocytochemistry images using the cellular marker of FUS in control and VCP INs at day 24, following patterning in RA only and terminal differentiation for 6 days in CE. Scale bar set at 20 μm. (D) Box and

whisker plot representing quantitative immunocytochemistry cell-by-cell analysis of the nuclear/cytoplasmic ratio of FUS in >10,000 neurons. Data is plotted per well, with error bars displayed as mean ± minimum and maximum values. n=3 for MNs and INs, per cell line with 5 independent control lines (CTRL1, 3-6) and 4 VCP-mutant cell lines (GLiA, GLiB, CB1D, CB1E) used. p value calculated using unpaired two-tailed t-test with Welch's correction, *** represents $p < 0.001$.

5.3.3 Intron retention in VCP-mutant motor neurons and interneurons

As mentioned previously, a recent study highlighted an aberrant program of alternative splicing (AS), driven by the upregulation of IRTs in hiPSC-derived MNs detailed in Chapter 3 (Luisier et al. 2018). These AS defects were found to be a dominant feature of the splicing programme during early neural differentiation. Importantly, this wave of IR was observed to occur prematurely in hiPSC-derived VCP-mutant MNs (between day 7 and day 14 of the protocol). The most differentially regulated IRTs in VCP MNs were observed in SFPQ intron 9, FUS intron 6 and DDX39A intron 6 (all IRTs upregulated). Therefore, experiments were next carried out in order to i) assess the persistence of the increase IRT phenotype beyond early developmental timepoints, and ii) evaluate differences in IRT expression between MNs and INs as a potential cause of selective vulnerability. Subsequently, SFPQ intron 9, FUS intron 6 and DDX39A intron 6 IRTs were assessed in day 7 cultures, day 18 IN and MN NPCs - representing the end of patterning, and day 25 post-mitotic INs and MNs. It should be noted that, since the protocols diverge from day 7 onwards, INs and MNs were assessed separately at day 18 NPC and day 25 timepoints only.

qPCR analysis for SFPQ IRTs within intron 9 at day 7 timepoints revealed similar findings to those seen in the original study (Luisier et al. 2018); with a significant increase in IRT observed in VCP-mutant lines, when compared to controls (Figure 5.9A). In addition, a significant decrease in spliced transcript levels was found in VCP lines, coinciding with a decrease in total SFPQ levels, when compared to controls (Figure 5.9B&C). A separate analysis was also carried out, assessing the ratio of IRT/spliced transcript in order to eliminate confounding variables such as changes in total gene or spliced transcript expression levels, that could affect measures of IRT. Subsequent analysis revealed a significant increase in SFPQ IRT/spliced transcript ratio further

validating previous findings (Figure 5.9D). Next, FUS intron 6 IRTs were assessed at day 7 timepoints, revealing a significant increase in VCP-mutant lines, when compared to controls and confirming previous findings (Figure 5.10A) (Luisier et al. 2018). This coincided with a trend towards a decrease in spliced transcript levels and a significant decrease in total FUS levels in VCP-mutant lines, when compared to controls (Figure 5.10B&C). However, adjusting for these variables, a significant increase in FUS IRT/spliced transcript ratio was observed in VCP lines, supporting findings of increased FUS intron 6 IRT levels in VCP-mutant ALS lines (Figure 5.10D). Assessment of IRTs in intron 6 of DDX39A yielded similar results; however, only a trend towards an increase in IRT was observed in VCP lines (Figure 5.11A). Additionally, no change in spliced transcript levels was found, along with a trend towards a decrease in total DDX39A transcript (Figure 5.11B&C). Interestingly, a significant increase in DDX39A IRT/spliced ratio was found in VCP lines, when compared to control suggesting an increase in IRTs in intron 6 of DDX39A (Figure 5.11D). Taken together, these data support the original findings identified by Luisier et al (2018) of early aberrant IRTs in SFPQ and DDX39A in neutrally induced VCP-mutant hiPSC-derived cultures.

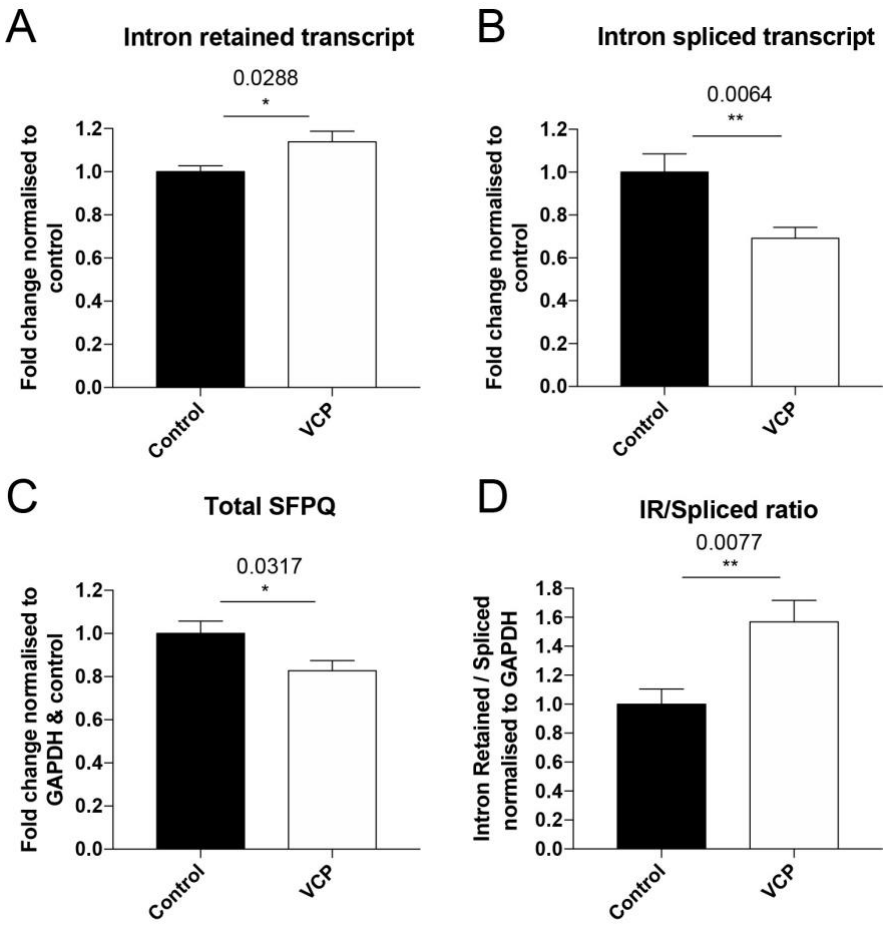

Figure 5.9 SFPQ intron retention in day 7 neuroepithelial cells

Bar plots quantifying mRNA expression levels of (A) SFPQ intron 9 retained transcript normalised over constitutive SFPQ expression and additionally to the average of controls. (B) SFPQ intron 9 spliced transcript normalised to constitutive SFPQ expression and to the average of controls. (C) Total SFPQ expression normalised to GAPDH and to the average of controls in day 7 neuroepithelial cells from control and VCP-mutant lines, as assessed by qPCR. (D) Bar plot depicting mRNA expression ratio of SFPQ intron 9 retained transcript over SFPQ spliced transcript (both normalised over their GAPDH expression) and normalised to control lines, as indicated on each graph. n=2 per cell line with 6 independent control lines (CTRL1-6) and 4 VCP-mutant cell lines (GLiA, GLiB, CB1D, CB1E) used. Data is plotted per line, with error bars displayed as mean ± SEM. p value calculated using unpaired two-tailed t-test with Welch's correction, * represents $p < 0.05$ and ** $p < 0.01$.

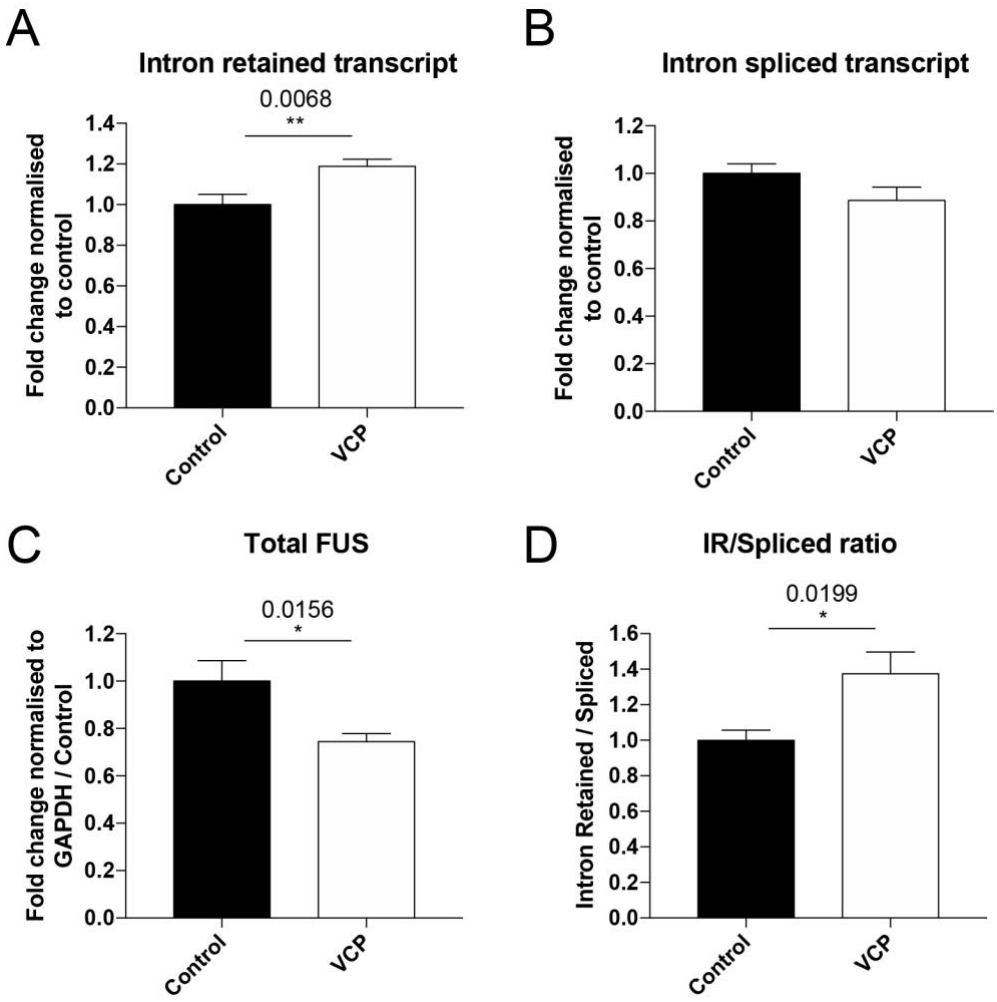

Figure 5.10 FUS intron retention in day 7 neuroepithelial cells

Bar plots quantifying mRNA expression levels of (A) FUS intron 6/7 retained transcript normalised over constitutive FUS expression and additionally to the average of controls. (B) SFPQ intron 6/7 spliced transcript normalised to constitutive FUS expression and to the average of controls. (C) Total FUS expression normalised to GAPDH and to the average of controls in day 7 neuroepithelial cells from control and VCP-mutant lines, as assessed by qPCR. (D) Bar plot depicting mRNA expression ratio of FUS intron 6/7 retained transcript and FUS spliced transcript (both normalised over their GAPDH expression) and normalised to control lines. n=2 per cell line with 6 independent control lines (CTRL1-6) and 4 VCP-mutant cell lines (GLiA, GLiB, CB1D, CB1E) used. Data is plotted per line, with error bars displayed as mean ± SEM. p value calculated using unpaired two-tailed t-test with Welch's correction, * represents $p < 0.05$ and ** $p < 0.01$.

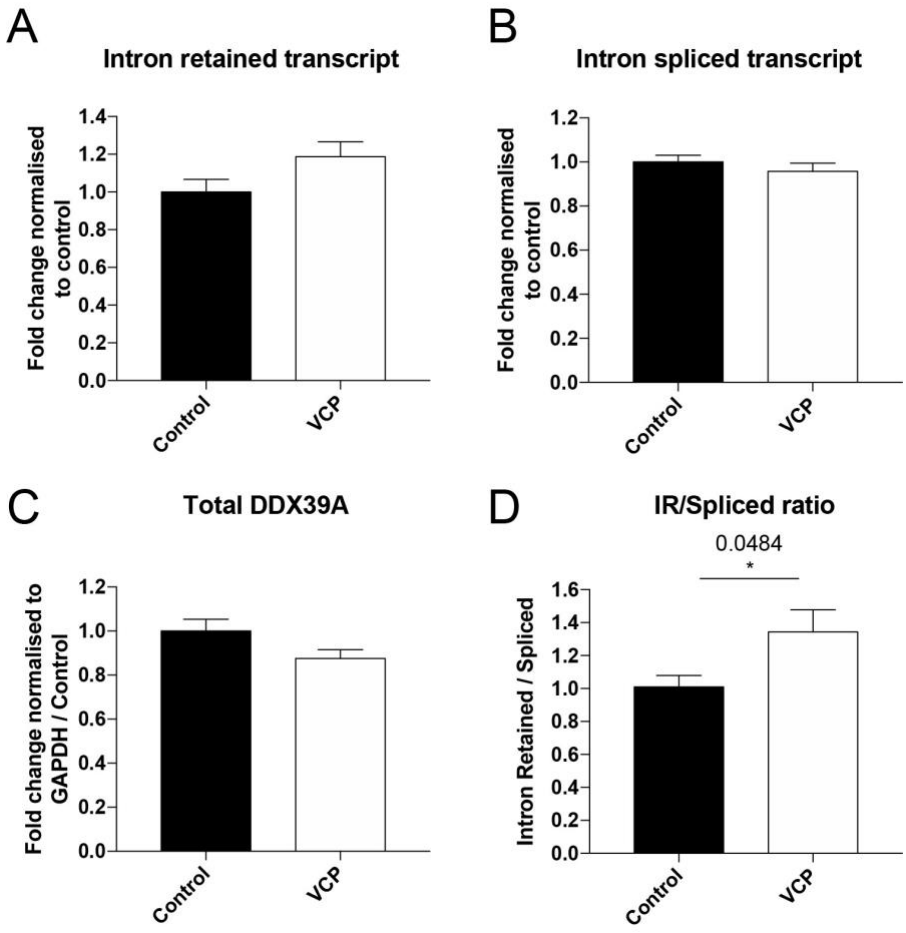

Figure 5.11 DDX39A intron retention in day 7 neuroepithelial cells

Bar plots quantifying mRNA expression levels of (A) DDX39A intron 6 retained transcript normalised over constitutive DDX39A expression and additionally to the average of controls. (B) DDX39A intron 6 spliced transcript normalised to constitutive DDX39A expression and to the average of controls. (C) Total DDX39A expression normalised to GAPDH and to the average of controls in day 7 neuroepithelial cells from control and VCP-mutant lines, as assessed by qPCR. (D) Bar plot depicting mRNA expression ratio of DDX39A intron 6 retained transcript and DDX39A spliced transcript (both normalised over their GAPDH expression) and normalised to control lines, as indicated on each graph. n=3 per cell line with 6 independent control lines (CTRL1-6) and 4 VCP-mutant cell lines (GLiA, GLiB, CB1D, CB1E) used. Data is plotted per line, with error bars displayed as mean ± SEM. p value calculated using unpaired two-tailed t-test with Welch's correction, * represents $p < 0.05$.

Whilst the findings of the original study specified the aberrant program of AS between days 7 and 14, the end of patterning for IN and MN NPCs is at day 18, whereby NPCs are then terminally differentiate into neurons. Therefore, the same experimental paradigm

and analysis pipeline were applied to day 18 IN and MN NPC cultures, whereby the full course of NPC fate specification has taken place and ventral and dorsal NPCs fully characterised (see Chapters 3 and 4). In contrast to observations on day 7, day 18 IN NPCs displayed a seemingly reversed SFPQ IR profile. This included a trend towards a decrease in SFPQ intron 9 IRT, coinciding with an increase in spliced transcript and total SFPQ gene expression in VCP lines, when compared to controls (Figure 5.12A-C). Additionally, the IR/spliced transcript ratio was significantly decreased in VCP lines, when compared to controls (Figure 5.12D). Interestingly, the differences seen in day 18 IN NPCs appeared to be mirrored in day 18 MN NPCs with trends towards a difference in VCP and control lines, including a decrease in IR levels, increased spliced transcript expression, increased total SFPQ levels and IR/spliced transcript ratio (Figure 5.12E-H). However, these trends failed to reach significance. This could suggest some form of compensatory measure, following the earlier AS aberrancies. A similar pattern was also observed for FUS intron 6 IRT splicing events in day 18 IN NPCs. However, only a trend towards a decrease in FUS IRT was detected in VCP lines compared to control, along with no significant differences in spliced transcript, total FUS mRNA expression levels, and only a trend towards a decrease in FUS IRT/spliced ratio (Figure 5.13A-D). This was mirrored in day 18 MNs, which also displayed insignificant differences between VCP and control lines (Figure 5.13E-H). Assessment of DDX39A IRTs at day 18 NPC timepoints revealed a much ‘dampened’ response, with no significant differences between control and VCP lines in both INs and MNs and across all mRNA expression levels and ratios (Figure 5.11). This suggests that aberrant IRTs in DDX39A intron 6 appeared to normalise by day 18 NPC timepoints in both INs and MNs.

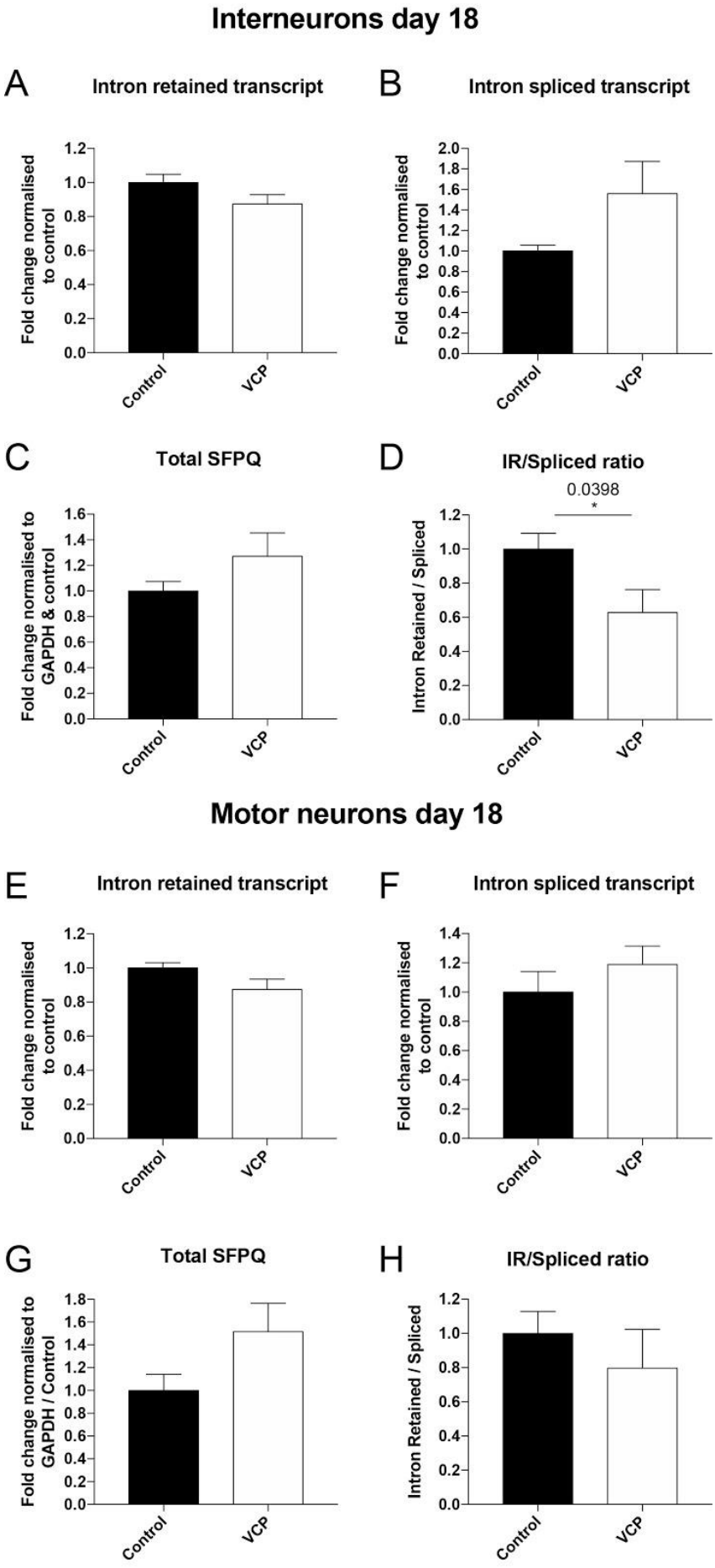
Interneurons day 18
A
Intron retained transcript
Fold change normalised to control
Control
VCP
B
Intron spliced transcript
Fold change normalised to control
Control
VCP
C
Total SFPQ
Fold change normalised to GAPDH & control
Control
VCP
D
IR/Spliced ratio
0.0398
*
Intron Retained / Spliced
Control
VCP
Motor neurons day 18
E
Intron retained transcript
Fold change normalised to control
Control
VCP
F
Intron spliced transcript
Fold change normalised to control
Control
VCP
G
Total SFPQ
Fold change normalised to GAPDH / Control
Control
VCP
H
IR/Spliced ratio
Intron Retained / Spliced
Control
VCP

Figure 5.12 SFPQ intron retention in day 18 motor neuron and interneuron NPCs

Bar plots quantifying day 18 IN NPC mRNA expression levels of (A) SFPQ intron 9 retained transcript normalised over constitutive SFPQ expression and additionally to the average of controls. (B) SFPQ intron 9 spliced transcript normalised to constitutive SFPQ expression and to the average of controls. (C) Total SFPQ expression normalised to GAPDH and to the average of controls, in VCP-mutant lines compared to controls, as assessed by qPCR. (D) Bar plot depicting day 18 IN NPC mRNA expression ratio of SFPQ intron 9 retained transcript and SFPQ spliced transcript (both normalised over their GAPDH expression) and normalised to control lines, as indicated on each graph. Bar graphs quantifying day 18 MN NPC mRNA expression levels of (E) SFPQ intron 9 retained transcript normalised over constitutive SFPQ expression and additionally to the average of controls. (F) SFPQ intron 9 spliced transcript normalised to constitutive SFPQ expression and to the average of controls. (G) Total SFPQ expression normalised to GAPDH and to the average of controls, in VCP-mutant lines compared to controls, as assessed by qPCR. (H) Bar plot depicting day 18 MN NPC mRNA expression ratio of SFPQ intron 9 retained transcript and SFPQ spliced transcript (both normalised over their GAPDH expression) and normalised to control lines, as indicated on each graph. n=2 per cell line with 6 independent control lines (CTRL1-6) and 4 VCP-mutant cell lines (GLiA, GLiB, CB1D, CB1E) used. Data is plotted per line, with error bars displayed as mean ± SEM. p value calculated using unpaired two-tailed t-test with Welch's correction * represents $p < 0.05$.

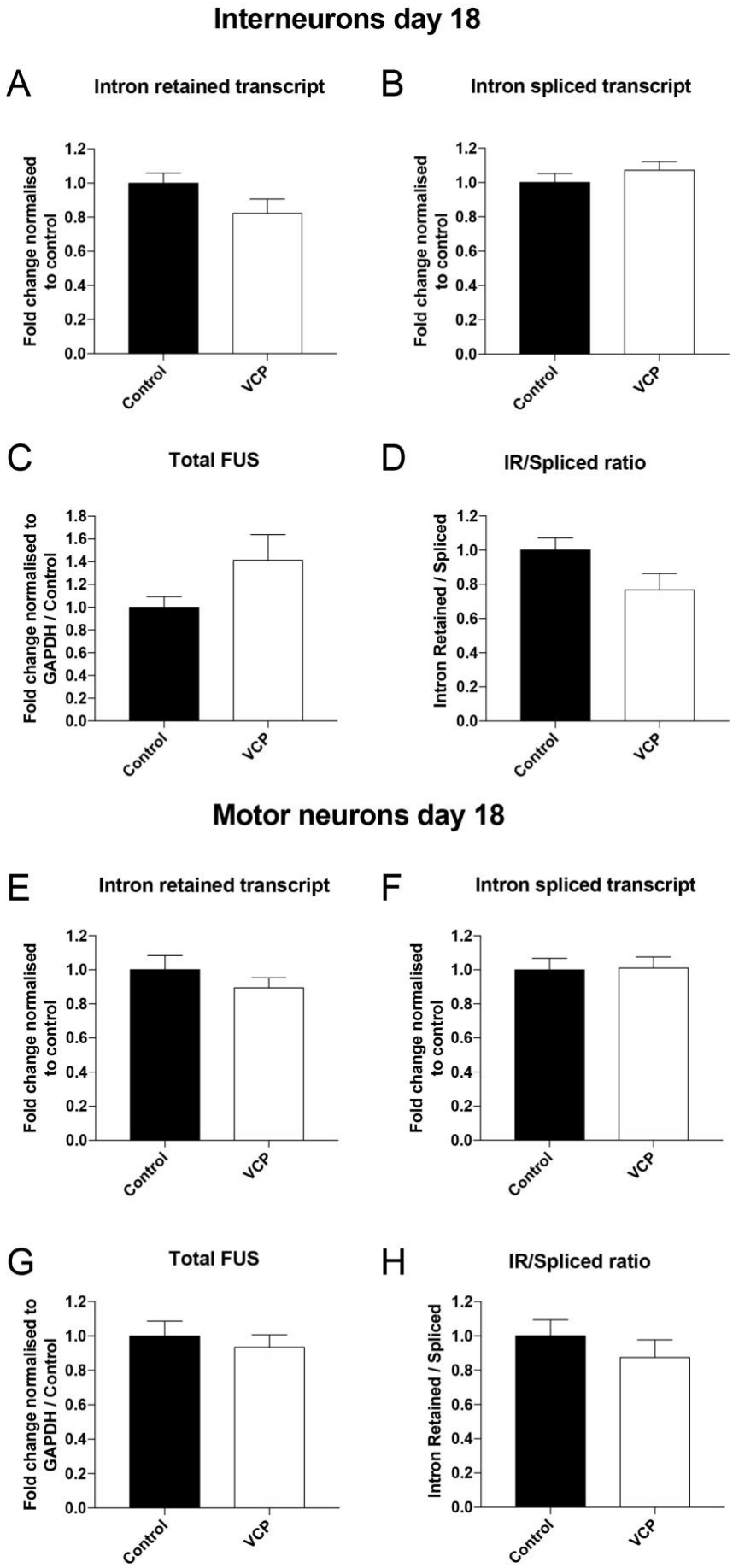
Interneurons day 18
A
Intron retained transcript
Fold change normalised to control
B
Intron spliced transcript
Fold change normalised to control
C
Total FUS
Fold change normalised to GAPDH / Control
D
IR/Spliced ratio
Intron Retained / Spliced
Control
VCP
Motor neurons day 18
E
Intron retained transcript
Fold change normalised to control
F
Intron spliced transcript
Fold change normalised to control
G
Total FUS
Fold change normalised to GAPDH / Control
H
IR/Spliced ratio
Intron Retained / Spliced
Control
VCP

Figure 5.13 FUS intron retention in day 18 motor neuron and interneuron NPCs

Bar plots quantifying day 18 IN NPC mRNA expression levels of (A) FUS intron 6/7 retained transcript normalised over constitutive FUS expression and additionally to the average of controls. (B) FUS intron 6/7 spliced transcript normalised to constitutive FUS expression and to the average of controls. (C) Total FUS expression normalised to GAPDH and to the average of controls, in VCP-mutant lines compared to controls, as assessed by qPCR. (D) Bar plot depicting day 18 IN NPC mRNA expression ratio of FUS intron 6/7 retained transcript and FUS spliced transcript (both normalised over their GAPDH expression) and normalised to control lines, as indicated on each graph. Bar graphs quantifying day 18 MN NPC mRNA expression levels of (E) FUS intron 6/7 retained transcript normalised over constitutive FUS expression and additionally to the average of controls. (F) FUS intron 6/7 spliced transcript normalised to constitutive FUS expression and to the average of controls. (G) Total FUS expression normalised to GAPDH and to the average of controls, in VCP-mutant lines compared to controls, as assessed by qPCR. (H) Bar plot depicting day 18 MN NPC mRNA expression ratio of FUS intron 6/7 retained transcript and FUS normally spliced transcript (both normalised over their GAPDH expression) and normalised to control lines, as indicated on each graph. n=2 per cell line with 6 independent control lines (CTRL1-6) and 4 VCP-mutant cell lines (GLiA, GLiB, CB1D, CB1E) used. Data is plotted per line, with error bars displayed as mean ± SEM. p value calculated using unpaired two-tailed t-test with Welch's correction.

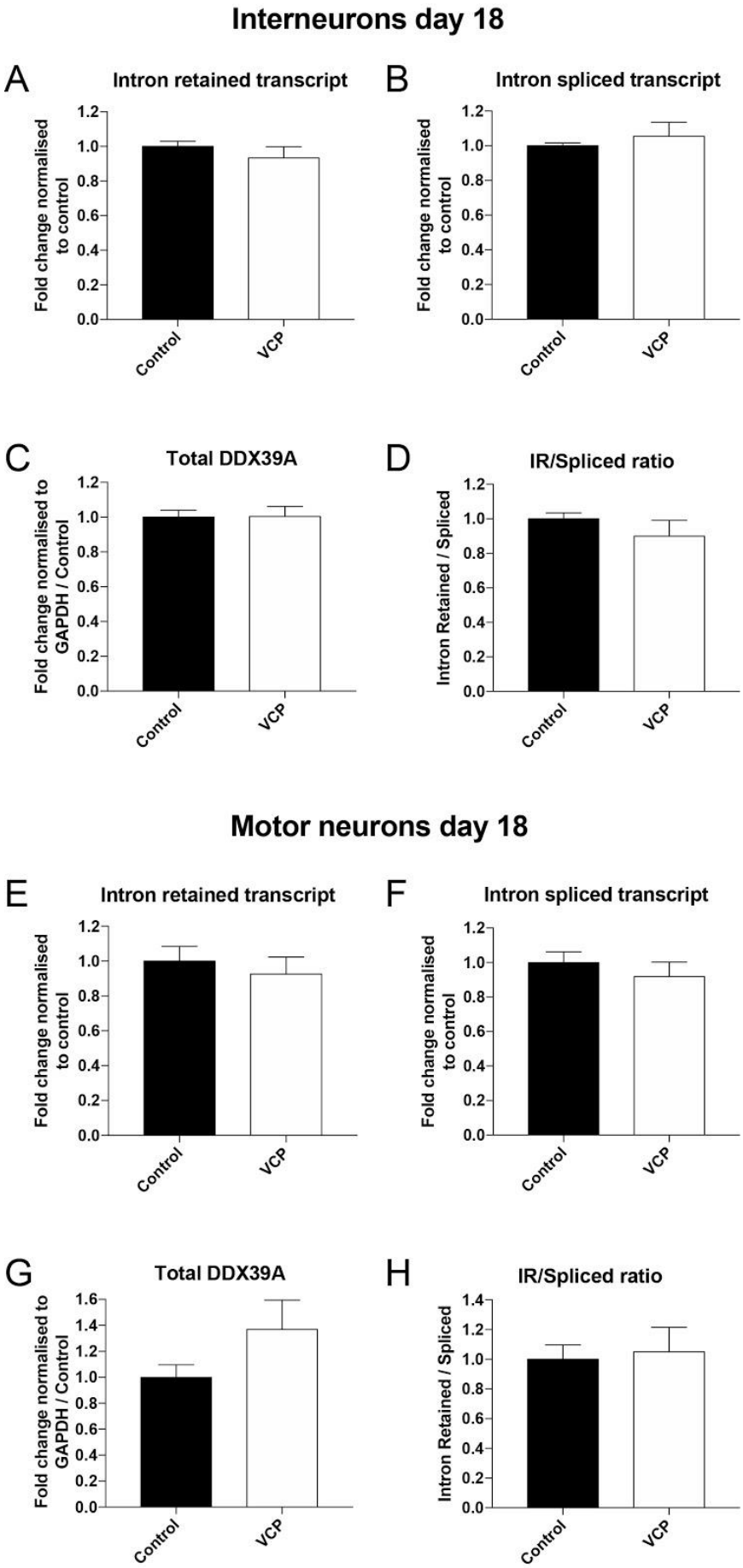
Interneurons day 18
A
Intron retained transcript
Fold change normalised to control
B
Intron spliced transcript
Fold change normalised to control
C
Total DDX39A
Fold change normalised to GAPDH / Control
D
IR/Spliced ratio
Intron Retained / Spliced
Motor neurons day 18
E
Intron retained transcript
Fold change normalised to control
F
Intron spliced transcript
Fold change normalised to control
G
Total DDX39A
Fold change normalised to GAPDH / Control
H
IR/Spliced ratio
Intron Retained / Spliced
Control
VCP

Figure 5.14 DDX39A intron retention in day 18 motor neuron and interneuron NPCs

Bar plots quantifying day 18 IN NPC mRNA expression levels of (A) DDX39A intron 6 retained transcript normalised over constitutive DDX39A expression and additionally to the average of controls. (B) DDX39A intron 6 spliced transcript normalised to constitutive DDX39A expression and to the average of controls. (C) Total DDX39A expression normalised to GAPDH and to the average of controls, in VCP-mutant lines compared to controls, as assessed by qPCR. (D) Bar plot depicting day 18 IN NPC mRNA expression ratio of DDX39A intron 6 retained transcript and DDX39A normally spliced transcript (both normalised over their GAPDH expression) and normalised to control lines, as indicated on each graph. Bar graphs quantifying day 18 MN precursor mRNA expression levels of (E) DDX39A intron 6 retained transcript normalised over constitutive DDX39A expression and additionally to the average of controls. (F) DDX39A intron 6 spliced transcript normalised to constitutive DDX39A expression and to the average of controls. (G) Total DDX39A expression normalised to GAPDH and to the average of controls, in VCP-mutant lines compared to controls, as assessed by qPCR. (H) Bar plot depicting day 18 MN NPC mRNA expression ratio of DDX39A intron 6 retained transcript and DDX39A normally spliced transcript (both normalised over their GAPDH expression) and normalised to control lines, as indicated on each graph. n=2 per cell line with 6 independent control lines (CTRL1-6) and 4 VCP-mutant cell lines (GLiA, GLiB, CB1D, CB1E) used. Data is plotted per line, with error bars displayed as mean ± SEM. p value calculated using unpaired two-tailed t-test with Welch's correction.

In order to assess the temporal manifestation of aberrant SFPQ, FUS and DDX39A IRTs and their persistence beyond embryonic timepoints, day 25 samples were assessed in INs and MNs following 7 days of terminal differentiation in CE. Following on from the mostly insignificant changes in aberrant IRTs observed at day 18 NPC stage in INs and MNs, a similar pattern was observed at day 25 timepoints in both MNs and INs. Indeed, no significant difference was observed in SFPQ intron 9 IRTs in INs or normally spliced transcript, coinciding with no change in total SFPQ or IR/spliced ratio (Figure 5.15A-D). Similar findings were also observed for day 25 MNs (Figure 5.15E-H). In addition, no significant difference in FUS intron 6 IRT was detected in INs between VCP-mutant and control lines at day 25 timepoints, coinciding with spliced and total FUS transcript levels and IR/spliced ratio, which were also not statistically different (Figure 5.16A-D). Interestingly; however, a significant decrease in FUS intron 6 IRT was observed in VCP

MNs, when compared to control (Figure 5.16E). Whilst no significant difference was detected in spliced or total FUS expression levels, a trend towards a decrease was observed in IRT/spliced ratio in VCP lines, when compared to control (Figure 5.16F-H). Assessment of DDX39A intron 6 IRTs revealed insignificant differences in IRT, normally spliced and total DDX39A transcript levels, coinciding with no differences in IR/spliced ratio in both INs (Figure 5.13A-D) and MNs (Figure 5.13E-H). Interestingly, however, there was a trend towards an increase in DDX39A intron 6 IRT in INs at day 25, including measures by IR/spliced ratio (Figure 5.13A&D). Conversely, MNs at day 25 displayed an opposite trend towards a decrease in DDX39A intron 6 retention, also seen in the IR/spliced ratio. However, these data were not statistically significant.

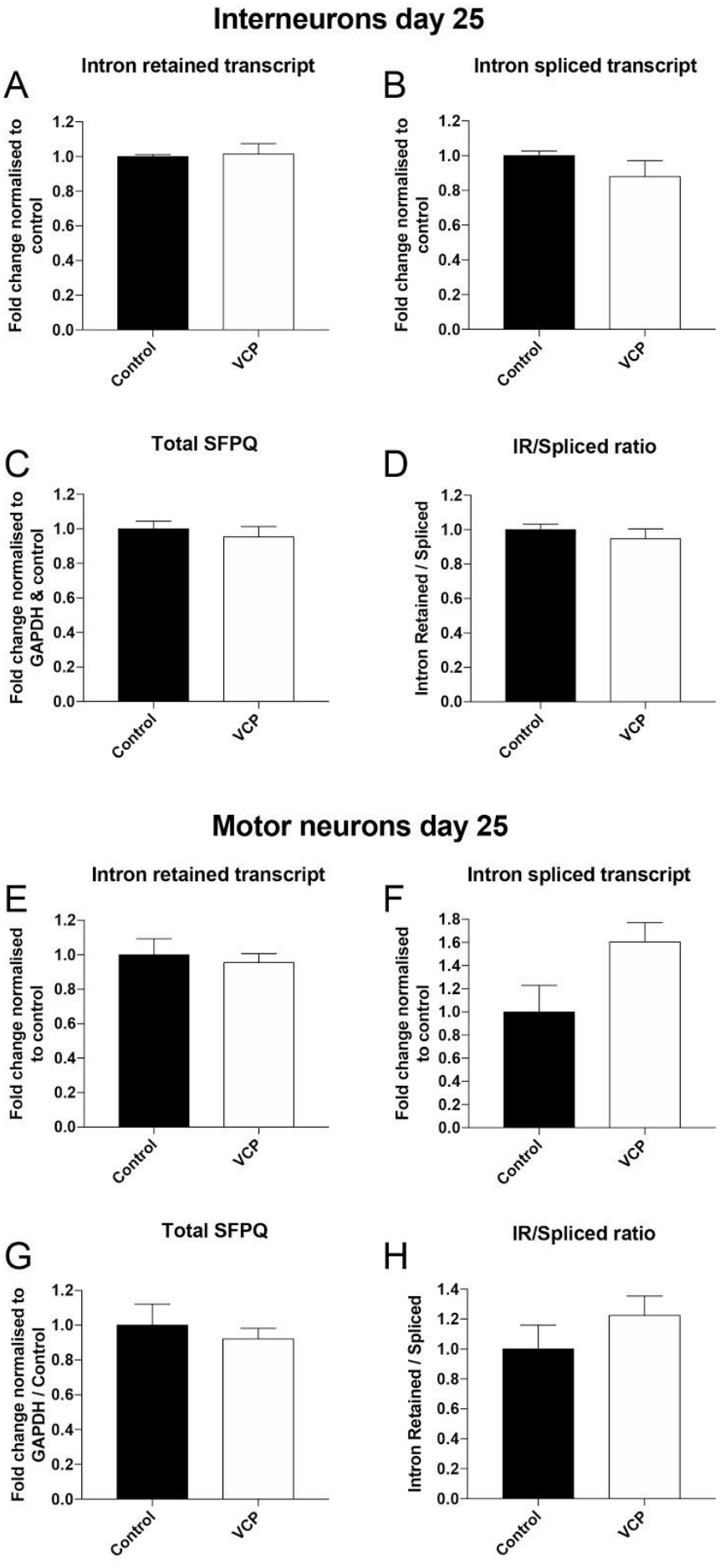
Interneurons day 25
A
Intron retained transcript
Fold change normalised to control
B
Intron spliced transcript
Fold change normalised to control
C
Total SFPQ
Fold change normalised to GAPDH & control
D
IR/Spliced ratio
Intron Retained / Spliced
Motor neurons day 25
E
Intron retained transcript
Fold change normalised to control
F
Intron spliced transcript
Fold change normalised to control
G
Total SFPQ
Fold change normalised to GAPDH / Control
H
IR/Spliced ratio
Intron Retained / Spliced
Control
VCP

Figure 5.15 SFPQ intron retention in day 25 motor neurons and interneurons

Bar plots quantifying day 25 post-mitotic IN mRNA expression levels of (A) SFPQ intron 9 retained transcript normalised over constitutive SFPQ expression and additionally to the average of controls. (B) SFPQ intron 9 spliced transcript normalised to constitutive SFPQ expression and to the average of controls. (C) Total SFPQ expression normalised to GAPDH and to the average of controls, in VCP-mutant lines compared to controls, as assessed by qPCR. (D) Bar plot depicting day 25 post-mitotic IN mRNA expression ratio of SFPQ intron 9 retained transcript and SFPQ normally spliced transcript (both normalised over their GAPDH expression) and normalised to control lines, as indicated on each graph. Bar graphs quantifying day 25 post-mitotic MN mRNA expression levels of (E) SFPQ intron 9 retained transcript normalised over constitutive SFPQ expression and additionally to the average of controls. (F) SFPQ intron 9 spliced transcript normalised to constitutive SFPQ expression and to the average of controls. (G) Total SFPQ expression normalised to GAPDH and to the average of controls, in VCP-mutant lines compared to controls, as assessed by qPCR. (H) Bar plot depicting day 25 post-mitotic MN mRNA expression ratio of SFPQ intron 9 retained transcript and SFPQ normally spliced transcript (both normalised over their GAPDH expression) and normalised to control lines, as indicated on each graph. n=2 per cell line with 6 independent control lines (CTRL1-6) and 4 VCP-mutant cell lines (GLiA, GLiB, CB1D, CB1E) used. Data is plotted per line, with error bars displayed as mean ± SEM. p value calculated using unpaired two-tailed t-test with Welch's correction.

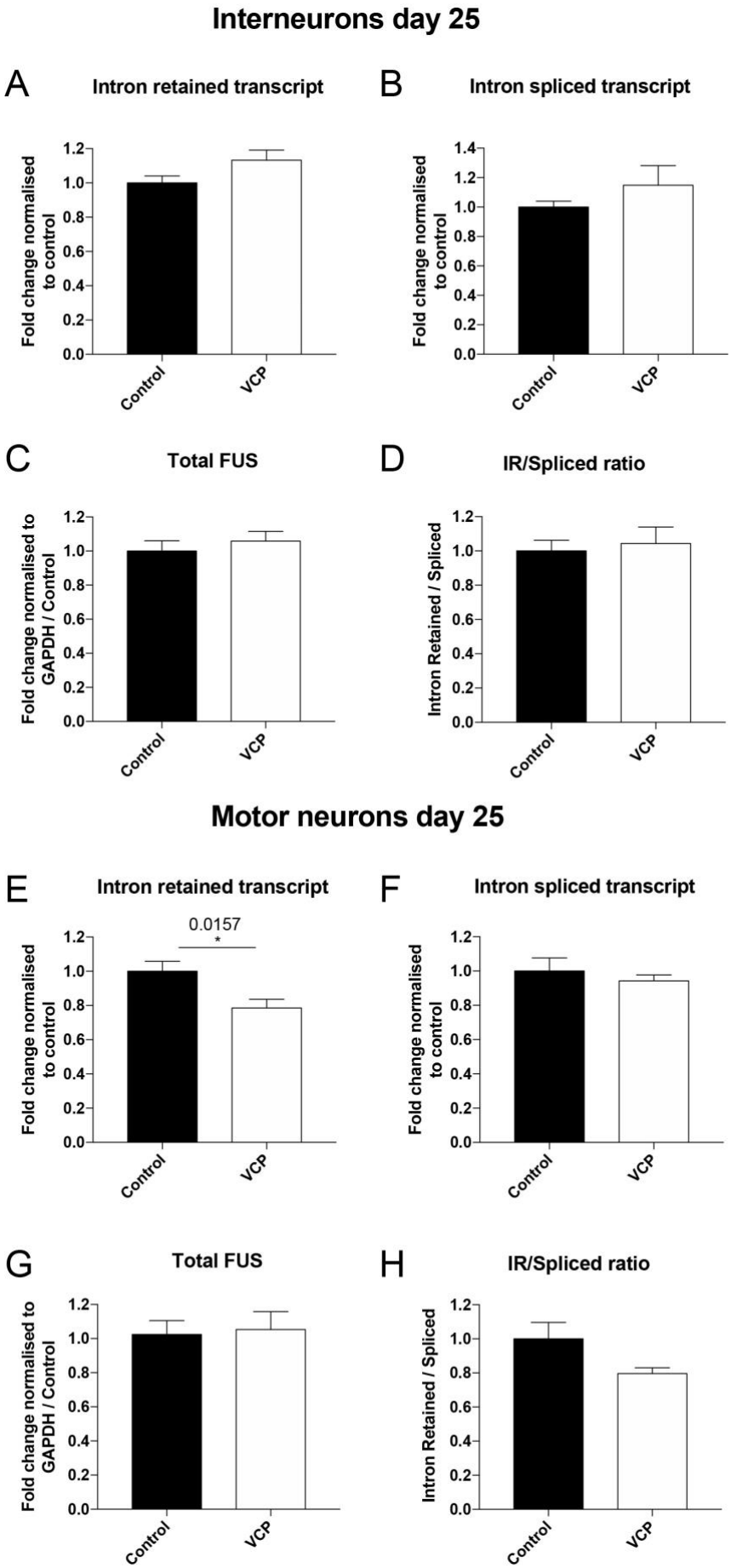
Interneurons day 25
A
Intron retained transcript
Fold change normalised to control
B
Intron spliced transcript
Fold change normalised to control
C
Total FUS
Fold change normalised to GAPDH / Control
D
IR/Spliced ratio
Intron Retained / Spliced
Motor neurons day 25
E
Intron retained transcript
0.0157
*
Fold change normalised to control
F
Intron spliced transcript
Fold change normalised to control
G
Total FUS
Fold change normalised to GAPDH / Control
H
IR/Spliced ratio
Intron Retained / Spliced
Control
VCP

Figure 5.16 FUS intron retention in day 25 motor neurons and interneurons

Bar plots quantifying day 25 post-mitotic IN mRNA expression levels of (A) FUS intron 6/7 retained transcript normalised over constitutive FUS expression and additionally to the average of controls. (B) FUS intron 6/7 spliced transcript normalised to constitutive FUS expression and to the average of controls. (C) Total FUS expression normalised to GAPDH and to the average of controls, in VCP-mutant lines compared to controls, as assessed by qPCR. (D) Bar plot depicting day 25 post-mitotic IN mRNA expression ratio of FUS intron 6/7 retained transcript and FUS normally spliced transcript (both normalised over their GAPDH expression) and normalised to control lines, as indicated on each graph. Bar graphs quantifying day 25 post-mitotic MN mRNA expression levels of (E) FUS intron 6/7 retained transcript normalised over constitutive FUS expression and additionally to the average of controls. (F) FUS intron 6/7 spliced transcript normalised to constitutive FUS expression and to the average of controls. (G) Total FUS expression normalised to GAPDH and to the average of controls, in VCP-mutant lines compared to controls, as assessed by qPCR. (H) Bar plot depicting day 25 post-mitotic MN mRNA expression ratio of FUS intron 6/7 retained transcript and FUS normally spliced transcript (both normalised over their GAPDH expression) and normalised to control lines, as indicated on each graph. n=3 per cell line with 3-6 independent control lines (CTRL1-6) and 4 VCP-mutant cell lines (GLiA, GLiB, CB1D, CB1E) used. Data is plotted per line, with error bars displayed as mean ± SEM. p value calculated using unpaired two-tailed t-test with Welch's correction.

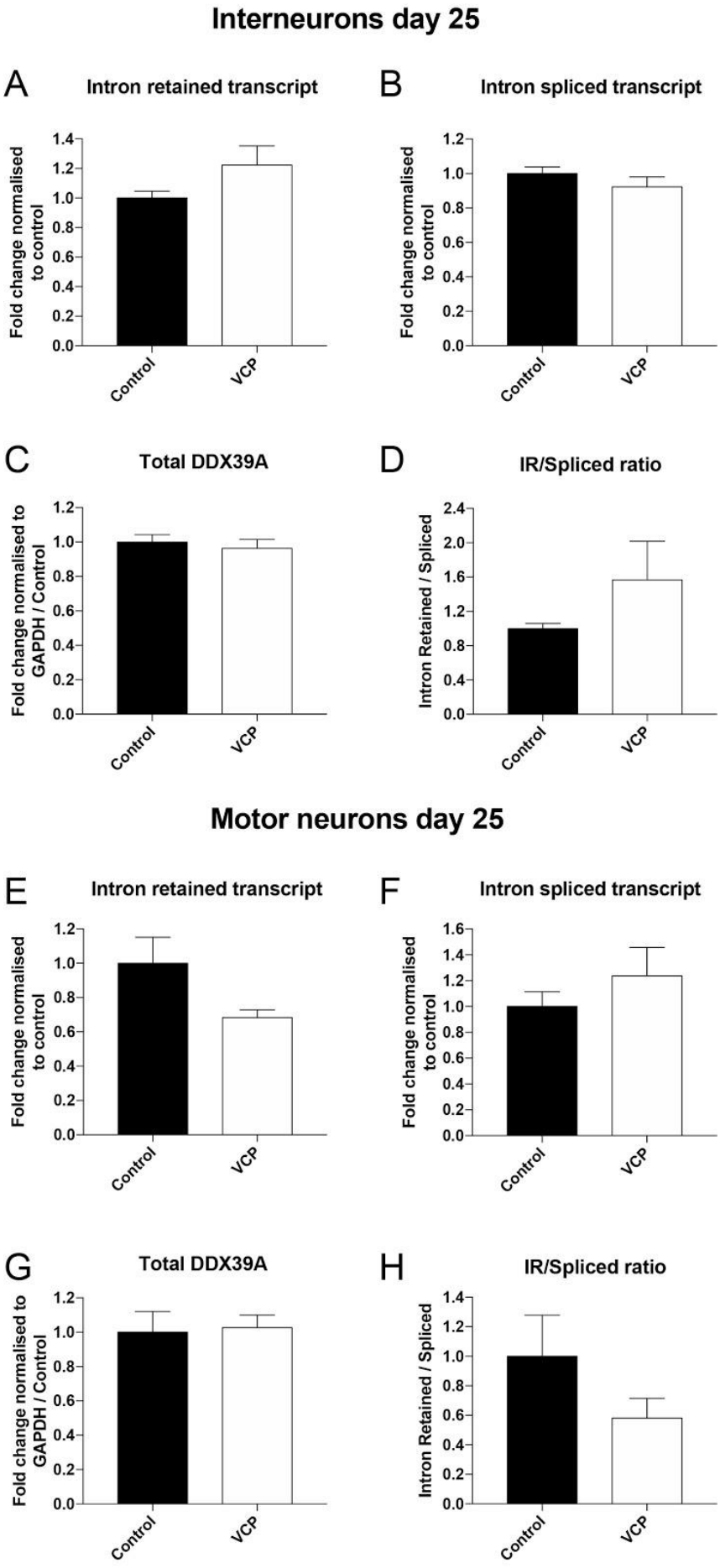
Interneurons day 25
A
Intron retained transcript
Fold change normalised to control
B
Intron spliced transcript
Fold change normalised to control
C
Total DDX39A
Fold change normalised to GAPDH / Control
D
IR/Spliced ratio
Intron Retained / Spliced
Motor neurons day 25
E
Intron retained transcript
Fold change normalised to control
F
Intron spliced transcript
Fold change normalised to control
G
Total DDX39A
Fold change normalised to GAPDH / Control
H
IR/Spliced ratio
Intron Retained / Spliced
Control
VCP

Figure 5.17 DDX39A intron retention in day 25 motor neurons and interneurons

Bar plots quantifying day 25 post-mitotic IN mRNA expression levels of (A) DDX39A intron 6 retained transcript normalised over constitutive DDX39A expression and additionally to the average of controls. (B) DDX39A intron 6 spliced transcript normalised to constitutive DDX39A expression and to the average of controls. (C) Total DDX39A expression normalised to GAPDH and to the average of controls, in VCP-mutant lines compared to controls, as assessed by qPCR. (D) Bar plot depicting day 25 post-mitotic IN mRNA expression ratio of DDX39A intron 6 retained transcript and DDX39A normally spliced transcript (both normalised over their GAPDH expression) and normalised to control lines, as indicated on each graph. Bar graphs quantifying day 25 post-mitotic MN mRNA expression levels of (E) DDX39A intron 6 retained transcript normalised over constitutive DDX39A expression and additionally to the average of controls. (F) DDX39A intron 6 spliced transcript normalised to constitutive DDX39A expression and to the average of controls. (G) Total DDX39A expression normalised to GAPDH and to the average of controls, in VCP-mutant lines compared to controls, as assessed by qPCR. (H) Bar plot depicting day 25 post-mitotic MN mRNA expression ratio of DDX39A intron 6 retained transcript and DDX39A normally spliced transcript (both normalised over their GAPDH expression) and normalised to control lines, as indicated on each graph. n=2 per cell line with 6 independent control lines (CTRL1-6) and 4 VCP-mutant cell lines (GLiA, GLiB, CB1D, CB1E) used. Data is plotted per line, with error bars displayed as mean ± SEM. p value calculated using unpaired two-tailed t-test with Welch's correction.

5.4 Discussion

The specification of hiPSC-derived spinal cord neurons from distinct regions of the neural tube has clear utility as a powerful model for elucidating mechanisms of cell type-specific vulnerability in disease (Pandya & Patani. 2020). This is particularly relevant to ALS where pathology manifests in a seemingly focal manner in the spinal cord, with pMN domain MNs exhibiting progressive loss throughout the disease timecourse (Brown & Al-Chalabi. 2017). In contrast, cell types situated in adjacent and further dorsal regions, of which INs comprise the majority, are not thought to be affected until late-stages of disease (Stephens et al. 2006; Hoissaini et al. 2011). However, the roles of alternate cell types in the pathogenesis of ALS are becoming increasingly scrutinised. Indeed, the results of this Chapter demonstrate an intriguing difference in the specification of dorsal subtypes of INs in VCP-mutant ALS lines. Furthermore, aberrant AS programs present

in VCP-mutant MNs during neurogenesis, were found not to manifest beyond these early timepoints in MNs and INs, suggesting that this could indeed be a pathological feature during early embryonic development. However, it should be noted that increased SFPQ intron 9 IRT has been observed in later post-mitotic timepoints using independent RNAseq datasets on hiPSC-derived SOD1 and FUS-mutant MNs and also in ALS post-mortem tissue, indicated additional nuance and complexity (Luisier et al. 2018; Hogan et al. 2020). Finally, hiPSC-derived dorsal INs were not found to exhibit RBP mislocalisation from the nucleus to the cytoplasm, an ALS pathology that was observed in striking contrast to VCP-mutant hiPSC-derived MNs.

5.4.1 Specification of dorsal interneurons in VCP lines

Experiments to address VCP mutation-specific changes in dorsal IN specification from hiPSCs (see Chapter 4) were first undertaken. This revealed no difference in the generation of dorsal precursors between control and VCP lines, with similar proportions of OLIG3 and PAX3 expressing NPCs, indicating similar dorsal progenitor fate specification. Additionally, there were negligible levels of NKX6.1 positive NPCs in VCP-mutant and control lines demonstrating little / no ventralisation of NPCs. Interestingly, a trend towards an increase in PAX6 expression was observed by qPCR in VCP-mutant NPCs, when compared to control. PAX6 has a gradient of expression within the neural tube, with highest levels found in the dP4-6 and P0 domains. Furthermore, assessment at day 25 timepoints following 7 days of terminal differentiation in CE revealed a significant upregulation in the number of LHX5 positive neurons in VCP-mutant lines, when compared to controls; with a coincidental increase in LBX1 mRNA expression. LHX5 has an expression profile similar to PAX6, being expressed by dP4, dP6 and P0 domain NPCs but absent from dP5 NPCs. This; in itself, is an intriguing observation, particularly when considering that no differences was observed in the specification of post-mitotic MNs (both >85%) between control and VCP-mutant lines (Hall et al. 2017; Luisier et al. 2018). Indeed, these data highlight a potential defect in IN subtype specification, or a compensatory change in specification towards an IN subtype/s less vulnerable to ALS pathology (noting that hiPSC-derived INs did not display RBP mislocalisation). Although more experiments are needed to characterise this difference, one could speculate at a dysregulation in the generation of dP5 domain NPCs in VCP-mutant lines. dI5 INs are known to be involved in somatosensory relay of itch, touch and

pain in particular (Abraira et al. 2017; Duan et al. 2014; Bourane et al. 2015). Further disruption of IN circuitry during development could have a detrimental effect on MNs, altering motor output and even MN excitability, as demonstrated in SOD1 G93A mice (Allodi et al. 2020). Moreover, LHX5 expression in the dorsal neural tube delineates INs of dI4 and dI6 identity (Alaynick et al. 2011; Lai et al. 2016). Whilst INs with dI4 domain identity convey somatosensory pain, touch, itch and temperature sensations, dI6 INs comprise GABAergic inhibitory commissural with direct synaptic contact onto ventral MNs (Gross et al. 2002; Glasgow et al. 2005; Pillai et al. 2007; Goulding et al. 2009). As a result, dI6 INs have roles relating to the maintenance of left-right alternation, similar to the juxtaposed V0 INs that also comprise Renshaw cells. There is little / no literature citing a role of VCP in the development of neural tube subtypes, or any role involving spinal cord domain specification. However, one could speculate that, should a difference in constituent spinal cord INs be present in VCP-mutant ALS patients, this could directly impact MN output, particularly in dI6 IN subtypes that innervate ventral MNs. An important factor to consider is that this phenotypic observation in IN subtype specification may not be caused by the ALS-related VCP mutations, but as a result of genetic background differences between lines. Therefore, in order to address this, a set of isogenic knock-in lines has been generated with a R191Q VCP point mutation inserted. Employment of these lines would enable a direct genotype-phenotype link, thereby providing evidence for causality.

5.4.2 RBP mislocalisation in interneurons and motor neurons

Whilst ALS is widely considered a heterogeneous disorder with a range of multifactorial pathologies, many causative ALS mutations have been identified in genes encoding RBPs (Mejzini et al. 2019). Subsequent studies have detailed changes in RNA metabolism, cytoplasmic mislocalisation, dysfunction in stress granule dynamics and increased propensity for aggregation in RBPs. As such, RBPs are a key research focus aimed at both elucidating ALS-related neurodegenerative mechanisms and providing tractable targets for therapeutic intervention (Xue et al. 2020). RBP mislocalisation from the nucleus to the cytoplasm has been described as a key pathological hallmark of ALS. Indeed, many RBPs are mislocalised in ALS including TDP-43, FUS and SFPQ (Neumann et al. 2006; Vance et al. 2009; Hall et al 2017; Luisier et al. 2018; Tyzack et al. 2019). Most of these RBPs share common properties, not only in their ability to bind

to RNA, they also possess an intrinsically disordered low complexity domain that underpins their ability to associate with stress granules (Jain et al. 2016; Monahan et al. 2016). Importantly, in the presence of ALS-causing mutations, these RBPs undergo increased cytoplasmic mislocalisation and an increased propensity for fibrillar aggregation, coinciding with dysregulation of stress granule dynamics. The ability to model this in hiPSC-derived cultures represents a unique opportunity to interrogate the mechanisms underpinning these pathologies. Moreover, the incorporation of alternative cell types with altered pathological state in ALS-mutant lines, could be crucial in elucidating ALS-related pathomechanisms.

TDP-43 is a highly conserved and ubiquitously expressed DNA and RNA binding protein encoded by the TARDBP gene and is predominantly localised in the nucleus (Suk & Rosseaux. 2020). Importantly, TDP-43 pathology, in the form of mislocalisation from the nucleus and subsequent formation of cytoplasmic inclusions, provides a crucial link between sporadic and familial ALS (Neumann et al. 2006). Indeed, it is thought that 97% of all ALS patients present with TDP-43 pathology including VCP, but SOD1- and FUS-mutant ALS cases being notable exceptions (Arai et al. 2006; Neumann et al. 2006). Interestingly, TDP-43 pathology is not restricted to ALS; with mutations in the TARDBP gene also being linked to fronto-temporal lobar dementia (FTLD) where 45% of FTLD cases present with TDP-43 pathology (Arai et al. 2006; Neumann et al. 2006; Le et al. 2016). Recently, a study in this laboratory demonstrated that hiPSC-derived VCP-mutant MNs exhibited TDP-43 mislocalisation (but not aggregation) amongst a host of additional ALS-related pathologies (Hall et al. 2017). In itself, this study provides important evidence for the validity of hiPSCs to model neurodegenerative diseases and ALS. However, regarding TDP-43 pathology, these experiments were carried out in MNs at early stages representing immature cultures. Therefore, TDP-43 N/C mislocalisation was assessed in this hiPSC-derived MN model at a later and more mature stage in MNs, with dorsal INs additionally evaluated. Moreover, a robust analysis pipeline was employed using sensitive automated cell-by-cell analysis in >10,000 cells (Harley & Patani. 2020). Interestingly, this revealed a significant nuclear displacement of TDP-43 into the cytoplasm in VCP-mutant MNs, when compared to controls. This finding is in alignment with a study by Harley & Patani. (2020) and highlights the ability of this VCP-mutant hiPSC model to recapitulate a key pathological hallmark of ALS. Perhaps more

interesting, however, were observations that this phenotype was not replicated in VCP-mutant INs that displayed no difference in N/C ratio. These findings suggest that hiPSC-derived MNs may have an intrinsic susceptibility to TDP-43 mislocalisation that is not encountered in other cell types within the same spinal cord region. This strongly highlights the utility of hiPSCs to model neuronal subtype-specific vulnerability. There is some debate as to whether TDP-43 nuclear loss or gain of toxic cytoplasmic function accounts for the dominant pathomechanisms involved in ALS (Suk & Rousseaux. 2020). Some studies have suggested that the loss of TDP-43 in the nucleus dramatically impairs its role in mRNA maturation, alternative splicing, transport and DNA damage (Buratti et al. 2008; Tollervey et al. 2011; Polymenidou et al. 2011; Fallini et al. 2012; Amlie-Wolf et al. 2015; Melamed et al. 2019; Chu et al. 2019). Other studies have hypothesised that the involvement of TDP-43 as a primary component of polyubiquitinated and hyperphosphorylated cytoplasmic aggregates results in the production of stress granules, actively blocking normal cellular processes (Arai et al. 2006; Neumann et al. 2006; Gasset-Rosa et al. 2019; Mann et al. 2019). However, it should be noted that ALS pathogenesis can occur in the absence of stress granule formation (Mann et al. 2019; Gasset-Rosa et al. 2019). Instead, this could rely upon a shift towards an irreversible change in liquid-liquid phase separation (LLPS) and a subsequent fibrillar and highly aggregative state (Patani. 2020). Interestingly, ALS-causing TARDBP mutations often lead to a baseline elevation in TDP-43 mislocalisation to the cytoplasm and this has been hypothesised to drive early pathology (Suk & Rosseaux. 2020). This is potentially the case in 'young' hiPSC-derived MNs where early mislocalisation leads to more pronounced pathologies as the MNs age.

In contrast to TDP-43, FUS mislocalisation is a recognised pathology of FUS-mutant ALS, where it also forms cytoplasmic inclusions (Vance et al. 2009; Kwiatkowski et al. 2009). Interestingly, these FUS cytoplasmic inclusions do not manifest in other genetic forms of ALS. This, coupled with observations that ALS-causing mutations in FUS do not exhibit TDP-43 proteinopathy, presents a confusing picture of ALS-FUS pathology and its respective heterogeneity (Mackenzie et al. 2007). 60% of FUS-mutant ALS cases are classified as early-onset, and this accounts for around 35% of all early-onset ALS cases (<40 years of age) (Yan et al. 2010; Huang et al. 2010; Shang and Huang. 2016). Indeed, FUS-mutant ALS is associated with a particularly unique and aggressive

progression, especially in juvenile cases (Zou et al. 2015). Interestingly, a reduced N/C ratio of FUS was identified in a recent study from this laboratory using hiPSC-derived VCP-mutant ALS lines (Tyzack et al. 2019). However, these experiments were carried out in pMN domain NPCs and therefore were not characterised in more mature hiPSC-derived MNs and never in hiPSC-derived INs. A separate study assessed FUS mislocalisation at later MN timepoints, revealing a reduced N/C ratio, resulting from a loss of nuclear FUS and gain of cytoplasmic FUS (Harley & Patani. 2020; Harley et al. 2020). Subsequently, the localisation and N/C ratio of FUS was assessed in hiPSC-derived MNs and INs at a similar timepoint. As expected, FUS exhibited a predominantly nuclear localisation in control lines of both MNs and INs. However, the N/C ratio was significantly decreased in hiPSC-derived MNs in VCP-mutant ALS lines, suggesting a nuclear loss of FUS into the cytoplasm. Similar to TDP-43, hiPSC-derived INs did not display a FUS mislocalisation phenotype, further highlighting this hallmark as a selective vulnerability of MNs. MN-specific FUS mislocalisation has also been demonstrated in a recent study using VCP-mutant hiPSC-derived MN precursors, VCP-mutant and sporadic transgenic mouse models and post-mortem tissue from sporadic ALS cases (Tyzack et al. 2019). Here, FUS was not observed to form cytoplasmic inclusions, nor was FUS incorporated into TDP-43 aggregates. This unique feature of FUS-mutant ALS where FUS associates with cytoplasmic inclusions could relate to observations that mutations primarily occur in the nuclear localisation signal (NLS) region of FUS (Dormann et al. 2010; 2012; Dormann & Haas. 2013). This was demonstrated to significantly reduce its capacity to interact with the nuclear transport receptor transportin-1, but could also potentially increase its aggregation properties in the cytoplasm. FUS mislocalisation and aggregation have also been observed to be a heterogenous phenotype across post-mortem tissue from FUS-mutant ALS patients, potentially indicating some level of progression (Marrone et al. 2019). This was linked to an overall reduction in other RBPs such as hnRNPA1 and hnRNPA2B1, implicating significant additional effects on the RBPome.

5.4.3 Intron retention during interneuron and motor neuron specification

As mentioned previously, Luisier et al (2018) observed an early program of AS during pMN domain precursor specification using the MN protocol described in Chapter 3. It

was subsequently revealed that this program of AS, predominantly manifesting through IR, occurred prematurely in VCP-mutant lines (between day 7 and 14). SFPQ intron 9, FUS intron 6 and DDX39A intron 6 IR were found to be the most significantly differentially regulated IRTs (increased in VCP-mutant lines), and this coincided with the mislocalisation of SFPQ protein from the nucleus to the cytoplasm. Interestingly, the SFPQ protein was also demonstrated to bind to its own IRT and this was hypothesised to result in this mislocalisation of SFPQ protein to the cytoplasm. Indeed, additional research in a separate study demonstrated a compartment-specific accumulation of IRTs in the cytoplasm in VCP lines where they displayed increased binding affinities for RBPs such as TDP-43, SFPQ and FUS (Tyzack et al. 2021). Taken together, these data present a tractable model whereby an increase in IRTs in SFPQ, DDX39A and FUS mRNA; bind and sequester ALS-related RBPs such as TDP-43, SFPQ and FUS resulting in their mislocalisation from the nucleus to the cytoplasm. This in turn leads to nuclear RNA splicing dysregulation and altered cytoplasmic function, but the question of primacy is unresolved. Whilst these studies present a well-supported model for early aberrant splicing and RBP mislocalisation, ALS is a disease of aging. Therefore, an important question can be raised as to whether this phenotype is restricted to developmental stages, or do these IRTs persist through later timepoints? Furthermore, is this phenotype common to all cell types during development? And if so, how does this cause differential vulnerability in MNs? In order to begin to address some of these questions, IRTs in SFPQ intron 9, FUS intron 6 and DDX39A intron 6 were assessed at later developmental timepoints. This included day 7 neuroepithelial cells, representing a positive control since this timepoint was identified as the earliest at which differential IRTs manifested in VCP-mutant lines (Luisier et al. 2018). Day 18 NPC timepoints were also assessed; representing the end of patterning and the timepoint characterised for dorsal IN and ventral MN NPC specification (see Chapters 3 & 4). Lastly, day 25 timepoints were evaluated as a measure of post-mitotic INs and MNs.

As expected, a significant increase in IRTs was found with VCP mutation in SFPQ intron 9, FUS intron 6 and DDX39A intron 6 at day 7 timepoints in VCP lines, when compared to control lines and consistent with previous studies (Luisier et al. 2018; Tyzack et al. 2020). Interestingly, at day 18 NPC timepoints, VCP-mutant IN NPCs demonstrated a significant reduction in SFPQ intron 9 IRT/splice ratio and in contrast to day 18 MN

NPCs that showed no difference between VCP and control. This is an intriguing finding, potentially highlighting some form of compensatory mechanism for early aberrant SFPQ IRTs in VCP-mutant INs that does not occur in VCP-mutant MNs. However, day 18 VCP-mutant IN NPCs displayed only a trend towards a decrease in FUS intron 6 IRT, and DDX39A intron 6 IR was not statistically different in VCP-mutant IN NPCs compared to controls. This makes it difficult to speculate as to whether this is a genuine difference or an artefact. Analysis at day 25 post-mitotic timepoints revealed a uniform 'normalisation' of IRT levels with no significant differences detected with VCP-mutation in SFPQ or DDX39A IRTs, when compared to controls. Interestingly, a significant decrease in FUS intron 6 IRT was detected in VCP-mutant MNs. However, this difference was insignificant when measured by IRT/spliced transcript ratio. Taken together, these data suggest that VCP-mediated widespread aberrant IRT manifests during developmental timepoints and more specifically during early pMN domain NPC fate specification. It is interesting to note that day 7 neuroepithelial cells, representing a shared timepoint between hiPSC-derived MNs and INs, demonstrate a clear increase in SFPQ intron 9, FUS intron 6 and DDX39A intron 6 IRTs. However, this does not persist at day 18 or 25 timepoints. This also raises questions as to the role of IRTs in later-stage disease, since a number of studies have implicated aberrant IR in mature cultures / models (Tyzack et al. 2018; Adusumalli et al. 2019; Hogan et al. 2020). Indeed, increased IRTs were demonstrated as a key feature of SOD1 and FUS-mutant ALS in terminally differentiated MNs, VCP-mutant fibroblasts and in the motor cortices of sporadic ALS, AD and in aged patient post-mortem tissue (Tyzack et al. 2018; Adusumalli et al. 2019; Hogan et al. 2020). This suggests some temporal heterogeneity within the IR phenotype in ALS, potentially reflecting a more complex nature with mutation or stress-related factors at play. Indeed, the role of IRTs in late-stage disease could be influenced by other stressors, resulting in a dynamic process of IRTs throughout the timecourse of ALS pathogenesis. It should also be noted that the model system incorporated in this Chapter represents only a snapshot of a highly dynamic process and may not present the full picture. This could be further confounded by the heterogeneous presentation of ALS, with only a portion of neurons exhibiting pathological hallmarks of the disease. Moreover, imbalances in compartment-specific localisation of these IRTs were not assessed. Since this was demonstrated to be a key feature of these IRTs and leading to RBP mislocalisation, this

could provide essential information that is lacking in whole-cell experiments such as those performed in this chapter (Tyzack et al. 2021). Furthermore, a recent study on hiPSC-derived astrocytes revealed clear differences in IRT levels, when compared to hiPSC-derived MNs and in ALS-mutant lines (Ziff et al. 2021). Indeed, reduced nuclear IRT levels in ALS-mutant astrocytes was linked to increased translation and overall expression of a number of proteins involved in nonsense mediated decay and a reactive transformation of astrocytes. Taken together, this reveals key differential mechanisms of AS between cell types, resulting in a disease-related reactive transformation of hiPSC-derived astrocytes. Therefore, it is of increasing importance to analyse these phenotypes for their contribution to cell type-specific vulnerability in ALS.

5.5 Summary and conclusions

The mechanisms underlying the specific degeneration of MNs in ALS are largely unknown. How a specific domain of the spinal cord is targeted in ALS, resulting in severe and progressive pathology, ultimately leading to cell death in pMN domain MN populations, poses an important question to answer. This is further complicated by observations that MNs themselves exhibit a level of subtype selective vulnerability, with FF MNs innervating voluntary muscles more readily and earlier-affected than slower motor units in ALS (Kanning et al. 2009; Nijssen et al. 2017). A number of theories have been hypothesised, attempting to explain this intriguing phenomenon (reviewed by Ragagnin et al. 2019). The results of this study were based on the detailed and robust characterisation of populations of hiPSC-derived MNs and INs detailed in Chapter 3 and 4, respectively. These protocols were employed and characterised using VCP-mutant ALS lines and in order to assess ALS-related pathologies in hiPSC-derived MNs and INs. Taken together, these data provide a crucial platform for modelling cell type-specific vulnerability in ALS, with key pathological hallmarks recapitulated in hiPSC-derived MNs, but not in hiPSC-derived INs. Overall, these findings demonstrate that:

1. There is a VCP-mediated increase in the specification of LHX5 positive IN populations, revealing potential differences in neural tube dorsal fate specification.

2. Ventral MNs, but not dorsal INs, present key pathological hallmarks of ALS in RBP mislocalisation of TDP-43 and FUS following terminal differentiation.
3. Aberrant IRTs previously identified in SFPQ, FUS and DDX39A at early hiPSC-derived timepoints, are not altered in MNs or INs at later stages in development.

Chapter 6. General Discussion

The overarching aims of this thesis were to explore hiPSC-derived directed differentiation strategies in order to generate clinically relevant cell types and accurately model spinal cord cell type-specific vulnerability. The spinal cord is a complex structure, containing heterogenous populations of cells involved in a range of functions (Lu et al. 2015; Lai et al. 2016). Whilst ALS aggressively targets MNs that emanate from one domain of the spinal cord; the pMN domain, other cell types generated from juxtaposed or more dorsal regions appear to be relatively unaffected until late-stage disease (Ragagnin et al. 2019; Pandya & Patani. 2020). Interestingly, recent studies have indicated the presence of cell-autonomous and non-cell-autonomous mechanisms of degeneration in alternate spinal cell types, which contribute to MN degeneration in ALS (Hall et al. 2017; Ziff et al. 2021). Therefore, identifying the full spectrum of ALS pathogenesis and the relevant cell types involved, in addition to elucidating mechanisms of non-cell-autonomous toxicity, would be crucial for ALS research. This would not only improve our understanding of ALS, but also provide new potential therapeutic targets.

As such, modelling ALS in a patient-derived hiPSC culture system provides significant benefits when used in combination with transgenic mouse models and post-mortem tissue. hiPSCs provide a more relevant model system, being derived from *human* patients and are therefore genotypically identical, avoiding the need for artificial overexpression, knockdown or knock out. However, one limitation of using hiPSCs to model disease stems from the ontogeny-driven differentiation protocols themselves. Whilst many protocols exist for deriving a range of cell types; protocols are often limited by low yields of desired target populations, mixed cultures and a lack of deeper characterisation/phenotyping. Indeed, many hiPSC-derived differentiation strategies employ general markers for cell types, with further characterisation often revealing greater complexity and a larger array of sub-populations present (Thiry et al. 2020). With regards to modelling ALS using hiPSCs, this is important as any 'contamination' of cultures, leading to lower enrichment could dilute the sensitivity of any assay to identify a particular phenotype. Indeed, selective vulnerability is also observed in spinal MNs themselves. Therefore, whilst spinal MNs are all derived from a common progenitor pool, there is a large amount of MN subtype diversity following differentiation. This is

exemplified by the taxonomy of MNs by motor column, motor pool, innervating targets and molecular expression profile. This presents an important feature to investigate further. Subsequently, ontogeny-driven differentiation protocols work 'hand-in-hand' with our understanding of developmental biology and are closely aligned. Key developmental insights can be harnessed from hiPSC-derived protocols and vice versa.

Against this background, it is widely known that large diameter FF alpha MNs are the most susceptible lower MN subtype in ALS (Kanning et al. 2010; Swinnen & Robberecht. 2014). Almost 75% of spinal onset ALS patients present with focal onset in the limbs, exhibiting respective limb weakness and atrophy (Brown & Al-Chalabi. 2017). As a result, limb-innervating MNs within the LMC that innervate and control rapid limb movements are reportedly most vulnerable (Kanning et al. 2010; Swinnen & Robberecht. 2014). Whilst the mechanisms underlying the generation of the LMC and their further subdivision into lateral and medial LMC MNs have been detailed extensively (Sockanathan & Jessell. 1998), attempts to generate enriched populations of hiPSC-derived brachial LMC MNs, based on developmentally rationalised induced post-mitotic motor column manipulation have not yet, to my knowledge, been generated. Instead, studies have assessed generic levels of MN columnar subtype diversity within their hiPSC-derived MN protocols or induced motor column diversity during NPC patterning (Amoroso et al. 2013; Thiry et al. 2020). Subsequently, experiments were undertaken in order to generate MN columnar subtype diversity, noting that earlier-born LMCm MNs produce RALDH2 in response to retinoid signalling from adjacent somites, thereby synthesising and secreting RA and inducing a LMCl phenotype in later-born and adjacent *post-mitotic* MNs. Indeed, retinoid signalling during post-mitotic terminal differentiation was able to induce an LMC identity, with respective downregulation of LHX3 and upregulation of FOXP1. Furthermore, a significant proportion of LMCl MNs were also generated, as identified through the upregulation of LHX1. Importantly, this demonstrates the ability of this hiPSC model to induce post-mitotic columnar diversity using previously defined and temporally regulated extrinsic signalling cues (Sockanathan & Jessell. 1998). The replication of this 'post-mitotic patterning' period is of clear importance and suggests that MN diversity can be altered at late stages of neuronal differentiation. Indeed, it would be interesting to investigate the mechanisms underlying the generation of LMC MN phenotype and its subdivisions further and using this hiPSC model. Do the mechanisms

underlying LMC specification in this hiPSC model represent those seen endogenously? In this regard, the role of retinoid signalling in inducing the expression of RALDH2 in LMCm MNs, that can subsequently synthesise and secrete RA; thereby inducing the specification of LMCl phenotype should be investigated. This is of particular interest, considering that populations of LMCm and LMCl MNs were found in cultures exposed to retinoids during terminal differentiation in this model. Perhaps there is further temporal regulation of LMCm and LMCl MNs, with LMCl MNs becoming further enriched with longer exposure to RA during terminal differentiation? This would match *in vivo* studies where LMCl MNs were identified to be later-born. Single cell RNAseq would help to provide some important validation of these post-mitotic patterning principles.

In addition, whilst not investigated in this thesis, future experiments involving the interrogation of selective vulnerability in these MN subtypes would be of clear relevance to ALS. Indeed, another important finding from these data is that there appears to be a bias towards MMC MN specification in the absence of retinoid signalling during terminal differentiation. Therefore, do LMC MNs display exacerbated intrinsic vulnerability with VCP mutation and beyond what is currently observed in MMC MNs cultured in the absence of retinoid signalling during terminal differentiation? One could hypothesise that this could indeed be the case; however, the roles of alternate cell types in defining a FF alpha MN should not be understated. This involves myelination by Schwann cells, innervation by INs, astrocytes and peripheral target skeletal muscle and Schwann cells that could convey non-cell-autonomous effects that mediate enhanced vulnerability.

The role of INs in ALS is heavily debated, with no conclusive evidence of ALS-related IN pathology until late-stage disease in human post-mortem tissue (Stephens et al. 2007). However, other models such as transgenic zebrafish (McGown et al. 2013) and mouse models (Allodi et al. 2020) have demonstrated marked IN pathology in ALS, related to degeneration, heat shock response (HSR), oxidative stress and synaptic decoupling from MN targets that could significantly contribute to ALS pathogenesis. Whilst IN specification from hiPSCs has been achieved, this is often as a by-product of low yield MN specification protocols or in 3D culture systems (Ogura et al. 2018; Gupta et al. 2018). Whilst undoubtedly providing clear utility with regards to 3D spinal models and our understanding of human development and 3D regenerative therapies, the generation of highly enriched 2D cultures is often utilised for disease modelling. This is because

isolated and enriched cultures reduce the influence of confounding variables such as with non-cell-autonomous mediated toxicity, thereby permitting the evaluation of intrinsic cellular vulnerabilities as a direct consequence of disease state. Therefore, in order to assess the role of INs in ALS, their intrinsic vulnerability and provide a platform to model cell type-specific vulnerability, a novel hiPSC-derived protocol was generated.

The developmental principles underlying dorsal-ventral patterning of the neural tube rely upon the secretion of diffusible morphogens from two organising centres; the roof plate secreting BMPs, WNTs and TGF-β and the floor plate secreting SHH (Jessell. 2000). INs are generated from every domain of the spinal cord excepting the pMN domain, which is the domain that MNs arise. Therefore, in order to generate more dorsal populations, a number of directed differentiation strategies were employed, with the SHH agonist purmorphamine removed from all conditions and the addition of BMP4, the SHH antagonist cyclopamine or RA signalling alone. It was subsequently ascertained that the most effective strategy for inducing dorsal and importantly; *neuronal* populations, was through the use of RA signalling alone. This induced strong expression of PAX3 and PAX7; both markers of the dorsal neural tube (Lai et al. 2016) and the downregulation of ventral and pMN domain markers NKX6.1 and OLIG2 respectively. Importantly, unlike progenitors patterned with BMP4, these dorsal progenitors could be terminally differentiated into post-mitotic neurons from corresponding dI4-6 domains and displayed spontaneous and evoked calcium activity. Indeed, these findings aligned with separate studies using retinoid signalling to induce dorsal IN identity in spinal organoids (Ogura et al. 2018; Gupta et al. 2018). In order to fully validate and phenotype the cell types generated in this hiPSC-derived IN protocol, single cell RNAseq would provide important further validation. This is particularly relevant, considering that LHX5 is expressed across a range of neural tube domains. Furthermore, domain transcription factor expression profiles at the precursor stage appear to be particularly plastic as a result of gene regulatory network (GRN) properties during neural tube expansion (Sagner & Briscoe. 2019). Whilst the molecular identity of NPCs appears to be strictly confined to the dP4-6 domains, with low OLIG3 expression; there could be some ‘drift’ following terminal differentiation. Furthermore, single cell RNAseq would enable further and more detailed identification of IN subtypes specified using this protocol, including the potential presence of later-born dorsal INs that arise from dI4 and dI5 domains (Lai et al. 2016).

Indeed, the resolution of mechanisms underlying the generation of early and late-born INs in an hiPSC model would be of considerable value considering their roles in gating nociceptive signals such as mechanical pain, thermal sensation and itch (Foster et al. 2015).

Another important feature to consider is the specification of excitatory and inhibitory INs within these hiPSC-derived cultures. Indeed, each domain generates either a mix of excitatory and inhibitory INs, or isolated groups of inhibitory INs or excitatory INs. This is particularly relevant to the dI4-6 domains where dI4 and dIL_A INs are mainly inhibitory GABAergic or glycinergic (Betley et al. 2009; Fink et al. 2014; Duan et al. 2014; Foster et al. 2015; Kardon et al. 2015), dI5 and dIL_B INs predominantly excitatory glutamatergic INs (Xu et al. 2013; Duan et al. 2014; Szabo et al. 2015; Peirs et al. 2015), and dI6 INs comprise inhibitory GABAergic or glycinergic INs (Andersson et al. 2012; Goetz et al. 2015). Therefore, a combination of molecular, proteomic and functional assays would be important for revealing i) the proportion of excitatory/inhibitory INs in these *in vitro* cultures ii) whether they arise from the correct molecularly defined domains *in vitro* and iii) whether they can function similarly to their endogenous *in vivo* counterparts. It should be noted that much of the choice as to whether an IN becomes excitatory or inhibitory and their subsequent neurotransmitter released has been molecularly linked to the expression of specific transcription factors. This includes the role of PAX2 and PTF1a that are known to be essential for the specification of GABAergic INs across the spinal cord and, in particular, within the dI4-6 domains (Glasgow et al. 2005; Batista & Lewis. 2008). Furthermore, the generation of excitatory INs within the dI5 domain relies on their expression TLX3 that acts to inhibit LBX1 expression and subsequently represses PAX2 and a GABAergic fate (Cheng et al. 2004; 2005).

The role of INs and alternate cell types in the pathogenesis of ALS has become the subject of increasing speculation. Whilst there is no doubt that spinal cord MNs exhibit an enhanced state of vulnerability in ALS, cell-autonomous and non-cell-autonomous mechanisms of degeneration by alternate cell types have also been implicated. Indeed, non-cell-autonomous mechanisms of VCP-mutant astrocyte toxicity on VCP-mutant MNs was recently identified in an hiPSC-derived culture model from this lab (Hall et al. 2017). The position of INs in the spinal cord, being the most abundant spinal cell type, and their contribution to a large array of spinal circuitry and outputs places INs at a

precarious position whereby any defect could lead to detrimental consequences. Indeed, evidence of interneuronopathy in ALS stems from links to altered excitability, decoupling of IN and MN circuitry, pre-symptomatic IN degeneration in a zebrafish model and disrupted reflex arcs and SICI in spinal and cortical regions respectively. Subsequently, the aims of this thesis were to i) investigate whether hiPSC-derived spinal INs from dorsally situated domains develop ALS-related pathologies and ii) investigate the selective vulnerability of these INs in comparison to hiPSC-derived MNs. Interestingly, whilst the specification of dorsal NPCs was unaffected, there was a significant difference in the enrichment of LHX5 expressing dorsal INs with an increase in VCP-mutant lines. This could represent a form of selective vulnerability within populations of LHX5 negative dorsal IN populations. Indeed, these findings coincide with further observations of TDP-43 and FUS RBP mislocalisation, where no significant N/C difference was found in dorsal INs and in contrast to MNs that showed a significant cytoplasmic mislocalisation. Subsequently, a mutation-dependent developmental switch towards the specification of less vulnerable IN subtypes could resolve aberrant RBP mislocalisation in hiPSC-derived INs. In order to evaluate these findings in further detail, immunofluoresence for apoptosis markers such as Caspase III could be used at different time points to identify whether there is loss of LHX5 IN subtypes in VCP lines and during the timecourse of terminal differentiation.

Whilst the RBP mislocalisation experiments demonstrate a clear difference between INs and MNs, it is important to note that these experiments provide only a snapshot of a dynamic process. Indeed, these ICC experiments could reflect a timepoint at which there is no significant difference, but may not truly reflect the full picture of RBP mislocalisation. A more dynamic experimental paradigm would be crucial for further validation using fluorescent tagging of endogenous RBPs. Indeed, this has been achieved recently, using an eGFP tag of endogenous TDP-43 protein (Gasset-Rosa et al. 2019). Another interesting set of experiments are based on the co-culture paradigms of hiPSC-derived MNs and INs with control and VCP-mutant cell types. Indeed, this experimental paradigm was employed and revealed mechanisms of non-cell-autonomous degeneration of hiPSC-derived MNs by hiPSC-derived astrocytes (Hall et al. 2017). Based on this and regarding RBP mislocalisation, a commonly debated hypothesis for ALS pathogenesis is through the prion-like propagation of TDP-43 aggregates from one cell type to another

(reviewed by Smethurst et al. 2015). Indeed, application of serially passaged sporadic ALS post-mortem tissue extracts to hiPSC-derived MNs was able to propagate TDP-43 pathology to astrocytes using co-culture paradigms (Smethurst et al. 2020). Furthermore, hiPSC-derived astrocytes were found to be neuroprotective to TDP-43 seeded aggregation, in contrast to hiPSC-derived MNs, displaying reduced cytoplasmic TDP-43 mislocalisation. Employing these methods in a co-culture paradigm of hiPSC-derived spinal cord INs and MNs would present a tractable model system to evaluate synaptic propagation of ALS-related TDP-43 pathology.

How cells adapt and change throughout their lifetime and as a result of numerous intrinsic or extrinsic factors such as development, stress or in disease-state; is regulated by transcriptomic and proteomic changes (Hon et al. 2017). Importantly, whilst gene content remains constant, the transcriptomic and proteomic landscape can be significantly altered. AS defines any transcriptional modifications that deviate from the 'normal' constitutive profile (Nilsen & Graveley. 2010). This results in significant alterations to the mRNA transcript and generates alternative isoforms. These isoforms can subsequently display drastically differential properties from the constitutive form, with altered function, localisation and translation efficiency most commonly affected. Subsequently, the observations of altered IR in a number of ALS-mutant models presented a significant and novel pathological hallmark in ALS (Luisier et al. 2018; Tyzack et al. 2021). Indeed, the role of cytoplasmic IRTs and their increased binding affinity and ability to sequester ALS-related RBPs presents a tractable hypothesis for RBP pathology and RNA dysregulation in ALS. In addition, the identification of novel and differing mechanisms of AS resulting in a decrease in nuclear IRTs in hiPSC-derived astrocytes is interesting, potentially detailing mechanisms of cell type-specific vulnerability in ALS. As a result, the presence of IRTs was assessed in hiPSC-derived INs, in comparison to hiPSC-derived MNs in order to establish differences that could contribute to selective vulnerability and RBP mislcoaslisation. Additional timepoints were also assessed, including at day 18 NPC and day 25 terminally differentiated stages. Whilst the data mostly revealed little / no consistent or significant changes across all RBPs tested and between INs and MNs at later timepoints, there are several considerations to note. Firstly, whole-cell samples were used, that do not give any indication as to whether there is a shift in the compartment-specific localisation of IRTs. Subsequent nuclear and cytoplasmic fractionations would

provide important validation for IRT compartment localisation. Indeed, one could hypothesise that there could be differences in vulnerability and RBP mislocalisation between control and VCP-mutant INs and MNs stemming from altered cytoplasmic mislocalisation of IRTs between the cell types. This, rather than increased overall IR in VCP-mutant ALS lines, could be a significant contributing factor to ALS pathogenesis and vulnerability. Another form of experimental validation could be through the use of RNAseq on nuclear and cytoplasmic fractions, thereby conforming to the format previously used to demonstrate this phenomenon (Luisier et al. 2018; Tyzack et al. 2021). Lastly, whilst the use of day 18 NPC timepoints were employed because this represented the endpoint of precursor patterning, the IR phenotype was originally detected between day 7 and 14. Therefore, it would be important to assess any differences between control and VCP INs and MNs at day 14 timepoints, in order to assess differential vulnerability. It may be that VCP-mutant INs, that show increased IR at day 7 timepoints, may have some form of compensatory mechanism that is differential from VCP-mutant MNs between these timepoints.

The results of this thesis could also be complemented through the use of a number of additional experimental paradigms and resources. Firstly, one of the most important measures of cell type-specific vulnerability is the eventual death of that particular cell type. In VCP-mutant hiPSC-derived MNs this was demonstrated to be significantly increased at day 35, when compared to control lines (Hall et al. 2017). Therefore, it would be important to identify the presence, or lack of, a cell death phenotype in hiPSC-derived INs using similar cell viability assays at this timepoint. Furthermore, considering the range of IN phenotypes identified in ALS, predominantly demonstrated in ALS mouse models, it would be important to validate these findings in this hiPSC-derived IN model. Indeed, altered excitability (Allodi et al. 2020) and increased stress, shown through upregulated heat-shock response (McGown et al. 2013), present tractable phenotypes to investigate in this hiPSC-derived ALS-mutant IN model. This, coupled with co-culture paradigms between hiPSC-derived MNs and INs investigating synaptic decoupling; would present an interesting line of research. In addition, a number of other ALS-related pathologies were reported in by Hall et al (2017), including oxidative stress, synaptic and mitochondrial dysfunction that would be important to investigate in hiPSC-derived INs. As with most of the experiments relating to VCP-mutant ALS, it would also be beneficial

to validate findings in other models. Indeed, a VCP-mutant mouse model has been used in previous studies (Luisier et al. 2018; Tyzack et al. 2019; Tyzack et al. 2021) in addition to those harbouring alternate ALS-causing genetic backgrounds such as sporadic, C9orf72, TARDBP and FUS. Since ALS is a heterogenous and multifactorial disorder, using alternate genetic backgrounds would be an essential tool to assess whether pathologies are mutation-specific or also encompass sporadic forms of ALS with no known mutation. This is particularly relevant, considering that hiPSCs and their derivatives represent a fetal stage of development. With regards to the VCP-mutant ALS model system employed in this system, the addition of knock-in and knock-out point mutations generating and correcting physiological disease mutation in the VCP gene would significantly reinforce these findings.

Taken together, the results of this thesis contribute valuable and robust characterisation of novel patterning cues during NPC and neuronal subtype specification. Specifically, the generation of LMC MNs and dorsally positioned INs presents an important hiPSC-derived platform to model mechanisms of neuronal subtype selective vulnerability in ALS.

Reference List

Abraira VE, Kuehn ED, Chirila AM, Springel MW, Toliver AA, Zimmerman AL, Orefice LL, Boyle KA, Bai L, Song BJ, Bashista KA, O'Neill TG, Zhuo J, Tsan C, Hoynoski J, Rutlin M, Kus L, Niederkofler V, Watanabe M, Dymecki SM, Nelson SB, Heintz N, Hughes DI, Ginty DD. The Cellular and Synaptic Architecture of the Mechanosensory Dorsal Horn. Cell. 2017 Jan 12;168(1-2):295-310.e19.

Abramzon Y, Johnson JO, Scholz SW, Taylor JP, Brunetti M, Calvo A, Mandrioli J, Benatar M, Mora G, Restagno G, Chiò A, Traynor BJ. Valosin-containing protein (VCP) mutations in sporadic amyotrophic lateral sclerosis. Neurobiol Aging. 2012 Sep;33(9):2231.e1-2231.e6.

Adams KL, Rousso DL, Umbach JA, Novitch BG. Foxp1-mediated programming of limb-innervating motor neurons from mouse and human embryonic stem cells. *Nat Commun*. 2015;6:6778.

Adusumalli S, Ngian ZK, Lin WQ, Benoukraf T, Ong CT. Increased intron retention is a post-transcriptional signature associated with progressive aging and Alzheimer's disease. *Aging Cell*. 2019;18(3):e12928.

Agalliu D, Takada S, Agalliu I, McMahon AP, Jessell TM. Motor Neurons with Axial Muscle Projections Specified by Wnt4/5 Signalling. Neuron. 2009;61(5):708–20.

Akai, J., Halley, P. A., and Storey, K. G. (2005). FGF-dependent Notch signalling maintains the spinal cord stem zone. *Genes Dev.* 19, 2877–2887.

Alaynick WA, Jessell TM, Pfaff SL. SnapShot: spinal cord development. Cell. 2011 Jul 8;146(1):178-178.e1.

Allodi I, Montañana-Rosell R, Selvan R, Löw P, Kiehn O. Locomotor deficits in ALS mice are paralleled by loss of V1-interneuron-connections onto fast motor neurons. bioRxiv. 2020 Jan 1;2020.06.23.166389.

Alvarez-Medina R, Cayuso J, Okubo T, Takada S, Martí E. Wnt canonical pathway restricts graded Shh/Gli patterning activity through the regulation of Gli3 expression. Development. 2008 Jan;135(2):237-47.

Amlie-Wolf A, Ryvkin P, Tong R, Dragomir I, Suh E, Xu Y, Van Deerlin VM, Gregory BD, Kwong LK, Trojanowski JQ, Lee VM, Wang LS, Lee EB. Transcriptomic Changes Due to Cytoplasmic TDP-43 Expression Reveal Dysregulation of Histone Transcripts and Nuclear Chromatin. PLoS One. 2015 Oct 28;10(10):e0141836.

Amoroso MW, Croft GF, Williams DJ, O'Keeffe S, Carrasco MA, Davis AR, Roybon L, Oakley DH, Maniatis T, Henderson CE, Wichterle H. Accelerated high-yield generation of limb-innervating motor neurons from human stem cells. J Neurosci. 2013 Jan 9;33(2):574-86.

Anderson MA, Burda JE, Ren Y, Ao Y, O'Shea TM, Kawaguchi R, Coppola G, Khakh BS, Deming TJ, Sofroniew MV. Astrocyte scar formation aids central nervous system axon regeneration. Nature. 2016 Apr 14;532(7598):195-200.

Anderson RM, Lawrence AR, Stottmann RW, Bachiller D, Klingensmith J. Chordin and noggin promote organizing centers of forebrain development in the mouse. Development. 2002 Nov;129(21):4975-87.

Andrews MG, Del Castillo LM, Ochoa-Bolton E, Yamauchi K, Smogorzewski J, Butler SJ. BMPs direct sensory interneuron identity in the developing spinal cord using signal-specific not morphogenic activities. Elife. 2017 Sep 19;6:e30647.

Arai T, Hasegawa M, Akiyama H, Ikeda K, Nonaka T, Mori H, Mann D, Tsuchiya K, Yoshida M, Hashizume Y, Oda T. TDP-43 is a component of ubiquitin-positive tau-negative inclusions in frontotemporal lobar degeneration and amyotrophic lateral sclerosis. Biochem Biophys Res Commun. 2006 Dec 22;351(3):602-11.

Arber S. Motor circuits in action: specification, connectivity, and function. Neuron. 2012 Jun 21;74(6):975-89.

Arthur KC, Calvo A, Price TR, Geiger JT, Chiò A, Traynor BJ. Projected increase in amyotrophic lateral sclerosis from 2015 to 2040. Nat Commun. 2016 Aug 11;7:12408.

Aruga J, Shimoda K, Mikoshiba K. A 5' segment of the mouse Zic1 gene contains a region specific enhancer for dorsal hindbrain and spinal cord. Brain Res Mol Brain Res. 2000 May 31;78(1-2):15-25.

Aruga J, Tohmonda T, Homma S, Mikoshiba K. Zic1 promotes the expansion of dorsal neural progenitors in spinal cord by inhibiting neuronal differentiation. Dev Biol. 2002 Apr 15;244(2):329-41.

Balaskas N., Ribeiro A., Panovska J., Dessaud E., Sasai N., Page K.M., Briscoe J., Ribes V. Gene regulatory logic for reading the Sonic Hedgehog signalling gradient in the vertebrate neural tube. *Cell.* 2012;148:273–284.

Balmer JE, Blomhoff R. A robust characterization of retinoic acid response elements based on a comparison of sites in three species. *J Steroid Biochem Mol Biol*. 2005;96(5):347-354.

Bannwarth S, Ait-El-Mkadem S, Chaussenot A, et al. A mitochondrial origin for frontotemporal dementia and amyotrophic lateral sclerosis through CHCHD10 involvement. *Brain*. 2014;137(Pt 8):2329-2345.

Batista MF, Lewis KE. Pax2/8 act redundantly to specify glycinergic and GABAergic fates of multiple spinal interneurons. Dev Biol. 2008 Nov 1;323(1):88-97.

Bäumer D, Talbot K, Turner MR. Advances in motor neurone disease. J R Soc Med. 2014 Jan;107(1):14-21.

Bel-Vialar S, Itasaki N, Krumlauf R. Initiating Hox gene expression: in the early chick neural tube differential sensitivity to FGF and RA signalling subdivides the HoxB genes in two distinct groups. Development. 2002 Nov;129(22):5103-15.

Bermingham NA, Hassan BA, Wang VY, Fernandez M, Banfi S, Bellen HJ, Fritzsch B, Zoghbi HY. Proprioceptor pathway development is dependent on Math1. Neuron. 2001 May;30(2):411-22.

Bessou P, Emonet-Dénand F, Laporte Y. Motor fibres innervating extrafusal and intrafusal muscle fibres in the cat. J Physiol. 1965 Oct;180(3):649-72.

Betley JN, Wright CV, Kawaguchi Y, Erdélyi F, Szabó G, Jessell TM, Kaltschmidt JA. Stringent specificity in the construction of a GABAergic presynaptic inhibitory circuit. Cell. 2009 Oct 2;139(1):161-74.

Bikoff JB, Gabitto MI, Rivard AF, Drobac E, Machado TA, Miri A, Brenner-Morton S, Famojure E, Diaz C, Alvarez FJ, Mentis GZ, Jessell TM. Spinal Inhibitory Interneuron Diversity Delineates Variant Motor Microcircuits. Cell. 2016 Mar 24;165(1):207-219.

Boillée S, Vande Velde C, Cleveland DW. ALS: a disease of motor neurons and their nonneuronal neighbors. Neuron. 2006 Oct 5;52(1):39-59.

Bond AM, Bhalala OG, Kessler JA. The dynamic role of bone morphogenetic proteins in neural stem cell fate and maturation. Dev Neurobiol. 2012 Jul;72(7):1068-84.

Borghero G, Pugliatti M, Marrosu F, et al. TBK1 is associated with ALS and ALS-FTD in Sardinian patients. *Neurobiol Aging*. 2016;43:180.e1-180.e1805.

Bourane S, Duan B, Koch SC, Dalet A, Britz O, Garcia-Campmany L, Kim E, Cheng L, Ghosh A, Ma Q, Goulding M. Gate control of mechanical itch by a subpopulation of spinal cord interneurons. Science. 2015 Oct 30;350(6260):550-4.

Braun RJ, Zischka H. Mechanisms of Cdc48/VCP-mediated cell death: from yeast apoptosis to human disease. Biochim Biophys Acta. 2008 Jul;1783(7):1418-35.

Briscoe J, Novitch BG. Regulatory pathways linking progenitor patterning, cell fates and neurogenesis in the ventral neural tube. Philosophical Transactions of the Royal Society B: Biological Sciences. 2008;363:57-70.

Briscoe J, Pierani A, Jessell TM, Ericson J. A homeodomain protein code specifies progenitor cell identity and neuronal fate in the ventral neural tube. Cell. 2000 May 12;101(4):435-45.

Briscoe J, Small S. Morphogen rules: design principles of gradient-mediated embryo patterning. Development. 2015 Dec 1;142(23):3996-4009.

Brockington A, Ning K, Heath PR, Wood E, Kirby J, Fusi N, Lawrence N, Wharton SB, Ince PG, Shaw PJ. Unravelling the enigma of selective vulnerability in neurodegeneration: motor neurons resistant to degeneration in ALS show distinct gene expression characteristics and decreased susceptibility to excitotoxicity. Acta Neuropathol. 2013 Jan;125(1):95-109.

Brondani V, Klimkait T, Egly JM, Hamy F. Promoter of FGF8 reveals a unique regulation by unliganded RARalpha. *J Mol Biol*. 2002;319(3):715-728.

Brown CR, Butts JC, McCreedy DA, Sakiyama-Elbert SE. Generation of v2a interneurons from mouse embryonic stem cells. Stem Cells Dev. 2014 Aug 1;23(15):1765-76.

Brown RH, Al-Chalabi A. Amyotrophic Lateral Sclerosis. N Engl J Med. 2017 Jul 13;377(2):162-172.

Buchan JR, Kolaitis RM, Taylor JP, Parker R. Eukaryotic stress granules are cleared by autophagy and Cdc48/VCP function. Cell. 2013 Jun 20;153(7):1461-74.

Buchan JR, Parker R. Eukaryotic stress granules: the ins and outs of translation. Mol Cell. 2009 Dec 25;36(6):932-41.

Buchanan JT, Grillner S. Newly identified 'glutamate interneurons' and their role in locomotion in the lamprey spinal cord. Science. 1987 Apr 17;236(4799):312-4.

Bui TV, Akay T, Loubani O, Hnasko TS, Jessell TM, Brownstone RM. Circuits for grasping: spinal dI3 interneurons mediate cutaneous control of motor behavior. Neuron. 2013 Apr 10;78(1):191-204.

Buratti E, Baralle FE. Characterization and functional implications of the RNA binding properties of nuclear factor TDP-43, a novel splicing regulator of CFTR exon 9. J Biol Chem. 2001 Sep 28;276(39):36337-43.

Buratti E, Baralle FE. Multiple roles of TDP-43 in gene expression, splicing regulation, and human disease. Front Biosci. 2008 Jan 1;13:867-78.

Burke RE, Levine DN, Tsairis P, Zajac FE 3rd. Physiological types and histochemical profiles in motor units of the cat gastrocnemius. J Physiol. 1973 Nov;234(3):723-48.

Butler SJ, Bronner ME. From classical to current: analyzing peripheral nervous system and spinal cord lineage and fate. Dev Biol. 2015 Feb 15;398(2):135-46.

Butler SJ, Dodd J. A role for BMP heterodimers in roof plate-mediated repulsion of commissural axons. *Neuron.* 2003;38:389–401.

Butti Z, Patten SA. RNA Dysregulation in Amyotrophic Lateral Sclerosis. *Front Genet*. 2019;9:712. Published 2019 Jan 22.

Butts JC, McCreedy DA, Martinez-Vargas JA, Mendoza-Camacho FN, Hookway TA, Gifford CA, Taneja P, Noble-Haeusslein L, McDevitt TC. Differentiation of V2a interneurons from human pluripotent stem cells. Proc Natl Acad Sci U S A. 2017 May 9;114(19):4969-4974.

Camu W, Khoris J, Moulard B, Salachas F, Briolotti V, Rouleau GA, Meininger V. Genetics of familial ALS and consequences for diagnosis. French ALS Research Group. J Neurol Sci. 1999 Jun;165 Suppl 1:S21-6.

Casas C, Herrando-Grabulosa M, Manzano R, Mancuso R, Osta R, Navarro X. Early presymptomatic cholinergic dysfunction in a murine model of amyotrophic lateral sclerosis. Brain Behav. 2013 Mar;3(2):145-58.

Chambers SM, Fasano CA, Papapetrou EP, Tomishima M, Sadelain M, Studer L. Highly efficient neural conversion of human ES and iPS cells by dual inhibition of SMAD signaling. Nat Biotechnol. 2009 Mar;27(3):275-80.

Chen YZ, Bennett CL, Huynh HM, et al. DNA/RNA helicase gene mutations in a form of juvenile amyotrophic lateral sclerosis (ALS4). *Am J Hum Genet*. 2004;74(6):1128-1135.

Cheng L, Arata A, Mizuguchi R, Qian Y, Karunaratne A, Gray PA, Arata S, Shirasawa S, Bouchard M, Luo P, Chen CL, Busslinger M, Goulding M, Onimaru H, Ma Q. Tlx3 and Tlx1 are post-mitotic selector genes determining glutamatergic over GABAergic cell fates. Nat Neurosci. 2004 May;7(5):510-7.

Cheng L, Samad OA, Xu Y, Mizuguchi R, Luo P, Shirasawa S, Goulding M, Ma Q. Lbx1 and Tlx3 are opposing switches in determining GABAergic versus glutamatergic transmitter phenotypes. Nat Neurosci. 2005 Nov;8(11):1510-5.

Chiò A, Moglia C, Canosa A, Manera U, Vasta R, Brunetti M, Barberis M, Corrado L, D'Alfonso S, Bersano E, Sarnelli MF, Solara V, Zucchetti JP, Peotta L, Iazzolino B, Mazzini L, Mora G, Calvo A. Cognitive impairment across ALS clinical stages in a population-based cohort. Neurology. 2019 Sep 3;93(10):e984-e994.

Cho HH, Cargnin F, Kim Y, Lee B, Kwon RJ, Nam H, Shen R, Barnes AP, Lee JW, Lee S, Lee SK. Isl1 directly controls a cholinergic neuronal identity in the developing forebrain and spinal cord by forming cell type-specific complexes. PLoS Genet. 2014 Apr 24;10(4):e1004280.

Chow CY, Landers JE, Bergren SK, et al. Deleterious variants of FIG4, a phosphoinositide phosphatase, in patients with ALS. *Am J Hum Genet*. 2009;84(1):85-88.

Christian JL. Morphogen gradients in development: from form to function. *Wiley Interdiscip Rev Dev Biol*. 2012;1(1):3-15.

Chu JF, Majumder P, Chatterjee B, Huang SL, Shen CJ. TDP-43 Regulates Coupled Dendritic mRNA Transport-Translation Processes in Co-operation with FMRP and Staufen1. Cell Rep. 2019 Dec 3;29(10):3118-3133.e6.

Chung WS, Clarke LE, Wang GX, Stafford BK, Sher A, Chakraborty C, Joung J, Foo LC, Thompson A, Chen C, Smith SJ, Barres BA. Astrocytes mediate synapse elimination through MEGF10 and MERTK pathways. Nature. 2013 Dec 19;504(7480):394-400.

Cirulli ET, Lasseigne BN, Petrovski S, et al. Exome sequencing in amyotrophic lateral sclerosis identifies risk genes and pathways. *Science*. 2015;347(6229):1436-1441.

Clark BS, Stein-O'Brien GL, Shiau F, Cannon GH, Davis-Marcisak E, Sherman T, Santiago CP, Hoang TV, Rajaii F, James-Esposito RE, Gronostajski RM, Fertig EJ, Goff LA, Blackshaw S. Single-Cell RNA-Seq Analysis of Retinal Development Identifies NFI Factors as Regulating Mitotic Exit and Late-Born Cell Specification. Neuron. 2019 Jun 19;102(6):1111-1126.e5.

Clarke BE, Taha DM, Tyzack GE, Patani R. Regionally encoded functional heterogeneity of astrocytes in health and disease: A perspective. Glia. 2021 Jan;69(1):20-27.

Clarke LE, Barres BA. Emerging roles of astrocytes in neural circuit development. Nat Rev Neurosci. 2013 May;14(5):311-21.

Cleveland DW, Rothstein JD. From Charcot to Lou Gehrig: deciphering selective motor neuron death in ALS. Nat Rev Neurosci. 2001 Nov;2(11):806-19.

Cohen M, Page KM, Perez-Carrasco R, Barnes CP, Briscoe J. A theoretical framework for the regulation of Shh morphogen-controlled gene expression. Development. 2014 Oct;141(20):3868-78.

Colombrita C, Onesto E, Megiorni F, Pizzuti A, Baralle FE, Buratti E, Silani V, Ratti A. TDP-43 and FUS RNA-binding proteins bind distinct sets of cytoplasmic messenger RNAs and differently regulate their post-transcriptional fate in motoneuron-like cells. J Biol Chem. 2012 May 4;287(19):15635-47.

Conicella AE, Zerze GH, Mittal J, Fawzi NL. ALS Mutations Disrupt Phase Separation Mediated by α-Helical Structure in the TDP-43 Low-Complexity C-Terminal Domain. Structure. 2016 Sep 6;24(9):1537-49.

Connolly O, Le Gall L, McCluskey G, Donaghy CG, Duddy WJ, Duguez S. A Systematic Review of Genotype-Phenotype Correlation across Cohorts Having Causal Mutations of Different Genes in ALS. J Pers Med. 2020 Jun 29;10(3):58.

Couthouis J, Hart MP, Erion R, et al. Evaluating the role of the FUS/TLS-related gene EWSR1 in amyotrophic lateral sclerosis. *Hum Mol Genet*. 2012;21(13):2899-2911.

Couthouis J, Hart MP, Shorter J, et al. A yeast functional screen predicts new candidate ALS disease genes. *Proc Natl Acad Sci U S A*. 2011;108(52):20881-20890.

Crabé R, Aimond F, Gosset P, Scamps F, Raoul C. How Degeneration of Cells Surrounding Motoneurons Contributes to Amyotrophic Lateral Sclerosis. Cells. 2020 Nov 27;9(12):2550.

Crone SA, Quinlan KA, Zagoraiou L, Droho S, Restrepo CE, Lundfald L, Endo T, Setlak J, Jessell TM, Kiehn O, Sharma K. Genetic ablation of V2a ipsilateral interneurons disrupts left-right locomotor coordination in mammalian spinal cord. Neuron. 2008 Oct 9;60(1):70-83.

Crone SA, Zhong G, Harris-Warrick R, Sharma K. In mice lacking V2a interneurons, gait depends on speed of locomotion. J Neurosci. 2009 May 27;29(21):7098-109.

Dasen JS, De Camilli A, Wang B, Tucker PW, Jessell TM. Hox Repertoires for Motor Neuron Diversity and Connectivity Gated by a Single Accessory Factor, FoxP1. Cell. 2008;134(2):304–16.

Dasen JS, Liu JP, Jessell TM. Motor neuron columnar fate imposed by sequential phases of Hox-c activity. Nature. 2003 Oct 30;425(6961):926-33.

Dasen JS, Tice BC, Brenner-Morton S, Jessell TM. A Hox regulatory network establishes motor neuron pool identity and target-muscle connectivity. Cell. 2005 Nov 4;123(3):477-91.

Davalos D, Grutzendler J, Yang G, Kim JV, Zuo Y, Jung S, Littman DR, Dustin ML, Gan WB. ATP mediates rapid microglial response to local brain injury in vivo. Nat Neurosci. 2005 Jun;8(6):752-8.

Davis-Dusenbery BN, Williams LA, Klim JR, Eggan K. How to make spinal motor neurons. Dev. 2014;141(3):491–501.

DeJesus-Hernandez M, Mackenzie IR, Boeve BF, et al. Expanded GGGGCC hexanucleotide repeat in noncoding region of C9ORF72 causes chromosome 9p-linked FTD and ALS. *Neuron*. 2011;72(2):245-256.

Del Corral RD, Olivera-Martinez I, Goriely A, Gale E, Maden M, Storey K. Opposing FGF and retinoid pathways control ventral neural pattern, neuronal differentiation, and segmentation during body axis extension. Neuron. 2003 Sep 25;40(1):65–79.

Delile J, Rayon T, Melchionda M, Edwards A, Briscoe J, Sagner A. Single cell transcriptomics reveals spatial and temporal dynamics of gene expression in the developing mouse spinal cord. Development. 2019 Mar 27;146(12):dev173807.

Deneen B, Ho R, Lukaszewicz A, Hochstim CJ, Gronostajski RM, Anderson DJ. The transcription factor NFIA controls the onset of gliogenesis in the developing spinal cord. Neuron. 2006 Dec 21;52(6):953-68.

Deng HX, Chen W, Hong ST, et al. Mutations in UBQLN2 cause dominant X-linked juvenile and adult-onset ALS and ALS/dementia. *Nature*. 2011;477(7363):211-215.

Deshaies JE, Shkreta L, Moszczynski AJ, Sidibé H, Semmler S, Fouillen A, Bennett ER, Bekenstein U, Destroismaisons L, Toutant J, Delmotte Q, Volkening K, Stabile S, Aulas A, Khalfallah Y, Soreq H, Nanci A, Strong MJ, Chabot B, Vande Velde C. TDP-43 regulates the alternative splicing of hnRNP A1 to yield an aggregation-prone variant in amyotrophic lateral sclerosis. Brain. 2018 May 1;141(5):1320-1333.

Dessaud E, Ribes V, Balaskas N, Yang LL, Pierani A, Kicheva A, et al. Dynamic Assignment and Maintenance of Positional Identity in the Ventral Neural Tube by the Morphogen Sonic Hedgehog. PLoS Biol. 2010;8(6):e1000382.

Dessaud E, Yang LL, Hill K, Cox B, Ulloa F, Ribeiro A, et al. Interpretation of the sonic hedgehog morphogen gradient by a temporal adaptation mechanism. Nature. 2007;450(7170):717–20.

Devine H, Patani R. The translational potential of human induced pluripotent stem cells for clinical neurology : The translational potential of hiPSCs in neurology. Cell Biol Toxicol. 2017 Apr;33(2):129-144.

Do-Ha D, Buskila Y, Ooi L. Impairments in Motor Neurons, Interneurons and Astrocytes Contribute to Hyperexcitability in ALS: Underlying Mechanisms and Paths to Therapy. Mol Neurobiol. 2018 Feb;55(2):1410-1418.

Dormann D, Haass C. Fused in sarcoma (FUS): an oncogene goes awry in neurodegeneration. Mol Cell Neurosci. 2013 Sep;56:475-86.

Dormann D, Madl T, Valori CF, Bentmann E, Tahirovic S, Abou-Ajram C, Kremmer E, Ansorge O, Mackenzie IR, Neumann M, Haass C. Arginine methylation next to the PY-NLS modulates Transportin binding and nuclear import of FUS. EMBO J. 2012 Nov 14;31(22):4258-75.

Dormann D, Rodde R, Edbauer D, Bentmann E, Fischer I, Hruscha A, Than ME, Mackenzie IR, Capell A, Schmid B, Neumann M, Haass C. ALS-associated fused in sarcoma (FUS) mutations disrupt Transportin-mediated nuclear import. EMBO J. 2010 Aug 18;29(16):2841-57.

Du ZW, Chen H, Liu H, Lu J, Qian K, Huang CTL, et al. Generation and expansion of highly pure motor neuron progenitors from human pluripotent stem cells. Nat Commun. 2015;6:6626.

Duan B, Cheng L, Bourane S, Britz O, Padilla C, Garcia-Campmany L, Krashes M, Knowlton W, Velasquez T, Ren X, Ross S, Lowell BB, Wang Y, Goulding M, Ma Q. Identification of spinal circuits transmitting and gating mechanical pain. Cell. 2014 Dec 4;159(6):1417-1432.

Duval N, Vaslin C, Barata TC, Frarma Y, Contremoulins V, Baudin X, Nedelec S, Ribes VC. BMP4 patterns Smad activity and generates stereotyped cell fate organization in spinal organoids. Development. 2019 Jul 25;146(14):dev175430.

Ebert PJ, Timmer JR, Nakada Y, Helms AW, Parab PB, Liu Y, Hunsaker TL, Johnson JE. Zic1 represses Math1 expression via interactions with the Math1 enhancer and modulation of Math1 autoregulation. Development. 2003 May;130(9):1949-59.

Eccles JC, Eccles RM, Iggo A, Lundberg A. Electrophysiological studies on gamma motoneurones. Acta Physiol Scand. 1960 Sep 30;50:32-40.

Elden AC, Kim HJ, Hart MP, et al. Ataxin-2 intermediate-length polyglutamine expansions are associated with increased risk for ALS. *Nature*. 2010;466(7310):1069-1075.

Elsen GE, Choi LY, Millen KJ, Grinblat Y, Prince VE. Zic1 and Zic4 regulate zebrafish roof plate specification and hindbrain ventricle morphogenesis. Dev Biol. 2008 Feb 15;314(2):376-92.

Ensini M, Tsuchida TN, Belting HG, Jessell TM. The control of rostrocaudal pattern in the developing spinal cord: specification of motor neuron subtype identity is initiated by signals from paraxial mesoderm. Development. 1998 Mar;125(6):969-82.

Fallini C, Bassell GJ, Rossoll W. The ALS disease protein TDP-43 is actively transported in motor neuron axons and regulates axon outgrowth. Hum Mol Genet. 2012 Aug 15;21(16):3703-18.

Fecto F, Yan J, Vemula SP, et al. SQSTM1 mutations in familial and sporadic amyotrophic lateral sclerosis. *Arch Neurol*. 2011;68(11):1440-1446.

Feldman JL, Del Negro CA, Gray PA. Understanding the rhythm of breathing: so near, yet so far. Annu Rev Physiol. 2013;75:423-52.

Ferreira R, Napoli J, Enver T, Bernardino L, Ferreira L. Advances and challenges in retinoid delivery systems in regenerative and therapeutic medicine. Nat Commun. 2020 Aug 26;11(1):4265.

Fink AJ, Croce KR, Huang ZJ, Abbott LF, Jessell TM, Azim E. Presynaptic inhibition of spinal sensory feedback ensures smooth movement. Nature. 2014 May 1;509(7498):43-8.

Foster E, Wildner H, Tudeau L, Haueter S, Ralvenius WT, Jegen M, Johannssen H, Hösli L, Haenraets K, Ghanem A, Conzelmann KK, Bösl M, Zeilhofer HU. Targeted ablation, silencing, and activation establish glycinergic dorsal horn neurons as key components of a spinal gate for pain and itch. Neuron. 2015 Mar 18;85(6):1289-304.

Francius C, Clotman F. Generating spinal motor neuron diversity: a long quest for neuronal identity. Cell Mol Life Sci. 2014 Mar;71(5):813-29.

Franklin H, Clarke BE, Patani R. Astrocytes and microglia in neurodegenerative diseases: Lessons from human in vitro models. Prog Neurobiol. 2020 Dec 9:101973.

Frey D, Schneider C, Xu L, Borg J, Spooren W, Caroni P. Early and selective loss of neuromuscular synapse subtypes with low sprouting competence in motoneuron diseases. J Neurosci. 2000 Apr 1;20(7):2534-42.

Friesen WO. Reciprocal inhibition: a mechanism underlying oscillatory animal movements. Neurosci Biobehav Rev. 1994 Winter;18(4):547-53.

Fu H, Hardy J, Duff KE. Selective vulnerability in neurodegenerative diseases. *Nat Neurosci*. 2018;21(10):1350-1358.

Gabitto MI, Pakman A, Bikoff JB, Abbott LF, Jessell TM, Paninski L. Bayesian Sparse Regression Analysis Documents the Diversity of Spinal Inhibitory Interneurons. Cell. 2016 Mar 24;165(1):220-233.

Gail MR, Martin EJ. Multiple differentiation of clonal teratocarcinoma stem cells following embryoid body formation in vitro. Cell. 1975 Dec ;6(4):467-474.

Gasset-Rosa F, Lu S, Yu H, Chen C, Melamed Z, Guo L, Shorter J, Da Cruz S, Cleveland DW. Cytoplasmic TDP-43 De-mixing Independent of Stress Granules Drives Inhibition of Nuclear Import, Loss of Nuclear TDP-43, and Cell Death. Neuron. 2019 Apr 17;102(2):339-357.e7.

Gendron TF, Bieniek KF, Zhang YJ, Jansen-West K, Ash PE, Caulfield T, Daughrity L, Dunmore JH, Castanedes-Casey M, Chew J, Cosio DM, van Blitterswijk M, Lee WC, Rademakers R, Boylan KB, Dickson DW, Petrucelli L. Antisense transcripts of the expanded C9ORF72 hexanucleotide repeat form nuclear RNA foci and undergo repeat-associated non-ATG translation in c9FTD/ALS. Acta Neuropathol. 2013 Dec;126(6):829-44.

Gillespie RF, Gudas LJ. Retinoid regulated association of transcriptional co-regulators and the polycomb group protein SUZ12 with the retinoic acid response elements of Hoxa1, RARbeta(2), and Cyp26A1 in F9 embryonal carcinoma cells. *J Mol Biol*. 2007;372(2):298-316.

Ginhoux F, Greter M, Leboeuf M, Nandi S, See P, Gokhan S, Mehler MF, Conway SJ, Ng LG, Stanley ER, Samokhvalov IM, Merad M. Fate mapping analysis reveals that adult microglia derive from primitive macrophages. Science. 2010 Nov 5;330(6005):841-5.

Gitcho MA, Strider J, Carter D, Taylor-Reinwald L, Forman MS, Goate AM, Cairns NJ. VCP mutations causing frontotemporal lobar degeneration disrupt localization of TDP-43 and induce cell death. J Biol Chem. 2009 May 1;284(18):12384-98.

Glasgow SM, Henke RM, Macdonald RJ, Wright CV, Johnson JE. Ptf1a determines GABAergic over glutamatergic neuronal cell fate in the spinal cord dorsal horn. Development. 2005 Dec;132(24):5461-9.

Goetz C, Pivetta C, Arber S. Distinct limb and trunk premotor circuits establish laterality in the spinal cord. Neuron. 2015 Jan 7;85(1):131-144.

Goetz CG. Amyotrophic lateral sclerosis: early contributions of Jean-Martin Charcot. Muscle Nerve. 2000 Mar;23(3):336-43.

Gosgnach S, Bikoff JB, Dougherty KJ, El Manira A, Lanuza GM, Zhang Y. Delineating the Diversity of Spinal Interneurons in Locomotor Circuits. J Neurosci. 2017 Nov 8;37(45):10835-10841.

Gosgnach S, Lanuza GM, Butt SJ, Saueressig H, Zhang Y, Velasquez T, Riethmacher D, Callaway EM, Kiehn O, Goulding M. V1 spinal neurons regulate the speed of vertebrate locomotor outputs. Nature. 2006 Mar 9;440(7081):215-9.

Goulding M. Circuits controlling vertebrate locomotion: moving in a new direction. Nat Rev Neurosci. 2009 Jul;10(7):507-18.

Gouti M, Tsakiridis A, Wymeersch FJ, Huang Y, Kleinjung J, Wilson V, Briscoe J. In vitro generation of neuromesodermal progenitors reveals distinct roles for wnt signalling in the specification of spinal cord and paraxial mesoderm identity. PLoS Biol. 2014 Aug 26;12(8):e1001937.

Gowan K, Helms AW, Hunsaker TL, Collisson T, Ebert PJ, Odom R, Johnson JE. Crossinhibitory activities of Ngn1 and Math1 allow specification of distinct dorsal interneurons. Neuron. 2001 Aug 2;31(2):219-32.

Greenway MJ, Alexander MD, Ennis S, et al. A novel candidate region for ALS on chromosome 14q11.2. *Neurology*. 2004;63(10):1936-1938.

Griener A, Zhang W, Kao H, Wagner C, Gosgnach S. Probing diversity within subpopulations of locomotor-related V0 interneurons. Dev Neurobiol. 2015 Nov;75(11):1189-203.

Gros-Louis F, Larivière R, Gowing G, et al. A frameshift deletion in peripherin gene associated with amyotrophic lateral sclerosis. *J Biol Chem*. 2004;279(44):45951-45956.

Gross MK, Dottori M, Goulding M. Lbx1 specifies somatosensory association interneurons in the dorsal spinal cord. Neuron. 2002 May 16;34(4):535-49.

Grossman M. Amyotrophic lateral sclerosis - a multisystem neurodegenerative disorder. Nat Rev Neurol. 2019 Jan;15(1):5-6.

Guertin PA. Central pattern generator for locomotion: anatomical, physiological, and pathophysiological considerations. Front Neurol. 2013 Feb 8;3:183.

Gunes ZI, Kan VWY, Ye X, Liebscher S. Exciting Complexity: The Role of Motor Circuit Elements in ALS Pathophysiology. Front Neurosci. 2020 Jun 17;14:573.

Gupta S, Sivalingam D, Hain S, Makkar C, Sosa E, Clark A, Butler SJ. Deriving Dorsal Spinal Sensory Interneurons from Human Pluripotent Stem Cells. Stem Cell Reports. 2018 Feb 13;10(2):390-405.

Gurdon JB. The developmental capacity of nuclei taken from intestinal epithelium cells of feeding tadpoles. J Embryol Exp Morphol. 1962 Dec;10:622-40.

Haase G, Dessaud E, Garcès A, De Bovis B, Birling MC, Filippi P, et al. GDNF acts through PEA3 to regulate cell body positioning and muscle innervation of specific motor neuron pools. Neuron. 2002;35(5):893–905.

Hall CE, Yao Z, Choi M, Tyzack GE, Serio A, Luisier R, Harley J, Preza E, Arber C, Crisp SJ, Watson PMD, Kullmann DM, Abramov AY, Wray S, Burley R, Loh SHY, Martins LM, Stevens MM, Luscombe NM, Sibley CR, Lakatos A, Ule J, Gandhi S, Patani R. Progressive Motor Neuron Pathology and the Role of Astrocytes in a Human Stem Cell Model of VCP-Related ALS. Cell Rep. 2017 May 30;19(9):1739-1749.

Hammer RP Jr, Tomiyasu U, Scheibel AB. Degeneration of the human Betz cell due to amyotrophic lateral sclerosis. Exp Neurol. 1979 Feb;63(2):336-46.

Hardiman O, Al-Chalabi A, Chio A, Corr EM, Logroscino G, Robberecht W, Shaw PJ, Simmons Z, van den Berg LH. Amyotrophic lateral sclerosis. Nat Rev Dis Primers. 2017 Oct 5;3:17071.

Harley J, Hagemann C, Serio A, Patani R. FUS is lost from nuclei and gained in neurites of motor neurons in a human stem cell model of VCP-related ALS. Brain. 2020 Dec 1;143(12):e103.

Harley J, Patani R. Stress-Specific Spatiotemporal Responses of RNA-Binding Proteins in Human Stem-Cell-Derived Motor Neurons. Int J Mol Sci. 2020 Nov 6;21(21):8346.

Haston KM, Finkbeiner S. Clinical Trials in a Dish: The Potential of Pluripotent Stem Cells to Develop Therapies for Neurodegenerative Diseases. Annu Rev Pharmacol Toxicol. 2016;56:489-510.

Hedlund E, Karlsson M, Osborn T, Ludwig W, Isacson O. Global gene expression profiling of somatic motor neuron populations with different vulnerability identify molecules and pathways of degeneration and protection. Brain. 2010 Aug;133(Pt 8):2313-30.

Hegedus J, Putman CT, Gordon T. Time course of preferential motor unit loss in the SOD1 G93A mouse model of amyotrophic lateral sclerosis. Neurobiol Dis. 2007 Nov;28(2):154-64.

Helms AW, Johnson JE. Progenitors of dorsal commissural interneurons are defined by MATH1 expression. Development. 1998 Mar;125(5):919-28.

Helms AW, Johnson JE. Specification of dorsal spinal cord interneurons. Curr Opin Neurobiol. 2003 Feb;13(1):42-9.

Hinchcliffe M, Smith A. Riluzole: real-world evidence supports significant extension of median survival times in patients with amyotrophic lateral sclerosis. Degener Neurol Neuromuscul Dis. 2017 May 29;7:61-70.

Hinckley CA, Alaynick WA, Gallarda BW, Hayashi M, Hilde KL, Driscoll SP, Dekker JD, Tucker HO, Sharpee TO, Pfaff SL. Spinal Locomotor Circuits Develop Using Hierarchical Rules Based on Motorneuron Position and Identity. Neuron. 2015 Sep 2;87(5):1008-21.

Hoell JI, Larsson E, Runge S, Nusbaum JD, Duggimpudi S, Farazi TA, Hafner M, Borkhardt A, Sander C, Tuschl T. RNA targets of wild-type and mutant FET family proteins. Nat Struct Mol Biol. 2011 Nov 13;18(12):1428-31.

Hogan AL, Grima N, Fifita JA, McCann EP, Heng B, Fat SCM, et al. SFPQ intron retention, reduced expression and aggregate formation in central nervous system tissue are pathological features of amyotrophic lateral sclerosis. bioRxiv. 2020 Jan 1;2020.09.22.309062.

Hollyday M, Hamburger V. An autoradiographic study of the formation of the lateral motor column in the chick embryo. Brain Res. 1977 Aug 26;132(2):197-208.

Hollyday M, Jacobson RD. Location of motor pools innervating chick wing. J Comp Neurol. 1990 Dec 15;302(3):575-88.

Hon CC, Ramilowski JA, Harshbarger J, Bertin N, Rackham OJ, Gough J, Denisenko E, Schmeier S, Poulsen TM, Severin J, Lizio M, Kawaji H, Kasukawa T, Itoh M, Burroughs AM, Noma S, Djebali S, Alam T, Medvedeva YA, Testa AC, Lipovich L, Yip CW, Abugessaisa I, Mendez M, Hasegawa A, Tang D, Lassmann T, Heutink P, Babina M, Wells CA, Kojima S, Nakamura Y, Suzuki H, Daub CO, de Hoon MJ, Arner E, Hayashizaki Y, Carninci P, Forrest AR. An atlas of human long non-coding RNAs with accurate 5' ends. Nature. 2017 Mar 9;543(7644):199-204.

Hossaini M, Cardona Cano S, van Dis V, Haasdijk ED, Hoogenraad CC, Holstege JC, Jaarsma D. Spinal inhibitory interneuron pathology follows motor neuron degeneration independent of glial mutant superoxide dismutase 1 expression in SOD1-ALS mice. J Neuropathol Exp Neurol. 2011 Aug;70(8):662-77.

Huang C, Xia PY, Zhou H. Sustained expression of TDP-43 and FUS in motor neurons in rodent's lifetime. Int J Biol Sci. 2010 Jul 4;6(4):396-406.

Huang EJ, Zhang J, Geser F, Trojanowski JQ, Strober JB, Dickson DW, Brown RH Jr, Shapiro BE, Lomen-Hoerth C. Extensive FUS-immunoreactive pathology in juvenile amyotrophic lateral sclerosis with basophilic inclusions. Brain Pathol. 2010 Nov;20(6):1069-76.

Hughes JT. Pathology of amyotrophic lateral sclerosis. Adv Neurol. 1982;36:61-74.

Huntley ML, Gao J, Termsarasab P, Wang L, Zeng S, Thammongkolchai T, Liu Y, Cohen ML, Wang X. Association between TDP-43 and mitochondria in inclusion body myositis. Lab Invest. 2019 Jul;99(7):1041-1048.

Ikenaga C, Findlay AR, Seiffert M, Peck A, Peck N, Johnson NE, Statland JM, Weihl CC. Phenotypic diversity in an international Cure VCP Disease registry. Orphanet J Rare Dis. 2020 Sep 29;15(1):267.

Ingham PW, McMahon AP. Hedgehog signalling in animal development: paradigms and principles. Genes Dev. 2001 Dec 1;15(23):3059-87.

Ingre C, Roos PM, Piehl F, Kamel F, Fang F. Risk factors for amyotrophic lateral sclerosis. Clin Epidemiol. 2015 Feb 12;7:181-93.

Inoue M, Iida A, Hayashi S, Mori-Yoshimura M, Nagaoka A, Yoshimura S, Shiraishi H, Tsujino A, Takahashi Y, Nonaka I, Hayashi YK, Noguchi S, Nishino I. Two novel *VCP* missense variants identified in Japanese patients with multisystem proteinopathy. Hum Genome Var. 2018 May 30;5:9.

Ishigaki S, Masuda A, Fujioka Y, Iguchi Y, Katsuno M, Shibata A, Urano F, Sobue G, Ohno K. Position-dependent FUS-RNA interactions regulate alternative splicing events and transcriptions. Sci Rep. 2012;2:529.

Iyer NR, Huettner JE, Butts JC, Brown CR, Sakiyama-Elbert SE. Generation of highly enriched V2a interneurons from mouse embryonic stem cells. Exp Neurol. 2016 Mar;277:305-316.

Jain S, Wheeler JR, Walters RW, Agrawal A, Barsic A, Parker R. ATPase-Modulated Stress Granules Contain a Diverse Proteome and Substructure. Cell. 2016 Jan 28;164(3):487-98.

Jaiswal MK. Riluzole and edaravone: A tale of two amyotrophic lateral sclerosis drugs. Med Res Rev. 2019 Mar;39(2):733-748.

Jeong J., McMahon A.P. Growth and pattern of the mammalian neural tube are governed by partially overlapping feedback activities of the hedgehog antagonists patched 1 and Hhip1. *Development.* 2005;132:143–154.

Jessell TM, Sürmeli G, Kelly JS. Motor neurons and the sense of place. Neuron. 2011 Nov 3;72(3):419-24.

Jessell TM. Neuronal specification in the spinal cord: inductive signals and transcriptional codes. Nat Rev Genet. 2000 Oct;1(1):20-9.

Ji SJ, Periz G, Sockanathan S. Nolz1 is induced by retinoid signals and controls motoneuron subtype identity through distinct repressor activities. Development. 2009;136(2):231–40.

Joannides AJ, Fiore-Hériché C, Battersby AA, Athauda-Arachchi P, Bouhon IA, Williams L, Westmore K, Kemp PJ, Compston A, Allen ND, Chandran S. A scaleable and defined system for generating neural stem cells from human embryonic stem cells. Stem Cells. 2007 Mar;25(3):731-7.

Johnson JO, Mandrioli J, Benatar M, Abramzon Y, Van Deerlin VM, Trojanowski JQ, Gibbs JR, Brunetti M, Gronka S, Wuu J, Ding J, McCluskey L, Martinez-Lage M, Falcone D, Hernandez DG, Arepalli S, Chong S, Schymick JC, Rothstein J, Landi F, Wang YD, Calvo A, Mora G, Sabatelli M, Monsurrò MR, Battistini S, Salvi F, Spataro R, Sola P, Borghero G; ITALSGEN Consortium, Galassi G, Scholz SW, Taylor JP, Restagno G, Chiò A, Traynor BJ. Exome sequencing reveals VCP mutations as a cause of familial ALS. Neuron. 2010 Dec 9;68(5):857-64.

Johnson JO, Pioro EP, Boehringer A, et al. Mutations in the Matrin 3 gene cause familial amyotrophic lateral sclerosis. *Nat Neurosci*. 2014;17(5):664-666.

Johnston CA, Stanton BR, Turner MR, Gray R, Blunt AH, Butt D, Ampong MA, Shaw CE, Leigh PN, Al-Chalabi A. Amyotrophic lateral sclerosis in an urban setting: a population based study of inner city London. J Neurol. 2006 Dec;253(12):1642-3.

Ju JS, Fuentealba RA, Miller SE, Jackson E, Piwnica-Worms D, Baloh RH, Weihl CC. Valosin-containing protein (VCP) is required for autophagy and is disrupted in VCP disease. J Cell Biol. 2009 Dec 14;187(6):875-88.

Jung H, Lacombe J, Mazzoni EO, Liem KF Jr, Grinstein J, Mahony S, Mukhopadhyay D, Gifford DK, Young RA, Anderson KV, Wichterle H, Dasen JS. Global control of motor neuron topography mediated by the repressive actions of a single hox gene. Neuron. 2010 Sep 9;67(5):781-96.

Kamelgarn M, Chen J, Kuang L, et al. Proteomic analysis of FUS interacting proteins provides insights into FUS function and its role in ALS. *Biochim Biophys Acta*. 2016;1862(10):2004-2014.

Kanai K, Kuwabara S, Misawa S, Tamura N, Ogawara K, Nakata M, Sawai S, Hattori T, Bostock H. Altered axonal excitability properties in amyotrophic lateral sclerosis: impaired potassium channel function related to disease stage. Brain. 2006 Apr;129(Pt 4):953-62.

Kang P, Lee HK, Glasgow SM, Finley M, Donti T, Gaber ZB, Graham BH, Foster AE, Novitch BG, Gronostajski RM, Deneen B. Sox9 and NFIA coordinate a transcriptional regulatory cascade during the initiation of gliogenesis. Neuron. 2012 Apr 12;74(1):79-94.

Kania A. Concocting cholinergy. PLoS Genet. 2014 Apr 24;10(4):e1004313.

Kanning KC, Kaplan A, Henderson CE. Motor neuron diversity in development and disease. Annu Rev Neurosci. 2010;33:409-40.

Kardon AP, Polgár E, Hachisuka J, Snyder LM, Cameron D, Savage S, Cai X, Karnup S, Fan CR, Hemenway GM, Bernard CS, Schwartz ES, Nagase H, Schwarzer C, Watanabe M, Furuta T, Kaneko T, Koerber HR, Todd AJ, Ross SE. Dynorphin acts as a neuromodulator to inhibit itch in the dorsal horn of the spinal cord. Neuron. 2014 May 7;82(3):573-86.

Kiehn O. Decoding the organization of spinal circuits that control locomotion. Nat Rev Neurosci. 2016 Apr;17(4):224-38.

Kiernan MC, Vucic S, Cheah BC, Turner MR, Eisen A, Hardiman O, Burrell JR, Zoing MC. Amyotrophic lateral sclerosis. Lancet. 2011 Mar 12;377(9769):942-55.

Kim HJ, Kim NC, Wang YD, et al. Mutations in prion-like domains in hnRNPA2B1 and hnRNPA1 cause multisystem proteinopathy and ALS. *Nature*. 2013;495(7442):467-473.

Kim M, Habiba A, Doherty JM, Mills JC, Mercer RW, Huettner JE. Regulation of mouse embryonic stem cell neural differentiation by retinoic acid. Dev Biol. 2009 Apr 15;328(2):456-71.

Kleinsmith LJ, Pierce GB Jr. MULTIPOTENTIALITY OF SINGLE EMBRYONAL CARCINOMA CELLS. Cancer Res. 1964 Oct;24:1544-51.

Koshida S, Shinya M, Nikaido M, Ueno N, Schulte-Merker S, Kuroiwa A, Takeda H. Inhibition of BMP activity by the FGF signal promotes posterior neural development in zebrafish. Dev Biol. 2002 Apr 1;244(1):9-20.

Krampfl K, Petri S, Götz F, Mohammadi B, Bufler J. Amyotrophic lateral sclerosis (ALS) and mirror movements in a patient with polymicrogyria. Amyotroph Lateral Scler Other Motor Neuron Disord. 2003 Dec;4(4):266-9.

Kudoh T, Wilson SW, Dawid IB. Distinct roles for Fgf, Wnt and retinoic acid in posteriorizing the neural ectoderm. Development. 2002 Sep;129(18):4335-46.

Kumar DR, Aslinia F, Yale SH, Mazza JJ. Jean-Martin Charcot: the father of neurology. *Clin Med Res*. 2011;9(1):46-49.

Kumar S, Duester G. Retinoic acid controls body axis extension by directly repressing Fgf8 transcription. *Development*. 2014;141(15):2972-2977.

Kutejova E, Sasai N, Shah A, Gouti M, Briscoe J. Neural Progenitors Adopt Specific Identities by Directly Repressing All Alternative Progenitor Transcriptional Programs. Dev Cell. 2016 Mar 21;36(6):639-53.

Kwiatkowski TJ Jr, Bosco DA, Leclerc AL, Tamrazian E, Vanderburg CR, Russ C, Davis A, Gilchrist J, Kasarskis EJ, Munsat T, Valdmanis P, Rouleau GA, Hosler BA, Cortelli P, de Jong PJ, Yoshinaga Y, Haines JL, Pericak-Vance MA, Yan J, Ticozzi N, Siddique T, McKenna-Yasek D, Sapp PC, Horvitz HR, Landers JE, Brown RH Jr. Mutations in the FUS/TLS gene on chromosome 16 cause familial amyotrophic lateral sclerosis. Science. 2009 Feb 27;323(5918):1205-8.

Ladle D, Frank E. The role of the ETS gene PEA3 in the development of motor and sensory neurons. Physiol Behav. 2002;77(4–5):571–6.

Lagier-Tourenne C, Polymenidou M, Hutt KR, Vu AQ, Baughn M, Huelga SC, Clutario KM, Ling SC, Liang TY, Mazur C, Wancewicz E, Kim AS, Watt A, Freier S, Hicks GG, Donohue JP, Shiue L, Bennett CF, Ravits J, Cleveland DW, Yeo GW. Divergent roles of ALS-linked proteins FUS/TLS and TDP-43 intersect in processing long pre-mRNAs. Nat Neurosci. 2012 Nov;15(11):1488-97.

Lai HC, Seal RP, Johnson JE. Making sense out of spinal cord somatosensory development. Development. 2016 Oct 1;143(19):3434-3448.

Lance-Jones C, Omelchenko N, Bailis A, Lynch S, Sharma K. Hoxd10 induction and regionalization in the developing lumbosacral spinal cord. Development. 2001 Jun;128(12):2255-68.

Landmesser LT. The acquisition of motoneuron subtype identity and motor circuit formation. Int J Dev Neurosci. 2001 Apr;19(2):175-82.

Le Dréau G, Garcia-Campmany L, Rabadán MA, Ferronha T, Tozer S, Briscoe J, Martí E. Canonical BMP7 activity is required for the generation of discrete neuronal populations in the dorsal spinal cord. *Development.* 2012;139:259–268.

Le Dréau G, Martí E. Dorsal-ventral patterning of the neural tube: a tale of three signals. Dev Neurobiol. 2012 Dec;72(12):1471-81.

Le NT, Chang L, Kovlyagina I, Georgiou P, Safren N, Braunstein KE, Kvarta MD, Van Dyke AM, LeGates TA, Philips T, Morrison BM, Thompson SM, Puche AC, Gould TD, Rothstein JD, Wong PC, Monteiro MJ. Motor neuron disease, TDP-43 pathology, and memory deficits in mice expressing ALS-FTD-linked UBQLN2 mutations. Proc Natl Acad Sci U S A. 2016 Nov 22;113(47):E7580-E7589.

Lee KJ, Dietrich P, Jessell TM. Genetic ablation reveals that the roof plate is essential for dorsal interneuron specification. Nature. 2000 Feb 17;403(6771):734-40.

Leighton DJ, Newton J, Stephenson LJ, Colville S, Davenport R, Gorrie G, Morrison I, Swingler R, Chandran S, Pal S; CARE-MND Consortium. Changing epidemiology of motor neurone disease in Scotland. J Neurol. 2019 Apr;266(4):817-825.

Li WC, Moult PR. The control of locomotor frequency by excitation and inhibition. J Neurosci. 2012 May 2;32(18):6220-30.

Li XJ, Du ZW, Zarnowska ED, Pankratz M, Hansen LO, Pearce RA, Zhang SC. Specification of motoneurons from human embryonic stem cells. Nat Biotechnol. 2005 Feb;23(2):215-21.

Liddelow SA, Guttenplan KA, Clarke LE, Bennett FC, Bohlen CJ, Schirmer L, Bennett ML, Münch AE, Chung WS, Peterson TC, Wilton DK, Frouin A, Napier BA, Panicker N, Kumar M, Buckwalter MS, Rowitch DH, Dawson VL, Dawson TM, Stevens B, Barres BA. Neurotoxic reactive astrocytes are induced by activated microglia. Nature. 2017 Jan 26;541(7638):481-487.

Liem KF Jr, Jessell TM, Briscoe J. Regulation of the neural patterning activity of sonic hedgehog by secreted BMP inhibitors expressed by notochord and somites. Development. 2000 Nov;127(22):4855-66.

Liem KF Jr, Tremml G, Jessell TM. A role for the roof plate and its resident TGFbeta-related proteins in neuronal patterning in the dorsal spinal cord. Cell. 1997 Oct 3;91(1):127-38.

Liem KF Jr, Tremml G, Roelink H, Jessell TM. Dorsal differentiation of neural plate cells induced by BMP-mediated signals from epidermal ectoderm. Cell. 1995 Sep 22;82(6):969-79.

Lillo P, Hodges JR. Frontotemporal dementia and motor neurone disease: overlapping clinic-pathological disorders. J Clin Neurosci. 2009 Sep;16(9):1131-5.

Liu G, Byrd A, Warner AN, Pei F, Basha E, Buchanan A, Buchan JR. Cdc48/VCP and Endocytosis Regulate TDP-43 and FUS Toxicity and Turnover. Mol Cell Biol. 2020 Jan 30;40(4):e00256-19.

Liu JP, Laufer E, Jessell TM. Assigning the positional identity of spinal motor neurons: rostrocaudal patterning of Hox-c expression by FGFs, Gdf11, and retinoids. Neuron. 2001 Dec 20;32(6):997-1012.

Liu ZJ, Lin HX, Liu GL, Tao QQ, Ni W, Xiao BG, Wu ZY. The investigation of genetic and clinical features in Chinese patients with juvenile amyotrophic lateral sclerosis. Clin Genet. 2017 Sep;92(3):267-273.

Livet J, Sigrist M, Stroebel S, De Paola V, Price SR, Henderson CE, et al. ETS gene Pea3 controls the central position and terminal arborization of specific motor neuron pools. Neuron. 2002;29;35(5):877–92.

Logroscino G, Traynor BJ, Hardiman O, Chiò A, Mitchell D, Swingler RJ, Millul A, Benn E, Beghi E; EURALS. Incidence of amyotrophic lateral sclerosis in Europe. J Neurol Neurosurg Psychiatry. 2010 Apr;81(4):385-90.

Longinetti E, Fang F. Epidemiology of amyotrophic lateral sclerosis: an update of recent literature. *Curr Opin Neurol*. 2019;32(5):771-776.

Lu DC, Niu T, Alaynick WA. Molecular and cellular development of spinal cord locomotor circuitry. Front Mol Neurosci. 2015 Jun 16;8:25.

Luisier R, Tyzack GE, Hall CE, Mitchell JS, Devine H, Taha DM, Malik B, Meyer I, Greensmith L, Newcombe J, Ule J, Luscombe NM, Patani R. Intron retention and nuclear loss of SFPQ are molecular hallmarks of ALS. Nat Commun. 2018 May 22;9(1):2010.

Luty AA, Kwok JB, Dobson-Stone C, et al. Sigma nonopioid intracellular receptor 1 mutations cause frontotemporal lobar degeneration-motor neuron disease. *Ann Neurol*. 2010;68(5):639-649.

Lutz C. Mouse models of ALS: Past, present and future. Brain Res. 2018 Aug 15;1693(Pt A):1-10.

Mackenzie IR, Bigio EH, Ince PG, Geser F, Neumann M, Cairns NJ, Kwong LK, Forman MS, Ravits J, Stewart H, Eisen A, McClusky L, Kretzschmar HA, Monoranu CM, Highley JR, Kirby J, Siddique T, Shaw PJ, Lee VM, Trojanowski JQ. Pathological TDP-43 distinguishes sporadic amyotrophic lateral sclerosis from amyotrophic lateral sclerosis with SOD1 mutations. Ann Neurol. 2007 May;61(5):427-34.

Maekawa S, Al-Sarraj S, Kibble M, Landau S, Parnavelas J, Cotter D, Everall I, Leigh PN. Cortical selective vulnerability in motor neuron disease: a morphometric study. Brain. 2004 Jun;127(Pt 6):1237-51.

Mahony S, Mazzoni EO, McCuine S, Young RA, Wichterle H, Gifford DK. Ligand-dependent dynamics of retinoic acid receptor binding during early neurogenesis. Genome Biol. 2011;12(1):R2.

Mann JR, Gleixner AM, Mauna JC, Gomes E, DeChellis-Marks MR, Needham PG, Copley KE, Hurtle B, Portz B, Pyles NJ, Guo L, Calder CB, Wills ZP, Pandey UB, Kofler JK, Brodsky JL, Thathiah A, Shorter J, Donnelly CJ. RNA Binding Antagonizes Neurotoxic Phase Transitions of TDP-43. Neuron. 2019 Apr 17;102(2):321-338.e8.

Marder E, Bucher D. Central pattern generators and the control of rhythmic movements. Curr Biol. 2001 Nov 27;11(23):R986-96.

Marrone L, Drexler HCA, Wang J, Tripathi P, Distler T, Heisterkamp P, Anderson EN, Kour S, Moraiti A, Maharana S, Bhatnagar R, Belgard TG, Tripathy V, Kalmbach N, Hosseinzadeh Z, Crippa V, Abo-Rady M, Wegner F, Poletti A, Troost D, Aronica E, Busskamp V, Weis J, Pandey UB, Hyman AA, Alberti S, Goswami A, Sterneckert J. FUS pathology in ALS is linked to alterations in multiple ALS-associated proteins and rescued by drugs stimulating autophagy. Acta Neuropathol. 2019 Jul;138(1):67-84.

Marshall H, Nonchev S, Sham MH, Muchamore I, Lumsden A, Krumlauf R. Retinoic acid alters hindbrain Hox code and induces transformation of rhombomeres 2/3 into a 4/5 identity. Nature. 1992 Dec 24-31;360(6406):737-41.

Martí E, Bumcrot DA, Takada R, McMahon AP. Requirement of 19K form of Sonic hedgehog for induction of distinct ventral cell types in CNS explants. Nature. 1995 May 25;375(6529):322-5.

Maruyama H, Morino H, Ito H, et al. Mutations of optineurin in amyotrophic lateral sclerosis. *Nature*. 2010;465(7295):223-226.

Massagué J, Chen YG. Controlling TGF-beta signaling. Genes Dev. 2000 Mar 15;14(6):627-44.

Matej R, Tesar A, Rusina R. Alzheimer's disease and other neurodegenerative dementias in comorbidity: A clinical and neuropathological overview. Clin Biochem. 2019 Nov;73:26-31.

Maury Y, Côme J, Piskorowski RA, Salah-Mohellibi N, Chevaleyre V, Peschanski M, et al. Combinatorial analysis of developmental cues efficiently converts human pluripotent stem cells into multiple neuronal subtypes. Nat Biotechnol. 2015 Jan 1;33(1):89–96.

Mazzoni EO, Mahony S, Peljto M, Patel T, Thornton SR, McCuine S, Reeder C, Boyer LA, Young RA, Gifford DK, Wichterle H. Saltatory remodeling of Hox chromatin in response to rostrocaudal patterning signals. Nat Neurosci. 2013 Sep;16(9):1191-1198.

McGown A, McDearmid JR, Panagiotaki N, Tong H, Al Mashhadi S, Redhead N, Lyon AN, Beattie CE, Shaw PJ, Ramesh TM. Early interneuron dysfunction in ALS: insights from a mutant sod1 zebrafish model. Ann Neurol. 2013 Feb;73(2):246-58.

Mejzini R, Flynn LL, Pitout IL, Fletcher S, Wilton SD, Akkari PA. ALS Genetics, Mechanisms, and Therapeutics: Where Are We Now? Front Neurosci. 2019 Dec 6;13:1310.

Melamed Z, López-Erauskin J, Baughn MW, Zhang O, Drenner K, Sun Y, Freyermuth F, McMahon MA, Beccari MS, Artates JW, Ohkubo T, Rodriguez M, Lin N, Wu D, Bennett CF, Rigo F, Da Cruz S, Ravits J, Lagier-Tourenne C, Cleveland DW. Premature polyadenylation-mediated loss of stathmin-2 is a hallmark of TDP-43-dependent neurodegeneration. Nat Neurosci. 2019 Feb;22(2):180-190.

Menon P, Kiernan MC, Vucic S. Cortical hyperexcitability precedes lower motor neuron dysfunction in ALS. Clin Neurophysiol. 2015 Apr;126(4):803-9.

Metzis V, Steinhauser S, Pakanavicius E, Gouti M, Stamataki D, Ivanovitch K, Watson T, Rayon T, Mousavy Gharavy SN, Lovell-Badge R, Luscombe NM, Briscoe J. Nervous System Regionalization Entails Axial Allocation before Neural Differentiation. Cell. 2018 Nov 1;175(4):1105-1118.e17.

Meyer H, Bug M, Bremer S. Emerging functions of the VCP/p97 AAA-ATPase in the ubiquitin system. Nat Cell Biol. 2012 Feb 2;14(2):117-23.

Meyers EN, Martin GR. Differences in left-right axis pathways in mouse and chick: functions of FGF8 and SHH. *Science*. 1999;285(5426):403-406.

Miller RG, Mitchell JD, Moore DH. Riluzole for amyotrophic lateral sclerosis (ALS)/motor neuron disease (MND). Cochrane Database Syst Rev. 2012 Mar 14;2012(3):CD001447.

Millonig JH, Millen KJ, Hatten ME. The mouse Dreher gene Lmx1a controls formation of the roof plate in the vertebrate CNS. Nature. 2000 Feb 17;403(6771):764-9.

Mitchell J, Paul P, Chen HJ, et al. Familial amyotrophic lateral sclerosis is associated with a mutation in D-amino acid oxidase. *Proc Natl Acad Sci U S A*. 2010;107(16):7556-7561.

Molofsky AV, Krencik R, Ullian EM, Tsai HH, Deneen B, Richardson WD, Barres BA, Rowitch DH. Astrocytes and disease: a neurodevelopmental perspective. Genes Dev. 2012 May 1;26(9):891-907.

Monahan Z, Shewmaker F, Pandey UB. Stress granules at the intersection of autophagy and ALS. Brain Res. 2016 Oct 15;1649(Pt B):189-200.

Müller T, Anlag K, Wildner H, Britsch S, Treier M, Birchmeier C. The bHLH factor Olig3 coordinates the specification of dorsal neurons in the spinal cord. *Genes Dev*. 2005;19(6):733-743.

Müller T, Brohmann H, Pierani A, Heppenstall PA, Lewin GR, Jessell TM, et al. The homeodomain factor Lbx1 distinguishes two major programs of neuronal differentiation in the dorsal spinal cord. Neuron. 2002;34:551–562.

Münch C, Sedlmeier R, Meyer T, et al. Point mutations of the p150 subunit of dynactin (DCTN1) gene in ALS. *Neurology*. 2004;63(4):724-726.

Muroyama Y, Fujihara M, Ikeya M, Kondoh H, Takada S. Wnt signalling plays an essential role in neuronal specification of the dorsal spinal cord. Genes Dev. 2002 Mar 1;16(5):548-53.

Naiche LA, Holder N, Lewandoski M. FGF4 and FGF8 comprise the wavefront activity that controls somitogenesis. *Proc Natl Acad Sci U S A*. 2011;108(10):4018-4023.

Naiche LA, Holder N, Lewandoski M. FGF4 and FGF8 comprise the wavefront activity that controls somitogenesis. *Proc Natl Acad Sci U S A*. 2011;108(10):4018-4023.

Nalbandian A, Donkervoort S, Dec E, Badadani M, Katheria V, Rana P, Nguyen C, Mukherjee J, Caiozzo V, Martin B, Watts GD, Vesa J, Smith C, Kimonis VE. The multiple faces of valosin-containing protein-associated diseases: inclusion body myopathy with Paget's disease of bone, frontotemporal dementia, and amyotrophic lateral sclerosis. J Mol Neurosci. 2011 Nov;45(3):522-31.

Nalbandian A, Llewellyn KJ, Badadani M, Yin HZ, Nguyen C, Katheria V, Watts G, Mukherjee J, Vesa J, Caiozzo V, Mozaffar T, Weiss JH, Kimonis VE. A progressive translational mouse model of human valosin-containing protein disease: the VCP(R155H/+) mouse. Muscle Nerve. 2013 Feb;47(2):260-70.

Neumann M, Mackenzie IR, Cairns NJ, Boyer PJ, Markesbery WR, Smith CD, Taylor JP, Kretzschmar HA, Kimonis VE, Forman MS. TDP-43 in the ubiquitin pathology of frontotemporal dementia with VCP gene mutations. J Neuropathol Exp Neurol. 2007 Feb;66(2):152-7.

Neumann M, Sampathu DM, Kwong LK, Truax AC, Micsenyi MC, Chou TT, Bruce J, Schuck T, Grossman M, Clark CM, McCluskey LF, Miller BL, Masliah E, Mackenzie IR, Feldman H, Feiden W, Kretzschmar HA, Trojanowski JQ, Lee VM. Ubiquitinated TDP-43 in frontotemporal lobar degeneration and amyotrophic lateral sclerosis. Science. 2006 Oct 6;314(5796):130-3.

Nicolas A, Kenna KP, Renton AE, et al. Genome-wide Analyses Identify KIF5A as a Novel ALS Gene. *Neuron*. 2018;97(6):1268-1283.e6.

Niedermeyer S, Murn M, Choi PJ. Respiratory Failure in Amyotrophic Lateral Sclerosis. Chest. 2019 Feb;155(2):401-408.

Niederreither K, McCaffery P, Dräger UC, Chambon P, Dollé P. Restricted expression and retinoic acid-induced downregulation of the retinaldehyde dehydrogenase type 2 (RALDH-2) gene during mouse development. Mech Dev. 1997 Feb;62(1):67-78.

Niederreither K, Vermot J, Schuhbaur B, Chambon P, Dollé P. Retinoic acid synthesis and hindbrain patterning in the mouse embryo. Development. 2000 Jan;127(1):75-85.

Nihei K, McKee AC, Kowall NW. Patterns of neuronal degeneration in the motor cortex of amyotrophic lateral sclerosis patients. Acta Neuropathol. 1993;86(1):55-64.

Nijssen J, Comley LH, Hedlund E. Motor neuron vulnerability and resistance in amyotrophic lateral sclerosis. Acta Neuropathol. 2017 Jun;133(6):863-885.

Nilsen TW, Graveley BR. Expansion of the eukaryotic proteome by alternative splicing. Nature. 2010 Jan 28;463(7280):457-63.

Nimmerjahn A, Kirchhoff F, Helmchen F. Resting microglial cells are highly dynamic surveillants of brain parenchyma in vivo. Science. 2005 May 27;308(5726):1314-8.

Nishi Y, Zhang X, Jeong J, Peterson KA, Vedenko A, Bulyk ML, Hide WA, McMahon AP. A direct fate exclusion mechanism by Sonic hedgehog-regulated transcriptional repressors. Development. 2015 Oct 1;142(19):3286-93.

Nishimura AL, Mitne-Neto M, Silva HC, et al. A mutation in the vesicle-trafficking protein VAPB causes late-onset spinal muscular atrophy and amyotrophic lateral sclerosis. *Am J Hum Genet*. 2004;75(5):822-831.

Nordström U, Jessell TM, Edlund T. Progressive induction of caudal neural character by graded Wnt signaling. Nat Neurosci. 2002 Jun;5(6):525-32.

Nornes HO, Carry M. Neurogenesis in spinal cord of mouse: an autoradiographic analysis. Brain Res. 1978 Dec 22;159(1):1-6.

Novitch BG, Wichterle H, Jessell TM, Sockanathan S. A requirement for retinoic acid-mediated transcriptional activation in ventral neural patterning and motor neuron specification. Neuron. 2003;40(1):81–95.

Ogura T, Sakaguchi H, Miyamoto S, Takahashi J. Three-dimensional induction of dorsal, intermediate and ventral spinal cord tissues from human pluripotent stem cells. Development. 2018 Jul 30;145(16):dev162214.

Okada Y, Shimazaki T, Sobue G, Okano H. Retinoic-acid-concentration-dependent acquisition of neural cell identity during in vitro differentiation of mouse embryonic stem cells. Dev Biol. 2004;275(1):124–42.

Okigawa S, Mizoguchi T, Okano M, Tanaka H, Isoda M, Jiang YJ, Suster M, Higashijima S, Kawakami K, Itoh M. Different combinations of Notch ligands and receptors regulate V2 interneuron progenitor proliferation and V2a/V2b cell fate determination. Dev Biol. 2014 Jul 15;391(2):196-206.

Okita K, Matsumura Y, Sato Y, Okada A, Morizane A, Okamoto S, Hong H, Nakagawa M, Tanabe K, Tezuka K, Shibata T, Kunisada T, Takahashi M, Takahashi J, Saji H, Yamanaka S. A more efficient method to generate integration-free human iPS cells. Nat Methods. 2011 May;8(5):409-12.

Olivera-Martinez I, Storey KG. Wnt signals provide a timing mechanism for the FGF-retinoid differentiation switch during vertebrate body axis extension. Development. 2007 Jun;134(11):2125-35.

Orlacchio A, Babalini C, Borreca A, et al. SPATACSIN mutations cause autosomal recessive juvenile amyotrophic lateral sclerosis. *Brain*. 2010;133(Pt 2):591-598.

Orozco D, Tahirovic S, Rentzsch K, Schwenk BM, Haass C, Edbauer D. Loss of fused in sarcoma (FUS) promotes pathological Tau splicing. EMBO Rep. 2012 Aug;13(8):759-64.

Pan GJ, Chang ZY, Schöler HR, Pei D. Stem cell pluripotency and transcription factor Oct4. Cell Res. 2002 Dec;12(5-6):321-9.

Pandya VA, Patani R. Decoding the relationship between ageing and amyotrophic lateral sclerosis: a cellular perspective. Brain. 2020 Apr 1;143(4):1057-1072.

Pandya VA, Patani R. Region-specific vulnerability in neurodegeneration: lessons from normal ageing. Ageing Res Rev. 2021 May;67:101311.

Parkinson N, Ince PG, Smith MO, et al. ALS phenotypes with mutations in CHMP2B (charged multivesicular body protein 2B). *Neurology*. 2006;67(6):1074-1077.

Parr BA, Shea MJ, Vassileva G, McMahon AP. Mouse Wnt genes exhibit discrete domains of expression in the early embryonic CNS and limb buds. Development. 1993 Sep;119(1):247-61.

Patani R, Hollins AJ, Wishart TM, Puddifoot CA, Álvarez S, De Lera AR, et al. Retinoid-independent motor neurogenesis from human embryonic stem cells reveals a medial columnar ground state. Nat Commun. 2011;2(1):1–10.

Patani R. Generating Diverse Spinal Motor Neuron Subtypes from Human Pluripotent Stem Cells. Stem Cells Int. 2016;2016:1036974.

Patani R. The FUS about SFPQ in FTLD spectrum disorders. Brain. 2020 Aug 1;143(8):2330-2332.

Pearson KG. Generating the walking gait: role of sensory feedback. Prog Brain Res. 2004;143:123-9.

Peirs C, Williams SP, Zhao X, Walsh CE, Gedeon JY, Cagle NE, Goldring AC, Hioki H, Liu Z, Marell PS, Seal RP. Dorsal Horn Circuits for Persistent Mechanical Pain. Neuron. 2015 Aug 19;87(4):797-812.

Peterson KA, Nishi Y, Ma W, Vedenko A, Shokri L, Zhang X, McFarlane M, Baizabal JM, Junker JP, van Oudenaarden A, Mikkelsen T, Bernstein BE, Bailey TL, Bulyk ML, Wong WH, McMahon AP. Neural-specific Sox2 input and differential Gli-binding affinity provide context and positional information in Shh-directed neural patterning. Genes Dev. 2012 Dec 15;26(24):2802-16.

Philippidou P, Dasen JS. Hox genes: choreographers in neural development, architects of circuit organization. *Neuron*. 2013;80(1):12-34.

Philippidou P, Walsh CM, Aubin J, Jeannotte L, Dasen JS. Sustained Hox5 gene activity is required for respiratory motor neuron development. *Nat. Neurosci.* 2012;15:1636–1644.

Pierani A, Brenner-Morton S, Chiang C, Jessell TM. A sonic hedgehog-independent, retinoid-activated pathway of neurogenesis in the ventral spinal cord. Cell. 1999 Jun 25;97(7):903-15.

Pierani A, Moran-Rivard L, Sunshine MJ, Littman DR, Goulding M, Jessell TM. Control of interneuron fate in the developing spinal cord by the progenitor homeodomain protein Dbx1. Neuron. 2001 Feb;29(2):367-84.

Pillai A, Mansouri A, Behringer R, Westphal H, Goulding M. Lhx1 and Lhx5 maintain the inhibitory-neurotransmitter status of interneurons in the dorsal spinal cord. Development. 2007 Jan;134(2):357-66.

Polymenidou M, Lagier-Tourenne C, Hutt KR, Huelga SC, Moran J, Liang TY, Ling SC, Sun E, Wancewicz E, Mazur C, Kordasiewicz H, Sedaghat Y, Donohue JP, Shiue L, Bennett CF, Yeo GW, Cleveland DW. Long pre-mRNA depletion and RNA missplicing contribute to neuronal vulnerability from loss of TDP-43. Nat Neurosci. 2011 Apr;14(4):459-68.

Prasad A, Hollyday M. Development and migration of avian sympathetic preganglionic neurons. J Comp Neurol. 1991 May 8;307(2):237-58.

Protter DSW, Parker R. Principles and Properties of Stress Granules. Trends Cell Biol. 2016 Sep;26(9):668-679.

Purice MD, Taylor JP. Linking hnRNP Function to ALS and FTD Pathology. Front Neurosci. 2018 May 15;12:326.

Rakic P. The radial edifice of cortical architecture: from neuronal silhouettes to genetic engineering. *Brain Res Rev*. 2007;55(2):204-219.

Ravanelli AM, Appel B. Motor neurons and oligodendrocytes arise from distinct cell lineages by progenitor recruitment. Genes Dev. 2015;29(23):2504–15.

Ravits JM, La Spada AR. ALS motor phenotype heterogeneity, focality, and spread: deconstructing motor neuron degeneration. Neurology. 2009 Sep 8;73(10):805-11.

Raynor EM, Shefner JM. Recurrent inhibition is decreased in patients with amyotrophic lateral sclerosis. Neurology. 1994 Nov;44(11):2148-53.

Reber S, Stettler J, Filosa G, Colombo M, Jutzi D, Lenzken SC, Schweingruber C, Bruggmann R, Bachi A, Barabino SM, Mühlemann O, Ruepp MD. Minor intron splicing is regulated by FUS and affected by ALS-associated FUS mutants. EMBO J. 2016 Jul 15;35(14):1504-21.

Roelink H, Porter JA, Chiang C, Tanabe Y, Chang DT, Beachy PA, Jessell TM. Floor plate and motor neuron induction by different concentrations of the amino-terminal cleavage product of sonic hedgehog autoproteolysis. Cell. 1995 May 5;81(3):445-55.

Rosen DR, Siddique T, Patterson D, Figlewicz DA, Sapp P, Hentati A, Donaldson D, Goto J, O'Regan JP, Deng HX, et al. Mutations in Cu/Zn superoxide dismutase gene are associated with familial amyotrophic lateral sclerosis. Nature. 1993 Mar 4;362(6415):59-62.

Rousso DL, Gaber ZB, Wellik D, Morrisey EE, Novitch BG. Coordinated Actions of the Forkhead Protein Foxp1 and Hox Proteins in the Columnar Organization of Spinal Motor Neurons. Neuron. 2008;59(2):226–40.

Rowitch DH, Kriegstein AR. Developmental genetics of vertebrate glial-cell specification. Nature. 2010 Nov 11;468(7321):214-22.

Rowitch DH, Lu QR, Kessaris N, Richardson WD. An “oligarchy” rules neural development. Trends in Neurosciences 2002;25:417-422.

Saade M, Gonzalez-Gobartt E, Escalona R, Usieto S, Martí E. Shh-mediated centrosomal recruitment of PKA promotes symmetric proliferative neuroepithelial cell division. Nat Cell Biol. 2017;19(5):493–503.

Sagner A, Briscoe J. Establishing neuronal diversity in the spinal cord: a time and a place. Development. 2019 Nov 25;146(22):dev182154.

Sagner A, Gaber ZB, Delile J, Kong JH, Rousso DL, Pearson CA, et al. Olig2 and Hes regulatory dynamics during motor neuron differentiation revealed by single cell transcriptomics. PLoS Biol. 2018;16(2):e2003127.

Sama RR, Ward CL, Kaushansky LJ, Lemay N, Ishigaki S, Urano F, Bosco DA. FUS/TLS assembles into stress granules and is a prosurvival factor during hyperosmolar stress. J Cell Physiol. 2013 Nov;228(11):2222-31.

Sapkota D, Chintala H, Wu F, Fliesler SJ, Hu Z, Mu X. Onecut1 and Onecut2 redundantly regulate early retinal cell fates during development. Proc Natl Acad Sci U S A. 2014 Sep 30;111(39):E4086-95.

Schafer DP, Lehrman EK, Stevens B. The "quad-partite" synapse: microglia-synapse interactions in the developing and mature CNS. Glia. 2013 Jan;61(1):24-36.

Seguin SJ, Morelli FF, Vinet J, Amore D, De Biasi S, Poletti A, Rubinsztein DC, Carra S. Inhibition of autophagy, lysosome and VCP function impairs stress granule assembly. Cell Death Differ. 2014 Dec;21(12):1838-51.

Shah V, Drill E, Lance-Jones C. Ectopic expression of Hoxd10 in thoracic spinal segments induces motoneurons with a lumbosacral molecular profile and axon projections to the limb. Dev Dyn. 2004 Sep;231(1):43-56.

Shang Y, Huang EJ. Mechanisms of FUS mutations in familial amyotrophic lateral sclerosis. Brain Res. 2016 Sep 15;1647:65-78.

Sharma K, Leonard AE, Lettieri K, Pfaff SL. Genetic and epigenetic mechanisms contribute to motor neuron pathfinding. Nature. 2000 Aug 3;406(6795):515-9.

Sharma K, Sheng HZ, Lettieri K, Li H, Karavanov A, Potter S, et al. LIM homeodomain factors Lhx3 and Lhx4 assign subtype identities for motor neurons. Cell. 1998;95(6):817–28.

Sinha S, Chen JK. Purmorphamine activates the Hedgehog pathway by targeting Smoothened. Nat Chem Biol. 2006 Jan;2(1):29-30.

Sirbu IO, Duester G. Retinoic-acid signalling in node ectoderm and posterior neural plate directs left-right patterning of somitic mesoderm. *Nat Cell Biol*. 2006;8(3):271-277.

Smethurst P, Risse E, Tyzack GE, Mitchell JS, Taha DM, Chen Y-R, et al. Distinct responses of neurons and astrocytes to TDP-43 proteinopathy in amyotrophic lateral sclerosis. Brain. 2020;143(2):430–40.

Smethurst P, Sidle KC, Hardy J. Review: Prion-like mechanisms of transactive response DNA binding protein of 43 kDa (TDP-43) in amyotrophic lateral sclerosis (ALS). Neuropathol Appl Neurobiol. 2015 Aug;41(5):578-97.

Smith BN, Ticozzi N, Fallini C, et al. Exome-wide rare variant analysis identifies TUBA4A mutations associated with familial ALS. *Neuron*. 2014;84(2):324-331.

Sockanathan S, Jessell TM. Motor neuron-derived retinoid signalling specifies the subtype identity of spinal motor neurons. Cell. 1998;94(4):503–14.

Sockanathan S, Perlmann T, Jessell TM. Retinoid receptor signaling in postmitotic motor neurons regulates rostrocaudal positional identity and axonal projection pattern. Neuron. 2003 Sep 25;40(1):97-111.

Solter D, Skreb N, Damjanov I. Extrauterine growth of mouse egg-cylinders results in malignant teratoma. Nature. 1970 Aug 1;227(5257):503-4.

Song MR, Sun Y, Bryson A, Gill GN, Evans SM, Pfaff SL. Islet-to-LMO stoichiometries control the function of transcription complexes that specify motor neuron and V2a interneuron identity. Development. 2009 Sep;136(17):2923-32.

Stephens B, Guiloff RJ, Navarrete R, Newman P, Nikhar N, Lewis P. Widespread loss of neuronal populations in the spinal ventral horn in sporadic motor neuron disease. A morphometric study. J Neurol Sci. 2006 May 15;244(1-2):41-58.

Stern CD, Charité J, Deschamps J, Duboule D, Durston AJ, Kmita M, Nicolas JF, Palmeirim I, Smith JC, Wolpert L. Head-tail patterning of the vertebrate embryo: one, two or many unresolved problems? Int J Dev Biol. 2006;50(1):3-15.

Stevens LC, Little CC. Spontaneous Testicular Teratomas in an Inbred Strain of Mice. *Proc Natl Acad Sci U S A*. 1954;40(11):1080-1087.

Stifani N. Motor neurons and the generation of spinal motor neuron diversity. Front Cell Neurosci. 2014 Oct 9;8:293.

Stolt CC, Lommes P, Sock E, Chaboissier MC, Schedl A, Wegner M. The Sox9 transcription factor determines glial fate choice in the developing spinal cord. Genes Dev. 2003 Jul 1;17(13):1677-89.

Streit A, Berliner AJ, Papanayotou C, Sirulnik A, Stern CD. Initiation of neural induction by FGF signalling before gastrulation. Nature. 2000 Jul 6;406(6791):74-8.

Suk TR, Rousseaux MWC. The role of TDP-43 mislocalization in amyotrophic lateral sclerosis. Mol Neurodegener. 2020 Aug 15;15(1):45.

Sun X, Qiu H. Valosin-Containing Protein, a Calcium-Associated ATPase Protein, in Endoplasmic Reticulum and Mitochondrial Function and Its Implications for Diseases. Int J Mol Sci. 2020 May 28;21(11):3842.

Suter DM, Tirefort D, Julien S, Krause KH. A Sox1 to Pax6 switch drives neuroectoderm to radial glia progression during differentiation of mouse embryonic stem cells. Stem Cells. 2009 Jan;27(1):49-58.

Swinnen B, Robberecht W. The phenotypic variability of amyotrophic lateral sclerosis. Nat Rev Neurol. 2014 Nov;10(11):661-70.

Szabo NE, da Silva RV, Sotocinal SG, Zeilhofer HU, Mogil JS, Kania A. Hoxb8 intersection defines a role for Lmx1b in excitatory dorsal horn neuron development, spinofugal connectivity, and nociception. J Neurosci. 2015 Apr 1;35(13):5233-46.

Takahashi K, Tanabe K, Ohnuki M, Narita M, Ichisaka T, Tomoda K, Yamanaka S. Induction of pluripotent stem cells from adult human fibroblasts by defined factors. Cell. 2007 Nov 30;131(5):861-72.

Takahashi K, Yamanaka S. Induction of pluripotent stem cells from mouse embryonic and adult fibroblast cultures by defined factors. Cell. 2006 Aug 25;126(4):663-76.

Takebayashi H, Nabeshima Y, Yoshida S, Chisaka O, Ikenaka K, Nabeshima Y. The basic helix-loop-helix factor olig2 is essential for the development of motoneuron and oligodendrocyte lineages. Curr Biol. 2002 Jul 9;12(13):1157-63.

Thaler JP, Koo SJ, Kania A, Lettieri K, Andrews S, Cox C, Jessell TM, Pfaff SL. A postmitotic role for Isl-class LIM homeodomain proteins in the assignment of visceral spinal motor neuron identity. Neuron. 2004 Feb 5;41(3):337-50.

Thaler JP, Lee SK, Jurata LW, Gill GN, Pfaff SL. LIM factor Lhx3 contributes to the specification of motor neuron and interneuron identity through cell-type-specific protein-protein interactions. Cell. 2002;110(2):237–49.

Thiry L, Hamel R, Pluchino S, Durcan T, Stifani S. Characterization of Human iPSC-derived Spinal Motor Neurons by Single-cell RNA Sequencing. Neuroscience. 2020 Dec 1;450:57-70.

Thomson JA, Itskovitz-Eldor J, Shapiro SS, Waknitz MA, Swiergiel JJ, Marshall VS, Jones JM. Embryonic stem cell lines derived from human blastocysts. Science. 1998;282:1145–7.

Timmer J, Chesnutt C, Niswander L. The Activin signalling pathway promotes differentiation of dI3 interneurons in the spinal neural tube. Developmental Biology. 2005;285:1–10.

Timmer JR, Wang C, Niswander L. BMP signalling patterns the dorsal and intermediate neural tube via regulation of homeobox and helix-loop-helix transcription factors. Development. 2002;129:2459–2472.

Tollervey JR, Curk T, Rogelj B, Briese M, Cereda M, Kayikci M, König J, Hortobágyi T, Nishimura AL, Zupunski V, Patani R, Chandran S, Rot G, Zupan B, Shaw CE, Ule J. Characterizing the RNA targets and position-dependent splicing regulation by TDP-43. Nat Neurosci. 2011 Apr;14(4):452-8.

Tosney KW, Hotary KB, Lance-Jones C. Specifying the target identity of motoneurons. Bioessays. 1995 May;17(5):379-82.

Tozer S, Le Dréau G, Marti E, Briscoe J. Temporal control of BMP signalling determines neuronal subtype identity in the dorsal neural tube. *Development.* 2013;140:1467–1474.

Tsuchida T, Ensini M, Morton SB, Baldassare M, Edlund T, Jessell TM, Pfaff SL. Topographic organization of embryonic motor neurons defined by expression of LIM homeobox genes. Cell. 1994 Dec 16;79(6):957-70.

Turakhiya A, Meyer SR, Marincola G, Böhm S, Vanselow JT, Schlosser A, Hofmann K, Buchberger A. ZFAND1 Recruits p97 and the 26S Proteasome to Promote the Clearance of Arsenite-Induced Stress Granules. Mol Cell. 2018 Jun 7;70(5):906-919.e7.

Tyzack GE, Luisier R, Taha DM, Neeves J, Modic M, Mitchell JS, Meyer I, Greensmith L, Newcombe J, Ule J, Luscombe NM, Patani R. Widespread FUS mislocalization is a molecular hallmark of amyotrophic lateral sclerosis. Brain. 2019 Sep 1;142(9):2572-2580.

Tyzack GE, Neeves J, Crerar H, Klein P, Ziff O, Taha DM, Luisier R, Luscombe NM, Patani R. Aberrant cytoplasmic intron retention is a blueprint for RNA binding protein mislocalization in amyotrophic lateral sclerosis. Brain. 2021 Mar 9:awab078.

Van Deerlin VM, Leverenz JB, Bekris LM, et al. TARDBP mutations in amyotrophic lateral sclerosis with TDP-43 neuropathology: a genetic and histopathological analysis. *Lancet Neurol*. 2008;7(5):409-416

Vance C, Rogelj B, Hortobágyi T, De Vos KJ, Nishimura AL, Sreedharan J, Hu X, Smith B, Ruddy D, Wright P, Ganesalingam J, Williams KL, Tripathi V, Al-Saraj S, Al-Chalabi A, Leigh PN, Blair IP, Nicholson G, de Belleroche J, Gallo JM, Miller CC, Shaw CE. Mutations in FUS, an RNA processing protein, cause familial amyotrophic lateral sclerosis type 6. Science. 2009 Feb 27;323(5918):1208-1211.

Vasile F, Dossi E, Rouach N. Human astrocytes: structure and functions in the healthy brain. Brain Struct Funct. 2017 Jul;222(5):2017-2029.

Vermot J, Schuhbaur B, Le Mouellic H, McCaffery P, Garnier JM, Hentsch D, Brûlet P, Niederreither K, Chambon P, Dollé P, Le Roux I. Retinaldehyde dehydrogenase 2 and Hoxc8 are required in the murine brachial spinal cord for the specification of Lim1+ motoneurons and the correct distribution of Islet1+ motoneurons. Development. 2005 Apr;132(7):1611-21.

Vijayakumar UG, Milla V, Cynthia Stafford MY, Bjourson AJ, Duddy W, Duguez SM. A Systematic Review of Suggested Molecular Strata, Biomarkers and Their Tissue Sources in ALS. Front Neurol. 2019 May 14;10:400.

Vucic S, Kiernan MC. Axonal excitability properties in amyotrophic lateral sclerosis. Clin Neurophysiol. 2006 Jul;117(7):1458-66.

Wang RN, Green J, Wang Z, Deng Y, Qiao M, Peabody M, Zhang Q, Ye J, Yan Z, Denduluri S, Idowu O, Li M, Shen C, Hu A, Haydon RC, Kang R, Mok J, Lee MJ, Luu HL, Shi LL. Bone Morphogenetic Protein (BMP) signalling in development and human diseases. Genes Dis. 2014 Sep;1(1):87-105.

Wang Z, Li L, Goulding M, Frank E. Early postnatal development of reciprocal Ia inhibition in the murine spinal cord. J Neurophysiol. 2008 Jul;100(1):185-96.

Weihl CC, Temiz P, Miller SE, et al. TDP-43 accumulation in inclusion body myopathy muscle suggests a common pathogenic mechanism with frontotemporal dementia. *J Neurol Neurosurg Psychiatry*. 2008;79(10):1186-1189.

White N, Sakiyama-Elbert SE. Derivation of Specific Neural Populations From Pluripotent Cells for Understanding and Treatment of Spinal Cord Injury. *Dev Dyn*. 2019;248(1):78-87.

Wilson L, Gale E, Chambers D, Maden M. Retinoic acid and the control of dorsoventral patterning in the avian spinal cord. Developmental Biology. 2004;269:433–446.

Wilson L, Gale E, Maden M. The role of retinoic acid in the morphogenesis of the neural tube. J Anat. 2003;203(4):357–68.

Wine-Lee L, Ahn KJ, Richardson RD, Mishina Y, Lyons KM, Crenshaw EB 3rd. Signaling through BMP type 1 receptors is required for development of interneuron cell types in the dorsal spinal cord. Development. 2004 Nov;131(21):5393-403.

Wodarz A, Nusse R. Mechanisms of Wnt signalling in development. Annu Rev Cell Dev Biol. 1998;14:59-88.

Wu CH, Fallini C, Ticozzi N, et al. Mutations in the profilin 1 gene cause familial amyotrophic lateral sclerosis. *Nature*. 2012;488(7412):499-503.

Wu S, Wu Y, Capecchi MR. Motoneurons and oligodendrocytes are sequentially generated from neural stem cells but do not appear to share common lineage-restricted progenitors in vivo. Development. 2006;133(4):581–90.

Xia D, Tang WK, Ye Y. Structure and function of the AAA+ ATPase p97/Cdc48p. *Gene*. 2016;583(1):64-77.

Xu H, Sakiyama-Elbert SE. Directed Differentiation of V3 Interneurons from Mouse Embryonic Stem Cells. Stem Cells Dev. 2015 Nov 15;24(22):2723-32.

Xu Y, Lopes C, Wende H, Guo Z, Cheng L, Birchmeier C, Ma Q. Ontogeny of excitatory spinal neurons processing distinct somatic sensory modalities. J Neurosci. 2013 Sep 11;33(37):14738-48.

Xue YC, Ng CS, Xiang P, Liu H, Zhang K, Mohamud Y, Luo H. Dysregulation of RNA-Binding Proteins in Amyotrophic Lateral Sclerosis. Front Mol Neurosci. 2020 May 29;13:78.

Yan J, Deng HX, Siddique N, Fecto F, Chen W, Yang Y, Liu E, Donkervoort S, Zheng JG, Shi Y, Ahmeti KB, Brooks B, Engel WK, Siddique T. Frameshift and novel mutations in FUS in familial amyotrophic lateral sclerosis and ALS/dementia. Neurology. 2010 Aug 31;75(9):807-14.

Yang Y, Hentati A, Deng HX, et al. The gene encoding alsin, a protein with three guanine-nucleotide exchange factor domains, is mutated in a form of recessive amyotrophic lateral sclerosis. *Nat Genet*. 2001;29(2):160-165.

Yasuda K, Zhang H, Loiselle D, Haystead T, Macara IG, Mili S. The RNA-binding protein Fus directs translation of localized mRNAs in APC-RNP granules. J Cell Biol. 2013 Dec 9;203(5):737-46.

Yu WP, Collarini EJ, Pringle NP, Richardson WD. Embryonic expression of myelin genes: evidence for a focal source of oligodendrocyte precursors in the ventricular zone of the neural tube. Neuron. 1994 Jun;12(6):1353-62.

Yuengert R, Hori K, Kibodeaux EE, McClellan JX, Morales JE, Huang TP, Neul JL, Lai HC. Origin of a Non-Clarke's Column Division of the Dorsal Spinocerebellar Tract and the Role of Caudal Proprioceptive Neurons in Motor Function. Cell Rep. 2015 Nov 10;13(6):1258-1271.

Zagorski M, Tabata Y, Brandenberg N, Lutolf MP, Tkačik G, Bollenbach T, et al. Decoding of position in the developing neural tube from antiparallel morphogen gradients. Science. 2017;356(6345):1379–83.

Zechner D, Fujita Y, Hülsken J, Müller T, Walther I, Taketo MM, et al. β-Catenin signals regulate cell growth and the balance between progenitor cell expansion and differentiation in the nervous system. Developmental Biology. 2003;258:406–418.

Zechner D, Müller T, Wende H, Walther I, Taketo MM, Crenshaw EB, et al. Bmp and Wnt/β-catenin signals control expression of the transcription factor Olig3 and the specification of spinal cord neurons. Developmental Biology. 2007;303:181–190.

Zhang J, Lanuza GM, Britz O, Wang Z, Siembab VC, Zhang Y, Velasquez T, Alvarez FJ, Frank E, Goulding M. V1 and v2b interneurons secure the alternating flexor-extensor motor activity mice require for limbed locomotion. Neuron. 2014 Apr 2;82(1):138-50.

Zhang S, Cui W. Sox2, a key factor in the regulation of pluripotency and neural differentiation. World J Stem Cells. 2014 Jul 26;6(3):305-11.

Zhang Y, Narayan S, Geiman E, Lanuza GM, Velasquez T, Shanks B, Akay T, Dyck J, Pearson K, Gosgnach S, Fan CM, Goulding M. V3 spinal neurons establish a robust and balanced locomotor rhythm during walking. Neuron. 2008 Oct 9;60(1):84-96.

Zhao M, Kim JR, van Bruggen R, Park J. RNA-Binding Proteins in Amyotrophic Lateral Sclerosis. *Mol Cells*. 2018;41(9):818-829.

Zhou Q, Anderson DJ. The bHLH transcription factors OLIG2 and OLIG1 couple neuronal and glial subtype specification. Cell. 2002 Apr 5;109(1):61-73.

Ziemann U, Winter M, Reimers CD, Reimers K, Tergau F, Paulus W. Impaired motor cortex inhibition in patients with amyotrophic lateral sclerosis. Evidence from paired transcranial magnetic stimulation. Neurology. 1997 Nov;49(5):1292-8.

Ziff OJ, Taha DM, Crerar H, Clarke BE, Chakrabarti AM, Kelly G, Neeves J, Tyzack GE, Luscombe NM, Patani R. Reactive astrocytes in ALS display diminished intron retention. Nucleic Acids Res. 2021 Apr 6;49(6):3168-3184.

Zirra A, Wiethoff S, Patani R. Neural Conversion and Patterning of Human Pluripotent Stem Cells: A Developmental Perspective. Stem Cells Int. 2016;2016:8291260.

Zou ZY, Liu MS, Li XG, Cui LY. Mutations in SOD1 and FUS caused juvenile-onset sporadic amyotrophic lateral sclerosis with aggressive progression. Ann Transl Med. 2015 Sep;3(15):221.

Zou ZY, Zhou ZR, Che CH, Liu CY, He RL, Huang HP. Genetic epidemiology of amyotrophic lateral sclerosis: a systematic review and meta-analysis. J Neurol Neurosurg Psychiatry. 2017 Jul;88(7):540-549.